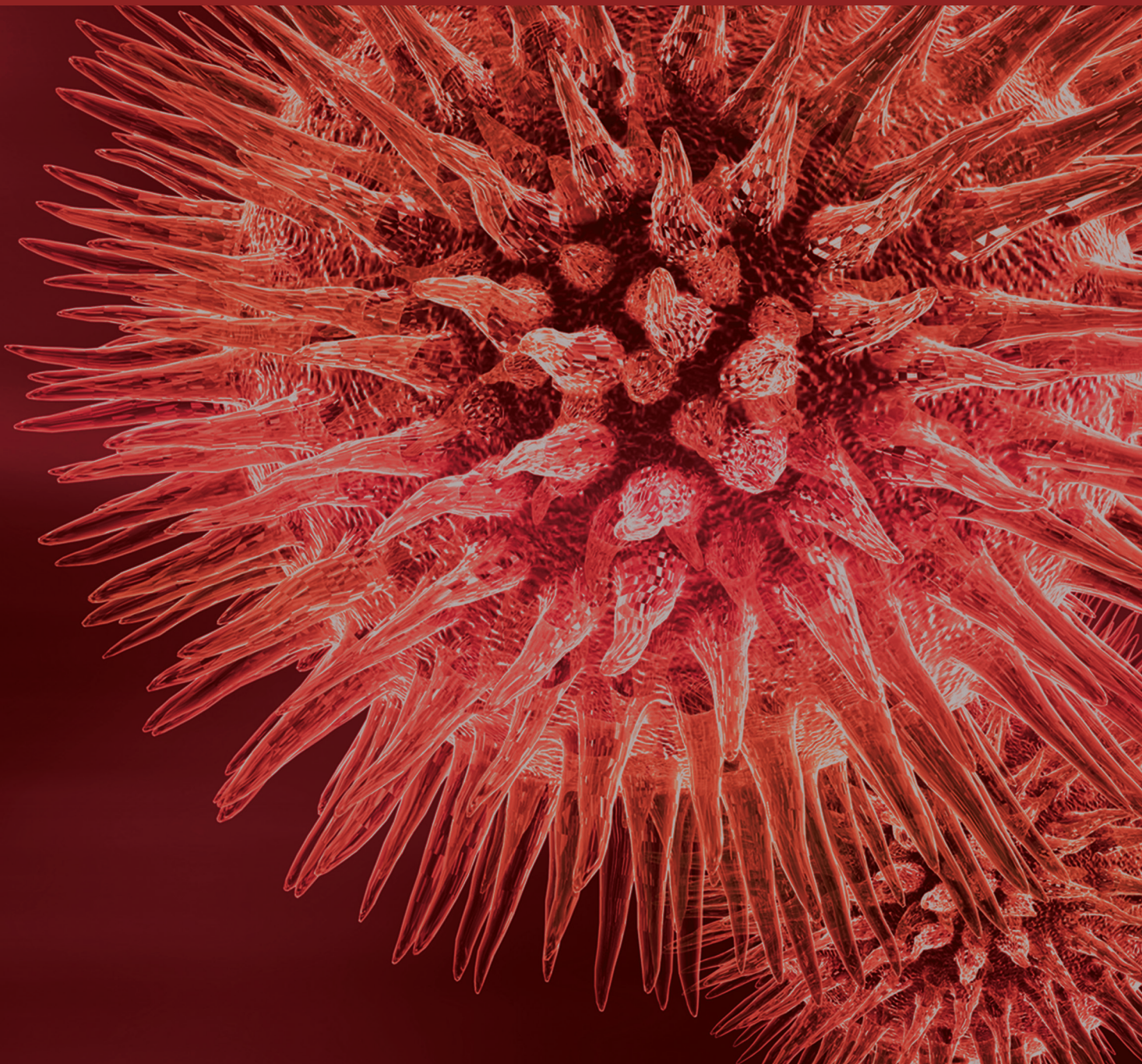


Diagnostic and Interventional Radiology for Liver Diseases

Guest Editors: Satoru Murata, Pascal Niggemann, Edward W. Lee,
and Per Kristian Hol





Diagnostic and Interventional Radiology for Liver Diseases

BioMed Research International

Diagnostic and Interventional Radiology for Liver Diseases

Guest Editors: Satoru Murata, Pascal Niggemann,
Edward W. Lee, and Per Kristian Hol



Copyright © 2015 Hindawi Publishing Corporation. All rights reserved.

This is a special issue published in “BioMed Research International.” All articles are open access articles distributed under the Creative Commons Attribution License, which permits unrestricted use, distribution, and reproduction in any medium, provided the original work is properly cited.

Contents

Diagnostic and Interventional Radiology for Liver Diseases, Satoru Murata, Pascal Niggemann, Edward W. Lee, and Per Kristian Hol
Volume 2015, Article ID 147583, 2 pages

Recent Advances in Molecular Magnetic Resonance Imaging of Liver Fibrosis, Zhiming Li, Jihong Sun, and Xiaoming Yang
Volume 2015, Article ID 595467, 12 pages

Ultrafast Cone-Beam Computed Tomography: A Comparative Study of Imaging Protocols during Image-Guided Therapy Procedure, Jijo Paul, Annamma Chacko, Mohammad Farhang, Shahram Kamali, Mohsen Tavanania, Thomas Vogl, and Bitu Panahi
Volume 2015, Article ID 467850, 8 pages

Measurement of Liver Iron Concentration by MRI Is Reproducible, José María Alústiza, José I. Emparanza, Agustín Castiella, Alfonso Casado, Adolfo Garrido, Pablo Aldazábal, Manuel San Vicente, Nerea Garcia, Ana Belén Asensio, Jesús Banales, Emma Salvador, Aranzazu Moyua, Xabier Arozena, Miguel Zarco, Lourdes Jauregui, and Ohiana Vicente
Volume 2015, Article ID 294024, 8 pages

Diffusion-Weighted MRI for the Assessment of Liver Fibrosis: Principles and Applications, Stefano Palmucci, Giuseppina Cappello, Giancarlo Attinà, Giovanni Fuccio Sanzà, Pietro Valerio Foti, Giovanni Carlo Ettorre, and Pietro Milone
Volume 2015, Article ID 874201, 7 pages

Diagnostic Value of MRI Proton Density Fat Fraction for Assessing Liver Steatosis in Chronic Viral C Hepatitis, Francesco Paparo, Giovanni Cenderello, Matteo Revelli, Lorenzo Bacigalupo, Mariangela Rutigliani, Daniele Zefiro, Luca Cevasco, Maria Amico, Roberto Bandelloni, Giovanni Cassola, Gian Luca Forni, and Gian Andrea Rollandi
Volume 2015, Article ID 758164, 11 pages

Partial Splenic Embolization with Transarterial Chemoembolization in Patients with Hepatocellular Carcinoma Accompanied by Thrombocytopenia, Yoshihiko Ooka, Tetsuhiro Chiba, Sadahisa Ogasawara, Tenyu Motoyama, Eiichiro Suzuki, Akinobu Tawada, Fumihiko Kanai, and Osamu Yokosuka
Volume 2014, Article ID 960628, 6 pages

Volume Change and Liver Parenchymal Signal Intensity in Gd-EOB-DTPA-Enhanced Magnetic Resonance Imaging after Portal Vein Embolization prior to Hepatectomy, Ayako Akiba, Satoru Murata, Takahiko Mine, Shiro Onozawa, Tetsuro Sekine, Yasuo Amano, Youichi Kawano, Eiji Uchida, and Shin-ichiro Kumita
Volume 2014, Article ID 684754, 7 pages

Improved Efficacy of Transcatheter Arterial Chemoembolization Using Warmed Miriplatin for Hepatocellular Carcinoma, Daisuke Yasui, Satoru Murata, Shiro Onozawa, Takahiko Mine, Tatsuo Ueda, Fumie Sugihara, Chiaki Kawamoto, Eiji Uchida, and Shin-ichiro Kumita
Volume 2014, Article ID 359296, 10 pages



Radiofrequency Thermoablation of HCC Larger Than 3 cm and Less Than 5 cm Proximal to the Gallbladder without Gallbladder Isolation: A Single Center Experience, Antonio Orlacchio, Fabrizio Chegai, Costantino Del Giudice, Mariangela Massaccesi, Elisa Costanzo, Elena Di Caprera, and Giovanni Simonetti

Volume 2014, Article ID 896527, 5 pages

New Imaging Strategies Using a Motion-Resistant Liver Sequence in Uncooperative Patients, Bong Soo Kim, Kyung Ryeol Lee, and Myeng Ju Goh

Volume 2014, Article ID 142658, 11 pages

Editorial

Diagnostic and Interventional Radiology for Liver Diseases

Satoru Murata,¹ Pascal Niggemann,² Edward W. Lee,³ and Per Kristian Hol⁴

¹*Department of Radiology/Center for Advanced Medical Technology, Nippon Medical School, 1-1-5 Sendagi, Bunkyo-ku, Tokyo 113-8602, Japan*

²*Department of Radiology, Diakoniekrankenhaus Mannheim, Speyererstr. 91, 68163 Mannheim, Germany*

³*Department of Radiology, UCLA Medical Center, David Geffen School of Medicine at UCLA 757, Westwood Plaza, Suite 2125B, Los Angeles, CA 90095, USA*

⁴*The Intervention Centre, Oslo University Hospital Rikshospitalet, Pb 4950 Nydalen, 0424 Oslo, Norway*

Correspondence should be addressed to Satoru Murata; genji@nms.ac.jp

Received 28 January 2015; Accepted 28 January 2015

Copyright © 2015 Satoru Murata et al. This is an open access article distributed under the Creative Commons Attribution License, which permits unrestricted use, distribution, and reproduction in any medium, provided the original work is properly cited.

Diseases of the liver are common and often chronic. Moreover, the mortality rate associated with chronic liver diseases remains high, despite the constant development of novel diagnostic and therapeutic modalities; therefore, numerous efforts are being made to improve imaging techniques, especially in this decade. Currently available imaging procedures allow us to ascertain the morphology, circulation, metabolism, parenchymal texture, fibrosis, and/or tumor viability in the liver. New modalities and protocols, such as magnetic resonance (MR) perfusion, MR elastography, and dual-energy computed tomography (CT), enable the potential evaluation of liver function via imaging studies. Thus, the utilization of advanced imaging techniques and contemporary interventional radiology (IR) devices has realized novel multimodality treatments for liver diseases, resulting in promising outcomes in many patients who cannot be surgically treated.

This special issue of BioMed Research International reviews recent diagnostic and interventional radiological aspects of various liver diseases such as liver cancer, fibrosis, chronic hepatitis, liver steatosis, and portal hypertension. In particular, new advances in imaging devices and protocols to evaluate fibrosis or hepatitis are described, as well as functional magnetic resonance imaging (MRI) techniques for the liver. On the other hand, various interventional radiological techniques to provide more efficient therapy to patients with advanced liver cancer are also introduced.

MRI is often performed to assess the liver in patients with chronic liver diseases. In this special issue, B. S. Kim et al. present a well-written review on a range of most utilized liver MR sequences to image patients with poor breath-hold capabilities. Recent updates on robust liver imaging as well as the advantages and disadvantages of these new methods are discussed in detail.

Liver fibrosis is a life-threatening condition with high morbidity and mortality owing to its diverse causes. Liver biopsy is the gold-standard method for diagnosing and staging liver fibrosis in chronic liver diseases, but it has several limitations, including sample variability and its invasive nature with potential complications. To resolve these problems, different noninvasive imaging-based methods have been developed for the accurate diagnosis of liver fibrosis. However, these techniques can only evaluate morphological or perfusion-related alterations of the liver, and thus, they are useful for the diagnosis of only late-stage liver fibrosis, which is characterized by “irreversible” anatomic and hemodynamic changes. Therefore, the early identification of hepatic fibrosis is of clinical significance to timely initiate therapy and to effectively achieve disease regression. In this special issue, S. Palmucci et al. and Z. Li et al. review liver fibrosis evaluated by diffusion-weighted MRI and molecular MRI techniques, respectively, to offer valuable perspectives on the development and limitations of diagnosing early-stage liver fibrosis.

The two MRI-related original research reports in this issue are authored by J. M. Alústiza et al. and F. Paparo et al. who describe MRI liver iron quantification by using the liver-to-muscle ratio and report the reproducibility of such a method on different MRI machines. Their results confirm its practicality and suggest the possibly wider acceptance of this elegant noninvasive technique. F. Paparo et al. report that MRI proton density fat fraction is a useful technique for the noninvasive assessment of liver steatosis in patients with chronic viral C hepatitis.

Diagnostic imaging is increasingly being performed to enable the treatment of liver diseases, and this trend is expected to persist. Hepatectomy is considered the first choice of treatment for early hepatocellular carcinoma (HCC) and resectable cholangiocellular carcinoma. Although extended resection is sometimes required for a cure, a sufficient volume of the remnant liver should be preserved, unless hepatic failure ensues after surgery. Portal vein embolization (PVE) is an established and effective method to increase the volume of the future liver remnant and allows more extensive resections. In this issue, A. Akiba et al. describe the usefulness of gadolinium-ethoxybenzyl-diethylenetriamine pentaacetic acid (Gd-EOB-DTPA) MRI for the prediction of liver volume change after PVE. They evaluated signal intensity (SI) contrast between nonembolized and embolized areas after PVE as well as the change in SI contrast before and after PVE (SI ratio) to conclude that either parameter had a negative correlation with the percentage of the future liver remnant. Such a result indicated that EOB-MRI might be useful for the prediction of hepatic hypertrophy after PVE.

Many IR techniques have been introduced for the treatment of liver cancers in the last few decades. Transarterial chemoembolization (TACE) is a major IR method to treat unresectable HCC. However, there is an ongoing controversy regarding which chemoembolization materials should be used to achieve good tumor control and reduce side effects. D. Yasui et al. reported the superior efficacy of TACE with warmed miriplatin compared to nonwarmed miriplatin. Because miriplatin, a recently developed anticancer drug with few toxic side effects on the vessel wall during arterial injection, is highly viscous, it yielded suboptimal tumor response. Thus, the study by D. Yasui et al. is significant in demonstrating how to increase the efficiency of TACE with miriplatin. Maximizing TACE visualization of the hepatic tumor and identification of tumor feeding vessels is very important and may require repeated injection of contrast media, possibly leading to renal failure. J. Paul et al. describe an ultrafast cone-beam CT imaging protocol during image-guided hepatic TACE, which reduces the required volume of contrast media and radiation dose, thus allowing more extensive treatment.

TACE results in both tumor hypoxia and longer activity periods of anticancer drugs trapped in the tumor tissue. However, it also induces a posttreatment surge of angiogenic factors, such as vascular endothelial growth factor (VEGF), as early as a few hours after the procedure. Such a process may contribute to tumor revascularization, thus reducing the efficacy of TACE. Therefore, several researchers have combined sorafenib, an antiangiogenic drug that blocks tumor

cell proliferation and angiogenesis by inhibiting the activity of VEGF receptors, with TACE to potentially improve treatment outcomes. However, sorafenib cannot be used in patients with severe thrombocytopenia, one of the complications of hypersplenism, owing to its platelet-decreasing effect. Y. Ooka et al. evaluated the long-term outcome of partial splenic embolization (PSE) with selective TACE in patients with advanced HCC accompanied by severe thrombocytopenia and reported that the procedure allowed these patients to receive additional sorafenib chemotherapy.

Radiofrequency ablation (RFA) is known to be an effective minimally invasive treatment for small HCC. However, its efficacy is equivocal for HCC larger than 3 cm, and RFA-related complications might depend heavily on the lesion location. A. Orlacchio et al. demonstrated that RFA with careful preprocedural planning could be safely performed even for lesions larger than 3 cm located in close proximity to the gallbladder. They report a complete necrosis rate of 87% without major complications in a small patient cohort.

In conclusion, the present special issue summarizes recent advances in both diagnostic radiology and interventional radiology, providing us with valuable perspectives in this ever-progressing field.

*Satoru Murata
Pascal Niggemann
Edward W. Lee
Per Kristian Hol*

Review Article

Recent Advances in Molecular Magnetic Resonance Imaging of Liver Fibrosis

Zhiming Li,¹ Jihong Sun,¹ and Xiaoming Yang^{1,2}

¹Department of Radiology, Sir Run Run Shaw Hospital, Zhejiang University School of Medicine, Hangzhou, Zhejiang 310016, China

²Image-Guided Bio-Molecular Intervention Research, Department of Radiology, University of Washington School of Medicine, P.O. Box 358056, Seattle, WA 98109, USA

Correspondence should be addressed to Xiaoming Yang; xmyang@u.washington.edu

Received 30 June 2014; Accepted 3 September 2014

Academic Editor: Satoru Murata

Copyright © 2015 Zhiming Li et al. This is an open access article distributed under the Creative Commons Attribution License, which permits unrestricted use, distribution, and reproduction in any medium, provided the original work is properly cited.

Liver fibrosis is a life-threatening disease with high morbidity and mortality owing to its diverse causes. Liver biopsy, as the current gold standard for diagnosing and staging liver fibrosis, has a number of limitations, including sample variability, relatively high cost, an invasive nature, and the potential of complications. Most importantly, in clinical practice, patients often reject additional liver biopsies after initiating treatment despite their being necessary for long-term follow-up. To resolve these problems, a number of different noninvasive imaging-based methods have been developed for accurate diagnosis of liver fibrosis. However, these techniques only reflect morphological or perfusion-related alterations in the liver, and thus they are generally only useful for the diagnosis of late-stage liver fibrosis (liver cirrhosis), which is already characterized by “irreversible” anatomic and hemodynamic changes. Thus, it is essential that new approaches are developed for accurately diagnosing early-stage liver fibrosis as at this stage the disease may be “reversed” by active treatment. The development of molecular MR imaging technology has potential in this regard, as it facilitates noninvasive, target-specific imaging of liver fibrosis. We provide an overview of recent advances in molecular MR imaging for the diagnosis and staging of liver fibrosis and we compare novel technologies with conventional MR imaging techniques.

1. Introduction

Chronic liver disease is a worldwide health problem, which has a common process-liver fibrosis [1, 2]. There are several etiologies resulting in chronic liver diseases, including chronic infection by hepatotropic viruses (hepatitis B and hepatitis C viruses), chronic exposure to toxins or drugs (e.g., alcohol abuse), chronic alteration of metabolics, and persisting autoimmune reaction. Chronic liver damages may induce both inflammatory response and activation of fibrogenesis. Given persisting fibrogenesis without removal of exposure to the specific etiology, liver fibrosis progresses. Liver fibrosis is characterized by the excess deposition of collagenous extracellular matrix (ECM) components, which often lead to hepatic dysfunction, portal hypertension, and hepatocellular carcinoma [1, 3, 4]. Histologically, liver fibrosis can be classified into a number of different stages, and these stages are directly related to decisions regarding the management of liver fibrosis. Early-stage liver fibrosis can be “reversed” by

efficient treatment, while advanced fibrosis and cirrhosis are usually “irreversible” [4–7]. Accurate differentiation of stages is thus critical for efficient management of liver fibrosis. Currently, liver biopsy is the gold standard for diagnosing and staging liver fibrosis. However, due to its invasive nature and relatively high cost, as well as variability in samples and the risk of complications such as procedure-related bleeding and infection, additional biopsies are often rejected by patients after they have initiated treatment, thereby preventing effective long-term follow-up.

Conventional imaging techniques, such as ultrasonography (US), computed tomography (CT), and magnetic resonance imaging (MRI), are noninvasive methods for diagnosing and staging liver fibrosis. However, these techniques are primarily dependent on the detection of morphological alterations in the liver, and these alterations are usually only detected in advanced or late-stage fibrosis, such as cirrhosis [8]. Transient elastography (TE) (fibroscan), which relies on a low-frequency wave generated by a mechanical vibrator,

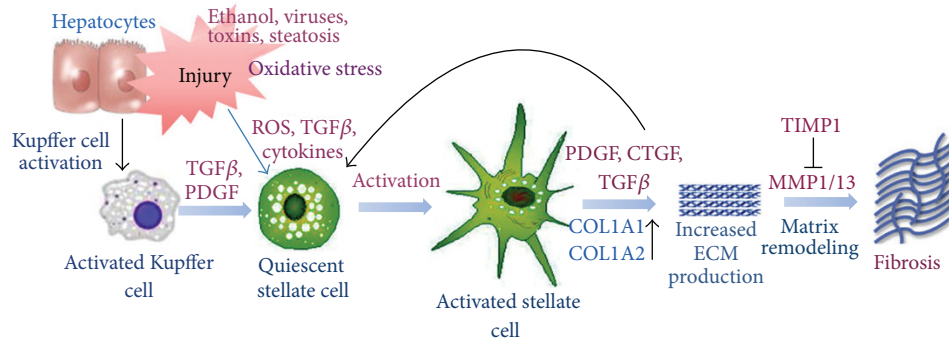


FIGURE 1: Key agents involved in the activation of hepatic stellate cells during the pathogenesis of liver fibrosis. (Reprinted with permission from [13].)

has been used to assess liver fibrosis with relatively high specificity and sensitivity. By using liver stiffness measurement (LSM) value, TE can differentiate patients with no fibrosis from those with mild fibrosis (METAVIR stages F1 and F2) or advanced fibrosis (stages F3 and F4) [9]. Acoustic radiation force impulse (ARFI) imaging is another ultrasound elastography technique, which uses focused high-intensity, short-duration acoustic pulses in order to produce shear waves in the target tissues. According to the findings of a multicenter study, there was a significant correlation between the ARFI measurement and liver fibrosis [10]. MR diffusion-weighted imaging (DWI) can depict the movement of water molecules, but it does not directly reflect the deposition of the ECM. Contrast-enhanced MR imaging (CE-MRI) and MR perfusion-weighted imaging (MR-PWI) rely on the intravenous administration of MR contrast agents that can more precisely reveal hemodynamic changes in the liver. However, these MR techniques are only useful for the diagnosis of advanced liver fibrosis or cirrhosis after long-term hepatic damage. It is therefore essential that a noninvasive, direct, and highly sensitive method for diagnosing early-stage liver fibrosis be developed. Molecular MRI is one such technique, and, in this paper, we present an overview of recent advances in molecular MRI for the diagnosis and staging of liver fibrosis.

2. Pathologic Liver Fibrosis and Staging

Liver fibrosis is a common process that occurs in response to liver injury; it is characterized by the excess deposition of ECM. The ECM comprises a group of macromolecules that together form the scaffolding of normal and fibrotic livers. These include collagens, noncollagen glycoproteins, matrix-bound growth factors, glycosaminoglycans, proteoglycans, and matricellular proteins [11]. Liver fibrosis occurs when the rate of ECM synthesis by myofibroblasts exceeds the rate of repair required due to chronic hepatic injuries [4, 12]. Hepatic myofibroblasts mainly stem from resident mesenchymal cells and bone marrow-derived myofibroblasts [1].

Hepatic stellate cells (HSCs) are mesenchymal cells that are resident in the liver, and they play a crucial role in fibrogenesis (Figure 1) [13]. Activation of HSCs occurs via a complex process that includes signal transmission, gene

expression, and receptor expression. Numerous cytokines are involved in fibrogenesis, including platelet-derived growth factor (PDGF), transforming growth factor- β (TGF- β), tumor necrosis factor- α (TNF- α), and interleukin [2, 14].

Different staging systems are used for the pathological classification of liver fibrosis: the IASL (International Association for the Study of the Liver), Metavir, and Batts-Ludwig systems. These systems have a number of common features, and all basically classify liver fibrosis into five stages (Figure 2): no fibrosis; portal fibrous expansion; thin fibrous septa emanating from portal triads; fibrous septa bridging portal triads and central veins; and cirrhosis [8, 15].

3. MRI of Liver Fibrosis

Magnetic resonance imaging is a unique modality that has several advantages over other imaging techniques, including its ability to obtain high resolution images with excellent contrast against a soft tissue background, the flexibility to acquire images using a number of different techniques to facilitate the diagnostic evaluation of organ morphology, physiology, and function, and the ability to project data in an infinite number of imaging planes with no risk of ionizing radiation.

Because it is dependent on the detection of alterations in hepatic morphology, conventional MRI has a high specificity for cirrhosis, but a low sensitivity for earlier stages of liver fibrosis, and it is thus not suitable for staging the disease [8]. Recently, a number of modified MRI-based techniques, including DWI, MRE, PWI, and CE-MRI, have been developed for diagnosing and staging liver fibrosis. These are described in detail below.

3.1. MR Diffusion-Weighted Imaging (MR-DWI). The MR-DWI technique monitors the Brownian motion of water molecules relative to the temperature and viscosity of the studied environment, and it is routinely used for liver imaging (Figure 3) [16]. Calculation of the apparent diffusion coefficient (ADC) with DWI can facilitate the assessment of liver fibrosis. For example, one recent study showed that ADC values are decreased as the stage of liver fibrosis increases from F0 to F4, but no significant differences in ADC values were detected between stages F0 and F1, as well as F1 and

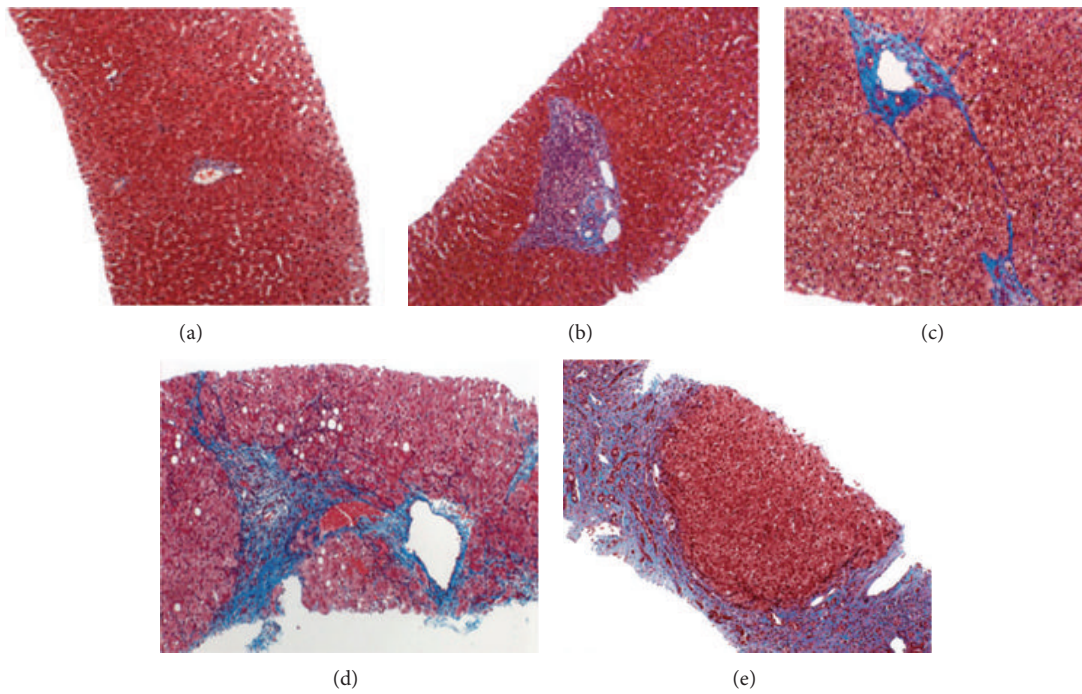


FIGURE 2: Histological staging of liver fibrosis (photomicrographs of liver biopsy specimens; trichrome stain, $\times 40$): stage F0 (a), stage F1 (b), stage F2 (c), stage F3 (d), and stage F4 (e). (Reprinted with permission from [8].)

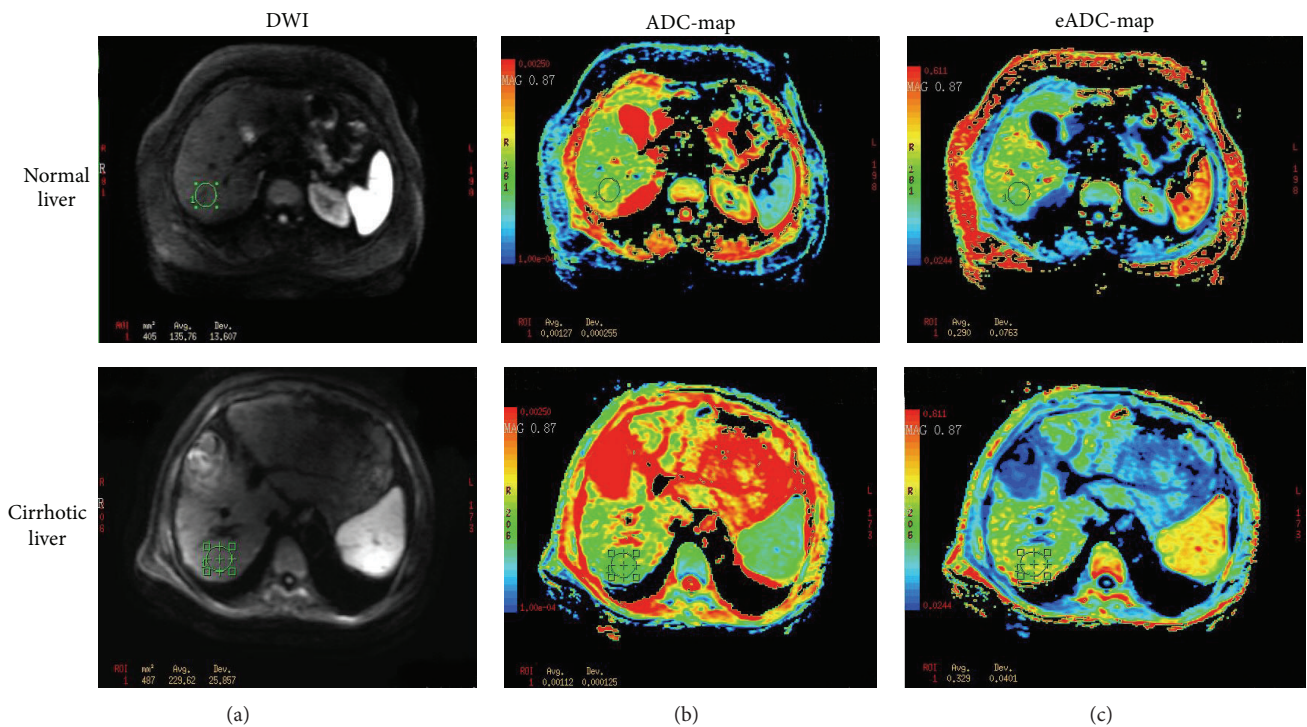


FIGURE 3: MR-DWI in a normal and cirrhotic liver (b value 600 s/mm^2). DWI images are shown in the far left column. The middle column shows ADC maps superimposed on the corresponding anatomic images. The exponential ADC maps are shown in the far right column. The ADC maps show that the mean ADC value of the cirrhotic liver is lower than that of the normal liver ($1.12 \times 10^{-3} \text{ mm}^2/\text{s}$ versus $1.27 \times 10^{-3} \text{ mm}^2/\text{s}$, resp.).

F2 [17]. Another study reported that ADC values were only significantly different between stages F0 and F4 [18]. Together, these findings suggest that DWI is not a reliable method for distinguishing early-stage liver fibrosis [17, 18].

Intravoxel incoherent motion (IVIM) diffusion-weighted (DW) imaging developed for quantitative assessment of the microscopic translational motions of both intracellular and extracellular water molecules, which occur in each voxel of MR imaging [19]. By using IVIM imaging, several factors, such as pure molecular diffusion and microcirculation or blood perfusion, can be distinguished with multiple b values [19, 20]. One pilot study demonstrated the usefulness of using IVIM DW imaging with ten b factors to determine the difference of pure molecular-based (D) and perfusion-related (D^* , f) diffusion parameters, between patients with cirrhosis and patients without liver fibrosis [21]. They found that both ADC and D^* were significantly reduced in the cirrhotic liver group compared with those in the healthy liver group, while there was no significant difference between D and f measurements in the healthy liver and cirrhotic liver groups. Another study showed a significant decrease of both pure molecular diffusion coefficient (D_{slow}) and perfusion-related diffusion coefficient (D_{fast}) in the advanced fibrosis group compared to nonadvanced fibrosis group ($P < 0.05$ and $P < 0.01$, resp.) [22]. Furthermore, the IVIM parameters, including pseudo-diffusion coefficient (D_p) and perfusion fraction (f), can be used for differentiating stages between fibroses \geq F2 and F0-1 ($P < 0.05$) [23].

3.2. $T1\rho$ MR Imaging. $T1\rho$ is the spin-lattice relaxation time constant in the rotating frame, which describes the decay of transverse magnetization under the special condition of a spin-lock radiofrequency field [24]. $T1\rho$ is sensitive to both low-frequency motional process and static process and thus can be used to investigate macromolecular composition [25]. Because of the fact that liver fibrosis is featured by excess ECM deposition, $T1\rho$ MR imaging can be used to assess liver fibrosis. One study using a rat biliary duct ligation model showed that liver fibrosis can be detected with $T1\rho$ MR imaging, and the $T1\rho$ value increase correlated with liver collagen levels [26]. Another study was conducted with patients of fibrosis stage F4 and healthy volunteers by using $T1\rho$ MR imaging, demonstrating that the mean $T1\rho$ values increased as Child-Pugh stage increased, and there were significant differences of mean $T1\rho$ values among Child-Pugh classes [27]. A recent study further indicated that liver $T1\rho$ could be a valuable biomarker for liver injury and fibrosis [28]. Liver $T1\rho$ value increased mildly on 48 hours and further increased as the degeneration and necrosis of hepatocytes, while fibrosis appeared and progressed at weeks 2, 4, and 6. In addition, liver $T1\rho$ values decreased at weeks 1 and 4 after the withdrawing of the carbon tetrachloride (CCl_4). These results indicate that $T1\rho$ MR imaging is a potential promising technique in monitoring liver injury, as well as liver fibrosis regression and progression.

3.3. MR Elastography (MRE). Magnetic resonance elastography is a state-of-the-art MRI-based technique that can

noninvasively quantify the stiffness of the liver by analyzing the propagation of mechanical waves through liver tissue (Figure 4). It is based on the concept that the stiffness of the hepatic parenchyma is increased as fibrosis advances [8, 29, 30]. One study has shown that MRE has a high sensitivity and specificity for detecting liver fibrosis: predicted sensitivity and specificity scores were 91% and 97% for liver fibrosis \geq stage F2, 92% and 95% for liver fibrosis \geq stage F3, and 95% and 87% for liver fibrosis \geq stage F4 [30]. A meta-analysis that compared the effectiveness of MRE and DWI for staging liver fibrosis concluded that MRE was more reliable and resulted in a better combination of sensitivity and specificity, likelihood ratio, diagnostic odds ratio, and area under the summary receiver operating characteristic curve values [31].

However, MRE also has some disadvantages that limit its clinical acceptance: (i) it cannot be performed in livers with high iron overload because of signal-to-noise limitations; (ii) the examination time is longer than that required for ultrasound elastography [32].

3.4. MR Perfusion-Weighted Imaging (MR-PWI). Perfusion-weighted imaging requires intravenous administration of MR contrast agents, and it is used to quantify the microcirculatory status of the liver parenchyma or liver lesions. Perfusion MR parameters are derived from dynamic contrast-enhanced MRI (DCE-MRI) using model-based or model-free techniques [33]. The deposition of collagen in the space of Disse and sinusoidal capillarization result in an increase in the resistance to incoming sinusoidal blood flow [34], which leads to a decrease in portal venous flow to the liver, an increase in hepatic arterial flow, and the subsequent formation of intrahepatic shunts [8]. Transfer of the low-molecular-weight gadolinium contrast medium from the vascular sinusoids into the interstitial space is thus increasingly impeded by liver fibrosis [33]. One dual-input, single-compartment, model-based study reported an increase in absolute arterial blood flow (F_a), arterial fraction (ART), distribution volume (DV), and mean transit time (MTT) and a decrease in portal venous fraction (PV), in patients with advanced liver fibrosis compared with patients with early-stage liver fibrosis [35]. When the DV was used to predict advanced liver fibrosis, the technique had a sensitivity of 76.9% and a specificity of 78.5%. Other researchers have found that when dynamic contrast-enhanced MRI is combined with gadolinium ethoxybenzyl diethylenetriamine pentaacetic acid (Gd-EOB-DTPA), the slope (10–90% ascending slope of the curve) and area under the curve (AUC) are the two best perfusion parameters to use for predicting the severity of liver fibrosis ($>$ F2 versus \leq F2); F_a was the best predictor of early liver fibrosis [36].

The MR-PWI technique also has some disadvantages: (i) many factors can affect correlations between perfusion parameters and fibrosis, including cardiac status, fasting state, hepatic congestion, hepatic inflammation, hepatic lesions, and portal venous flow; (ii) an assumption model is required as well as very rapid imaging to reduce image artifacts; (iii) the technique is not suitable for the assessment of structural abnormalities; and (iv) there are a number of technical problems with the technique, including difficulties with image analysis and misregistration corrections [8].

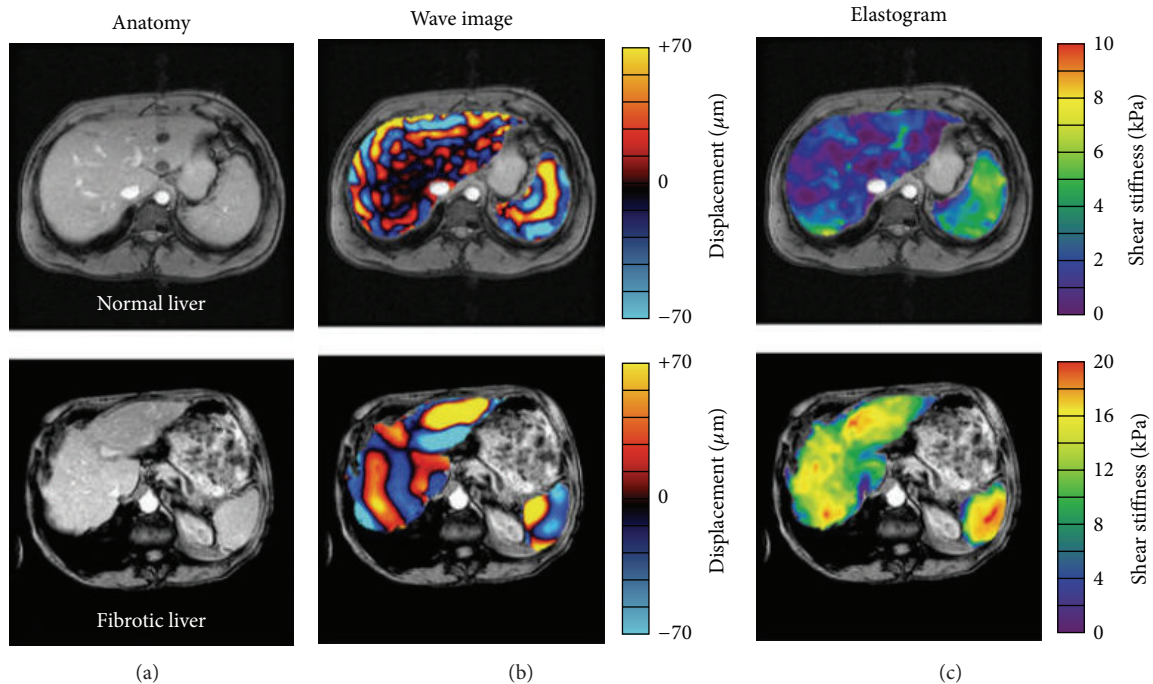


FIGURE 4: MR elastography images of the livers of a normal volunteer and a patient with cirrhosis. Anatomic images of a normal volunteer and of a patient with grade 4 fibrosis are shown in the far left column (a). The middle column of images shows wave image data in the liver and spleen superimposed on the corresponding anatomic images (b). The resulting elastograms are shown in the far right column (c). The wave images show that the shear wavelength was higher in the fibrotic liver than in the normal liver. The elastograms show that the mean shear stiffness of the fibrotic liver was much higher than that of the normal liver (12.1 ± 1.2 kPa versus 1.8 ± 0.3 kPa, resp.). (Reprinted with permission from [29].)

3.5. Magnetization Transfer MR Imaging. Magnetization transfer (MT) MR imaging can provide information of reduced signal from macromolecule-rich tissues with exchange of the applied radiofrequency energy between pools of bound and of free protons. MT imaging can be used as a noninvasive technique for imaging collagen and other macromolecules, for example, liver fibrosis. One study with a Niemann Pick type C mouse model showed that collagen deposition was consistent with the observed elevation in MT ratio. There was a 10% increase in collagen content, which produced an increase of MT ratio at approximately 9% [37]. However, due to the complex pathological change of the cirrhotic liver tissues, the MT effects (signal intensity of magnetization transfer contrast (MTC)/signal intensity of non-MTC) were widely variable [38]. Another study reported that the MT ratio was nearly identical between healthy (range 26.0%–80.0%) and cirrhotic livers (range 26.7%–81.2%) by using eight different frequency offsets of the MT pulses [39]. To the best of our knowledge, no literature indicates that MT MR imaging is a valuable technique in assessing liver fibrosis so far.

Thus, conventional MRI techniques, such as DWI, PWI, MRE, and MT imaging, are of limited use for diagnosing and staging liver fibrosis because they are generally focused on morphological or perfusion-related changes in the liver caused by liver fibrosis, rather than molecular changes of fibrosis itself [8], which are the “roots” of fibrotic livers.

4. Molecular MR Imaging

Molecular imaging is motivated to directly visualize, characterize, and measure biological processes at the molecular and cellular levels in humans and other living systems, and the techniques include radiotracer imaging/nuclear medicine, MR imaging, MR spectroscopy, optical imaging, ultrasonography, and others [45]. Molecular MR imaging has become a novel technique for assessing specific cellular or subcellular events and is becoming one of the core integrative technologies in biomedicine [46]. In contrast to US, CT, and PET (positive emission tomography) or SPECT (single photon emission computed tomography), molecular MR imaging has several superior advantages, including offering high spatial resolution images, simultaneously extracting anatomic, physiologic, and functional information [47], and more importantly avoiding harmful ionizing radiation.

The strength of MR signals depends upon the longitudinal (T1) and transverse (T2) proton relaxation times of water, and thus differences in proton relaxation times cause various contrasts on MR images. To maximize image quality, MR contrast agents are often needed to decrease T1 and T2 relaxation times. In general, there are two types of MR contrast agents: paramagnetic and superparamagnetic compounds. Paramagnetic contrast agents, also called T1 or positive contrast agents, are usually composed of Gadolinium³⁺ or Mn²⁺, which generates positive signals on T1-weighted images.

TABLE 1: Studies that have assessed molecular MRI of liver fibrosis.

Study/year	Targeted molecules	Targeting probes	Animal model	MR effect	Significance
Polasek et al., 2012 [40]	Type I collagen	EP-3533	The rat DEN model & the CCl ₄ mouse model	Shortening the T1 relaxation time	Identifies fibrotic tissue in animal models of liver fibrosis
Fuchs et al., 2013 [41]	Type I collagen	EP-3533	The CCl ₄ mouse model	Shortening the T1 relaxation time	Diagnoses and stage sliver fibrosis in an animal model
Chow et al., 2013 [42]	Fibrin-fibronectin	CLT1-peptide-targeted nanoglobular contrast agent (CLT1(Gd-DOTA))	The CCl ₄ mouse model	Shortening the T1 relaxation time	Detected and stage sliver fibrosis by probing the accumulation of fibronectin
Ehling et al., 2013 [43]	Elastin	ESMA	The CCl ₄ mouse model	Shortening the T1 relaxation time	Elastin-based molecular MRI may be suitable for noninvasive monitoring of ECM remodeling during liver fibrosis
Wang et al., 2011 [44]	$\alpha_v\beta_3$ -Integrin	c(RGDyC)-USPIO	The CCl ₄ mouse model	Shortening the T2 relaxation time	Targets HSC imaging with c(RGDyC)-USPIO

Superparamagnetic contrast agents, also called T2 or negative contrast agents, are usually constructed with iron oxide, which generates negative signal or signal void on T2- and T2*-weighted images [48].

The specific contrast agents for molecular MR imaging are defined as “probes used to visualize, characterize, and measure biological processes in living systems. Both endogenous molecules and exogenous probes can be molecular imaging agents” [45]. These MR imaging probes are usually constructed by different nanoparticles that contain paramagnetic or superparamagnetic metals, such as nanoscaffolds loaded with gadolinium chelates or nanoparticles carrying superparamagnetic iron oxide.

In general, systemically administrated molecular MRI probes are target-specific, which depend on the ligands conjugated onto the MRI probes. These ligands can specifically target molecules overexpressing at the diseased site or lesion. The ligands can be monoclonal antibodies or their fragments, peptides, small molecular peptidomimetics, vitamins, or aptamers. The target-specific molecular MRI probes function by following the mechanism of ligand-molecule binding, that is, the specific interaction of ligands with their corresponding molecules of the targets (such as receptors expressed on cell surfaces) to form an antigen-antibody pair like complex [49].

As mentioned above, the molecular MR imaging of liver fibrosis is based on the development of contrast agents, known as activatable MR imaging probes to elicit detectable MR signal changes in response to the local environment or to “sense” specific molecular states [50]. The contrast agents are usually designed and synthesized as a category of nanoparticulate probes composed of molecular targets and contrast-generating metals. The probes of detecting liver fibrosis ought to have the capability of specifically targeting and binding

ECM, of which excessive accumulation can result in fibrosis. ECM is under the dynamic balance of synthesis and degradation in the normal liver. ECM is a normal component of Glisson’s capsule, portal tracts, central veins, and the subendothelial space of Disse and accounts for less than 3% of the relative area on a liver tissue section and approximately 0.5% of the wet weight [14]. In the fibrotic liver, remarkable changes present in ECM quantitatively and qualitatively.

A number of molecules are present in increased amounts in fibrotic livers, including fibrillar collagens (types I, III, and IV), some nonfibrillar collagens (types IV and VI), a number of glycoproteins (cellular fibronectin, laminin, SPARC, osteonectin, tenascin, and von Willebrand factor), proteoglycans, and glycosaminoglycans (perlecan, decorin, aggrecan, lumican, and fibromodulin). Of these molecules, the fibrillar collagens (especially types I and III) and elastin are the most abundant in the ECM [51]. Accordingly, the type of ECM in the space of Disse changes from a normal, low-density, basement membrane-like matrix primarily composed of types IV and VI collagens to a matrix primarily composed of interstitial type I and III collagens and fibronectin [14]. Thus, the components of the ECM are potential important cellular and molecular targets for molecular MRI to diagnose and stage liver fibrosis. Table 1 summarizes ligand-molecule pairs that have previously been used for molecular MRI to diagnose and stage liver fibrosis.

5. Application of Molecular MRI in Liver Fibrosis

Molecular MRI of liver fibrosis has been used to directly detect molecular changes in the ECM and HSCs.

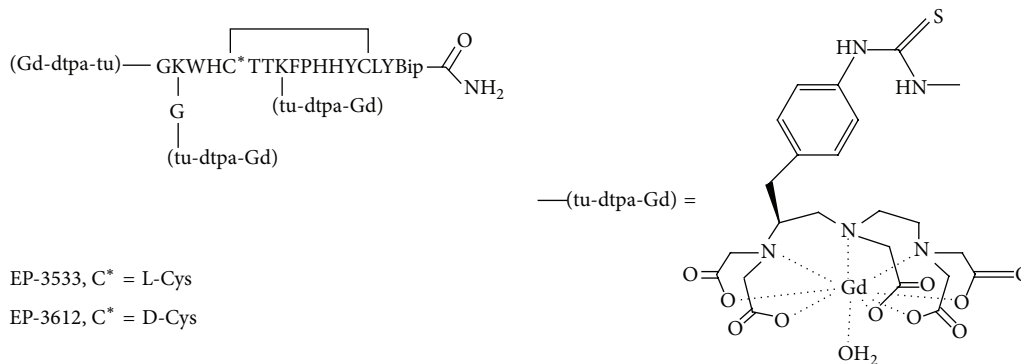


FIGURE 5: Collagen-targeting contrast agent: L-amino acids are designated by letter, except where otherwise noted; Gd chelates are appended through the N terminus, through branched Lys-Gly residues at the N terminus, and through a Lys side chain within the cyclic portion of the peptide. (Reprinted with permission from [52].)

5.1. EP-3533 Probe Targeting Type I Collagen. Compared with the normal liver, the amount of type I collagen in fibrotic livers is significantly increased (from 36% to 53%) [53]. Therefore, type I collagen can be used as a molecular target for detecting liver fibrosis by molecular MRI. EP-3533 (gadolinium-diethylenetriamine pentaacetic acid-GKWHCTTKFPHHYCLY) is a type I collagen-targeting MR contrast agent that has previously been used for myocardial infarction [54, 55], pulmonary fibrosis [56], and liver fibrosis [40, 41]. It is composed of a 16-amino-acid peptide that has three amino acids flanking each side of a cyclic peptide of 10 amino acids joined by disulfide bonds (Figure 5) [52]. The peptide contains three primary amines (the N terminus and two lysine side chains), and these are used to append three gadopentate dimeglumine moieties via a thiourea linkage [54]. The relaxivity of EP-3533 is $16.1 \text{ mM}^{-1} \text{ s}^{-1}$ per Gd^{III} ion at 1.41 Tesla and 37°C (PBS) or $5.4 \text{ mM}^{-1} \text{ s}^{-1}$ per Gd^{III} ion at 4.7 Tesla and 25°C (PBS) [57].

Molecular MRI has been trialed in two animal models of liver fibrosis [40]: (i) a diethylnitrosamine (DEN) rat model, which is created by feeding rats 100 mg/kg/week DEN for 4 weeks, which results in moderate to advanced liver fibrosis (Ishak scores 3–6); and (ii) the carbon tetrachloride (CCl_4) mouse model, which is created by feeding mice 0.1 mL of a 40% solution of CCl_4 in olive oil three times a week for 20 weeks, which also results in moderate to advanced liver fibrosis (Ishak scores 3–6). EP-3533 is administered intravenously and a nontargeted gadolinium-diethylenetriamine pentaacetic acid (Gd-DTPA) is used as a control. The cyclic peptide of EP-3533 has a specific affinity for type I collagen, whereas the gadolinium moieties generate strong T1 MR signals. By correlating MR imaging, tissue analysis, and real-time polymerase chain reaction (PCR) findings, it was concluded that molecular MRI of liver fibrosis with the EP-3533 collagen-targeting probe was capable of identifying fibrotic tissues in both the DEN rat and CCl_4 mouse models.

Another study attempted to use EP-3533-based molecular MRI to detect type I collagen in liver fibrosis in the CCl_4 mouse model [41]. By comparing the technique with

other conventional MRI methods, the authors found that there was a strong positive linear correlation between the muscle contrast-to-noise ratio (ΔCNR) and liver hydroxyproline levels (hydroxyproline is an amino acid [$\text{C}_5\text{H}_9\text{NO}_3$] that is a natural constituent of collagen) as well as the ΔCNR and conventional Ishak fibrosis scoring, which indicates the potential usefulness of this technique for staging liver fibrosis.

5.2. CLT1 Peptide Probe Targeting Fibrin-Fibronectin Complexes. The accumulation of fibrin in the liver occurs during acute as well as chronic experimental liver injury [59]. Fibronectin is a type of structural glycoprotein present in the liver ECM [53]. Fibrin-fibronectin complexes exist in fibrotic livers because of cross-linkages between fibrin/fibrinogen and fibronectin [59]. Some authors have shown that the CLT1 and CLT2 peptides can specifically bind to fibrin-fibronectin complexes in the ECM of different tumors with little binding to normal tissues, suggesting that CLT peptides may bind to an epitope in the fibrin-fibronectin complex formed as a result of plasma clotting within tumors and at sites of tissue injury [60]. It is thus feasible that liver fibrosis can be detected by using the CLT1 peptide as a probe for targeting fibrin-fibronectin complexes. One group of researchers synthesized CLT1 peptide-targeting nanoglobular contrast agents by conjugating gadoteric acid (Gd-DOTA) and peptides on the surfaces of generation 2 (G2) and generation 3 (G3) nanoglobules (lysine dendrimers with a cubic silsesquioxane core) [61]. Approximately two peptides and 25 Gd-DOTA chelates have reportedly been conjugated onto the surfaces of 32 amine groups of the G2 nanoglobule, and 3 peptides and 43 Gd-DOTA chelates have been conjugated onto the surfaces of 64 amine groups of the G3 nanoglobule. The T1 relaxivities of peptide-targeted G2 and G3 nanoglobules are $7.92 \text{ mM}^{-1} \text{ s}^{-1}$ and $8.20 \text{ mM}^{-1} \text{ s}^{-1}$, respectively, at 3 Tesla. Other studies have shown that a CLT1 peptide-targeting contrast agent, CLT1-(Gd-DTPA), which is conjugated to a cyclic decapeptide, CGLIIQKNEC (CLT1), and Gd-DTPA can be used for molecular MRI of fibrin-fibronectin complexes in

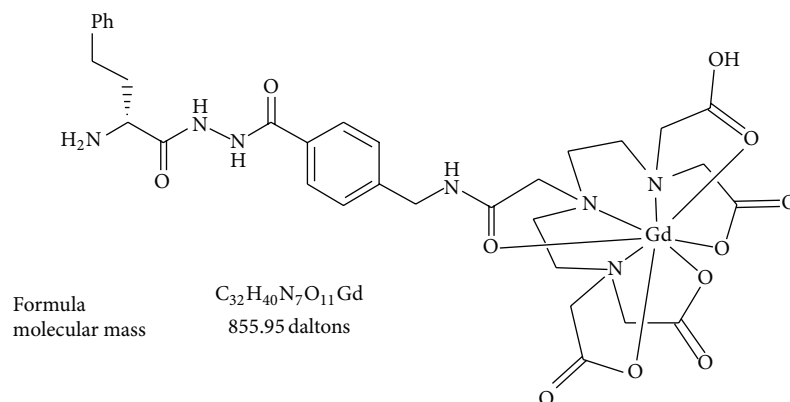


FIGURE 6: Structural diagram of ESMA showing the molecular mass. (Reprinted with permission from [58].)

tumor tissues, with CLT1-(Gd-DTPA) T1 and T2 relaxivities of $4.22 \text{ mM}^{-1} \text{ s}^{-1}$ and $4.45 \text{ mM}^{-1} \text{ s}^{-1}$, respectively, at 3 Tesla [62].

Knowledge of CLT1-binding to fibrin-fibronectin complexes has been adapted for the evaluation of liver fibrosis, and some authors have produced a cyclic decapeptide CLT1-targeting contrast agent for molecular MRI of liver fibrosis [42], based on CLT1's specific binding to the fibrin-fibronectin complex [60]. A CLT1 peptide-targeting nanoglobular contrast agent (Gd-P) was used for dynamic molecular MRI of a mouse model to detect and characterize liver fibrosis at 7.0 Tesla. Compared with the control KAREC-conjugated nanoglobular contrast agent (Gd-CP) and a nontargeting nanoglobular contrast agent (Gd-C), different enhancements were observed between normal and fibrotic livers when Gd-P was used, which is indicative of the usefulness of this molecular MRI approach employing a CLT1 peptide-targeting nanoglobular contrast agent for the detection and staging of liver fibrosis [42].

5.3. ESMA Probe Targeting Elastin. Elastin is a type of noncollagenous protein found in the ECM that is secreted by HSCs; it is also associated with the stage of liver fibrosis. Elastin is an essential component of the ECM and elastic fibers, and, together with fibrillins, it provides resilience and elastic recoil in tissues. ESMA (BMS-753951) is an elastin-specific MR contrast agent that has previously been used for assessing atherosclerotic plaques [58] and coronary wall remodeling [63]. It is a Gd-DTPA chelate that is linked to the D-amino acid D-phenylalanine to form a low-molecular-weight MR contrast agent with moderate specificity for elastin. ESMA has a similar blood half-life to current commercially available extracellular Gd-based MR contrast agents [63].

The feasibility of monitoring ECMs with ESMA (Figure 6), the elastin-specific MR contrast agent, has previously been assessed, and the study findings suggested that elastin-based molecular MRI has potential as a noninvasive method for monitoring ECM remodeling during liver fibrosis [43].

5.4. RGD Peptide Probe Targeting Integrins. As noted above, HSCs play an important role in liver fibrogenesis. Integrins

are a special type of heterodimeric transmembrane receptor expressed in HSCs. They are composed of α and β subunits that transduce signals from the ECM to HSCs and other mesenchymal cell types [64]. Integrins are upregulated in fibrotic liver disease or during HSC activation [65, 66], and $\alpha_v\beta_3$ -integrin is highly expressed in HSCs [44, 67, 68]. As cell surface receptors, integrins mediate communication between cells and the ECM, and they appear to play a major role in the development of profibrogenic effects since integrin-linked adhesions (cell-cell and cell-matrix) can promote the migration and proliferation of HSCs and inhibit their apoptosis during liver fibrogenesis [68, 69]. A common feature of integrins such as $\alpha_v\beta_3$ is that they bind to ECM proteins via a three-amino-acid sequence, RGD (arginine-glycine-aspartic acid).

A previous review has provided a detailed examination of molecular MRI targeting integrin $\alpha_v\beta_3$ and the RGD peptide [70]. Most of the literature on RGD-mediated molecular MRI has focused on tumors, and there are few reports on its efficacy in liver fibrosis. Two RGD-based molecular imaging probes have been reported previously. One consists of cRGD conjugated to Gd-DOTA; it has a relaxivity of $9 \text{ mM}^{-1} \text{ s}^{-1}$ at 1.41 Tesla and 40°C and can bind the $\alpha_{IIb}\beta_3$ -receptor as well as the $\alpha_v\beta_3$ -receptor. The other consists of cRGD conjugated to Gd-DOTA and is used for selective imaging of $\alpha_v\beta_3$ -integrin; it has a relaxivity of $7.4 \text{ mM}^{-1} \text{ s}^{-1}$ at 1.5 Tesla and 25°C [57].

Other researchers have used the cyclic peptide c(RGDyC) to bind $\alpha_v\beta_3$ -integrin-conjugated ultrasmall superparamagnetic iron oxide to form USPIO, a T2 contrast agent. This probe (c(RGDyC)-USPIO) has then been used to specifically target activated HSCs [44]. Rats with normal and fibrotic livers were subjected to MR scanning with either c(RGDyC)-USPIO or USPIO, and it was found that the reduction in T2 relaxation times in fibrotic rats was much greater with c(RGDyC)-USPIO than USPIO.

5.5. Biodistribution and Clearance of Targeted Molecular Imaging Probes. The biodistribution and clearance of molecular imaging probes depend on their sizes. By using a mouse model, some authors investigated the biodistribution of EP3533 at 15 min after its systemic administration, showing

the biodistribution as nmol Gd per gram wet tissue: kidney (223), spleen (77.3), liver (50.4), and lung (29.1) [52]. The blood half-life of EP3533 was 19 ± 2 min, and EP3533 was largely eliminated from the mouse body by 24 hours [41]. One study showed that CLT1-targeted G2 nanoglobular led to its much lower tissue accumulation compared to the targeted G3 agent 48 hours after the systemic administration, because of smaller sizes and less CLT1 peptides conjugated with the G2 agent [61]. Due to a smaller size, the targeted G2 nanoglobular contrast agent cleared more rapidly from the body than the relatively larger G3 agent. In addition, some authors reported the fact that a molecular imaging probe, c(RGDyC)-USPIOs, distributed more extensively in the perisinusoidal space of Disse where the HSCs resided preferentially in the fibrotic liver [44].

One recent study demonstrated a rapid biliary excretion of relative large nanoparticles (~250 nm), while nanoparticles less than 5~6 nm can be bioeliminated through the kidneys. Such small-size nanoparticles can be also cleared by the mononuclear phagocyte system and may be metabolized further or eliminated via bile, urine, or respiration [71].

6. Conclusion

Liver fibrosis is a common process that occurs in response to chronic liver injuries. While conventional MRI techniques are useful for assessing advanced liver fibrosis, molecular MRI may be a more valuable tool for noninvasive detection of early-stage liver fibrosis. Recent studies of molecular MRI of liver fibrosis have been confined to producing target-specific molecular MRI probes (such as iron oxides) that can specifically target certain components of the ECM or HSCs in early-stage fibrotic livers. Moreover, nuclear imaging techniques have been used for achieving of molecular information. Radioisotope can be conjugated to a target-specific probe, which thereby can specifically bind targeting molecules in vivo. As the development of molecular imaging agents, nuclear imaging using ECM-specific probes may become a valuable technique for assessing liver fibrosis. Although molecular MRI of liver fibrosis is still at its developing phase, the conception of a target-specific molecular MRI approach is opening new avenues for effective management of this life-threatening disease.

Abbreviations

US:	Ultrasonography
CT:	Computed tomography
CTPI:	Computed tomography perfusion imaging
MR-DWI:	Magnetic resonance diffusion-weighted imaging
IVIM:	Intravoxel incoherent motion
MRE:	Magnetic resonance elastography
MR-PWI:	Magnetic resonance perfusion-weighted imaging
ECM:	Extracellular matrix
MRI:	Magnetic resonance imaging

CE-MRI:	Contrast-enhanced magnetic resonance imaging
LSM:	Liver stiffness measurement
ARFI:	Acoustic radiation force impulse
HSC:	Hepatic stellate cell
PDGF:	Platelet-derived growth factor
TGF- β :	Transforming growth factor- β
TNF- α :	Tumor necrosis factor- α
IASL:	International Association for the Study of the Liver
ADC:	Apparent diffusion coefficient
DCE-MRI:	Dynamic contrast-enhanced magnetic resonance imaging
F_a :	Absolute arterial blood flow
ART:	Arterial fraction
DV:	Distribution volume
MTT:	Mean transit time
PV:	Portal venous fraction
Gd-EOB-DTPA:	Gadolinium ethoxybenzyl diethylenetriamine pentaacetic acid
MT:	Magnetization transfer
AUC:	Area under the curve
PET:	Positive emission tomography
SPECT:	Single photon emission computed tomography
DEN:	Diethylnitrosamine
CCl ₄ :	Carbon tetrachloride
Gd-DTPA:	Gadolinium-diethylenetriamine pentaacetic acid
PCR:	Polymerase chain reaction
Gd-DOTA:	Gadoteric acid.

Conflict of Interests

The authors declare that there is no conflict of interests regarding the publication of this paper.

Acknowledgments

This study was supported by Program for National Science and Technology Major Project of China (2013ZX10002004-001-005), National Basic Research Program of China (973 Program, 2014CB744505), NIH RO1EBO12467 Grant, Qianjiang Talent Program of Zhejiang Province in China (2012-R10027), Scientific Research Foundation of the Health Bureau of Zhejiang Province in China (WKJ2012-2-030), Fundamental Research Funds for the Central Universities (2012QNA-7037) and SRF for ROCS, SEM.

References

- [1] A. Mallat and S. Lotersztajn, "Cellular mechanisms of tissue fibrosis. 5. novel insights into liver fibrosis," *American Journal of Physiology: Cell Physiology*, vol. 305, no. 8, pp. C789–C799, 2013.
- [2] D. A. Brenner, "Molecular pathogenesis of liver fibrosis.," *Transactions of the American Clinical and Climatological Association*, vol. 120, pp. 361–368, 2009.

- [3] E. Novo, S. Cannito, C. Paternostro, C. Bocca, A. Miglietta, and M. Parola, "Cellular and molecular mechanisms in liver fibrogenesis," *Archives of Biochemistry and Biophysics*, vol. 548, pp. 20–37, 2014.
- [4] P. Ramachandran and J. P. Iredale, "Liver fibrosis: a bidirectional model of fibrogenesis and resolution," *QJM*, vol. 105, no. 9, Article ID hcs069, pp. 813–817, 2012.
- [5] E. L. Ellis and D. A. Mann, "Clinical evidence for the regression of liver fibrosis," *Journal of Hepatology*, vol. 56, no. 5, pp. 1171–1180, 2012.
- [6] A. Pellicoro, P. Ramachandran, and J. P. Iredale, "Reversibility of liver fibrosis," *Fibrogenesis & Tissue Repair*, vol. 5, supplement 1, p. S26, 2012.
- [7] D. Povero, C. Busletta, E. Novo et al., "Liver fibrosis: a dynamic and potentially reversible process," *Histology and Histopathology*, vol. 25, no. 8, pp. 1075–1091, 2010.
- [8] S. C. Faria, K. Ganesan, I. Mwangi et al., "MR imaging of liver fibrosis: current state of the art," *Radiographics*, vol. 29, no. 6, pp. 1615–1635, 2009.
- [9] P. Sharma, S. Dhawan, R. Bansal et al., "The usefulness of transient elastography by fibroscan for the evaluation of liver fibrosis," *Indian Journal of Gastroenterology*, vol. 33, no. 5, pp. 445–451, 2014.
- [10] I. Sporea, S. Bota, M. Peck-Radosavljevic et al., "Acoustic radiation force impulse elastography for fibrosis evaluation in patients with chronic hepatitis C: an international multicenter study," *European Journal of Radiology*, vol. 81, no. 12, pp. 4112–4118, 2012.
- [11] P. Bedossa and V. Paradis, "Liver extracellular matrix in health and disease," *Journal of Pathology*, vol. 200, no. 4, pp. 504–515, 2003.
- [12] T. A. Wynn, "Cellular and molecular mechanisms of fibrosis," *Journal of Pathology*, vol. 214, no. 2, pp. 199–210, 2008.
- [13] E. Mormone, J. George, and N. Nieto, "Molecular pathogenesis of hepatic fibrosis and current therapeutic approaches," *Chemico-Biological Interactions*, vol. 193, no. 3, pp. 225–231, 2011.
- [14] V. Hernandez-Gea and S. L. Friedman, "Pathogenesis of liver fibrosis," *Annual Review of Pathology: Mechanisms of Disease*, vol. 6, pp. 425–456, 2011.
- [15] Z. D. Goodman, "Grading and staging systems for inflammation and fibrosis in chronic liver diseases," *Journal of Hepatology*, vol. 47, no. 4, pp. 598–607, 2007.
- [16] M. Chiaradia, L. Baranes, F. Pigneur et al., "Liver magnetic resonance diffusion weighted imaging: 2011 update," *Clinics and Research in Hepatology and Gastroenterology*, vol. 35, no. 8-9, pp. 539–548, 2011.
- [17] A. A. Bakan, E. Inci, S. Bakan, S. Gokturk, and T. Cimilli, "Utility of diffusion-weighted imaging in the evaluation of liver fibrosis," *European Radiology*, vol. 22, no. 3, pp. 682–687, 2012.
- [18] K. Sandrasegaran, F. M. Akisik, C. Lin et al., "Value of diffusion-weighted MRI for assessing liver fibrosis and cirrhosis," *The American Journal of Roentgenology*, vol. 193, no. 6, pp. 1556–1560, 2009.
- [19] D. Le Bihan, E. Breton, D. Lallemand, M.-L. Aubin, J. Vignaud, and M. Laval-Jeantet, "Separation of diffusion and perfusion in intravoxel incoherent motion MR imaging," *Radiology*, vol. 168, no. 2, pp. 497–505, 1988.
- [20] D. Le Bihan, R. Turner, and J. R. Macfall, "Effects of intravoxel incoherent motions (IVIM) in steady-state free precession (SSFP) imaging: application to molecular diffusion imaging," *Magnetic Resonance in Medicine*, vol. 10, no. 3, pp. 324–337, 1989.
- [21] A. Luciani, A. Vignaud, M. Cavet et al., "Liver cirrhosis: intravoxel incoherent motion MR imaging-pilot study," *Radiology*, vol. 249, no. 3, pp. 891–899, 2008.
- [22] B. Leporq, H. Saint-Jalmes, C. Rabrait et al., "Optimization of intra-voxel incoherent motion imaging at 3.0 Tesla for fast liver examination," *Journal of Magnetic Resonance Imaging*, 2014.
- [23] J. H. Yoon, J. M. Lee, J. H. Baek et al., "Evaluation of hepatic fibrosis using intravoxel incoherent motion in diffusion-weighted liver MRI," *Journal of Computer Assisted Tomography*, vol. 38, no. 1, pp. 110–116, 2014.
- [24] Y. X. Wang and J. Yuan, "Evaluation of liver fibrosis with T1 ρ MR imaging," *Quantitative Imaging in Medicine and Surgery*, vol. 4, no. 3, pp. 152–155, 2014.
- [25] J. Yuan and Y. X. Wang, "Chapter 20. T1 ρ MR imaging: principle, technology, and application," in *Medical Imaging: Technology and Applications*, T. Farncombe and K. Iniewski, Eds., pp. 565–592, CRC Press, New York, NY, USA, 2013.
- [26] Y.-X. J. Wang, J. Yuan, E. S. H. Chu et al., "T1 ρ MR imaging is sensitive to evaluate liver fibrosis: an experimental study in a rat biliary duct ligation model," *Radiology*, vol. 259, no. 3, pp. 712–719, 2011.
- [27] T. Allkemper, F. Sagmeister, V. Cicinnati et al., "Evaluation of fibrotic liver disease with whole-liver t1 ρ MR imaging: a feasibility study at 1.5 T," *Radiology*, vol. 271, no. 2, pp. 408–415, 2014.
- [28] F. Zhao, Y.-X. J. Wang, J. Yuan et al., "MR T1 ρ as an imaging biomarker for monitoring liver injury progression and regression: an experimental study in rats with carbon tetrachloride intoxication," *European Radiology*, vol. 22, no. 8, pp. 1709–1716, 2012.
- [29] M. Yin, J. A. Talwalkar, K. J. Glaser et al., "Assessment of hepatic fibrosis with magnetic resonance elastography," *Clinical Gastroenterology and Hepatology*, vol. 5, no. 10, pp. 1207–e2, 2007.
- [30] Y. Wang, D. R. Ganger, J. Levitsky et al., "Assessment of chronic hepatitis and fibrosis: comparison of MR elastography and diffusion-weighted imaging," *The American Journal of Roentgenology*, vol. 196, no. 3, pp. 553–561, 2011.
- [31] Q.-B. Wang, H. Zhu, H.-L. Liu, and B. Zhang, "Performance of magnetic resonance elastography and diffusion-weighted imaging for the staging of hepatic fibrosis: a meta-analysis," *Hepatology*, vol. 56, no. 1, pp. 239–247, 2012.
- [32] L. Huwart, C. Sempoux, E. Vicaud et al., "Magnetic resonance elastography for the noninvasive staging of liver fibrosis," *Gastroenterology*, vol. 135, no. 1, pp. 32–40, 2008.
- [33] C. H. Thng, T. S. Koh, D. J. Collins, and D. M. Koh, "Perfusion magnetic resonance imaging of the liver," *World Journal of Gastroenterology*, vol. 16, no. 13, pp. 1598–1609, 2010.
- [34] P. V. Pandharipande, G. A. Krinsky, H. Rusinek, and V. S. Lee, "Perfusion imaging of the liver: current challenges and future goals," *Radiology*, vol. 234, no. 3, pp. 661–673, 2005.
- [35] M. Hagiwara, H. Rusinek, V. S. Lee et al., "Advanced liver fibrosis: diagnosis with 3D whole-liver perfusion MR imaging—initial experience," *Radiology*, vol. 246, no. 3, pp. 926–934, 2008.
- [36] B.-B. Chen, C.-Y. Hsu, C.-W. Yu et al., "Dynamic contrast-enhanced magnetic resonance imaging with Gd-EOB-DTPA for the evaluation of liver fibrosis in chronic hepatitis patients," *European Radiology*, vol. 22, no. 1, pp. 171–180, 2012.

- [37] J. Guo, R. Erickson, T. Trouard, J.-P. Galons, and R. Gillies, "Magnetization transfer contrast imaging in Niemann pick type C mouse liver," *Journal of Magnetic Resonance Imaging*, vol. 18, no. 3, pp. 321–327, 2003.
- [38] J.-H. Chen, J.-W. Chai, and W.-C. Shen, "Magnetization transfer contrast imaging of liver cirrhosis," *Hepato-Gastroenterology*, vol. 46, no. 29, pp. 2872–2877, 1999.
- [39] A. B. Rosenkrantz, P. Storey, A. G. Gilet et al., "Magnetization transfer contrast-prepared MR imaging of the liver: inability to distinguish healthy from cirrhotic liver," *Radiology*, vol. 262, no. 1, pp. 136–143, 2012.
- [40] M. Polasek, B. C. Fuchs, R. Uppal et al., "Molecular MR imaging of liver fibrosis: a feasibility study using rat and mouse models," *Journal of Hepatology*, vol. 57, no. 3, pp. 549–555, 2012.
- [41] B. C. Fuchs, H. Wang, Y. Yang et al., "Molecular MRI of collagen to diagnose and stage liver fibrosis," *Journal of Hepatology*, vol. 59, no. 5, pp. 992–998, 2013.
- [42] A. M. Chow, M. Tan, D. S. Gao et al., "Molecular MRI of liver fibrosis by a peptide-targeted contrast agent in an experimental mouse model," *Investigative Radiology*, vol. 48, no. 1, pp. 46–54, 2013.
- [43] J. Ehling, M. Bartneck, V. Fech et al., "Elastin-based molecular MRI of liver fibrosis," *Hepatology*, vol. 58, no. 4, pp. 1517–1518, 2013.
- [44] Q.-B. Wang, Y. Han, T.-T. Jiang et al., "MR Imaging of activated hepatic stellate cells in liver injured by CCl₄ of rats with integrin-targeted ultrasmall superparamagnetic iron oxide," *European Radiology*, vol. 21, no. 5, pp. 1016–1025, 2011.
- [45] D. A. Mankoff, "A definition of molecular imaging," *Journal of Nuclear Medicine*, vol. 48, no. 6, pp. 18N–21N, 2007.
- [46] M. M. J. Modo and J. W. M. Bulte, "Molecular and cellular MR imaging," *Journal of Nuclear Medicine*, vol. 48, no. 12, article 2087, 2007.
- [47] R. Weissleder, "Molecular imaging: exploring the next frontier," *Radiology*, vol. 212, no. 3, pp. 609–614, 1999.
- [48] C. Burtea, S. Laurent, L. Vander Elst, and R. N. Muller, "Contrast agents: magnetic resonance," *Handbook of Experimental Pharmacology*, vol. 185, no. 1, pp. 135–165, 2008.
- [49] X. Yang, "Nano- and microparticle-based imaging of cardiovascular interventions: overview," *Radiology*, vol. 243, no. 2, pp. 340–347, 2007.
- [50] M. F. Kircher and J. K. Willmann, "Molecular body imaging: MR imaging, CT, and US. Part I. Principles," *Radiology*, vol. 263, no. 3, pp. 633–643, 2012.
- [51] H. Hayashi and T. Sakai, "Animal models for the study of liver fibrosis: new insights from knockout mouse models," *The American Journal of Physiology—Gastrointestinal and Liver Physiology*, vol. 300, no. 5, pp. G729–G738, 2011.
- [52] P. Caravan, B. Das, S. Dumas et al., "Collagen-targeted MRI contrast agent for molecular imaging of fibrosis," *Angewandte Chemie International Edition in English*, vol. 46, pp. 8171–8173, 2007.
- [53] A. M. Gressner and R. Weiskirchen, "Modern pathogenetic concepts of liver fibrosis suggest stellate cells and TGF- β as major players and therapeutic targets," *Journal of Cellular and Molecular Medicine*, vol. 10, no. 1, pp. 76–99, 2006.
- [54] P. A. Helm, P. Caravan, B. A. French et al., "Postinfarction myocardial scarring in mice: molecular MR imaging with use of a collagen-targeting contrast agent," *Radiology*, vol. 247, no. 3, pp. 788–796, 2008.
- [55] A. Phinikaridou, M. E. Andia, A. M. Shah, and R. M. Botnar, "Advances in molecular imaging of atherosclerosis and myocardial infarction: shedding new light on in vivo cardiovascular biology," *American Journal of Physiology—Heart and Circulatory Physiology*, vol. 303, no. 12, pp. H1397–H1410, 2012.
- [56] P. Caravan, Y. Yang, R. Zachariah et al., "Molecular magnetic resonance imaging of pulmonary fibrosis in mice," *American Journal of Respiratory Cell and Molecular Biology*, vol. 49, no. 6, pp. 1120–1126, 2013.
- [57] S. M. Vithanarachchi and M. J. Allen, "Strategies for target-specific contrast agents for magnetic resonance imaging," *Current Molecular Imaging*, vol. 1, no. 1, pp. 12–25, 2012.
- [58] M. R. Makowski, A. J. Wiethoff, U. Blume et al., "Assessment of atherosclerotic plaque burden with an elastin-specific magnetic resonance contrast agent," *Nature Medicine*, vol. 17, no. 3, pp. 383–388, 2011.
- [59] K. Neubauer, T. Knittel, T. Armbrust, and G. Ramadori, "Accumulation and cellular localization of fibrinogen/fibrin during short-term and long-term rat liver injury," *Gastroenterology*, vol. 108, no. 4, pp. 1124–1135, 1995.
- [60] J. Pilch, D. M. Brown, M. Komatsu et al., "Peptides selected for binding to clotted plasma accumulate in tumor stroma and wounds," *Proceedings of the National Academy of Sciences of the United States of America*, vol. 103, no. 8, pp. 2800–2804, 2006.
- [61] M. Tan, X. Wu, E.-K. Jeong, Q. Chen, and Z.-R. Lu, "Peptide-targeted nanoglobular Gd-DOTA monoamide conjugates for magnetic resonance cancer molecular imaging," *Biomacromolecules*, vol. 11, no. 3, pp. 754–761, 2010.
- [62] F. Ye, E.-K. Jeong, Z. Jia, T. Yang, D. Parker, and Z.-R. Lu, "A peptide targeted contrast agent specific to fibrin-fibronectin complexes for cancer molecular imaging with MRI," *Bioconjugate Chemistry*, vol. 19, no. 12, pp. 2300–2303, 2008.
- [63] C. von Bary, M. Makowski, A. Preissel et al., "MRI of coronary wall remodeling in a swine model of coronary injury using an elastin-binding contrast agent," *Circulation: Cardiovascular Imaging*, vol. 4, no. 2, pp. 147–155, 2011.
- [64] S. L. Friedman, "Hepatic stellate cells: protean, multifunctional, and enigmatic cells of the liver," *Physiological Reviews*, vol. 88, no. 1, pp. 125–172, 2008.
- [65] M. Dodig, B. Ogunwale, S. Dasarathy, M. Li, B. Wang, and A. J. McCullough, "Differences in regulation of type I collagen synthesis in primary and passaged hepatic stellate cell cultures: the role of $\alpha 5\beta 1$ -integrin," *The American Journal of Physiology—Gastrointestinal and Liver Physiology*, vol. 293, no. 1, pp. G154–G164, 2007.
- [66] X. Zhou, Y. Zhang, J. J. Zhang et al., "Expression of fibronectin receptor, integrin $\alpha 5\beta 1$ of hepatic stellate cells in rat liver fibrosis," *Chinese Medical Journal*, vol. 113, no. 3, pp. 272–276, 2000.
- [67] G. Huang and D. R. Brigstock, "Integrin expression and function in the response of primary culture hepatic stellate cells to connective tissue growth factor (CCN2)," *Journal of Cellular and Molecular Medicine*, vol. 15, no. 5, pp. 1087–1095, 2011.
- [68] X. Zhou, F. R. Murphy, N. Gehdu, J. Zhang, J. P. Iredale, and R. C. Benyon, "Engagement of $\alpha_v\beta_3$ integrin regulates proliferation and apoptosis of hepatic stellate cells," *The Journal of Biological Chemistry*, vol. 279, no. 23, pp. 23996–24006, 2004.
- [69] Y. Zhang, T. Ikegami, A. Honda et al., "Involvement of integrin-linked kinase in carbon tetrachloride-induced hepatic fibrosis in rats," *Hepatology*, vol. 44, no. 3, pp. 612–622, 2006.

- [70] I. Dijkgraaf, A. J. Beer, and H.-J. Wester, "Application of RGD-containing peptides as imaging probes for alphavbeta3 expression," *Frontiers in Bioscience*, vol. 14, no. 3, pp. 887–899, 2009.
- [71] J. W. M. Bulte, A. H. Schmieder, J. Keupp, S. D. Caruthers, S. A. Wickline, and G. M. Lanza, "MR cholangiography demonstrates unsuspected rapid biliary clearance of nanoparticles in rodents: implications for clinical translation," *Nanomedicine: Nanotechnology, Biology and Medicine*, vol. 10, no. 7, pp. 1385–1388, 2014.

Clinical Study

Ultrafast Cone-Beam Computed Tomography: A Comparative Study of Imaging Protocols during Image-Guided Therapy Procedure

Jijo Paul,¹ Annamma Chacko,² Mohammad Farhang,¹ Shahram Kamali,¹
Mohsen Tavanania,¹ Thomas Vogl,¹ and Bitu Panahi¹

¹Diagnostic and Interventional Radiology, University Hospital, Goethe University Frankfurt,
Theodor-Stern-Kai 7, 60590 Frankfurt, Germany

²Division of Mathematics and Statistics, Dougherty System, Albany, GA 31705, USA

Correspondence should be addressed to Jijo Paul; jijopaul1980@gmail.com

Received 5 June 2014; Revised 30 October 2014; Accepted 16 November 2014

Academic Editor: Edward Lee

Copyright © 2015 Jijo Paul et al. This is an open access article distributed under the Creative Commons Attribution License, which permits unrestricted use, distribution, and reproduction in any medium, provided the original work is properly cited.

Objective. To evaluate two ultrafast cone-beam CT (UF-CBCT) imaging protocols with different acquisition and injection parameters regarding image quality and required contrast media during image-guided hepatic transarterial chemoembolization (TACE). **Methods.** In 80 patients (male: 46, female: 34; mean age: 56.8 years; range: 33–83) UF-CBCT was performed during TACE for intraprocedural guidance. Imaging was performed using two ultrafast CBCT acquisition protocols with different acquisition and injection parameters (imaging protocol 1: acquisition time 2.54 s, and contrast 6 mL with 3 s delay; imaging protocol 2: acquisition time 2.72 s, and contrast 7 mL with 6 s delay). Image evaluation was performed with both qualitative and quantitative methods. Contrast injection volume and dose parameters were compared using values from the literature. **Results.** Imaging protocol 2 provided significantly better ($P < 0.05$) image quality than protocol 1 at the cost of slightly higher contrast load and patient dose. Imaging protocol 1 provided good contrast perfusion but it mostly failed to delineate the tumors ($P < 0.05$). On the contrary, imaging protocol 2 showed excellent enhancement of hepatic parenchyma, tumor, and feeding vessels. **Conclusion.** Tumor delineation, visualization of hepatic parenchyma, and feeding vessels are clearly possible using imaging protocol 2 with ultrafast CBCT imaging. A reduction of required contrast volume and patient dose were achieved due to the ultrafast CBCT imaging.

1. Introduction

Cone-beam computed tomography (CBCT) is routinely used for many clinical applications in the fields of neurology, vascular, radiology, oncology, and cardiovascular interventions [1–9]. As an interventional oncology application, this system is routinely used for image-guiding purpose during transarterial chemoembolization (TACE) therapy procedures [10–12]. TACE guidelines recommend the use of contrast enhanced CBCT to delineate tumour and tumour feeding vessels [13, 14]. Many publications showed how intraprocedurally acquired CBCT images help to map out an adequate embolization strategy by visualizing the vessel tree that feeds hepatic tumors and metastases [8, 9, 14–17]. Modern angiographic systems are capable of acquiring cross-sectional

CBCT image datasets during interventional procedures and improve the visualization of hepatic tumors as well as vascular anatomy [10–14]. However, CBCT implicates certain important limitations such as limited soft tissue resolution, limited field of view, and long acquisition times (typically 5 to 10 seconds in abdominal imaging) in general.

For contrast enhanced CBCT as performed during TACE procedures the long acquisition time also results in a long injection time as the contrast bolus has to be maintained during the whole time of the acquisition to provide a consistent filling of the imaged vessels and tumors. This means that the longer the acquisition time is the longer the contrast injection has to last and the more the contrast medium is required which can become a serious problem for patients with poor kidney function. The long acquisition time of image data is

due to the limited maximum detector readout speed (30–60 f/s), limited maximum mechanical speed of CBCT system (40–60°/s), and number of projection images required for certain image quality. The present study intended to evaluate ultrafast CBCT (UF-CBCT) imaging protocols on a multiaxis robotic CBCT system regarding the capability to create image datasets suitable for guiding TACE procedures while at the same time save contrast media and radiation dose compared to values in the literature.

2. Material and Methods

2.1. Patient Characteristics. This is a prospective study conducted from October 2011 to June 2013 using 80 patients and the study protocol was accepted by institutional review board. The patient selection was randomly performed for each protocol without bias. The selection of the patients for UF-CBCT imaging was completely dependent on TACE inclusion and exclusion criteria, based on previous publication [12]. Inclusion criteria for the TACE therapy were as follows: confirmation of at least a single tumor in the liver parenchyma, unresectable metastatic tumor(s), contraindication to surgery, and tumor(s) not responsive to radiotherapy or chemotherapy. Exclusion criteria were as follows: existence of extrahepatic tumor(s), poor patient performance status, poor hepatic function, renal failure, contraindication to angiography, respiratory or cardiovascular failure, obstructive jaundice, portal vein thrombosis or occlusion, and recently received radiotherapy (in last two months). MRI is considered to be gold standard imaging modality for detection of tumors present in the hepatic parenchyma. Pretreatment T1 weighted unenhanced/contrast enhanced and T2 weighted unenhanced/contrast enhanced magnetic resonance images (MRI) were acquired for all patients to assess the hepatic tumor details such as size, shape, number, and position.

2.2. Cone-Beam CT Imaging. We used a multiaxis robotic CBCT system (Artis zeego, Siemens Healthcare, Forchheim Germany) to conduct patient examinations during TACE therapy. This UF-CBCT system offers the possibility to rotate the tube-detector system around the patient with a maximum speed of up to 100°/sec. The system is equipped with a latest generation 30 × 40 cm flat panel detector made of amorphous silicon with cesium iodide scintillator (aSi:CsI). During UF-CBCT acquisition the system acquires projection images on a 200° circular trajectory with a constant angular frame increment (AI); that is, each AI degree the system acquired an image. This means that the image acquisition frame rate differs between the acceleration phase, the phase with constant speed, and the deceleration phase of the CBCT.

The correlation between UF-CBCT rotation speed (v_{cbct}), readout speed (v_{ro}), and angular frame increment (AI) is as follows:

$$AI (^{\circ}/\text{image}) = \frac{v_{cbct} (^{\circ}/\text{s})}{v_{ro} (\text{image}/\text{s})}. \quad (1)$$

With a given angular increment for a UF-CBCT acquisition the maximum readout speed of the detector may limit the maximum CBCT rotation speed.

2.3. Data Acquisition Protocols. In this study we evaluated two UF-CBCT imaging protocols, each consisting of a CBCT acquisition protocol and a contrast injection protocol (Table 1). The angular increment of acquisition protocol 1 (Table 1) was set to 1.5° per image, resulting in 133 images on the 200° circular trajectory. The angular increment of acquisition protocol 2 was set to 1.2° per image, resulting in 166 images on the 200° circular trajectory.

For the UF-CBCT protocols the CBCT system had to be positioned in a head side position so that the acquisition is performed in a “propeller-like” mode where only one axis of the multiaxis robotic UF-CBCT system is moved. The 200° acquisition trajectory reaches from right-anterior-oblique (RAO) 170° to left-anterior-oblique (LAO) 30°. During TACE, the patients were positioned head-first in supine position on table top and their arms were positioned above the head during data acquisition. Furthermore, UF-CBCT image data was acquired for all patients on expiration condition. The UF-CBCT acquisition was performed with a 0.36 $\mu\text{Gy}/\text{image}$ detector entrance dose setting. The tube voltage is preset to 90 kV but is modulated together with the tube current during the rotational run to keep the detector entrance dose constant.

2.4. Image Data Reconstruction. From the projection images a 3D dataset with isotropic voxels of 0.5 mm is automatically reconstructed on the connected workstation (syngo XWP, Siemens Healthcare, Forchheim, Germany) using a filtered back-projection (Feldkamp) algorithm. This 3D dataset is then loaded into the software application syngo InSpace, which allows the user to visualize the dataset in different rendering modes like multiplanar reformatted (MPR), maximum intensity projection (MIP), or volume rendered (VRT) images.

2.5. Contrast Injection Protocol. A UF-CBCT acquisition with contrast material injection (Visipaque 320 from GE Healthcare Braunschweig, Germany) was performed for all examined patients. The injection was performed into the right or left hepatic artery using a coaxial microcatheter (2.7F/2.4F × 150 cm; Trevo Pro 18 microcatheter, Concentric medical, CA, USA). A road mapping of the target tumor is possible using contrast material injection as described by Wallace et al. [18]. Contrast injection protocol 1 was used in conjunction with acquisition protocol 1 (Table 1) on forty patients (22 male, 18 female; mean age: 56.3 years; range: 33–73 years) during imaging (imaging protocol 1). Contrast injection protocol 2 was used in conjunction with acquisition protocol 2 on another forty patients (24 male, 16 female; mean age: 57.3 years; range 43–83 years) during TACE (imaging protocol 2). Complete information regarding the parameters used for contrast material injection during both image acquisitions is provided in Table 1.

2.6. Image Analysis. After the examination of patients using UF-CBCT, the images were evaluated by three radiologists with 4, 6, and 20 years of experience in abdominal imaging. They used a scoring system to analyze image data qualitatively based on tumor delineation, vascular contrast material

TABLE 1: Described specifications of the clinical imaging parameters and contrast material injection protocol used for the ultrafast cone-beam CT imaging of patients during transarterial chemoembolization treatment.

Imaging parameters	Acquisition protocol 1	Acquisition protocol 2
Set kilo-voltage	90 kV	90 kV
Number of images	133	166
Angular increment (°/ima)	1.5	1.2
Maximum CBCT speed (°/s)	100	88.8
Maximum readout speed (ima/s)	67	74
Total acquisition time (s)	2.54	2.72
Detector entrance dose (uGy/frame)	0.36	0.36
Contrast injection parameters	Injection protocol 1	Injection protocol 2
Contrast volume (mL)	6	7
Iodine/mL	320	320
Saline (mL)	12	20
Flow rate (mL/s)	3	3
X-ray delay (s)	3	6
Injection duration (s)	6	9

TABLE 2: Classification of grading score based on tumor delineation, vascular contrast material perfusion, and appearance of the artifacts.

Grading point score	Tumor delineation, vascular contrast material perfusion, and appearance of artifacts. Description
1	Not suitable for diagnosis (nondiagnostic image data)
2	Suboptimal contrast perfusion and tumor delineation, strong appearance of artifacts
3	Less than standard contrast perfusion and tumor delineation with hazy appearance of artifacts
4	Standard contrast perfusion and tumor delineation with hazy appearance of artifacts
5	Vascular contrast material perfusion and tumor delineation are higher than necessary with little or no artifacts

perfusion, and appearance of artifacts on the cross-sectional images (Table 2). Readers were blinded regarding imaging protocols and associate parameters used for the study but they were informed the images were generated during TACE therapy procedure. The number of tumors which appeared on image data was assessed by the same radiologists. The hepatic tumors were classified as three categories during analysis based on its enhancement characteristics: hypoenhanced tumor, heterogeneously enhanced tumor, and homogeneously enhanced tumor (Table 3). Moreover, quantitative image quality parameters such as Hounsfield unit (HU), image noise, signal-to-noise ratio ($SNR = HU/noise$), and tumor-to-liver contrast ($TLC = HU_{tumor} - HU_{liver}$) were also determined using the acquired UF-CBCT image datasets. Quantitative measurements were performed by the same radiologists according to the previous publications [2, 12, 14]. HU was measured using a circular region of interest (ROI) placed on the hepatic parenchyma away from the tumor for normal parenchymal measurements and on the tumor for tumor HU measurements. Diameter of the circular ROI used for measurement of HU was 2 cm; however, this mentioned diameter may change according to the size of the tumor during tumor HU measurements. Two ROI measurements were performed using adjacent CBCT slices and average value was taken into account for calculating mean HU values. A standard deviation of pixel values in the ROI circle was considered as image noise (HU). All measurements were

performed using a dedicated syngo X-Leonardo workstation from Siemens Healthcare, Forchheim, Germany.

2.7. Patient Dose Analysis. Two radiation dose parameters, dose area product (DAP) and patient entrance dose (PED), were obtained during exposure from the patient examination protocol generated on the UF-CBCT system [10]. Calculated values were compared using the data available in the literature.

2.8. Statistical Analysis. Results of the present study are displayed as means \pm standard deviation and range for continuous variables. The statistical analyses were performed using computer based BiAS software (BiAS for Windows, Epsilon 2008, version 8.4.2). A *P* value less than or equal to 0.05 is considered as statistically significant results. The normality of data distribution was examined using Kolmogorov-Smirnov-Lilliefors test. Qualitative image quality assessment comparisons were performed using Wilcoxon rank sum test; furthermore, interobserver comparisons were performed using Cohen's Kappa during qualitative analysis. Kappa agreement was considered $k < 0$ (less than chance agreement), $k = 0.01-0.20$ (slight agreement), $k = 0.21-0.40$ (fair agreement), $k = 0.41-0.60$ (moderate agreement), $k = 0.61-0.80$ (substantial agreement), and $k = 0.81-0.99$ (almost perfect agreement). Regarding comparison of the quantitative results, paired Student's *t*-test was used to test the significance between

TABLE 3: Details of patient tumor characteristics determined using gold standard MR-image data. The determined tumor characteristics using MRI displayed separately for UF-CBCT imaging protocols 1 (P1) and 2 (P2) patient groups.

Type of hepatic tumor	Tumor involvement (P1/P2)	Hepatic tumor groups	Number of patients		Number of tumors		Mean dimension in cm ($l \times b$)	
			P1	P2	P1	P2	P1	P2
Hypoenhanced tumor	Right lobe: 21/21	Metastasis from:						
	Left lobe: 13/14	Thyroid carcinoma	5	6	16	20	4.4×3.9	4×3.8
	Caudate lobe: 2/5	Colorectal carcinoma	6	7	25	23	4.8×4.7	4.5×4.4
	Quadrate lobe: 5/3							
Heterogeneously enhanced tumor	Right lobe: 21/24	Cholangiocarcinoma	5	4	17	15	4×3.8	3.8×3.6
	Left lobe: 15/12	Metastasis from:						
	Caudate lobe: 7/3	Colorectal carcinoma	4	7	12	12	4.3×3.7	4.5×4
	Quadrate lobe: 1/2	Breast carcinoma	4	3	15	14	4.8×4.3	4.3×3.9
Homogeneously enhanced tumor	Right lobe: 26/22	Hepatocell. carcinoma	7	5	28	20	4.1×3.6	4×3.6
	Left lobe: 15/14	Cholangiocarcinoma	5	5	9	13	4.9×4.2	4.2×3.8
	Caudate lobe: 2/4	Metastasis from:						
	Quadrate lobe: 3/5	Colorectal carcinoma	4	3	9	12	4.7×4.4	4.5×3.8

TABLE 4: Details of the patient tumor characteristics obtained using ultrafast CBCT image data (P1: imaging protocol 1; P2: imaging protocol 2).

Type of hepatic tumor	Tumor involvement (P1/P2)	Hepatic tumor groups	Number of patients		Number of tumors		Mean dimension in cm ($l \times b$)	
			P1	P2	P1	P2	P1	P2
Hypoenhanced tumor	Right lobe: 16/19	Metastasis from:						
	Left lobe: 10/13	Thyroid carcinoma	5	6	11	19	3.9×3.4	3.8×3.5
	Caudate lobe: 0/5	Colorectal carcinoma	6	7	17	21	4.5×4.2	4.3×4.1
	Quadrate lobe: 2/3							
Heterogeneously enhanced tumor	Right lobe: 18/21	Cholangiocarcinoma	5	4	13	13	3.5×3.4	3.6×3.4
	Left lobe: 11/11	Metastasis from:						
	Caudate lobe: 4/3	Colorectal carcinoma	4	7	9	11	3.8×3.2	4.2×3.7
	Quadrate lobe: 0/2	Breast carcinoma	4	3	11	13	4.2×3.7	4×3.7
Homogeneously enhanced tumor	Right lobe: 19/21	Hepatocell. carcinoma	7	5	21	19	3.6×3.1	3.7×3.3
	Left lobe: 11/13	Cholangiocarcinoma	5	5	6	12	4.6×3.6	3.9×3.5
	Caudate lobe: 2/4	Metastasis from:						
	Quadrate lobe: 2/5	Colorectal carcinoma	4	3	7	12	4×3.8	4.2×3.5

data categories. A gold standard pretreatment MR-image data was used as standard of reference for statistical analysis during tumor detection. Sensitivity and predictive values were determined in relation to the detectability of hepatic tumors.

3. Result

Details of the patient hepatic tumor characteristics obtained using gold standard MRI are displayed in Table 3 and tumor characteristics determined using images of both UF-CBCT imaging protocols are provided in Table 4. The evaluated imaging protocol 2 produced an excellent tumor delineation, contrast perfusion, and parenchymal visualization (Figure 1; Table 5) with adequate enhancement due to the use of proper bolus timing, mixing ratio, and X-ray delay time during

ultrafast imaging. However, using imaging protocol 1 the identification of hepatic tumors was difficult because of reduced contrast material (Figure 1) as a result of improper delay time for ultrafast imaging. Qualitative analysis showed large difference of image quality between the two imaging protocols (Table 5). Image quality was significantly higher (all $P < 0.05$) in imaging protocol 2 compared to imaging protocol 1 (Table 5; Figure 1). Interreader agreement performed using Kappa during qualitative analysis showed almost perfect agreement ($K = 0.832-0.947$).

Quantitative image quality analysis also showed similar results to qualitative analysis (Table 6). Based on quantitative analysis HU was significantly higher (all $P < 0.05$) in imaging protocol 2 compared to 1 (Table 6). The calculated SNR values were significantly higher (all $P < 0.05$) in protocol 2 image data compared to the other protocol evaluated. The TLC

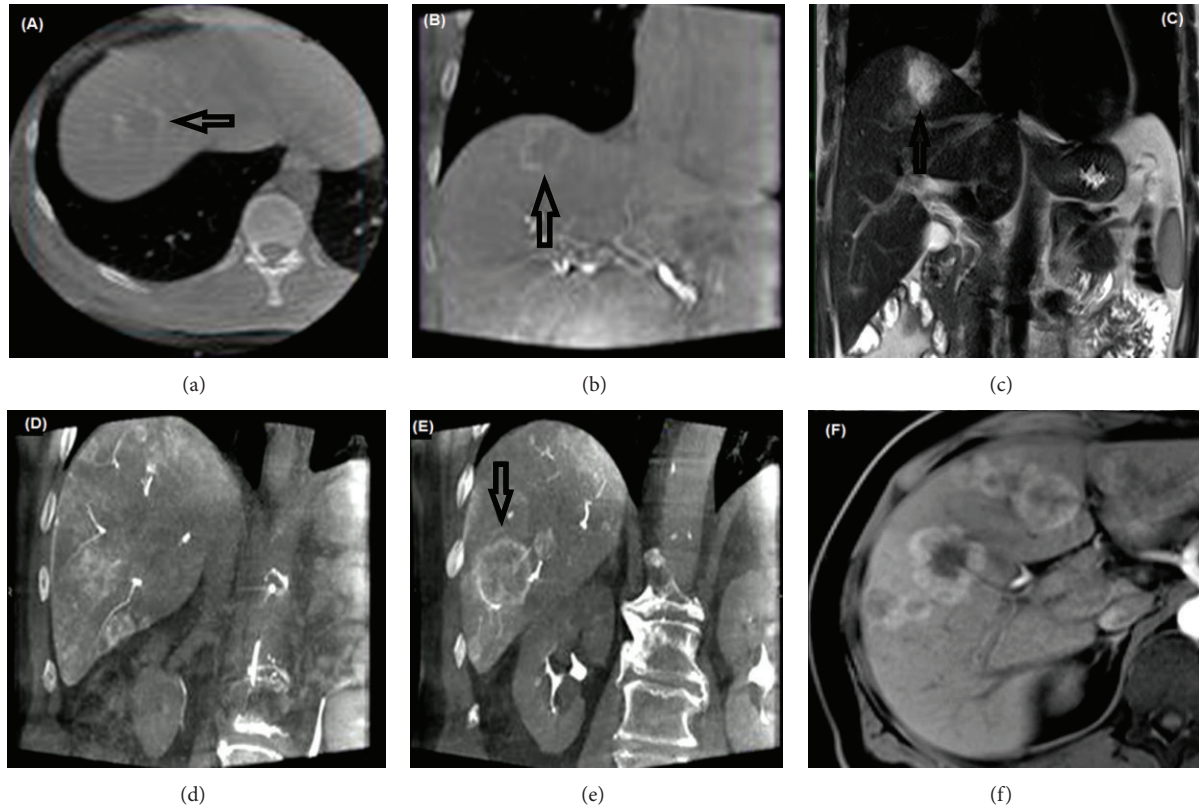


FIGURE 1: Frames (a) and (b) represented the images obtained from a 62-year-old patient during TACE therapy, generated using ultrafast cone-beam CT with imaging protocol 1. Pretreatment magnetic resonance cross-sectional images ((c) and (f)) show a clear view of embedded tumor in the hepatic parenchyma. Hepatic tumor detection was insufficient using imaging protocol 1 data (tumor indicated using black arrow) compared to imaging protocol 2 due to a reduction of contrast material in the tumors. Coronal reconstructed images ((d) and (e)) were acquired using imaging protocol 2 during a 60-year-old patient TACE examination. The images show excellent tumor(s), feeding vessels, and hepatic parenchymal visualization; furthermore, notice the strong contrast material enhancement of the tumors with little or no artifacts.

TABLE 5: Displayed image quality qualitative analysis scores (mean ± standard deviation and range) obtained from the readers using both ultrafast CBCT patient imaging protocols.

Imaging protocol	Tumor classification:		
	Hypoenhanced tumor (A)	Heterogeneously enhanced tumor (B)	Homogenously enhanced tumor (C)
Protocol 1	2.9 ± 0.4 (2.6–3.1)	3 ± 0.4 (2.6–3.25)	3.1 ± 0.5 (2.7–3.4)
Protocol 2	4 ± 0.6 (3.7–4.2)	4.3 ± 0.4 (4–4.5)	4.6 ± 0.3 (4.3–4.8)
<i>P</i> value	0.0001	0.0001	0.0001

computation to determine quantitative tumor delineation showed significantly higher (all $P < 0.05$) results for protocol 2 compared to 1 (Table 6).

The volume of iodine injected into the patients during UF-CBCT was 1920 mg and 2240 mg, respectively, for injection protocols 1 and 2 during contrast material injection. In [14], authors performed three conventional CBCT patient examinations during TACE therapy. They used 4800 mg, 6400 mg, and 8000 mg of iodine in the injected volume of contrast material during hepatic CBCT imaging. In [19] authors used 4625 mg and [20] used 9000 mg of iodine in the injected volume of contrast for patient examinations. UF-CBCT imaging protocol 2 used a marked reduction of iodine volume compared to [14] by 53%, 65%, and 72% and [19]

by 51.5%. Moreover, a significant reduction of iodine (75%) was observed during UF-CBCT protocol 2 compared with [20]. Tumor detection sensitivity and predictive values were calculated using the image data obtained from UF-CBCT and MRI. Determined sensitivity showed a remarkable increase in UF-CBCT imaging protocol 2 data compared to 1 (Table 7).

Mean PED estimated for UF-CBCT imaging protocols 1 and 2 were 77.5 ± 12.2 mGy (69–91) and 81.6 ± 12.8 mGy (72–104), respectively, while the mean DAP obtained for imaging protocols 1 and 2 were 18.37 ± 4.4 Gy·cm² (11–26) and 22.55 ± 4.9 Gy·cm² (15–29), respectively. Reference [12] showed a mean PED of 111.8 ± 12.8 mGy (101–128) and DAP value of 29.2 ± 8 Gy·cm² (21–36) during TACE therapy using 5s tube-detector rotation. However, [2] displayed a mean PED

TABLE 6: Quantitative image quality parameters and tumor delineation obtained from ultrafast CBCT image data with contrast material injection for both examined protocols. Furthermore, TLC represents tumor-to-liver contrast.

Image quality parameter	Measurement locations			
	Normal hepatic parenchyma	Hypoenhanced tumor (A)	Heterogeneously enhanced tumor (B)	Homogeneously enhanced tumor (C)
Protocol 1				
Hounsfield unit (HU)	54 ± 13 (41–68)	25 ± 8 (14–37)	63 ± 15 (47–77)	151 ± 17 (119–196)
Image noise (HU)	42 ± 11 (37–49)	52 ± 18 (39–59)	62 ± 17 (51–73)	83 ± 22 (69–99)
Signal-to-noise ratio (SNR)	1.3 (1.15–1.4)	0.48 (0.35–0.58)	1 (0.98–1.1)	1.8 (1.7–1.93)
Tumor-to-liver contrast (TLC)	—	−29 (−18–−39)	9 (4–14)	97 (91–113)
Protocol 2				
Hounsfield unit (HU)	83 ± 14 (69–95)	10 ± 3 (6–15)	115 ± 20 (74–147)	217 ± 21 (169–244)
Image noise (HU)	29 ± 9 (25–35)	17 ± 7 (13–23)	44 ± 15 (32–52)	60 ± 19 (49–66)
Signal-to-noise ratio (SNR)	2.85 (2.75–3)	0.7 (0.4–0.8)	2.6 (2.3–2.8)	3.6 (3.5–3.7)
Tumor-to-liver contrast (TLC)	—	−73 (−59–−89)	32 (21–41)	134 (119–162)
<i>P</i> value (protocol 1 versus protocol 2):	0.0001	0.0001	0.0001	0.0001

TABLE 7: Displayed sensitivity and predictive values, calculated using UF-CBCT imaging protocols 1 and 2 and magnetic resonance image data.

Type of tumor	Interpreted as tumor on		True positive	False negative	False positive	True negative	Sensitivity (%)	Specificity (%)	Positive predictive value (%)	Negative predictive value (%)
	MRI	UF-CBCT protocol 1								
Hypoenhanced tumors	41	28	23	18	5	0	56	0	82	0
Heterogeneously enhanced tumors	44	33	27	17	6	0	61.3	0	81.8	0
Homogeneously enhanced tumors	46	34	29	17	5	0	63	0	85.3	0
	MRI	UF-CBCT protocol 2								
Hypoenhanced tumors	43	40	36	7	4	0	83.7	0	90	0
Heterogeneously enhanced tumors	41	37	34	7	3	0	82.9	0	91.9	0
Homogeneously enhanced tumors	45	43	41	4	2	0	91	0	95.3	0

of 124.4 ± 19.5 mGy (109.5–136) and DAP of 32.3 ± 5 Gy·cm² (26–37) during TACE using 5s protocol. UF-CBCT imaging protocol 2 showed a reduction of radiation dose by 22.8% (DAP)/27% (PED) from [12] and 30.3% (DAP)/34.4% (PED) from [2], respectively, during comparison.

4. Discussion

Long patient breath hold is necessary for conventional CBCT image data acquisition to avoid motion artifacts and thus obtain reasonable image quality. A continuous contrast

material injection should be maintained in entire duration during contrast enhanced CBCT data acquisition. These two conditions directly affect image quality as well as contrast material load in the patients. The high rotation speed of the tube-detector system and shorter acquisition time of the UF-CBCT make it easier for patients to comply with the breath-hold requirements and thus reduce the occurrence of motion artifacts, which produce good image quality. Ultrafast CBCT imaging bears the potential to reduce volume of contrast material (up to 6 and 7 mL) required for contrast enhanced CBCT during TACE therapy of patients due

to a reduction of imaging time and appropriate contrast protocol used for imaging. The volume of iodine in the contrast material injected during CBCT imaging as regards TACE is significantly different in various published materials [14, 19–21] ranging from 4000 to 9000 mg. In the present study, we used only 1920 mg and 2240 mg of iodine in the injected volume of contrast using injection protocols 1 and 2, respectively. Since many patients with malignant liver tumors require multiple embolization sessions, the evaluated UF-CBCT imaging protocols could help to reduce the “life-time” volume of contrast material significantly [2].

We obtained a reduced radiation dose on patients due to ultrafast imaging time compared to published data [2, 12]. The evaluated UF-CBCT imaging protocols generate a reduced number of images (from 248 to 133 during imaging protocol 1 and 166 during imaging protocol 2) with the same per frame system dose compared to imaging protocols evaluated in previous publications [2, 12]. At least imaging protocol 2 proved to produce sufficient image quality for TACE guidance with reduced patient dose.

Injection protocols and delay time are highly influencing parameters on the enhancement of hepatic parenchyma and tumors. Imaging protocol 1 produced an insufficient visualization of hepatic tumors/metastasis. This is due to the short X-ray delay time of 3 seconds, which prevented proper tumor enhancement before the UF-CBCT data acquisition. In imaging protocol 2, the X-ray delay was extended to 6 seconds which allowed the further perfusion of the tumor feeding vessels with contrast material. To keep the contrast load for the patient at a reasonable level the contrast dilution was increased from a mixing level of 1:2 (contrast/saline) in imaging protocol 1 to 1:3 in imaging protocol 2. Despite the higher contrast/water dilution compared to imaging protocol 1, imaging protocol 2 produced excellent tumor enhancement with the possibility of good tumor delineation during UF-CBCT imaging. The reasons are the higher delay time and the higher number of frames acquired. To obtain reasonable image quality for CBCT image data a certain number of projection images (frames) are required [10]. Ideally a CBCT system should be able to acquire certain desired number of projection images in a very short time and the tube-detector system should be able to rotate at a very high speed while these projection images are acquired. In this study we utilized high frame rate and a robotic CBCT system with ultrafast rotation capabilities resulting in a very short data acquisition time for UF-CBCT acquisition. During acquisition protocol 1 imaging, the UF-CBCT is rotating with its highest possible speed, that is, $100^\circ/\text{sec}$; based on formula 1 a frame rate of 67 images per second is required to read out an image every 1.5° . The system accelerates to the maximum speed in approximately 1 second and drives at maximum speed for about 1 sec before it decelerates in 0.5 sec to a stop again. Hence, the total acquisition time of protocol 1 is 2.54 seconds. In protocol 2, the maximum readout speed of the available detector is limited to 74 frames per second; the maximum CBCT speed had to be limited to $88.8^\circ/\text{s}$ (see formula (1)). With an acceleration phase of ~ 0.8 seconds, a phase of maximum speed of ~ 1.5 seconds, and a deceleration phase of 0.4 seconds the total acquisition time of protocol 2 sums up to 2.72 seconds.

In the present study we used an ultrafast robotic CBCT imaging system and protocols with less than 3 seconds image acquisition time acquiring image data during TACE. Imaging protocol 2 provided an excellent visualization of tumor(s) and feeding vasculature as well as hepatic parenchyma due to adequate bolus timing, mixing ratio X-ray delay time, and higher number of acquired frames compared to imaging protocol 1. Ultrafast image acquisitions reduce contrast material injection volume to patients during TACE examination using UF-CBCT. Furthermore, UF-CBCT imaging achieved a reduction of radiation dose due to reduction of total number of acquired frames during imaging. The reduction of imaging time helps to prevent the appearance of motion artifacts which was previously reported as a problem with longer CBCT acquisitions. Based on image quality results of imaging protocol 2 we recommend that this imaging protocol should be used for UF-CBCT image acquisitions during patient imaging.

Conflict of Interests

The authors declare that there is no conflict of interests regarding the publication of this paper.

References

- [1] R. C. Orth, M. J. Wallace, and M. D. Kuo, “C-arm cone-beam CT: general principles and technical considerations for use in interventional radiology,” *Journal of Vascular and Interventional Radiology*, vol. 19, no. 6, pp. 814–820, 2008.
- [2] J. Paul, E. C. Mbalisike, and T. J. Vogl, “Radiation dose to procedural personnel and patients from an X-ray volume imaging system,” *European Radiology*, vol. 23, no. 12, pp. 3262–3270, 2013.
- [3] U. B. Jeon, J. W. Lee, K. S. Choo et al., “Iodized oil uptake assessment with cone-beam CT in chemoembolization of small hepatocellular carcinomas,” *World Journal of Gastroenterology*, vol. 15, no. 46, pp. 5833–5837, 2009.
- [4] J. Iwazawa, S. Ohue, N. Hashimoto, H. Abe, M. Hamuro, and T. Mitani, “Detection of hepatocellular carcinoma: comparison of angiographic C-arm CT and MDCT,” *American Journal of Roentgenology*, vol. 195, no. 4, pp. 882–887, 2010.
- [5] M. Morimoto, K. Numata, M. Kondo et al., “C-arm cone beam CT for hepatic tumor ablation under real-time 3D imaging,” *The American Journal of Roentgenology*, vol. 194, no. 5, pp. W452–W454, 2010.
- [6] J. Kempfert, A. Noetling, M. John, A. Rastan, F. W. Mohr, and T. Walther, “Automatically segmented DynaCT: enhanced imaging during transcatheter aortic valve implantation,” *Journal of the American College of Cardiology*, vol. 58, no. 25, p. e211, 2011.
- [7] M. L. Dijkstra, M. J. Eagleton, R. K. Greenberg, T. Mastracci, and A. Hernandez, “Intraoperative C-arm cone-beam computed tomography in fenestrated/branched aortic endografting,” *Journal of Vascular Surgery*, vol. 53, no. 3, pp. 583–590, 2011.
- [8] J. G. Schwartz, A. M. Neubauer, T. E. Fagan, N. J. Noordhoek, M. Grass, and J. D. Carroll, “Potential role of three-dimensional rotational angiography and C-arm CT for valvular repair and implantation,” *International Journal of Cardiovascular Imaging*, vol. 27, no. 8, pp. 1205–1222, 2011.

- [9] A. Dörfler, T. Struffert, T. Engelhorn, and C. Richter, "Rotational flat-panel computed tomography in diagnostic and interventional neuroradiology," *RoFo*, vol. 180, no. 10, pp. 891–898, 2008.
- [10] J. Paul, V. Jacobi, M. Farhang, B. Bazrafshan, T. J. Vogl, and E. C. Mbalisike, "Radiation dose and image quality of X-ray volume imaging systems: cone-beam computed tomography, digital subtraction angiography and digital fluoroscopy," *European Radiology*, vol. 23, no. 6, pp. 1582–1593, 2013.
- [11] S. Miyayama, M. Yamashiro, M. Okuda et al., "Detection of corona enhancement of hypervascular hepatocellular carcinoma by C-arm dual-phase cone-beam CT during hepatic arteriography," *CardioVascular and Interventional Radiology*, vol. 34, no. 1, pp. 81–86, 2011.
- [12] J. Paul, T. J. Vogl, and E. C. Mbalisike, "Radiation dose and image quality evaluation relative to different contrast media using cone-beam CT," *Imaging in Medicine*, vol. 4, no. 5, pp. 505–513, 2012.
- [13] R. Lencioni, T. de Baere, M. Burrel et al., "Transcatheter treatment of hepatocellular carcinoma with doxorubicin-loaded dc bead (DEBDOX): technical recommendations," *CardioVascular and Interventional Radiology*, vol. 35, no. 5, pp. 980–985, 2012.
- [14] C. Koelblinger, W. Schima, V. Berger-Kulemann et al., "C-arm CT during hepatic arteriography tumour-to-liver contrast: intraindividual comparison of three different contrast media application protocols," *European Radiology*, vol. 23, no. 4, pp. 938–942, 2013.
- [15] J.-H. Sun, L.-G. Wang, H.-W. Bao et al., "Usefulness of C-arm angiographic computed tomography for detecting iodized oil retention during transcatheter arterial chemoembolization of hepatocellular carcinoma," *Journal of International Medical Research*, vol. 38, no. 4, pp. 1259–1265, 2010.
- [16] M. Lin, R. Loffroy, N. Noordhoek et al., "Evaluating tumors in transcatheter arterial chemoembolization (TACE) using dual-phase cone-beam CT," *Minimally Invasive Therapy and Allied Technologies*, vol. 20, no. 5, pp. 276–281, 2011.
- [17] R. Loffroy, M. Lin, P. Rao et al., "Comparing the detectability of hepatocellular carcinoma by C-arm dual-phase cone-beam computed tomography during hepatic arteriography with conventional contrast-enhanced magnetic resonance imaging," *CardioVascular and Interventional Radiology*, vol. 35, no. 1, pp. 97–104, 2012.
- [18] M. J. Wallace, M. D. Kuo, C. Glaiberman, C. A. Binkert, R. C. Orth, and G. Soulez, "Three-dimensional C-arm Cone-beam CT: applications in the Interventional Suite," *Journal of Vascular and Interventional Radiology*, vol. 20, no. 7, pp. S523–S537, 2009.
- [19] S. Miyayama, M. Yamashiro, M. Okuda et al., "Usefulness of cone-beam computed tomography during ultraselective transcatheter arterial chemoembolization for small hepatocellular carcinomas that cannot be demonstrated on angiography," *CardioVascular and Interventional Radiology*, vol. 32, no. 2, pp. 255–264, 2009.
- [20] H. Higashihara, K. Osuga, H. Onishi, A. Nakamoto, T. Tsuboyama, and N. Maeda, "Diagnostic accuracy of C-arm CT during selective transcatheter angiography for hepatocellular carcinoma: comparison with intravenous contrast-enhanced, biphasic, dynamic MDCT," *European Radiology*, vol. 22, no. 4, pp. 872–879, 2012.
- [21] J. Iwazawa, S. Ohue, T. Mitani et al., "Identifying feeding arteries during TACE of hepatic tumors: comparison of C-Arm CT and digital subtraction angiography," *American Journal of Roentgenology*, vol. 192, no. 4, pp. 1057–1063, 2009.

Research Article

Measurement of Liver Iron Concentration by MRI Is Reproducible

José María Alústiza,¹ José I. Emparanza,² Agustín Castiella,³ Alfonso Casado,⁴ Adolfo Garrido,⁵ Pablo Aldazábal,⁶ Manuel San Vicente,¹ Nerea Garcia,⁶ Ana Belén Asensio,⁶ Jesús Banales,⁷ Emma Salvador,¹ Aranzazu Moyua,⁸ Xabier Aroza,⁹ Miguel Zarco,⁹ Lourdes Jauregui,¹⁰ and Ohiana Vicente¹⁰

¹ Osatek, Donostia University Hospital, P. Dr. Beguiristain 109, 20014 Donostia/San Sebastián, Spain

² Clinical Epidemiology, Donostia University Hospital, P. Dr. Beguiristain 117, 20080 Donostia/San Sebastián, Spain

³ Gastroenterology, Mendaro Hospital, Mendarozabal s/n, Mendaro, Spain

⁴ Basque Country University, Avenida Tolosa 54, 20018 Donostia/San Sebastián, Spain

⁵ Biochemical Laboratory, Donostia University Hospital, P. Dr. Beguiristain 117, 20080 Donostia/San Sebastián, Spain

⁶ Experimental Department, Donostia University Hospital, P. Dr. Beguiristain 117, 20080 Donostia/San Sebastián, Spain

⁷ Liver Diseases Unit, Biodonostia Research Institute, P. Dr. Beguiristain s/n, 20014 Donostia/San Sebastián, Spain

⁸ Policlínica Gipúzkoa, Paseo Miramón 174, 20014 Donostia/San Sebastián, Spain

⁹ Radiology, Quirón Donostia Hospital, Alkolea Parkea 7, 20012 Donostia/San Sebastián, Spain

¹⁰ Onkologikoa, P. Dr. Beguiristain s/n, 20011 Donostia/San Sebastián, Spain

Correspondence should be addressed to José María Alústiza; jmalustiza@osatek.net

Received 22 May 2014; Accepted 14 September 2014

Academic Editor: Pascal Niggemann

Copyright © 2015 José María Alústiza et al. This is an open access article distributed under the Creative Commons Attribution License, which permits unrestricted use, distribution, and reproduction in any medium, provided the original work is properly cited.

Purpose. The objectives were (i) construction of a phantom to reproduce the behavior of iron overload in the liver by MRI and (ii) assessment of the variability of a previously validated method to quantify liver iron concentration between different MRI devices using the phantom and patients. **Materials and Methods.** A phantom reproducing the liver/muscle ratios of two patients with intermediate and high iron overload. Nine patients with different levels of iron overload were studied in 4 multivendor devices and 8 of them were studied twice in the machine where the model was developed. The phantom was analysed in the same equipment and 14 times in the reference machine. **Results.** FeCl₃ solutions containing 0.3, 0.5, 0.6, and 1.2 mg Fe/mL were chosen to generate the phantom. The average of the intramachine variability for patients was 10% and for the intermachines 8%. For the phantom the intramachine coefficient of variation was always below 0.1 and the average of intermachine variability was 10% for moderate and 5% for high iron overload. **Conclusion.** The phantom reproduces the behavior of patients with moderate or high iron overload. The proposed method of calculating liver iron concentration is reproducible in several different 1.5 T systems.

1. Introduction

Measurement of liver iron concentration (LIC) is the best parameter to assess iron deposits in the body. Accordingly, it is a key parameter to guide the clinical management of patients with primary or secondary hemochromatosis, characterized by iron overload. Indeed, an accurate quantitative assessment of iron levels should be obtained before initiating therapy [1, 2]. Although chemical analysis of liver biopsies

is the method employed for the analysis of LIC (i.e., gold standard), it is an invasive approach and results vary widely [3–5]. On the other hand, serum markers of iron metabolism such as ferritin and the transferrin saturation index are imprecise for the assessment of iron overload [1, 6].

Magnetic resonance imaging (MRI) is noninvasive and has been shown to provide accurate results compared to the gold standard. It is widely available across the world and several different models for calculating LIC using MRI; both

T2 relaxometry [7–9] and signal intensity ratio (SIR) methods [10–13] are being used with successful results. Nevertheless, these MRI-based approaches have not yet been standardized. Our working group has validated an SIR method to estimate LIC. The model strongly correlated with the true LIC ($r = 0.937$) [11].

To standardize an MRI technique, it is necessary to demonstrate the reproducibility of results of both intra- and inter-machine. Various recently published clinical guidelines have recommended individual calibration of each MRI machine to quantify LIC [1, 14]. Phantoms are artificial devices that simulate tissues in imaging techniques. The use of phantoms simulating liver with iron overload in MRI to assess the transferability of results and to calibrate different equipment is attractive for ethical, financial, and practical reasons [1, 12, 15–18].

Thus, our objectives were (i) construction of a phantom to reproduce the behavior of iron overload in the liver by MRI and (ii) assessment of the variability of a previously validated method to quantify LIC between different MRI devices using the phantom and patients.

2. Materials and Methods

2.1. Generation of a New Phantom for the Measurement of Liver Iron Concentration (LIC). Our goal was to construct a phantom with various different concentrations of an iron solution that gave SIRs similar to those of patients with moderate or high iron overload. The first step was to calculate the mean liver-to-muscle signal intensity ratios of a cohort of 112 patients divided into normal ($<36 \mu\text{mol Fe/g}$), moderate ($36\text{--}80 \mu\text{mol Fe/g}$), or high iron concentration ($>80 \mu\text{mol Fe/g}$) [11].

The second step was to test different iron solutions in distilled water using MRI to identify close matches to these average liver-to-muscle ratios of patients with moderate and high iron overload. One tube with only distilled water simulated the non-iron-containing muscle of the patients. Then, ratios were calculated between the signal intensities from each iron-containing tube and that from the distilled water tube.

These tests were conducted in a 1.5 Tesla MRI scan (Gyrosan ACS-NT; Philips, Best, the Netherlands), which was named the “reference machine” because it was the equipment in which our model for LIC quantification was developed. A bottle with 2 litres of diluted CuSO_4 was placed in the center to give more signal intensity to the whole of the system. The tubes were surrounded by water to avoid susceptibility artifacts in the tube walls. We investigated several different iron solutions such as Lumirem R, iron 3-chloride (FeCl_3), and ammonium 2-sulphate ($(\text{NH}_4)_2\text{Fe}(\text{SO}_4)_2$). First, we assessed Lumirem (Guerbet, France), a ferrous MRI contrast agent with superparamagnetic iron oxides particles (Ferumoxides) previously reported by Ernst et al. [16]. This type of solution was ruled out for lack of stability due to iron precipitation at the bottom of the tubes. Subsequently, we tested FeCl_3 and $(\text{NH}_4)_2\text{Fe}(\text{SO}_4)_2$ solutions [17], which have shown relaxation rates in MRI and that are linearly correlated with the wet-weight iron concentration in human liver. The

solutions were acidified with 0.1 M nitric acid to avoid Fe oxidation and thus prevent iron precipitation. Of these, FeCl_3 was selected because the decrease in the MRI signal showed a better linear correlation with the increase in iron concentration.

12 different solutions of FeCl_3 with concentrations ranging from 0.05 to 4 mg Fe/mL were prepared in 5 mL tubes. A curve of SI ratios against Fe concentration was created using 12 tubes. The concentrations with SI ratios best mimicking the average liver-to-muscle ratios for intermediate and high iron overload were selected.

2.2. Analysis of the Variability of MRI Measurements in the Same Machine (Repeatability) and in Different Machines (Reproducibility) Using Patients. The repeatability of the measurements was evaluated with eight subjects with different LICs (a volunteer with normal iron metabolism, six patients with primary hemochromatosis, and one with post-transfusional iron overload) being analyzed twice in the reference machine. The interval between two measurements was less than 1 week.

To assess the reproducibility, 9 subjects with different LICs were studied in the reference machine and in four additional different units placed in several hospitals of the same city (i.e., General Electric Signa LX (Waukesha, WI) named “A,” General Electric Signa Excite II (Waukesha, WI) named “B,” Siemens Symphony (Erlangen, Germany) named “C,” and a Philips Intera (Best, the Netherlands) named “D”). These subjects were the aforementioned 8 and an additional one with untreated hereditary hemochromatosis. Each patient was studied once in each machine. The interval between the first and the last MRI scan for each patient was always less than 1 week and no patients underwent therapeutic phlebotomy or received iron chelation therapy during this time.

2.3. Analysis of the Repeatability and the Reproducibility of MRI Measurements Using the Phantom. The repeatability of the phantom was tested once a week for 14 weeks in the reference machine.

To analyze the reproducibility, the same phantom was studied on the same five 1.5 T systems (previously named as “reference machine,” “A,” “B,” “C,” and “D” machines).

2.4. MRI Technique. We scanned the phantom and the human subjects with the two gradient echo (GRE) sequences used in our previously validated method [13] (IW sequence: TR/TE/flip angle = 120 ms/4 ms/20° and T2 sequence: 120 ms/14 ms/20°) with no surface coils. For subjects, the data acquisition was performed in a breath-hold, with 1 NSA, 10 mm thickness, and 10 and 5 slices for IW and T2 sequences, respectively. For the phantom, 5 perpendicular (axial) 7 mm slices were acquired for each tube (gap = 1 mm, FOV = 300 mm, 2 NSA).

2.5. Data Analysis. In scans of the subjects, signal intensity was measured with regions of interest (ROI) $> 1 \text{ cm}^2$: 3 in the right lobe of the liver, avoiding vascular structures, and 2 in the paraspinous muscles. For each sequence, the ROIs were

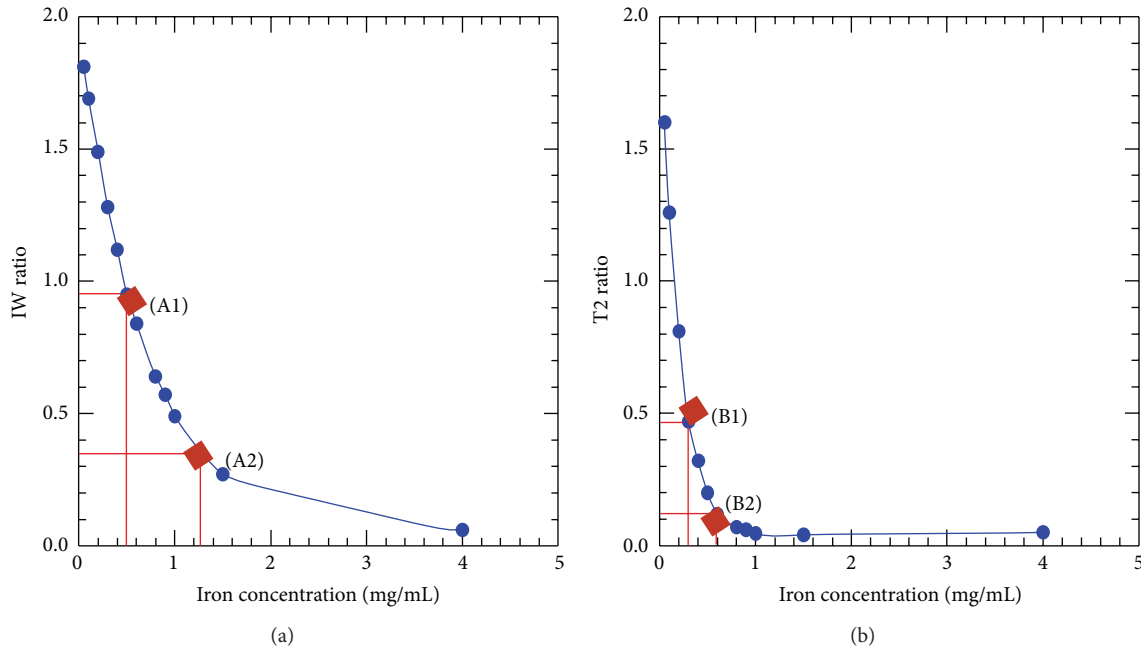


FIGURE 1: Test of 12 different FeCl_3 solutions, ranging from 0.05 to 4 mg Fe/mL, to identify signal intensity ratios (SIR) close matches to average liver-to-muscle ratios of patients with moderate or high iron overload. Relationship between the iron concentration and the corresponding SIR in the two sequences of the method. (a) IW sequence (TR/TE/Flip 120/4/20°); (b) T2 sequence (TR/TE/Flip 120/14/20°). SIR was calculated between the signal intensities from each FeCl_3 solution and that from distilled water, without any iron. In both sequences SIR decreases with increasing iron concentration and it falls more steeply in T2 sequence, as occurs in clinical measurements. It is necessary to have one solution with specific concentration of FeCl_3 for each sequence and for each level of iron overload. For intermediate iron overload, the solution containing 0.5 mg Fe/mL (A1) gave the required IW signal intensity ratio (0.95) and the one with 0.3 mg Fe/mL (B1) gave the required T2 signal intensity ratio (0.47). For the high iron overload, 1.2 mg Fe/mL (A2) and 0.6 mg Fe/mL (B2) were necessary to obtain the desired IW and T2 ratios (0.35 and 0.6, resp.).

always measured in the same slice. Then, for each subject, the liver-to-muscle ratio was obtained with the mean signal intensities of the liver and muscle tissue, and LIC was calculated using the aforementioned equation [11].

For the phantom, the top and bottom axial sections were excluded from the analysis to avoid partial volume effects. In the three central sections, signal intensity was measured in all tubes and using both sequences, with ROIs greater than 0.5 cm^2 and placed away from the walls. The signal intensity average was obtained for each tube and the signal intensity ratios of each solution to the iron-free tube were calculated. The equation was then used to obtain estimated LIC using the phantom's intermediate and high iron overload data. As described before, we used the ratios of the 0.3 mg Fe/gr and 0.5 mg Fe/gr tubes to represent moderate iron overload with the IW and T2-weighted sequences, respectively, while the 0.6 and 1.2 mg Fe/gr tubes were used for high iron overload.

2.6. Statistical Analysis. Appropriate statistics were calculated for each type of data. Coefficients of variation and ranges (minimum and maximum) were calculated for continuous data.

Comparison of the signal intensity ratios for each tube over the 14 days was performed using one-way repeated measures ANOVA.

Agreement between the estimated LIC for both the tubes and the subjects in the four machines tested and the reference machine was assessed using the Bland-Altman method. Diagnostic concordance (no overload, moderate and high iron overload) between the four machines tested and the reference machine was assessed using Cohen's unweighted kappa.

Calibration of each machine against the reference was studied graphically using calibration curves.

The statistical analysis was carried out using the SYSTAT v13 statistical package.

3. Results

3.1. Generation of a New Phantom with a Range between $62 \mu\text{mol Fe/g}$ and $180 \mu\text{mol Fe/g}$. Patients with intermediate iron overload in liver biopsies have had a liver-to-muscle signal intensity ratio average of 0.95 in the IW sequence and of 0.47 in the T2, while the corresponding liver-to-muscle ratios averages for patients with high iron overload were 0.35 and 0.12, respectively.

Figure 1 illustrates the relationship between the signal intensity ratio in 12 tubes with different FeCl_3 concentrations ranging from 0.05 to 4 mg Fe/mL for the two sequences. In both cases, signal intensity inversely correlates with the iron concentration, but the signal falls more steeply in the T2

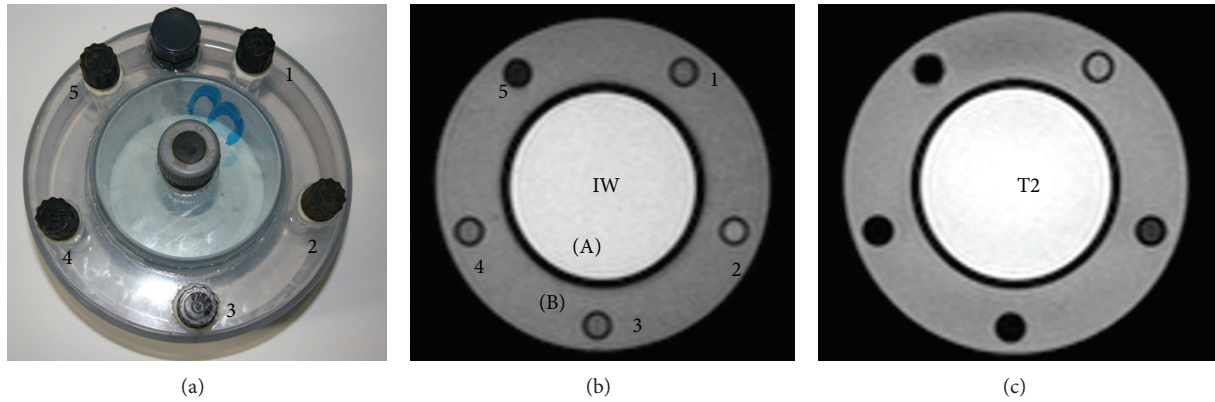


FIGURE 2: Phantom with different iron (III) chloride solutions and MRI in IW (TR/TE/Flip angle = 120/4/20°) and T2 (120/14/20°) sequences. (a) Photograph of the first prototype. (b) MRI in IW sequence. (c) MRI in T2 sequence. 1. Fe-free solution. 2. Solution of 0.3 mg Fe/mL. 3. Solution of 0.5 mg Fe/mL. 4. Solution of 0.6 mg Fe/mL. 5. Solution of 1.2 mg Fe/mL. (A) CuSO₄ solution. (B) Water.

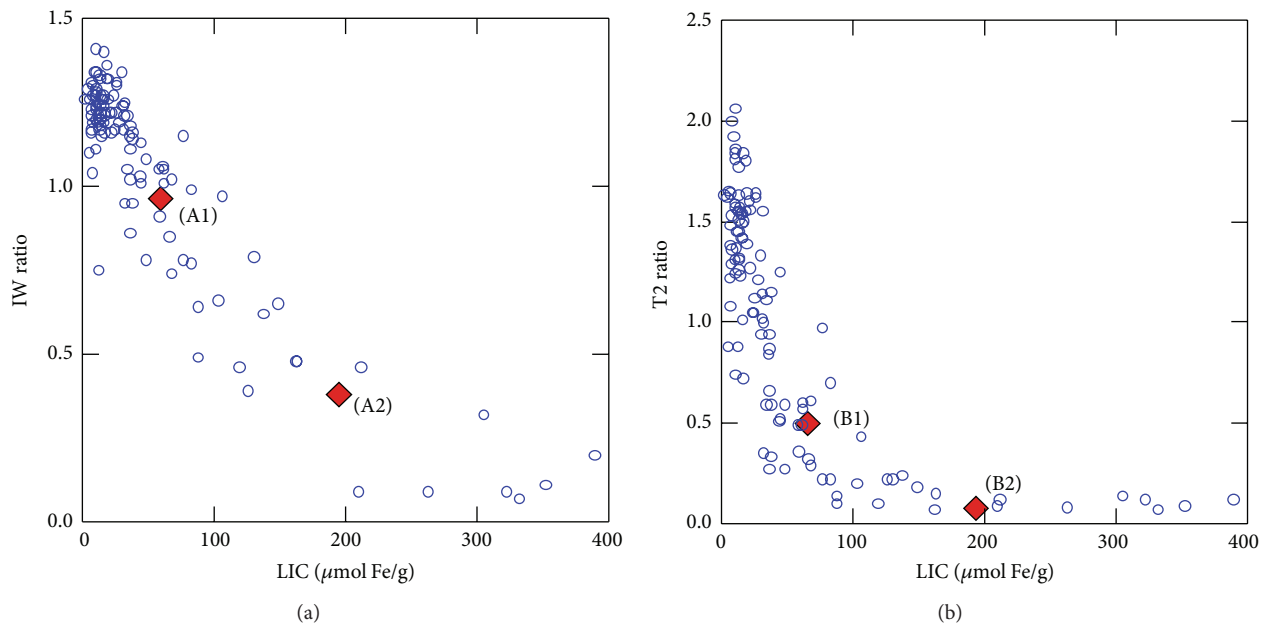


FIGURE 3: Relationship between liver-to-muscle signal intensity ratio (SIR) and liver iron concentration (LIC) for 112 patients. SIRs of the phantom for moderate (A1-B1) and for high iron overload (A2-B2) in the two sequences of the method have also been included in the graph. (a) IW sequence (TR/TE/Flip 120/4/20°); (b) T2 sequence (TR/TE/Flip 120/14/20°). The values A1 and B1 correspond to the same LIC value in each of the two sequences: 62 $\mu\text{mol Fe/g}$ and they maintain the same correlation SIR/LIC as patients in the two sequences. The same applies to A2 and B2 values for high iron overload, with a value of LIC of $\mu\text{mol Fe/g}$ in both sequences.

sequence, as occurs in clinical measurements [11]. Two different tubes were necessary to obtain the SI ratios of each level of iron overload. For intermediate iron overload, the solution containing 0.5 mg Fe/mL (A1) gave the required IW signal intensity ratio (0.95) and 0.3 mg Fe/mL (B1) the required T2 signal intensity ratio (0.47). For high iron overload, 1.2 mg Fe/mL (A2) and 0.6 mg Fe/mL (B2) were necessary to obtain the desired IW and T2 ratios (0.35 and 0.6 mg Fe/mL, resp.). Based on this data, the phantom was constructed using one tube without iron and each of the four different FeCl₃ solutions (Figure 2).

A subject with IW and T2 ratios corresponding to intermediate iron overload would be predicted to have an

LIC of 62 $\mu\text{mol Fe/g}$ by our equation. On the other hand, a person with high iron overload ratios would be estimated to have an LIC of 180 $\mu\text{mol Fe/g}$. These values are very similar to those obtained in our groups of real patients with moderate (51 $\mu\text{mol Fe/g}$) and high (187 $\mu\text{mol Fe/g}$) iron overload (Figure 3).

3.2. The Patients Show Good Reproducibility of Measurements Intra- and Intermachines. Of the 9 patients studied, 3 have a normal value of LIC (<36 $\mu\text{mol Fe/g}$), 2 have a moderate iron overload (37–80 $\mu\text{mol Fe/g}$), and 4 have high iron overload (>80 $\mu\text{mol Fe/g}$).

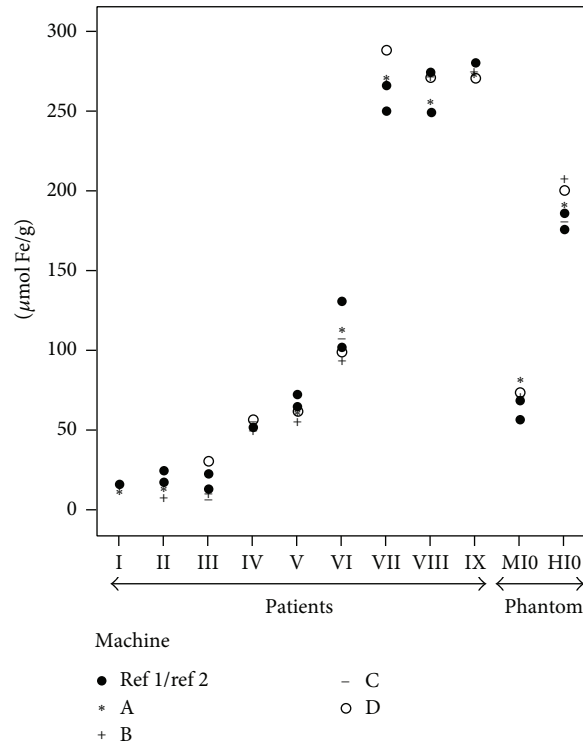


FIGURE 4: Variability of estimates by MRI of liver iron concentration (LIC) in 9 patients and in the phantom. I–IX: real patients with different values of LIC. MIO: moderate iron overload in the phantom. HIO: high iron overload in the phantom. Black rounds: measurements on the reference machine. “*”: measurements on machine A. “+”: measurements on machine B. “-”: measurements on machine C. “o”: measurements on machine “D”. High reproducibility can be observed, intra- and intermachines, for every patient. Phantom behavior is very similar to the patients.

Between the 8 patients studied twice in the reference machine, the average of intramachine variability was 10% (2-22) (Figure 4). There were no clinically relevant differences between the two measurements.

The variability of all machines analyzed with respect to the reference machine was low, ranging from 0 to 28%, with a mean difference of 8% in patients with iron overload (Figure 4).

The Bland-Altman plot (Figure 5) displays an agreement within the limits of clinical usefulness, with the mean of differences always being less than 20%. Specifically, the differences ranged from -3.4 to 7.4 μmol Fe/g, which can be considered negligible values.

All the subjects without iron overload (<36 μmol Fe/g) were classified with the other four machines (A–D). Importantly, none of the patients with moderate (37–80 μmol Fe/g) or high (>80 μmol Fe/g) iron overload were classified as not having iron overload by any of the four machines tested. In addition, the patients were all classified in the correct iron overload group by the tested machines. Cohen’s kappa was 1, reflecting the almost perfect agreement in diagnosing the severity of iron overload.

3.3. *The Phantom Has Similar Behavior to Patients Intra- and Intermachines.* The variability in the 14 measurements of the

phantom made in the reference machine was also very low, with a coefficient of variation between 0.02 and 0.09.

All the estimated values for moderate iron overload were between 56 and 68 μmol Fe/g and for high iron overload between 176.1 and 186.2 μmol Fe/g. (Figure 3).

The variability of the measurements in the phantom of all the analyzed machines with respect to the reference machine was also very low. It was 10% (1-19) for moderate iron overload and 5% (1-10) to high overload (Figure 4).

4. Discussion

In this study we have generated a new phantom ranking between 62 μmol Fe/g and 180 μmol Fe/g. We show that patients have good reproducibility of measurements and that the phantom has similar intra- and intermachines.

We designed an MRI phantom which accurately reproduces the LIC of two typical groups of patients, namely, those with moderate and high iron overload, which is stable over time. Other studies have used phantoms based on various different components including agarose, ferritin, manganese, and Lumirem [15–18]. Clearly it is not feasible to construct an artificial phantom with only one component which exactly reproduces the behavior of the liver with various different iron concentrations in MRI, as the liver is a highly complex

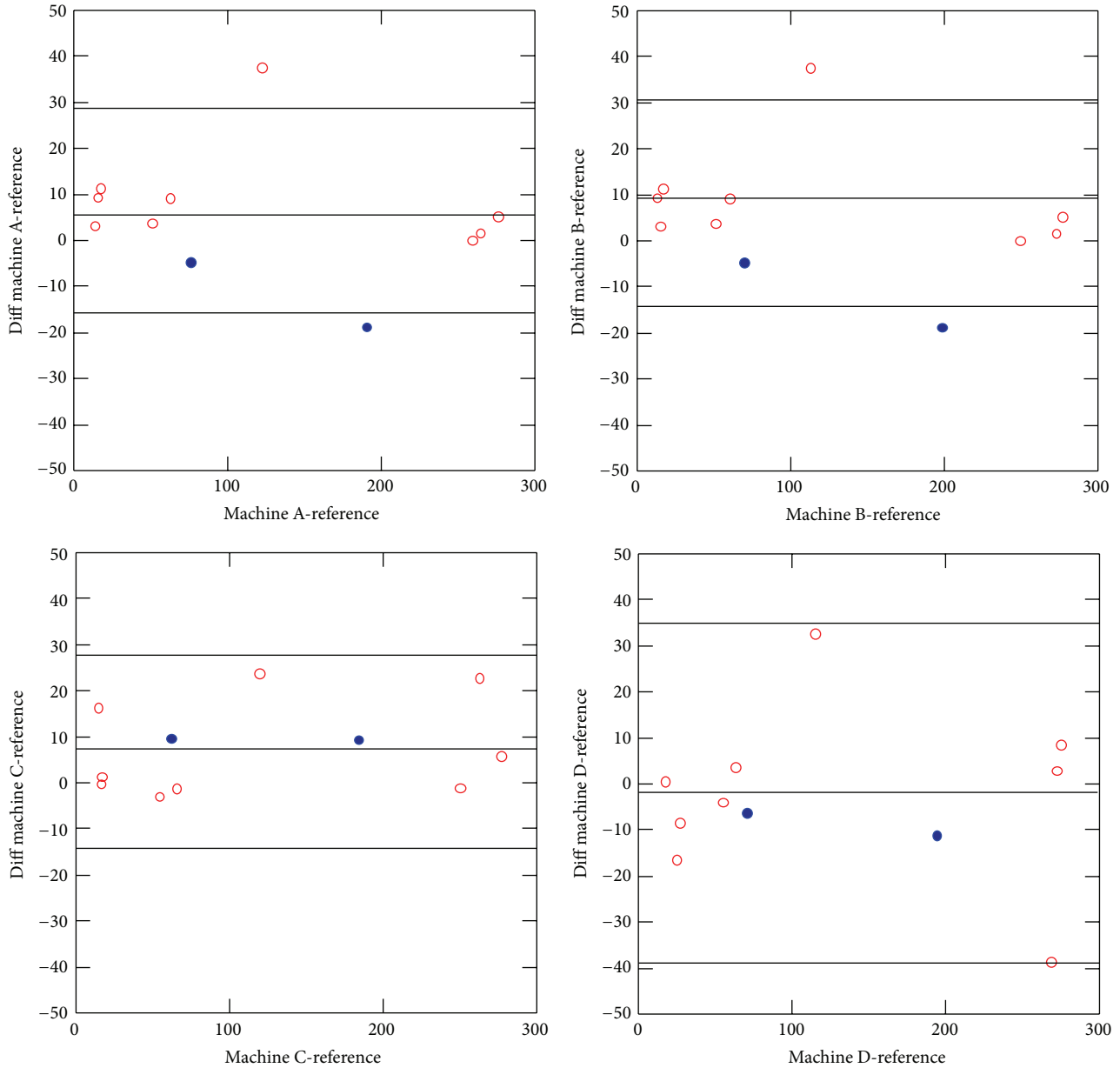


FIGURE 5: Bland-Altman plots for each machine (machines A, B, C, and D) and the reference machine. The Bland-Altman plot shows an agreement within the limits of clinical usefulness, with the mean of differences (bias) always being less than 20%. Specifically, the bias ranged from -3.4 to $7.4 \mu\text{mol Fe/g}$, which can be considered negligible values.

biological structure. The aqueous solution of ferric chloride and water without iron that we have used in this study has different T1 and T2 values compared to liver tissue with iron overload or to the muscle.

On the other hand, in constructing a phantom, the most important issue is to employ a properly studied and validated gold standard. We have based our design on the data of a cohort of 112 patients, analyzed using the same MRI machine and who also have an LIC quantified using chemical measurements in liver biopsies, provided that, using tubes with different FeCl_3 solutions, we were able to reproduce

accurately the behavior seen in patients with different levels of iron overload. In this regard, as stated in Figure 1, the change in the signal from the tubes with the increase in iron concentration was very similar to that from the patients with different values of LIC in the two gradient echo sequences used in the model. In addition, in both sequences, the theoretical LICs of patients as mimicked by the phantom were perfectly correlated with the gold standard (Figure 4).

To summarize, there cannot be a single solution of FeCl_3 that gives the same SIR as the liver in different sequences. Therefore it is necessary to have a specific tube for each

sequence and for each level of iron overload. Hence, the phantom consists of four tubes with different FeCl_3 concentrations and one tube without iron.

This study shows that the SIR model for the estimation of LIC using MRI designed by our research group [11] is reproducible in 1.5 T machines of various different companies. In particular, none of the patients without iron overload was diagnosed as having iron overload by results from any of the machines. Furthermore, the patients with iron overload were also correctly classified in all cases.

SIR methods to quantify LIC by MRI are more available than T2 relaxometry methods and they are widely used in clinical practice. However, very few have analyzed the reproducibility of the measurements in different machines. So far there are no published studies that have compared the measures of so many patients and machines as this study [15]. The variability we found is very similar intra- and inter-machines (8–10%) and it is better than that observed and implicitly accepted in clinical practice in the measurement of LIC by biopsy, in which results vary by 19% in healthy liver and 40% in cirrhotic liver tissue [3–5].

The phantom has shown similar behavior to the patients with moderate and high iron overload. Indeed, an important future use of the phantom, freely available on request, will be to undertake calibrations in more centres. Such data, in a multicentre study, would ensure consistency between the calculated values of LIC from different machines. This will be a necessary step towards the standardization of the technique that will optimize their use in the differential diagnosis of disorders of iron metabolism.

This study has some limitations. It is based on only nine subjects and four machines. However, it is difficult to identify patients and healthy individuals willing to undergo repeated measurements in different hospitals in a short period of time. Iron concentrations were not confirmed by biopsy. On the other hand, we have previously demonstrated that the method provides accurate estimates of LIC; for this reason, biopsies are no longer taken to measure liver iron concentration in our hospital. All results of this study are only valid for the used quantification method, previously designed and validated by our team.

In conclusion, this study demonstrates that the proposed signal-to-intensity ratio method to calculate LIC by MRI is reproducible in several different 1.5 T systems (from different companies) and also that the behavior of the constructed phantom reproduces the behavior of patients with moderate or high iron overload.

Conflict of Interests

The authors declare that there is no conflict of interests regarding the publication of this paper.

Authors' Contribution

The study design was done by José María Alústiza, José I. Emparanza, Agustín Castiella, Pablo Aldazábal, Emma Salvador, Aranzazu Moyua, Xabier Arozena, Miguel Zarco,

Lourdes Jauregui, and Ohiana Vicente. The literature research was done by José María Alústiza, Alfonso Casado, and Nerea Garcia. Data acquisition (Osatek-San Sebastian) and MSV Data acquisition (Basque Country) were done by Emma Salvador, Aranzazu Moyua, Xabier Arozena, Miguel Zarco, Lourdes Jauregui, and Ohiana Vicente. Data analysis interpretation was done by José María Alústiza, Pablo Aldazábal, Nerea Garcia, Ana Belén Asensio, Agustín Castiella, and Jesús Banales. Statistical analysis was performed by José I. Emparanza, Nerea Garcia, and Ana Belén Asensio. Paper preparation was done by José María Alústiza, José I. Emparanza, Agustín Castiella, and Jesús Banales. Phantom design and construction were done by José María Alústiza, José I. Emparanza, Pablo Aldazábal, Alfonso Casado, and Adolfo Garrido.

Acknowledgment

Public funding: this work was partially sponsored by the General State Administration of Spain (Health Research Found, Carlos III Health Institute, Madrid).

References

- [1] G. M. Brittenham and D. G. Badman, "Noninvasive measurement of iron: report of an NIDDK workshop," *Blood*, vol. 101, no. 1, pp. 15–19, 2003.
- [2] A. Pietrangelo, Y. Deugnier, J. Dooley, A. Erhardt, H. Zoller, and R. Safadi, "EASL clinical practice guidelines for HFE hemochromatosis. European Association for the Study of the Liver," *Journal of Hepatology*, vol. 53, no. 1, pp. 3–22, 2010.
- [3] J.-P. Villeneuve, M. Bilodeau, R. Lepage, J. Côté, and M. Lefebvre, "Variability in hepatic iron concentration measurement from needle-biopsy specimens," *Journal of Hepatology*, vol. 25, no. 2, pp. 172–177, 1996.
- [4] G. Crisponi, R. Ambu, F. Cristiani et al., "Does iron concentration in a liver needle biopsy accurately reflect hepatic iron burden in β -thalassemia?" *Clinical Chemistry*, vol. 46, no. 8, pp. 1185–1188, 2000.
- [5] M. J. Emond, M. P. Bronner, T. H. Carlson, M. Lin, R. F. Labbe, and K. V. Kowdley, "Quantitative study of the variability of hepatic iron concentrations," *Clinical Chemistry*, vol. 45, no. 3, pp. 340–346, 1999.
- [6] M. D. Beaton and P. C. Adams, "Treatment of hyperferritinemia," *Annals of Hepatology*, vol. 11, no. 3, pp. 294–300, 2012.
- [7] T. G. St. Pierre, P. R. Clark, W. Chua-Anusorn et al., "Noninvasive measurement and imaging of liver iron concentrations using proton magnetic resonance," *Blood*, vol. 105, no. 2, pp. 855–861, 2005.
- [8] J. C. Wood, C. Enriquez, N. Ghugre et al., "MRI R2 and R2* mapping accurately estimates hepatic iron concentration in transfusion-dependent thalassemia and sickle cell disease patients," *Blood*, vol. 106, no. 4, pp. 1460–1465, 2005.
- [9] J. S. Hankins, M. B. McCarville, R. B. Loeffler et al., "R2* magnetic resonance imaging of the liver in patients with iron overload," *Blood*, vol. 113, no. 20, pp. 4853–4855, 2009.
- [10] Y. Gandon, D. Olivie, D. Guyader et al., "Non-invasive assessment of hepatic iron stores by MRI," *The Lancet*, vol. 363, no. 9406, pp. 357–362, 2004.

- [11] J. M. Alústiza, J. Artetxe, A. Castiella et al., “MR quantification of hepatic iron concentration,” *Radiology*, vol. 230, no. 2, pp. 479–484, 2004.
- [12] H. L. Bonkovsky, R. B. Rubin, E. E. Cable, A. Davidoff, T. H. P. Rijcken, and D. D. Stark, “Hepatic iron concentration: noninvasive estimation by means of MR imaging techniques,” *Radiology*, vol. 212, no. 1, pp. 227–234, 1999.
- [13] C. Rose, P. Vandevenne, E. Bourgeois, N. Cambier, and O. Ernst, “Liver iron content assessment by routine and simple magnetic resonance imaging procedure in highly transfused patients,” *European Journal of Haematology*, vol. 77, no. 2, pp. 145–149, 2006.
- [14] E. Angelucci, G. Barosi, C. Camaschella et al., “Italian Society of Hematology practice guidelines for the management of iron overload in thalassemia major and related disorders,” *Haematologica*, vol. 93, no. 5, pp. 741–752, 2008.
- [15] P. A. Sukerkar, U. G. Rezvi, K. W. MacRenaris, P. C. Patel, J. C. Wood, and T. J. Meade, “Polystyrene microsphere-ferritin conjugates: a robust phantom for correlation of relaxivity and size distribution,” *Magnetic Resonance in Medicine*, vol. 65, no. 2, pp. 522–530, 2011.
- [16] O. Ernst, C. Rose, and C. L’Hermine, “Hepatic iron overload: quantification with MR imaging at 1.5T,” *American Journal of Roentgenology*, vol. 172, no. 4, pp. 1141–1142, 1999.
- [17] R. Engelhardt, “Liver iron quantification: studies in aqueous iron solutions, iron overloaded rats, and patients with hereditary hemochromatosis,” *Magnetic Resonance Imaging*, vol. 12, no. 7, pp. 999–1007, 1994.
- [18] J. M. Virtanen, M. E. Komu, and R. K. Parkkola, “Quantitative liver iron measurement by magnetic resonance imaging: in vitro and in vivo assessment of the liver to muscle signal intensity and the R2* methods,” *Magnetic Resonance Imaging*, vol. 26, no. 8, pp. 1175–1182, 2008.

Review Article

Diffusion-Weighted MRI for the Assessment of Liver Fibrosis: Principles and Applications

Stefano Palmucci, Giuseppina Cappello, Giancarlo Attinà, Giovanni Fuccio Sanzà, Pietro Valerio Foti, Giovanni Carlo Ettore, and Pietro Milone

Radiodiagnostic and Radiotherapy Unit, University Hospital "Policlinico-Vittorio Emanuele", 95123 Catania, Italy

Correspondence should be addressed to Stefano Palmucci; spalmucci@sirm.org

Received 11 July 2014; Revised 14 December 2014; Accepted 1 January 2015

Academic Editor: Edward Lee

Copyright © 2015 Stefano Palmucci et al. This is an open access article distributed under the Creative Commons Attribution License, which permits unrestricted use, distribution, and reproduction in any medium, provided the original work is properly cited.

The importance of an early identification of hepatic fibrosis has been emphasized, in order to start therapy and obtain fibrosis regression. Biopsy is the gold-standard method for the assessment of liver fibrosis in chronic liver diseases, but it is limited by complications, interobserver variability, and sampling errors. Several noninvasive methods have been recently introduced into clinical routine, in order to detect liver fibrosis early. One of the most diffuse approaches is represented by diffusion-weighted liver MRI. In this review, the main technical principles are briefly reported in order to explain the rationale for clinical applications. In addition, roles of apparent diffusion coefficient, intravoxel incoherent motion, and relative apparent diffusion coefficient are also reported, showing their advantages and limits.

1. Introduction

Several chronic hepatic diseases may develop cirrhosis in the liver parenchyma. Hepatic steatosis, iron overload, autoimmune hepatitis, chronic viral hepatitis, sclerosing biliary cholangitis, alcohol, and drugs represent the most frequent causes of liver cirrhosis. All these chronic diseases, after an early phase of inflammation, lead to parenchymal fibrosis, which plays an important role in the development of cirrhosis [1].

Fibrogenesis has been defined as a “wound-healing response that engages a range of cell types and mediators to encapsulate injury” [2]. It consists of a progressive deposition of extracellular matrix proteins, which reduces widening of interstitial spaces and creates distortion of normal hepatic architecture [3]. It has been widely accepted that early recognition of fibrosis is crucial for preventing development of chronic parenchymal disease. New experimental treatments have emphasized the importance of an early identification of fibrogenesis, in order to start therapy and obtain fibrosis regression [4–6].

Biopsy is the gold-standard modality for assessing the degree of fibrosis and for evaluating necrosis or inflammation. However, it is affected by many complications, including

bleeding, pneumothorax, and procedure-related death, and could be limited by interobserver variability and sampling errors [3, 7–10]. In addition, liver biopsy is not used in the management of disease, especially when we have to repeat the examination after a short interval of time, as reported by Kim et al. [3].

For this reason, in the past years many noninvasive tests and diagnostic examinations have been introduced into clinical routine in order to detect liver fibrosis early.

The collection of serum markers of fibrosis, namely, fibrotest/fibrosure, has been widely used in the assessment of hepatic fibrosis [3, 11–14]. Serum levels of aptoglobulin, α_2 -macroglobulin, γ -globulin, γ -glutamyl transferase, apolipoprotein, and total bilirubin indicate a score of hepatic fibrosis with relatively good accuracy [12–14].

Other noninvasive modalities include Transient Elastography (TE), Acoustic Radiation Force impulse Imaging (ARFI), Real-Time Elastography (RTE), and Magnetic Resonance Elastography (MRE). Particularly, measurement using TE has been routinely introduced into the assessment of liver fibrosis [15, 16]. This technique is based on the measurement of liver hardness and stiffness. More specifically, a FibroScan test using TE measures the velocity of a vibration wave produced by an ultrasonography-like probe [17]. The time

required to reach a certain depth of parenchyma from skin is conditioned by liver stiffness and hardness, which are related to the degree of fibrosis developed. The fibrotic burden is large if the waves rapidly propagate [17–19].

Also, MR with diffusion-weighted sequences has been used for detection and quantification of hepatic fibrosis. Its introduction into liver MRI has fuelled high expectations with several encouraging studies [7]. In the assessment of diffuse but also of focal parenchymal disease, diffusion-weighted imaging (DWI) is currently one of the most important added values of liver MRI. In particular this review focuses on the main technical principles and clinical applications of diffusion-weighted MRI in the assessment of liver fibrosis.

2. Assessment of Hepatic Fibrosis Using Diffusion-Weighted MRI

2.1. DWI: Technical Principles. Diffusion-weighted imaging has been routinely introduced into liver MRI protocol [20]. Several studies, in the past fifteen years, have investigated its contribution in the assessment of diffuse and focal hepatic disease [7, 20, 21]. Important researches have evaluated DWI capability in the quantification of hepatic fibrosis in chronic liver disease [7, 22, 23], in characterization and detection of focal liver lesions [24–26], and in monitoring response to treatment in oncological patients [27, 28].

Diffusion imaging is based on the sensitivity of MRI to motion [29]. It consists of spin-echo sequence where the main 180° focalization pulse is preceded and followed by two additional gradient pulses [30–33]. Proton response to these gradient pulses is strongly related to their movements, which generally follow a Brownian motion. Applying the first gradient field before 180° refocusing RF pulse, protons develop a phase shift. For static molecules, the second gradient pulse will be able to compensate the phase shift produced by the first one; no additional shift is generated from movement. The refocusing introduced by the second gradient will be visible on MR diffusion images as high signal.

In case of molecules that move in the direction of the gradients, the phase shift created by the first gradient will not be rephased by the second gradient. In addition, if a net phase shift is observable for molecules with a certain degree of motion, the different phase shifts in case of Brownian motions—as reported in literature—“interfere with each other, resulting in imperfect refocusing of echo” [31]. Thus, the second gradient field, applied after 180° focalization pulse, is unable to obtain a full compensation of phase acquired after first gradient, for the fact that molecules proceed with different directions in a Brownian modality.

2.2. Apparent Diffusion Coefficient. Diffusion-weighted pulse sequences need relatively long echo times (between 60 and 120 ms) for the application of the two diffusion gradients [34]. Thus, DW images are also intrinsically T2-weighted. Consequently, areas of high intensity on T2-weighted images may lead to high signal on DW images, even if the diffusion of water molecules in tissue may not be reduced. This imaging

feature is called “T2 shine-through effect” [35]. To remove the T2-effect, it is recommended to acquire images with at least two b -values; the first one with a b -value of 0 and the second one with a higher b -value [36]. The greater the strength and timing of the gradients (collectively expressed by the b -value) are, the greater the sensitivity of sequence to microscopic diffusion is [36].

Apparent diffusion coefficient (ADC) is the main quantitative parameter used for quantifying proton diffusion motions in tissues and it is estimated using images acquired with two different b -values.

ADC is calculated with the following formula:

$$\text{ADC} = \frac{\ln(S_0/S_1)}{b}, \quad (1)$$

where S_0 is the signal intensity with $b = 0$, S_1 is the signal intensity after the application of a given b gradient, and b is the strength of the applied gradient [21].

It is important to say that the smaller the maximum b -value used, the greater the ADC values: that is caused by the contribution of intravoxel incoherent motion (IVIM) effects (e.g., capillary perfusion and flow phenomena), which are more than diffusion. For higher b -values ($\geq 300 \text{ s/mm}^2$), “perfusion effects are cancelled out,” whereas ADCs obtained using very low b -values “could be increased by capillary perfusion” [24]. Therefore, maximum b -values, also greater than 800 sec/mm^2 in Yamada’s opinion, are necessary in order to reduce intravoxel incoherent motion effects [37].

In any case, it is important to remember that at higher b -values, images become noisier, so a compromise is often required; higher b -values give ADC information; lower b -values improve lesions detection. For these reasons, multiple b -values are usually performed [38].

An ADC map, which is a sort of subtraction image between sequences acquired with given b -value and sequences acquired with b -value of 0, can be used to exclude “T2 shine through effect.” Lesions showing hyperintense signal on ADC maps generally have increased diffusivity and high ADC values, whereas lesions with low signal on ADC maps have restricted diffusivity and low ADC values. The ADC can also be calculated using a multi- b analysis by fitting an exponential function to the measured signal intensities on multi- b acquired images [34].

2.3. DWI: Rationale for Use. In diffusion images, tissues containing molecules with high degree of movement and diffusion will be represented as dark areas of low signal, whereas tissues in which protons are unable to move around freely will have high signals [29].

Molecular diffusivity is conditioned by widening of interstitial spaces. Some clinical conditions could modify interstitial spaces, and water molecules could become unable to process randomly. Main diseases characterized by interstitial spaces narrower than normal are ischemic injury, tumour, abscess, haemorrhage/hematoma, and parenchymal fibrosis [39].

More specifically, ischemia reduces activity of cellular transporters along the cellular wall, causing increase in

size of cells and contraction of interstitial spaces. Among neurological applications, DWI was the first to be introduced in the early assessment of cerebral stroke [40].

Also, a tumour could decrease Brownian motions, because of anarchic cell proliferation and hypercellularity. Anarchic proliferation reduces interstitial space and leads progressively to compression of small vessels, resulting in ischemic changes in the tissue. In view of these considerations, on diffusion-weighted images metastatic lesions reproduce different signal intensity on the basis of their cellularity [41]. Well-differentiated adenocarcinomas appear as hypointense lesions, whereas small and large cells neuroendocrine tumours show hyperintense signal [41].

Finally, several authors have postulated that fibrosis could also decrease the width of interstitial spaces. Fibrotic tissues generally develop as a consequence of chronic inflammation, with narrowing of interstitial spaces, and consequently proton motion reduction [42–45].

2.4. Diffusion-Weighted Sequences. DW imaging of the liver is influenced by motion, caused by breathing and cardiac pulsations, and lower T2 signal (liver is a tissue with intrinsically lower T2 signal, such as muscle) [46]. Thus, a different technique has been proposed for improving diffusion image quality and precision of ADC measurement.

Liver MRI protocol for assessing hepatic fibrosis is usually based on Single-Shot Echo Planar Imaging (SSEPI), which may be acquired in breath-hold modality, in respiratory-triggered or echo navigator modality, or also in free-breathing technique. Several studies have compared image quality and ADC reproducibility and repeatability among the different acquisition techniques mentioned.

Breath-hold SSEPI sequences are faster than triggered or free-breathing sequences and generally permit evaluation of the whole liver in one or two 20–30-second acquisitions. The short acquisition time reduces artifacts due to macroscopic physiological motions (respiratory, peristalsis). On the other hand, the higher acquisition speed causes low spatial resolution and signal-to-noise ratio (SNR), especially when images are acquired using higher b -values. They could also exhibit higher sensitivity to magnetic susceptibility artifacts caused by tissue/air interface [20, 47].

Respiratory-triggered DWI acquisitions require respiratory synchronization with patients' breath, generally obtained by placing a "respiratory" belt around their abdomen, and imaging data are usually acquired during end expiration phase. Respiratory-triggered sequences allow for high-quality images in patients with low-compliance for the exam, or in patients unable to maintain a breath-hold during the sequence acquisition [48, 49], at the expense of increased acquisition time [47]. For respiratory-triggered imaging, prospective acquisition correction technique (PACE) with a navigator sequence has been introduced, in order to better synchronize acquisition with patients' breath. This technique interleaves the imaging sequence with a navigator sequence [50]; the navigator is placed across the diaphragm [51]. It removes patients motion using a "real-time navigator pulse to trigger acquisition" at a specific point of respiratory cycle [50].

Free-breathing echo planar sequences could require a variable time for their acquisition; generally, many articles report about 3–6 minutes for whole liver evaluation [47]. These sequences may be performed when patients are not able to maintain breath-hold during the examination, due to the coexistence of respiratory or cardiac problems. Some patients with nonalcoholic steatohepatitis (NASH) could also be affected by obesity, with reduced pulmonary capacity. Long-time acquisition of free-breathing sequences is generally needed to improve the signal-to-noise ratio. Free-breathing diffusion images are slightly affected by cyclical respiration, because as reported by Kwee et al. "it is considered a coherent motion, where the acquired phase shift due to respiratory motion is equal in each phase-encoding step and then it does not result in additional signal attenuation" [52]. However, image blurring is not associated with breath-hold or respiratory triggered sequences. In view of these considerations, high signal averages or numbers of excitations are generally used for free-breathing diffusion sequences to increase the signal-to-noise ratio and reduce artifacts on images [52].

The efficacy of triggered sequences has been well documented in many articles published in literature. Naganawa et al. compared ADC values obtained with respiratory triggering and free-breathing [53]. They found higher ADC values in free-breathing sequences in the right lobe, suggesting that ADC values are influenced by respiratory motions. They also found that, in left lobe, ADC values are about the same in both types of sequence, supporting the fact that motion artifacts in the left lobe are mostly provoked by cardiac pulse [53]. Also Bruegel et al. suggest a pulse triggering in order to reduce cardiac motion artifacts [24].

Mürtz et al. also analyzed the influence of pulsatile motions on diffusion sequences and suggested acquiring data triggered by the cardiac cycle, in order to avoid data acquisition in different phases of the cardiac cycle [46]. The authors found that ADC values without triggering were artificially higher than those obtained with cardiac triggering [46]. However, simultaneous use of both respiratory and cardiac triggers make the sequence too long; thus Nasu et al. suggest use of an increased number of excitations, in order to increase the possibility of data acquisition during diastole, using only respiratory trigger [54].

Sandberg et al. compared respiratory triggered and breath-hold sequences and found better image quality for respiratory triggered DW-SSEPI [55].

Nasu et al. compared DW images acquired in free-breathing modality and with respiratory trigger; higher ADC measurement accuracy was reported using respiratory trigger [56].

Also, Bruegel et al. suggested use of DW-SSEPI using navigator-controlled respiratory triggering and parallel acquisition techniques in order to acquire high-quality diffusion-weighted images within a relatively short acquisition time (4–6 minutes) [24].

Taouli et al. evaluated the usefulness of navigator echo technique for triggered diffusion sequences; they found improvement in image quality and ADC measurement compared with standard breath-hold sequences. Of course, better image quality "is offset by longer acquisition time" [51].

In opposition to Taouli, Kwee et al. found higher ADC values with triggered acquisition [57], but they did not use a navigator echo.

In addition, respiratory triggered sequences could have artifacts, in particular a “pseudo-anisotropy artifact” which induces errors in ADC measurement [54]: it takes its origin “in localized hepatic movements, such as extension, contraction and rotation.” This thesis is supported by the fact that pseudo-anisotropy artifact is more frequent in noncirrhotic livers. However, in their series this artifact did not interfere with diagnostic image interpretation [54].

Lastly, a degree of ADC variability is also present across different MR platforms, depending on the coil systems, imagers, vendors, and field strengths used for MR imaging, with an intervender ADC measurement variability of 7% [58].

2.5. Quantification of Fibrosis: ADC. According to results published by one of the most important studies in this field [7], DWI was considered a “valid non-invasive method to predict the presence of moderate or advanced fibrosis.” Analyzing the study by Taouli et al., a total of 23 patients with chronic hepatitis and 7 healthy volunteers were examined using a 1.5-Tesla MR scanner [7]. Fibrosis was scored on a five-point scale: stage 0 = no fibrosis; stage 1 = portal fibrosis; stage 2 = periportal fibrosis; stage 3 = septal fibrosis; stage 4 = cirrhosis. ADC measurements were obtained by sampling different regions in the liver parenchyma and a Mann-Whitney U test was performed to predict the stage of fibrosis on the basis of ADC measurement. The authors found “lower hepatic ADCs in stage 2 or greater versus stage 1 or less fibrosis, and stage 3 or greater versus stage 2 or less fibrosis” [7]. ADC was a significant predictor of stage 2 or greater and stage 3 or greater fibrosis, with areas under the curve of 0.896 and 0.896. Moreover, a significant trend between degree of fibrosis and ADC values was reported; lower ADC values were associated to advanced fibrosis, whereas higher values were related to a mild degree of parenchymal fibrosis [7]. In a work by Bonekamp et al., significant differences were also reported comparing METAVIR stages F0 versus F1-4, F0-1 versus F > 1, F0-2 versus F3-4, and F0-3 versus F4 [Bonekamp]; a “substantial overlap” is also reported among ADC values [59].

However, a recent paper by Sandrasegaran et al. has investigated the usefulness of ADC in distinguishing different stages of fibrosis according to the METAVIR classification [60]. Mean ADCs were in fact calculated among different classes of fibrosis—including F0, F1, F2, F3, and F4 METAVIR stages. Contrarily to the previous study, ADC means was statistically different only between F0 and F4 classes, whereas no statistical difference was observed between patients with F2 stage or higher and patients with lower stages of fibrosis. The results obtained by Sandrasegaran et al. seem to challenge again the role of DWI in the evaluation of fibrosis [60].

In addition, a noninvasive method for evaluation of hepatic fibrosis should be reliable and able to completely substitute liver biopsy. The crucial point is that clinicians have to identify F2 stage of fibrosis early, because antifibrotic

treatment is generally required for patients with moderate to advanced stage of fibrosis (F2 to F4). On the basis of their results, Sandrasegaran et al. conclude that DWI with current scanners is not reliable enough to replace liver biopsy [60].

2.6. Quantification of Fibrosis: Intravoxel Incoherent Motion (IVIM). IVIM analysis means the “microscopic translational motions that occur in each image voxel” [61]. However, DWI imaging based on a monoexponential analysis could be limited, because it estimates molecular diffusion and the contribution of the perfusion effect. Perfusion is due to the random configuration of capillary network in each voxel. To separate diffusion and perfusion a biexponential model is required, with a multi- b fitting analysis.

Fifty-five patients with chronic liver disease were studied by diffusion-MRI using a 3-Tesla scanner [59]. IVIM-DWI was performed to evaluate the presence of hepatic fibrosis; true diffusion coefficient (D_t), pseudo-diffusion coefficient (D_p), perfusion fraction (f), and ADC total were calculated.

As reported by Yoon et al., all parameters “showed a significant correlation with the hepatic fibrosis stages,” and “were significantly higher in F0 to F1 than F4 ($P < 0.05$)” [62]. On the basis of their results, pseudo-diffusion coefficient was the best diagnostic tool in differentiating between $a \geq F2$ and a F0 to F1 degree of parenchymal fibrosis [62], showing greater diagnostic accuracy than ADC. Thus, an IVIM-DWI analysis was suggested for the assessment of hepatic fibrosis.

In a study by Pasquinelli et al., healthy volunteers and patients with chronic hepatic disease were classified into four groups on the basis of their METAVIR score and their Child-Pugh score [23]: group 1 included all healthy volunteers, group 2 F0–F2 patients, group 3 F3–F4 Child AB patients, and finally group 4 patients having F4 Child CD score.

ADC, diffusion (D) values, and perfusion parameters were calculated. ADC mean values progressively decreased from first to fourth group, with no statistical difference observed among groups. A wide overlap was reported for ADC values, and according to results obtained in the study, “stratification of patients with chronic liver disease for clinical purposes cannot be done with DWI” [23].

2.7. Quantification of Fibrosis: Variability of Measurement. Considering results of the mentioned studies, the diagnostic capability of DWI in the evaluation of hepatic fibrosis seems to be controversial, with some papers not considering DWI a valid diagnostic tool able to replace liver biopsy. In fact, many limitations have been described in liver MRI protocol. First of all, ADC repeatability and reproducibility in liver parenchyma have been evaluated in many studies, with some controversial results [63]. In a study performed by Colagrande et al., four different ROIs (Regions Of Interest) were adopted to calculate ADC of the liver parenchyma: ROIs of 70% and 30% of the liver volume, 4%-one-ROI-per-segment, and 4%-one-ROI-per-slice in the right-lobe. Authors reported that repeatability was “acceptable” for all methods, but reproducibility was low, with $ICC \leq 0.45$; for a large number of patients enrolled in their study (about 50%) it was impossible to obtain measurements in the left hepatic lobe [63].

Sampling parenchyma of left hepatic lobe could be very difficult due to the presence of magnetic susceptibility or motion artifacts in these locations, and even if the introduction of triggered-acquisition increases image quality, the evaluation of these areas could be limited [20].

Another important limitation for quantitative assessment of liver parenchyma is the possibility of magnetic susceptibility artifacts caused by colonic loop, often located very close to the caudal portion of the right liver. They reduce image quality on diffusion images, with low signal intensity of parenchyma and loss of liver profile [20].

2.8. Quantification of Fibrosis: Relative ADC. Quantification of fibrosis is conditioned by variability in the measurement process, as already reported in several articles [63–65]. To reduce variability, the possibility of calculating relative ADC has been considered. A recent article by Hong et al. evaluated sixty-seven patients affected by chronic B hepatitis and nine patients with focal liver lesions. They performed diffusion MR using different b -values and calculated liver ADCs and relative ADCs; the latter were obtained using splenic and renal parenchyma as references.

Namely, relative renal ADC was obtained according to the ratio between liver ADC and renal cortex ADC, whereas relative splenic ADC was calculated according to the ratio between liver ADC and splenic ADC [64]. All mean ADC values, absolute and relative, showed an inverse correlation with hepatic fibrosis and they were lower in increased fibrosis scores. The relative renal ADCs, obtained at $b = 600 \text{ mm}^2/\text{sec}$ diffusion images, showed a strong correlation with degree of hepatic fibrosis, with an r -value of -0.697 .

Moreover, Do et al. evaluated the contribution of a relative ADC measurement in the assessment of hepatic fibrosis [65]. The authors found that normalization of ADC, which means the ratio between liver ADC and spleen ADC, was more accurate than standard ADC measurement in the quantification of fibrosis [65]. For predicting moderate or advanced fibrosis (stage \geq F2), ROC analysis reported an area under the curve of 0.864 using “normalized ADC,” greater than the value obtained using liver ADC (0.655) [65]. However, studies which have investigated the role of relative ADC in the measurement of liver fibrosis show many limitations. Mainly, they are based on a retrospective population study, sometimes limited in number of patients. In addition, relative measurement could be time-consuming, because radiologists need to calculate the ADC of two organs, and then to create a ratio between values.

3. Conclusions

Diffusion MR in liver fibrosis quantification cannot replace liver biopsy. Several studies published on this topic have not shown univocal results. Although many articles have demonstrated statistically significant results, ADC measurements are conditioned by overlap in the evaluation of different stages of fibrosis.

In addition, variability among measurement still represents a limit in diffusion imaging. Further investigation and analysis are needed to increase the reliability of the technique.

A possible application for the future, in our opinion, could be the use of fibrosis monitoring in the management of the disease.

Conflict of Interests

The authors declare that there is no conflict of interests regarding the publication of this paper.

References

- [1] Y. Wang, D. R. Ganger, J. Levitsky et al., “Assessment of chronic hepatitis and fibrosis: comparison of MR elastography and diffusion-weighted imaging,” *American Journal of Roentgenology*, vol. 196, no. 3, pp. 553–561, 2011.
- [2] S. L. Friedman, “Mechanisms of hepatic fibrogenesis,” *Gastroenterology*, vol. 134, no. 6, pp. 1655–1669, 2008.
- [3] B. K. Kim, J. Fung, M.-F. Yuen, and S. U. Kim, “Clinical application of liver stiffness measurement using transient elastography in chronic liver disease from longitudinal perspectives,” *World Journal of Gastroenterology*, vol. 19, no. 12, pp. 1890–1900, 2013.
- [4] S. L. Friedman, D. C. Rockey, and D. M. Bissell, “Hepatic fibrosis 2006: report of the third AASLD single topic conference,” *Hepatology*, vol. 45, no. 1, pp. 242–249, 2007.
- [5] S. J. Hadziyannis, N. C. Tassopoulos, E. J. Heathcote et al., “long-term therapy with adefovir dipivoxil for HBeAg-negative chronic hepatitis B for up to 5 years,” *Gastroenterology*, vol. 131, no. 6, pp. 1743–1751, 2006.
- [6] S. Bruno, T. Stroffolini, M. Colombo et al., “Sustained virological response to interferon- α is with improved outcome in HCV-related cirrhosis: a retrospective study,” *Hepatology*, vol. 45, no. 3, pp. 579–587, 2007.
- [7] B. Taouli, A. J. Tolia, M. Losada et al., “Diffusion-weighted MRI for quantification of liver fibrosis: preliminary experience,” *American Journal of Roentgenology*, vol. 189, no. 4, pp. 799–806, 2007.
- [8] D. B. McGill, J. Rakela, A. R. Zinsmeister, and B. J. Ott, “A 21-year experience with major hemorrhage after percutaneous liver biopsy,” *Gastroenterology*, vol. 99, no. 5, pp. 1396–1400, 1990.
- [9] F. Froehlich, O. Lamy, M. Fried, and J. J. Gonvers, “Practice and complications of liver biopsy: results of a nationwide survey in Switzerland,” *Digestive Diseases and Sciences*, vol. 38, no. 8, pp. 1480–1484, 1993.
- [10] S. Y. Jin, “Role of liver biopsy in the assessment of hepatic fibrosis: its utility and limitations,” *The Korean Journal of Hepatology*, vol. 13, no. 2, pp. 138–145, 2007.
- [11] C.-T. Wai, J. K. Greenson, R. J. Fontana et al., “A simple noninvasive index can predict both significant fibrosis and cirrhosis in patients with chronic hepatitis C,” *Hepatology*, vol. 38, no. 2, pp. 518–526, 2003.
- [12] F. Imbert-Bismut, V. Ratziu, L. Pieroni, F. Charlotte, Y. Benhamou, and T. Poynard, “Biochemical markers of liver fibrosis in patients with hepatitis C virus infection: a prospective study,” *The Lancet*, vol. 357, no. 9262, pp. 1069–1075, 2001.
- [13] N. N. Salkic, P. Jovanovic, G. Hauser, and M. Brcic, “Fibrotest/fibrosure for significant liver fibrosis and cirrhosis in chronic hepatitis B: a meta-analysis,” *The American Journal of Gastroenterology*, vol. 109, pp. 796–809, 2014.

- [14] V. Papastergiou, E. Tsochatzis, and A. K. Burroughs, "Non-invasive assessment of liver fibrosis," *Annals of Gastroenterology*, vol. 25, no. 3, pp. 218–231, 2012.
- [15] A. Bonder and N. Afdhal, "Utilization of FibroScan in clinical practice," *Current Gastroenterology Reports*, vol. 16, no. 2, article 372, 2014.
- [16] C. Tatsumi, M. Kudo, K. Ueshima et al., "Noninvasive evaluation of hepatic fibrosis using serum fibrotic markers, transient elastography (FibroScan) and real-time tissue elastography," *Intervirolgy*, vol. 51, supplement 1, pp. 27–33, 2008.
- [17] T. Poynard, J. Vergniol, Y. Ngo et al., "Staging chronic hepatitis C in seven categories using fibrosis biomarker (FibroTest) and transient elastography (FibroScan)," *Journal of Hepatology*, vol. 60, no. 4, pp. 706–714, 2014.
- [18] S. Lee and D. Y. Kim, "Non-invasive diagnosis of hepatitis B virus-related cirrhosis," *World Journal of Gastroenterology*, vol. 20, no. 2, pp. 445–459, 2014.
- [19] W. C. Yeh, P. C. Li, Y. M. Jeng et al., "Elastic modulus measurements of human liver and correlation with pathology," *Ultrasound in Medicine and Biology*, vol. 28, no. 4, pp. 467–474, 2002.
- [20] S. Palmucci, L. A. Mauro, M. Messina et al., "Diffusion-weighted MRI in a liver protocol: its role in focal lesion detection," *World Journal of Radiology*, vol. 4, no. 7, pp. 302–310, 2012.
- [21] S. Colagrande, S. F. Carbone, L. M. Carusi, M. Cova, and N. Villari, "Magnetic resonance diffusion-weighted imaging: extraneurological applications," *Radiologia Medica*, vol. 111, no. 3, pp. 392–419, 2006.
- [22] B. Taouli, M. Chouli, A. J. Martin, A. Qayyum, F. V. Coakley, and V. Vilgrain, "Chronic hepatitis: role of diffusion-weighted imaging and diffusion tensor imaging for the diagnosis of liver fibrosis and inflammation," *Journal of Magnetic Resonance Imaging*, vol. 28, no. 1, pp. 89–95, 2008.
- [23] F. Pasquinelli, G. Belli, L. N. Mazzoni et al., "MR-diffusion imaging in assessing chronic liver diseases: does a clinical role exist?" *Radiologia Medica*, vol. 117, no. 2, pp. 242–253, 2012.
- [24] M. Bruegel, K. Holzapfel, J. Gaa et al., "Characterization of focal liver lesions by ADC measurements using a respiratory triggered diffusion-weighted single-shot echo-planar MR imaging technique," *European Radiology*, vol. 18, no. 3, pp. 477–485, 2008.
- [25] K. Holzapfel, M. Bruegel, M. Eiber et al., "Characterization of small (≤ 10 mm) focal liver lesions: value of respiratory-triggered echo-planar diffusion-weighted MR imaging," *European Journal of Radiology*, vol. 76, no. 1, pp. 89–95, 2010.
- [26] K. Coenegrachts, J. Delanote, L. ter Beek et al., "Improved focal liver lesion detection: comparison of single-shot diffusion-weighted echoplanar and single-shot T_2 weighted turbo spin echo techniques," *The British Journal of Radiology*, vol. 80, no. 955, pp. 524–531, 2007.
- [27] F. Mungai, F. Pasquinelli, L. N. Mazzoni et al., "Diffusion-weighted magnetic resonance imaging in the prediction and assessment of chemotherapy outcome in liver metastases," *Radiologia Medica*, vol. 119, no. 8, pp. 625–633, 2014.
- [28] N. Kokabi, J. C. Camacho, M. Xing et al., "Apparent diffusion coefficient quantification as an early imaging biomarker of response and predictor of survival following yttrium-90 radioembolization for unresectable infiltrative hepatocellular carcinoma with portal vein thrombosis," *Abdominal Imaging*, vol. 39, no. 5, pp. 969–978, 2014.
- [29] D. Le Bihan, R. Turner, P. Douek, and N. Patronas, "Diffusion MR imaging: clinical applications," *The American Journal of Roentgenology*, vol. 159, no. 3, pp. 591–599, 1992.
- [30] H. Y. Carr and E. M. Purcell, "Effects of diffusion on free precession in nuclear magnetic resonance experiments," *Physical Review*, vol. 94, no. 3, pp. 630–638, 1954.
- [31] D. Le Bihan, R. Turner, J. Pekar, and C. T. W. Moonen, "Diffusion and perfusion imaging by gradient sensitization: design, strategy and significance," *Journal of Magnetic Resonance Imaging*, vol. 1, pp. 7–28, 1991.
- [32] D. Le Bihan, "Molecular diffusion nuclear magnetic resonance imaging," *Magnetic Resonance Quarterly*, vol. 7, no. 1, pp. 1–30, 1991.
- [33] R. Turner, D. Le Bihan, and A. S. Chesnick, "Echo-planar imaging of diffusion and perfusion," *Magnetic Resonance in Medicine*, vol. 19, no. 2, pp. 247–253, 1991.
- [34] M. F. Reiser, W. Semmler, and H. Hricak, *Magnetic Resonance Tomography*, Springer, Berlin, Germany, 2008.
- [35] J. H. Burdette, A. D. Elster, and P. E. Ricci, "Acute cerebral infarction: quantification of spin-density and T2 shine-through phenomena on diffusion-weighted MR images," *Radiology*, vol. 212, no. 2, pp. 333–339, 1999.
- [36] G. Liney, *MRI in Clinical Practice*, Springer, Berlin, Germany, 2007.
- [37] I. Yamada, W. Aung, Y. Himeno, T. Nakagawa, and H. Shibuya, "Diffusion coefficients in abdominal organs and hepatic lesions: evaluation with intravoxel incoherent motion echo-planar MR imaging," *Radiology*, vol. 210, no. 3, pp. 617–623, 1999.
- [38] A. D. Culverwell, M. B. Sheridan, J. A. Guthrie, and A. F. Scarsbrook, "Diffusion-weighted MRI of the liver—interpretative pearls and pitfalls," *Clinical Radiology*, vol. 68, no. 4, pp. 406–414, 2013.
- [39] M. Kanematsu, S. Goshima, H. Watanabe et al., "Diffusion/perfusion MR imaging of the liver: practice, challenges, and future," *Magnetic Resonance in Medical Sciences*, vol. 11, no. 3, pp. 151–161, 2012.
- [40] K. Minematsu, L. Li, C. H. Sotak, M. A. Davis, and M. Fisher, "Reversible focal ischemic injury demonstrated by diffusion-weighted magnetic resonance imaging in rats," *Stroke*, vol. 23, no. 9, pp. 1304–1311, 1992.
- [41] Y. Hayashida, T. Hirai, S. Morishita et al., "Diffusion-weighted imaging of metastatic brain tumors: comparison with histologic type and tumor cellularity," *American Journal of Neuroradiology*, vol. 27, no. 7, pp. 1419–1425, 2006.
- [42] H. Ozkurt, F. Keskiner, O. Karatag, C. Alkim, S. M. Erturk, and M. Basak, "Diffusion weighted MRI for hepatic fibrosis: impact of b-value," *Iranian Journal of Radiology*, vol. 11, no. 1, Article ID e3555, 2014.
- [43] Y. Hong, Y. Shi, W. Liao et al., "Relative ADC measurement for liver fibrosis diagnosis in chronic hepatitis B using spleen/renal cortex as the reference organs at 3 T," *Clinical Radiology*, vol. 69, no. 6, pp. 581–588, 2014.
- [44] K. Fujimoto, T. Tonan, S. Azuma et al., "Evaluation of the mean and entropy of apparent diffusion coefficient values in chronic hepatitis C: correlation with pathologic fibrosis stage and inflammatory activity grade," *Radiology*, vol. 258, no. 3, pp. 739–748, 2011.
- [45] A. A. Bakan, E. Inci, S. Bakan, S. Gokturk, and T. Cimilli, "Utility of diffusion-weighted imaging in the evaluation of liver fibrosis," *European Radiology*, vol. 22, no. 3, pp. 682–687, 2012.

- [46] P. Mürtz, S. Flacke, F. Träber, J. S. van den Brink, J. Gieseke, and H. H. Schild, "Abdomen: diffusion-weighted MR imaging with pulse-triggered single-shot sequences," *Radiology*, vol. 224, no. 1, pp. 258–264, 2002.
- [47] B. Taouli and D.-M. Koh, "Diffusion-weighted MR imaging of the liver," *Radiology*, vol. 254, no. 1, pp. 47–66, 2010.
- [48] S. Palmucci, L. A. Mauro, M. Coppolino et al., "Evaluation of the biliary and pancreatic system with 2D SSFSE, breathhold 3D FRFSE and respiratory-triggered 3D FRFSE sequences," *Radiologia Medica*, vol. 115, no. 3, pp. 467–482, 2010.
- [49] L. S. Yoon, O. A. Catalano, S. Fritz, C. R. Ferrone, P. F. Hahn, and D. V. Sahani, "Another dimension in magnetic resonance cholangiopancreatography: comparison of 2- and 3-dimensional magnetic resonance cholangiopancreatography for the evaluation of intraductal papillary mucinous neoplasm of the pancreas," *Journal of Computer Assisted Tomography*, vol. 33, no. 3, pp. 363–368, 2009.
- [50] J. D. Barnwell, J. K. Smith, and M. Castillo, "Utility of navigator-prospective acquisition correction technique (PACE) for reducing motion in brain MR imaging studies," *American Journal of Neuroradiology*, vol. 28, no. 4, pp. 790–791, 2007.
- [51] B. Taouli, A. Sandberg, A. Stemmer et al., "Diffusion-weighted imaging of the liver: comparison of navigator triggered and breathhold acquisitions," *Journal of Magnetic Resonance Imaging*, vol. 30, no. 3, pp. 561–568, 2009.
- [52] T. C. Kwee, T. Takahara, R. Ochiai, R. A. J. Nievelstein, and P. R. Luijten, "Diffusion-weighted whole-body imaging with background body signal suppression (DWIBS): features and potential applications in oncology," *European Radiology*, vol. 18, no. 9, pp. 1937–1952, 2008.
- [53] S. Naganawa, H. Kawai, H. Fukatsu et al., "Diffusion-weighted imaging of the liver: technical challenges and prospects for the future," *Magnetic Resonance in Medical Sciences*, vol. 4, no. 4, pp. 175–186, 2005.
- [54] K. Nasu, Y. Kuroki, H. Fujii, and M. Minami, "Hepatic pseudo-anisotropy: a specific artifact in hepatic diffusion-weighted images obtained with respiratory triggering," *Magnetic Resonance Materials in Physics, Biology and Medicine*, vol. 20, no. 4, pp. 205–211, 2007.
- [55] A. Sandberg, T. Parikh, G. Johnson, A. Stemmer, and B. Taouli, "Feasibility of a respiratory-triggered SSEPI diffusion-weighted sequence for liver imaging using navigator echo technique: comparison with breath-hold diffusion-weighted sequence," *Proceedings of the International Society for Magnetic Resonance in Medicine*, vol. 14, 2006, abstract number 400.
- [56] K. Nasu, Y. Kuroki, R. Sekiguchi, and S. Nawano, "The effect of simultaneous use of respiratory triggering in diffusion-weighted imaging of the liver," *Magnetic Resonance in Medical Sciences*, vol. 5, no. 3, pp. 129–136, 2006.
- [57] T. C. Kwee, T. Takahara, D. M. Koh, R. A. Nievelstein, and P. R. Luijten, "Comparison and reproducibility of ADC measurements in breathhold, respiratory triggered, and free-breathing diffusion-weighted MR imaging of the liver," *Journal of Magnetic Resonance Imaging*, vol. 28, no. 5, pp. 1141–1148, 2008.
- [58] M. Sasaki, K. Yamada, Y. Watanabe et al., "Variability in absolute apparent diffusion coefficient values across different platforms may be substantial: a multivendor, multi-institutional comparison study," *Radiology*, vol. 249, no. 2, pp. 624–630, 2008.
- [59] S. Bonekamp, M. S. Torbenson, and I. R. Kamel, "Diffusion-weighted magnetic resonance imaging for the staging of liver fibrosis," *Journal of Clinical Gastroenterology*, vol. 45, no. 10, pp. 885–892, 2011.
- [60] K. Sandrasegaran, F. M. Akisik, C. Lin et al., "Value of diffusion-weighted MRI for assessing liver fibrosis and cirrhosis," *American Journal of Roentgenology*, vol. 193, no. 6, pp. 1556–1560, 2009.
- [61] D. le Bihan, E. Breton, D. Lallemand, M.-L. Aubin, J. Vignaud, and M. Laval-Jeantet, "Separation of diffusion and perfusion in intravoxel incoherent motion MR imaging," *Radiology*, vol. 168, no. 2, pp. 497–505, 1988.
- [62] J. H. Yoon, J. M. Lee, M. H. Yu, B. Kiefer, J. K. Han, and B. I. Choi, "Evaluation of hepatic focal lesions using diffusion-weighted MR imaging: comparison of apparent diffusion coefficient and intravoxel incoherent motion-derived parameters," *Journal of Magnetic Resonance Imaging*, vol. 39, no. 2, pp. 276–285, 2014.
- [63] S. Colagrande, F. Pasquinelli, L. N. Mazzoni, G. Belli, and G. Virgili, "MR-diffusion weighted imaging of healthy liver parenchyma: repeatability and reproducibility of apparent diffusion coefficient measurement," *Journal of Magnetic Resonance Imaging*, vol. 31, no. 4, pp. 912–920, 2010.
- [64] Y. Hong, Y. Shi, W. Liao et al., "Relative ADC measurement for liver fibrosis diagnosis in chronic hepatitis B using spleen/renal cortex as the reference organs at 3 T," *Clinical Radiology*, vol. 69, no. 6, pp. 581–588, 2014.
- [65] R. K. Do, H. Chandanara, E. Felker et al., "Diagnosis of liver fibrosis and cirrhosis with diffusion-weighted imaging: value of normalized apparent diffusion coefficient using the spleen as reference organ," *The American Journal of Roentgenology*, vol. 195, no. 3, pp. 671–676, 2010.

Research Article

Diagnostic Value of MRI Proton Density Fat Fraction for Assessing Liver Steatosis in Chronic Viral C Hepatitis

Francesco Paparo,¹ Giovanni Cenderello,² Matteo Revelli,³
Lorenzo Bacigalupo,¹ Mariangela Rutigliani,⁴ Daniele Zefiro,⁵
Luca Cevasco,³ Maria Amico,⁶ Roberto Bandelloni,⁴ Giovanni Cassola,²
Gian Luca Forni,⁷ and Gian Andrea Rollandi¹

¹Department of Radiology, E.O. Ospedali Galliera, Mura della Cappuccine 14, 16128 Genoa, Italy

²Unit of Infectious Diseases, E.O. Ospedali Galliera, Mura della Cappuccine 14, 16128 Genoa, Italy

³School of Radiology, University of Genoa, Via Leon Battista Alberti 4, 16132 Genoa, Italy

⁴Unit of Pathology, E.O. Ospedali Galliera, Mura della Cappuccine 14, 16128 Genoa, Italy

⁵Department of Medical Physics, ASL N. 5 "Spezzino", Via XXIV Maggio 139, 19124 La Spezia, Italy

⁶Section of Radiology, Department of Biotechnology and Legal Medicine, Policlinico Universitario "P. Giaccone", Via del Vespro 129, 90127 Palermo, Italy

⁷Unit of Microcitemia and Hereditary Anaemias, E.O. Ospedali Galliera, Mura della Cappuccine 14, 16128 Genoa, Italy

Correspondence should be addressed to Francesco Paparo; francesco.paparo@galliera.it

Received 2 July 2014; Accepted 8 October 2014

Academic Editor: Edward Lee

Copyright © 2015 Francesco Paparo et al. This is an open access article distributed under the Creative Commons Attribution License, which permits unrestricted use, distribution, and reproduction in any medium, provided the original work is properly cited.

Objective. To assess the diagnostic performance of a T1-independent, T2*-corrected multiecho magnetic resonance imaging (MRI) technique for the quantification of hepatic steatosis in a cohort of patients affected by chronic viral C hepatitis, using liver biopsy as gold standard. **Methods.** Eighty-one untreated patients with chronic viral C hepatitis were prospectively enrolled. All included patients underwent MRI, transient elastography, and liver biopsy within a time interval <10 days. **Results.** Our cohort of 77 patients included 43/77 (55.8%) males and 34/77 (44.2%) females with a mean age of 51.31 ± 11.27 (18–81) years. The median MRI PDFF showed a strong correlation with the histological fat fraction (FF) ($r = 0.754$, 95% CI 0.637 to 0.836, $P < 0.0001$), and the correlation was influenced by neither the liver stiffness nor the T2* decay. The median MRI PDFF result was significantly lower in the F4 subgroup ($P < 0.05$). The diagnostic accuracy of MRI PDFF evaluated by AUC-ROC analysis was 0.926 (95% CI 0.843 to 0.973) for $S \geq 1$ and 0.929 (95% CI 0.847 to 0.975) for $S = 2$. **Conclusions.** Our MRI technique of PDFF estimation allowed discriminating with a good diagnostic accuracy between different grades of hepatic steatosis.

1. Introduction

It is well known that hepatitis C virus (HCV), particularly genotype 3, can lead to steatotic change in hepatocytes. In fact, the proportion of chronic hepatitis C patients with steatosis is considerable, suggesting a direct role of HCV in the intrahepatic accumulation of triglycerides, with a reported prevalence ranging from 40 to 80% [1, 2]. In addition, steatosis has been recognized as one of the factors capable of influencing both liver fibrosis progression and

the rate of response to interferon-alpha-based therapy [3]. Currently, percutaneous liver biopsy remains the reference standard for the diagnosis and grading of hepatic steatosis, but its clinical application for purposes of screening, frequent monitoring, and epidemiologic studies is limited by the significant risk of bleeding, infection, and sampling error [4]. Different noninvasive imaging techniques have been proposed to assess the presence and severity of hepatic steatosis, including ultrasonography (US), computed tomography (CT), and magnetic resonance imaging (MRI) [5]. Due to its

power of tissue characterization, MRI has a pivotal role for the detection and quantification of liver fat content. To this regard, the main MRI-based tools include fat-suppressed and chemical-shift water-fat separation techniques (i.e., 2- and 3-point Dixon, multiecho and multi-interference methods) and magnetic resonance spectroscopy (MRS) [6–10]. Currently, MRS is regarded as the most accurate noninvasive imaging method for assessing fatty liver, and MRS-derived fat fraction (FF) represents an objective biomarker of this condition, characterized by a strong correlation with intracellular triglyceride content [11–15]. However, MRS is not widely available, is time consuming to perform and analyze, and samples only a small portion of the liver (i.e., a volume of about 4 cm³) [10, 12, 15]. Due to the limitations of spectroscopy, rapid chemical-shift methods are more commonly used in the clinical practice for estimating the liver FF [8, 11, 13, 16–18]. Otherwise, the application of these ready-available MRI techniques is hindered by the presence of different confounding factors (i.e., T1 relaxation effects, T2* decay, spectral complexity of fat, noise bias, B0 inhomogeneity, and eddy currents), that require proper correction [10, 12, 17–19]. More recently, in order to eliminate all major biases seen with conventional chemical shift-based methods, newer multiecho [8, 11, 13, 20] and multi-interference [10, 12, 19, 21–23] methods incorporating spectral modeling of fat have been described for the quantification of proton density fat fraction (PDFF). In addition, in chronic liver disease, hepatic steatosis may coexist with various other histological abnormalities, including fibrosis, necroinflammatory activity, and hemosiderin deposition, which may act as confounding factors on fat quantification by MRI [8]. From a clinical viewpoint, the issue regarding MRI quantification of hepatic steatosis in patients affected by chronic viral C hepatitis has been addressed in few previous works [24–26]. The purpose of our study was to assess the diagnostic performance of an original T1-independent, T2*-corrected multiecho MRI technique for the estimation and quantification of liver steatosis in a cohort of patients with chronic viral C hepatitis, using histology as standard of reference and assessing the influence of the other histological abnormalities on MRI PDFF measurements.

2. Methods

2.1. Inclusion of Patients. This was a prospective, monocentric, and institutional review board approved study and patient's enrollment was performed at the Unit of Infectious Diseases of our institution. From January 1st, 2013, through December 31st, 2013, 81 consecutive untreated patients with chronic viral C hepatitis were enrolled into the study after giving written informed consent. All patients were untreated (i.e., not under interferon-based therapies) at the time of enrollment. Exclusion criteria were the presence of major contraindications to 1.5T MRI (e.g., cardiac pacemaker, claustrophobia, foreign bodies, and implanted medical devices

with ferromagnetic properties [27]) and/or to liver biopsy (e.g., uncorrectable coagulopathy [28]). All included patients underwent MRI, transient elastography (TE), and liver biopsy within a time interval <10 days. Severe respiratory and motion artifacts on MR images were considered as an additional post-MRI exclusion criteria to avoid unreliable measurements of MRI PDFF. After inclusion, the following laboratory values were obtained for all patients: aspartate aminotransferase (AST, expressed in IU/l), alanine transaminase (ALT, expressed in IU/L), gamma-glutamyl transpeptidase (GGT, expressed in IU/L), total bilirubin (expressed in mg/dL), platelet count (10³ cells per μ L of blood), and serum ferritin levels (expressed in ng/mL). Serum HCV-RNA levels were assessed in all patients by means of a quantitative method (real time polymerase chain reaction) and expressed in IU/mL.

2.2. MRI Examinations and PDFF Measurements. MRI of the liver was performed in the supine position on a 1.5T MRI scanner (Sigma HDx, General Electric Medical Systems, Milwaukee, WI, USA) using a phased array, eight-element, and flexible torso coil. All patients were carefully instructed to suspend respiration at the end of inspiration during the MRI sequence acquisition. A two-dimensional, spoiled, and multiecho gradient-echo sequence with 16 echoes was performed in the axial plane to measure hepatic PDFF. The parameters of this sequence were adjusted in order to achieve a complete correction for confounding factors such as T1 bias, T2* decay, and water-fat signal interference [10, 12, 19]. To minimize T1 effects, a 20° flip angle was used at repetition time (TR) ranging from 120 to 270 msec, adjusted by the technologist to individual breath-hold capacity. To estimate water-fat signal interference and T2* effects, 16 echoes were obtained at serial opposed-phase and in-phase echo times (TE) (1.1, 2.25, 3.4, 4.55, 5.7, 6.85, 8, 9.15, 10.3, 11.45, 12.6, 13.75, 14.9, 16.05, 17.2, and 18.35 msec) during a single breath hold of 12–34 seconds. Other imaging parameters were 10 mm section thickness, 0 intersection gap, 125 kHz bandwidth, one signal average, and rectangular field of view with a 128 × 96 matrix adjusted to individual body habitus and breath-hold capacity. The multiecho gradient-echo MR images were exported in DICOM format for offline postprocessing.

2.3. Image Interpretation and Data Analysis. All MRI datasets derived from multiecho gradient-echo images were post-processed by a single experienced abdominal radiologist. The quantification of liver PDFF was performed with a publicly available software named C-Iron (Camelot Biomedical Systems SRL, Genoa, Italy; website: <http://www.c-iron.camelotbio.com>). C-Iron is a stand-alone software tool dedicated to the voxelwise measurement of T2* decay for the quantification of iron overload and liver PDFF. Once acquired, the multiecho gradient-echo MR images are imported into the software. T2* values and PDFFs are estimated by fitting the MRI signal (S) acquired at different

TEs with the following decay model proposed by Bydder et al. [19] as follows:

$$|S(\text{TE})| = \text{sqrt} \left[S_1^2 \exp\left(-\frac{2\text{TE}}{T_{2,w}^*}\right) + S_2^2 \exp\left(-\frac{2\text{TE}}{T_{2,f}^*}\right) + 2S_1S_2 \exp\left(-\frac{\text{TE}}{T_{2,w}^*}\right) \exp\left(-\frac{\text{TE}}{T_{2,f}^*}\right) \cos(\omega\text{TE}) \right], \quad (1)$$

where S_1 and S_2 are the signal amplitudes of water and fat, respectively, $T_{2,w}^*$ and $T_{2,f}^*$ are the transverse relaxation times of water and fat, and $\omega = 2\pi/4.6 \text{ ms}$ is the chemical shift between water and fat at 1.5 T. The algorithm simultaneously estimates T_2^* and PDFF in each voxel of the image by using nonlinear least-squares fitting from all 16 echoes, assuming exponential decay and considering that fat has its own inherent T_2 decay of 12 ms.

The quality of fit is assessed by means of the coefficient of determination R^2 and pixels with low-quality fit are excluded from further processing by applying appropriate thresholds on the R^2 value. The PDFF is then calculated by the following formula: $\text{FF} = S_2/(S_1 + S_2)$.

A color-coded map reflecting the estimated PDFF values in each pixel of the image is displayed and juxtaposed on the corresponding axial MRI slice. The histogram of pixel distribution with mean, median, and standard deviation of the PDFF values is computed in a freehand, elliptical, or rectangular user-adjustable ROI. A single abdominal radiologist, blind to the results of both TE and histology, performed ROI positioning. A single freehand ROI was drawn in a midhepatic axial slice including the right lobe of the liver and systematically excluding large blood vessels, biliary ducts, and focal lesions. The mean area of the ROIs was of about 40–60 cm^2 , depending on patient's anthropometric features (Figure 1). MRI PDFF and T_2^* decay were calculated in the same ROI. Clinically significant hepatic iron overload was defined by MRI T_2^* values less than 6.3 ms, corresponding to a liver iron concentration in dry tissue (LIC dry weight) of 4.2 mg/g [29, 30].

2.4. Transient Elastography. Transient elastography (TE) is a corroborate method for the assessment of liver fibrosis in patients with chronic C hepatitis. TE was performed with FibroScan (Echosens, Paris, France) with liver stiffness measurements expressed in kilopascals (values between 2.5 kPa and 75 kPa are expected) [31]. Acquisitions that do not have a correct vibration shape or a correct followup of the vibration propagation are automatically rejected by the software. Measurements of liver stiffness were performed on the right lobe of the liver through intercostal spaces in correspondence to the midaxillary line, while patients were lying in the supine position with the right arm in maximal abduction. In all included patients, TE measurements were successfully acquired (i.e., 10 correct measurements with an interquartile range lower than 30% of the median liver stiffness value [32]).

2.5. Liver Biopsy. Ultrasound-assisted percutaneous liver biopsy was performed with an intercostal approach using 15- to 18-gauge needles. All biopsy specimens were fixed in formalin and embedded in paraffin. A single expert liver pathologist, blind to the results of both TE and MRI, read the specimens on site. Fibrosis was semiquantitatively evaluated and staged on a 5-point scale from 0 to 4 according to the METAVIR scoring system (F0, absent; F1, enlarged fibrotic portal tract; F2, periportal or initial portal-portal septa but intact architecture; F3, architectural distortion but no obvious cirrhosis; and F4, cirrhosis) [33]. Necroinflammatory activity, represented by piecemeal necrosis and focal lobular necrosis, was semiquantitatively evaluated by using the histological activity index described in the METAVIR system and graded as follows: 0, no activity; 1, mild; 2, moderate; 3, severe [33, 34]. Liver steatosis was determined by estimating the percentage of fat-containing hepatocytes on hematoxylin-eosin stained specimens and graded according to the method of Kleiner et al. [35]: S0, steatosis in fewer than 5% of hepatocytes; S1, 5%–33% of fatty hepatocytes; S2, 34%–66%; and S3, more than 66%. We also considered the percentage of fatty hepatocytes as an absolute value which was defined as histological fat fraction. Following the clinical standard, a Perl's Prussian blue reaction was applied to detect the presence of hemosiderin granules in biopsy specimens. The following ordinal 4-point scoring system was employed: grade 0, no iron deposits; grade 1, mild; grade 2, moderate; grade 3, high iron content [36].

2.6. Statistical Analysis. Descriptive statistics were produced for demographic, clinical, and laboratory characteristics of patients. Categorical data were expressed as number and percentage, while continuous data were expressed as mean and standard deviation (SD) or median and range (from minimum to maximum). The normal distribution of different datasets was assessed by means of the D'Agostino-Pearson test. Nominal statistical significance was defined with a P of 0.05. The correlation of histological FF with MRI PDFF was tested by means of Spearman's rank test, using both the arithmetic mean and the median of MRI PDFF values. Spearman's rho (r) values were interpreted as follows: for values of r of 0.9 to 1, the correlation is very strong; for values of r between 0.7 and 0.89, correlation is strong; for values of r between 0.5 and 0.69, correlation is moderate; for values of r between 0.3 and 0.49, correlation is moderate to low; for values of r between 0.16 and 0.29, correlation is weak to low; for values of r below 0.16, correlation is too low to be meaningful. Since the median MRI PDFF showed a better correlation with the histological FF, this parameter was adopted for the subsequent statistical analysis. The correlation of median MRI PDFF values with histological FF was also tested using a partial correlation model, where liver stiffness, expressed in kPa, and T_2^* decay, expressed in ms, were introduced as confounding covariates. The cohort of patients was further stratified according to each histological feature of the METAVIR system, including fibrosis stage (F), inflammatory activity (A), and steatosis grade (S). Box plots were used to study the distribution of MRI PDFF according to each stage of fibrosis, inflammatory activity, and steatosis,

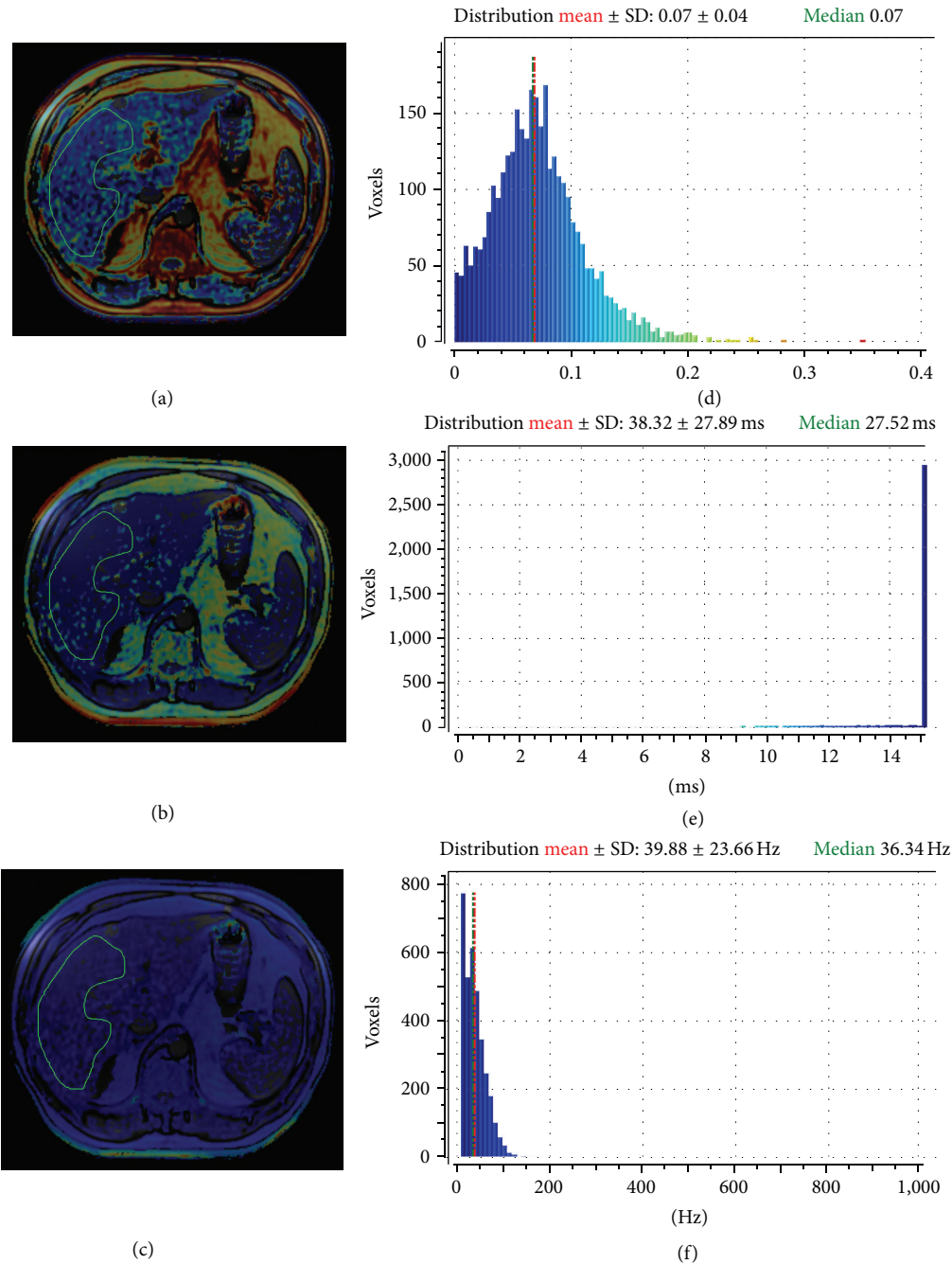


FIGURE 1: Example of ROI positioning for the calculation of MRI PDFF (a), T2* (b), and R2* decay (reciprocal of T2*, expressed in Hz) (c) in a 52-year-old male patient with chronic viral C hepatitis. The histological FF of this patient was 10%, corresponding to a steatosis grade 1 (S1). Images (d), (e), and (f) show the histogram of pixel distribution with mean values \pm standard deviation and medians.

and the presence of significant differences in the median MRI PDFF values among subgroups of patients was tested using the nonparametrical Kruskal-Wallis test. After a positive Kruskal-Wallis test (P value < 0.05), a post-hoc analysis was conducted performing pairwise comparisons between subgroups. The diagnostic performance of MRI for detecting the correct histological grade of hepatic steatosis was assessed by using receiver operating characteristic (ROC) curves. For the ROC curve analysis, the area under curve (AUC), optimal

cutoff values, sensitivity, specificity, and positive and negative predictive values were calculated. Optimal cutoff values of MRI PDFF were chosen to maximize the sum of sensitivity and specificity for two steatosis thresholds: S0 versus S1-S2 ($S \geq 1$) and S0-S1 versus S2 ($S = 2$). Ultimately, the MRI PDFF was introduced as dependent variable in a multiple regression model, using patient's age, BMI, TE liver stiffness values, MRI T2* values, METAVIR stage of fibrosis, inflammation, steatosis, and histological FF as independent variables.

TABLE 1: Characteristics of patients and results of histological analysis of liver biopsy specimens.

Characteristics of patients	Proportions, means \pm standard deviation	Percentages, medians, and range
Males	43/77	55.8%
Females	34/77	44.2%
Age	51.31 \pm 11.27	51 (18–81)
BMI	22.39 \pm 2.27	23 (18.43–27)
Serum AST level (U/L)	66.49 \pm 65.93	48 (18–293)
Serum ALT level (U/L)	62.83 \pm 53.13	51 (15–302)
Serum GGT level (U/L)	92.63 \pm 90.92	62 (11–368)
Total bilirubin (mg/dL)	1.05 \pm 1.26	0.7 (0.2–9)
Platelet count (10^3 cells/ μ L)	196.25 \pm 62.06	199 (99–462)
Serum ferritin level (ng/mL)	167.43 \pm 141.68	134.3 (13.3–700.4)
HCV-RNA (IU/mL)	$1.96 \times 10^6 \pm 1.91 \times 10^6$	1.34×10^6 (2.99×10^3 – 6.65×10^6)
Stiffness (kPa)	12.86 \pm 11.57	7.2 (3.8–55)
Histology		
Histological fat fraction	9.09 \pm 12.68	3 (0–45)
Steatosis grade (S)		
Grade 0 (<5%)	46/77	59.7%
Grade 1 (5–33%)	23/77	29.9%
Grade 2 (33–66%)	8/77	10.4%
Grade 3 (>66%)	0/77	0%
Necroinflammation (A)		
Grade 0	25/77	32.5%
Grade 1	33/77	42.8%
Grade 2	14/77	18.2%
Grade 3	5/77	6.5%
Fibrosis (F)		
F0 (none)	23/77	29.9%
F1 (perisinusoidal or periportal)	14/77	18.2%
F2 (perisinusoidal and portal/periportal)	12/77	15.5%
F3 (bridging fibrosis)	18/77	23.4%
F4 (cirrhosis)	10/77	13%
Histologically detectable iron		
Grade 0	73/77	94.8%
Grade 1	2/77	2.6%
Grade 2	2/77	2.6%
Grade 3	0/77	0%

Values are expressed as percentages, means \pm standard deviation, and medians (min–max).

Legend: BMI, body mass index.

3. Results

Four patients were excluded due to severe motion/respiratory artifacts in their MRIs, precluding an accurate measurement of PDFF. The resulting cohort of 77 patients with chronic C hepatitis included 43/77 (55.8%) males and 34/77 (44.2%) females with a mean age of 51.31 \pm 11.27 (from 18 to 81) years and a mean BMI of 22.39 \pm 2.27 (from 18.43 to 27). Seventy-one/77 patients (92.2%) presented detectable serum HCV-RNA levels (above the detection threshold of 15 IU/mL of our method), while 6/77 patients (7.8%) were in sustained virological response. In this latter subgroup, the standard treatment with peginterferon and ribavirin was stopped at least 18 months before the time of inclusion. Demographic,

clinical, and laboratory characteristics of patients are summarized in Table 1. The mean MRI PDFF of our cohort of patients, expressed in percentage units, was 11.76 \pm 4.73 with a median of 5.87 (from 0.7 to 17.01). The mean liver T2* value was 30.33 \pm 5.98 ms with a median of 31.32 ms (from 16.36 to 43.6 ms). We did not find patients with a histological steatosis of grade 3 (S3), and hemosiderin deposits were found in 4 patients. In addition, T2* values were not indicative of hepatic iron overload of clinical significance (i.e., below the threshold of 6.3 ms) in any patient. Therefore, we were not able to assess the diagnostic performance of MRI PDFF for the detection of severe steatosis (i.e., grade S3, >66% fat-containing hepatocytes) and the potential confounding effect of iron overload on MRI PDFF measurements. On the other

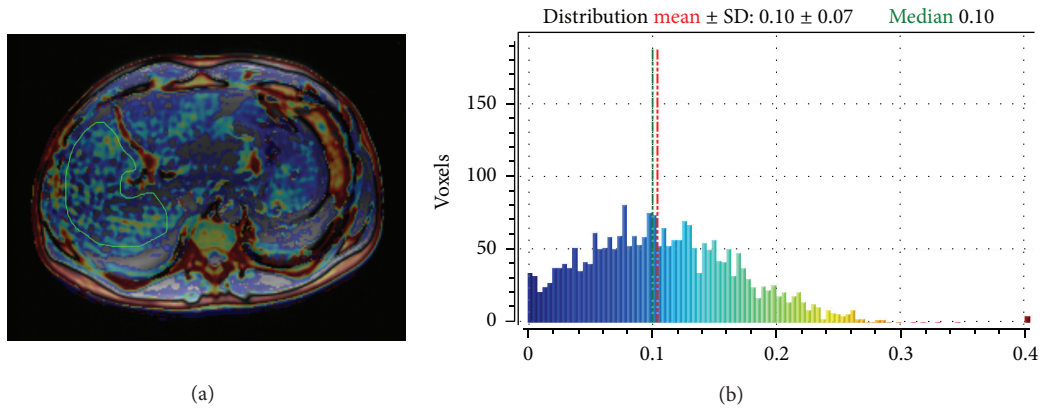


FIGURE 2: Calculation of MRI PDFF in a 45-year-old male patient with chronic viral C hepatitis (a). The median MRI PDFF value is 10% (b), while histological FF of the patient was 8%, corresponding to a steatosis grade 1 (S1).

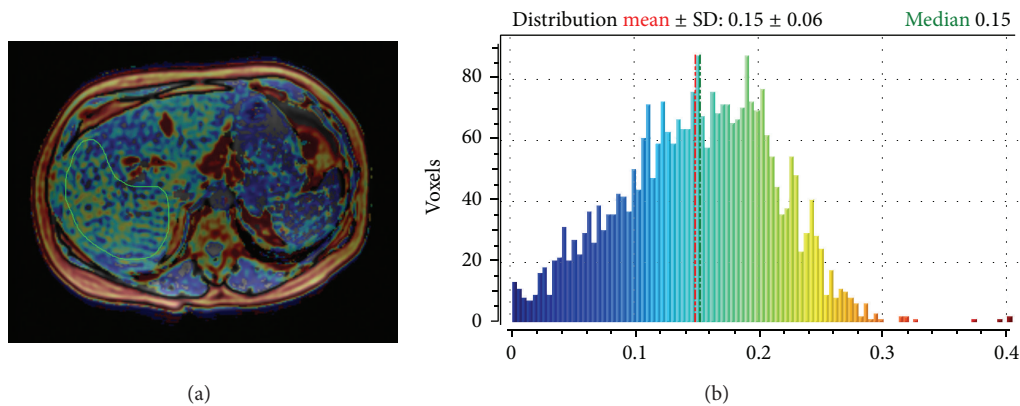


FIGURE 3: Calculation of MRI PDFF in a 45-year-old male patient with chronic viral C hepatitis (a). The median MRI PDFF value is 15% (b), while histological FF of the patient was 37%, corresponding to steatosis grade 2 (S2).

hand, we introduced T2* values in the partial correlation model in order to verify their influence on the correlation between MRI PDFF and histological FF.

3.1. Correlation and Subgroup Analysis. The correlation of the mean MRI PDFF value with the histological FF was moderate ($r = 0.624$, 95% CI for rho 0.465 to 0.744, $P < 0.0001$), while the correlation of the median MRI PDFF value with the histological FF was strong ($r = 0.754$, 95% CI for rho 0.637 to 0.836, $P < 0.0001$). The median MRI PDFF values for each steatosis grade were: 4.3 (0.7–10.09) for S0; 10.4 (3.7–16.2) for S1; 13.5 (8.4–17.01) for S2 ($P < 0.05$) (Figures 2 and 3). Stratifying the cohort of patients according to the METAVIR stages of parenchymal fibrosis, the median MRI PDFF values resulted in significantly different among different subgroups ($P < 0.05$ with the Kruskal-Wallis test). The post-hoc analysis showed that the median MRI PDFF in the F4 subgroup was significantly lower than in the other subgroups of patients ($P < 0.05$) (Table 2). Stratifying the cohort of patients according to the METAVIR stages of necroinflammatory activity, the Kruskal-Wallis test did not reveal a significant difference among the median MRI PDFF values of the four subgroups of patients ($P > 0.05$) (Figure 4). Box-and-whisker plots

for MRI PDFF measurements in relation to each grade of steatosis, fibrosis, and necroinflammatory activity are shown in Figure 4.

3.2. Diagnostic Accuracy of MRI PDFF. The diagnostic accuracy of MRI PDFF evaluated by AUC-ROC analysis was 0.926 (standard error 0.0354, 95% CI 0.843 to 0.973) for $S \geq 1$ and 0.929 (standard error 0.0363, 95% CI 0.847 to 0.975) for $S = 2$. The best MRI PDFF cutoff value to differentiate between S0 and S1-S2 patients was 6.87, showing a sensitivity of 87.10% (95% CI 70.2–96.4), a specificity of 97.83 (95% CI 88.5–99.9%), a positive predictive value (PPV) of 96.4% (95% CI 81.7–99.9), and a negative predictive value (NPV) of 91.8% (95% CI 80.4–97.7) (Figure 5(a)). The best MRI PDFF cutoff value to differentiate between S0-S1 and S2 patients was 11.08, showing a sensitivity of 87.5% (95% CI 47.3–99.7), a specificity of 88.41% (95% CI 78.4–94.9), a positive predictive value (PPV) of 46.7% (95% CI 20.5–74.3), and a negative predictive value (NPV) of 98.4% (95% CI 91.3–100) (Figure 5(b)).

3.3. Influence of Confounding Variables on MRI PDFF Measurements. The correlation between MRI PDFF and histological FF was strong even in a partial correlation model, using

TABLE 2: Distribution of MRI PDFF values according to different METAVIR stages of hepatic fibrosis. The Kruskal-Wallis test revealed a significant difference between groups ($P < 0.05$). The post-hoc analysis demonstrates that the median MRI PDFF value of the F4 subgroup is significantly lower than that of the other subgroups of patients.

Post-hoc analysis: distribution of PDFF according to METAVIR stages of fibrosis				
Factor	n	Median (range)	Average rank	Pairwise comparisons with a significant result ($P < 0.05$)
F0	23	6.7 (0.72–17.01)	44.61	F0 versus F4
F1	14	6.7 (0.7–15.54)	43.25	F1 versus F4
F2	12	6.07 (3.68–15.04)	40.33	F2 versus F4
F3	18	5.78 (3.7–15.54)	39.36	F3 versus F4
F4	10	3.43 (1.72–5.95)	17.90	F4 versus F0/F1/F2/F3

TABLE 3: Multiple regression analysis. MRI PDFF is the dependent variable of the model. Histological FF and the histological grade of steatosis were the only two factors independently and significantly correlated to MRI PDFF. P values below the level of statistical significance ($P < 0.05$) are marked with the asterisk.

Independent variables	Coefficient	Regression equation			
		Standard error	r_{partial}	t	P
(Constant)	8.3980				
Age	-0.01905	0.02438	-0.09435	-0.781	0.4372
BMI	-0.1480	0.1248	-0.1424	-1.186	0.2397
Necroinflammation (A)	0.07004	0.3184	0.02667	0.220	0.8266
Fibrosis (F)	-0.5041	0.3546	-0.1699	-1.422	0.1596
Steatosis (S)	2.3698	1.1144	0.2497	2.127	0.0371*
Liver stiffness	0.01464	0.04543	0.03903	0.322	0.7483
Histological FF	0.1325	0.05975	0.2597	2.218	0.0299*
T2*	0.03749	0.04626	0.09781	0.810	0.4205

TE liver stiffness values (expressed in kPa) and T2* decay (expressed in ms) as covariates ($r = 0.775$, $P < 0.0001$).

The multiple regression analysis showed that only steatosis grade at histology and histological FF were factors independently associated to the median MRI PDFF (Table 3).

4. Discussion

Liver biopsy with histological visualization of hepatocellular fat vacuoles remains the reference method in order to determine the grade of steatosis in chronic liver diseases, but it is an invasive procedure, which can study only a small portion of the liver (i.e., 1/50,000 of the total volume) [4, 30]. Discomfort and bleeding are well-known procedure-related complications. In addition to sampling errors, routine histological examination is semiquantitative and observer-dependent, and grading is performed with broad severity brackets [37]. Therefore, a noninvasive and objective assessment on a continuous scale may be preferable to biopsy in both clinical practice and research. Different noninvasive imaging methods, including US, CT, and MRI, have been employed to provide an estimate of liver steatosis. It causes reduced liver attenuation at CT, resulting in low hepatic density compared to spleen during precontrast and portal venous phase imaging [5]. Despite the development of quantitative methods of image analysis to assess the severity of hepatic steatosis with CT [5], the clinical implementation of this imaging modality is hampered by exposure to ionizing

radiation, which limits its application for repeated measurements in monitoring disease progression [9, 15]. Using B-mode US imaging, an indirect estimate of hepatic steatosis is obtained by comparing the echogenicity of the liver parenchyma with that of the cortex of the right kidney. This comparison may be performed in either semiquantitative (i.e., normal liver echotexture, minimal, mild, moderate, and severe hyperechogenicity [5]) or quantitative modality (i.e., hepatorenal index [38]). Hepatorenal index calculation has been presented as an effective tool for differentiating patients with steatosis from those without steatosis [38], showing a strong correlation with the histological FF ($r = 0.71$, $P < 0.0001$). However, it has to be kept in mind that a high echogenicity of the liver parenchyma is not synonymous of steatosis. In fact, this appearance of the liver at B-mode US may also be related to the presence of parenchymal fibrosis and liver iron overload, leading to overestimation of the true steatosis grade or misdiagnosis.

MRI-based techniques have been widely employed to determine the presence and grade the severity of hepatic steatosis, and MRS is regarded as the most accurate noninvasive method for assessing this condition [11–14]. In fact, FF calculated from spectroscopy-determined proton densities has shown a strong direct correlation with the intracellular triglyceride content [14, 15]. However, this expensive and time-consuming technique is not widely available and is mainly limited to research settings. Advanced multiecho and multiinterference MRI techniques allow measurement of

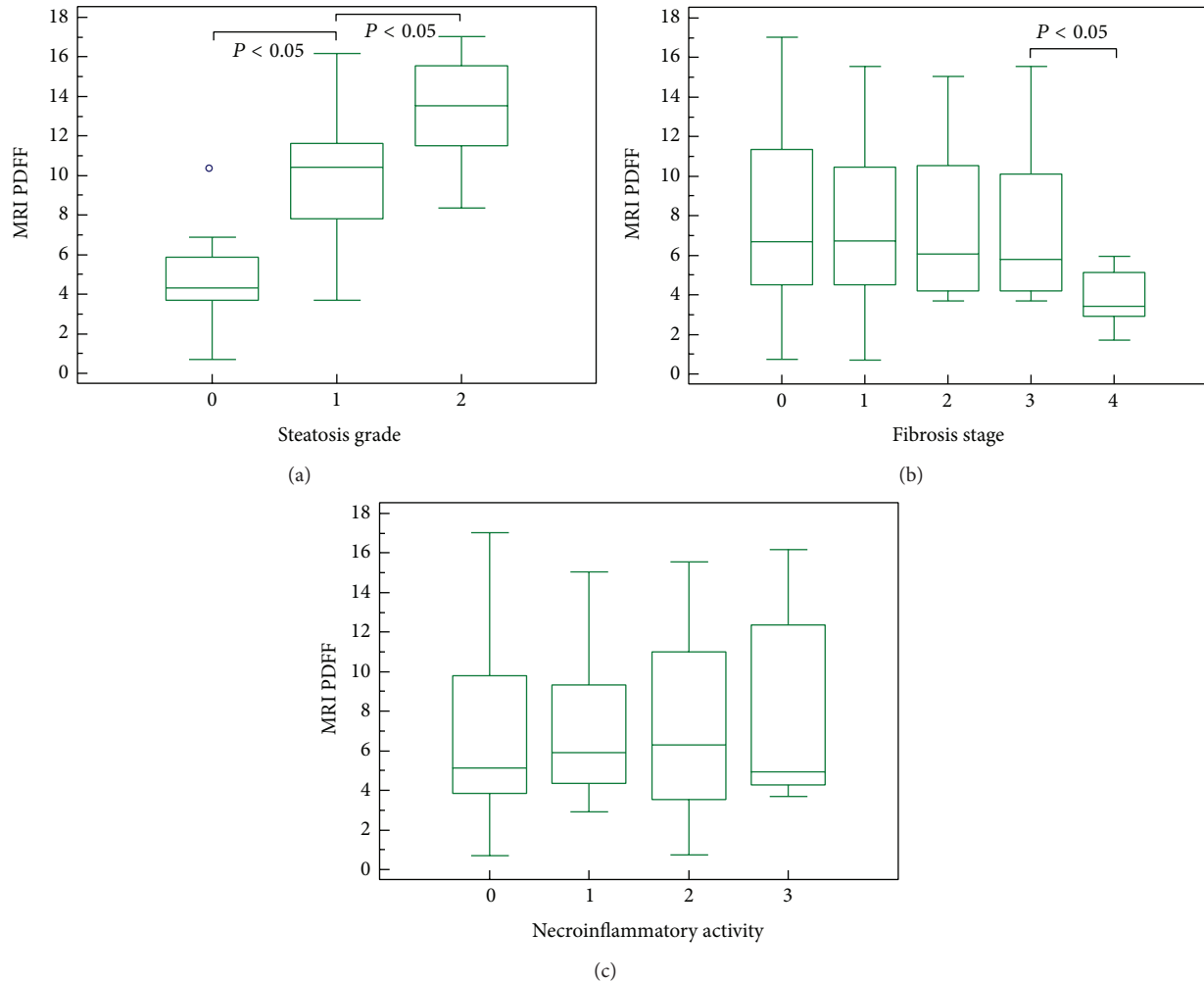


FIGURE 4: Box-and-whisker plots for MRI PDFF measurements in relation to each grade of steatosis (a), fibrosis (b), and necroinflammatory activity (c). The top and the bottom of the boxes are the first and third quartiles, respectively. The length of the box represents the interquartile range including 50% of the values. The line through the middle of each box represents the median. The error shows the minimum and maximum values (range). An outside value (separate point) is defined as a value that is smaller than the lower quartile minus 1.5 times the interquartile range or larger than the upper quartile plus 1.5 times the interquartile range.

PDFFs that are corrected for confounding factors, including B0 inhomogeneity, T1 bias, T2* decay, and multifrequency signal interference effects caused by protons in fat [10–13, 17–19]. The most recent studies are giving encouraging results on clinical grounds, demonstrating a strong correlation between MRI PDFF and hepatic steatosis grade determined by histological validation, and proposing MRI PDFF as a valid noninvasive biomarker for assessing liver fat content [21, 23]. Idilman et al. have recently shown that sequential MRI PDFF quantification may also be employed for monitoring the longitudinal changes of the liver fat content in NAFLD patients [23]. In our work, we performed the quantification of MRI PDFF by means of a comprehensive model derived from that proposed by Bydder et al. [19], incorporating correction for T1- and T2* relaxation effects, B0 inhomogeneity, and spectral complexity of fat. This method of analysis has never been employed in a homogeneous cohort of patients with chronic C hepatitis. The prevalence of steatosis in chronic C

hepatitis is about 40%, which represents an approximately 2-fold increase compared to the prevalence of steatosis in chronic B hepatitis (i.e., 20%) [1]. In fact, HCV infection is considered to be directly involved in the accumulation of triglycerides in hepatocytes (the so-called “viral” steatosis) [39]. According to the literature, we found in our cohort of patients a prevalence of steatosis of 40.26%. In HCV-related steatosis, the percentage of fat-containing hepatocytes is usually mild to moderate (i.e., 10–20%) [34], as it was observed in our study, with a median histological FF in patients with relevant steatosis ($S \geq 1$) of 15%. In addition, we observed a lack of patients with grade 3 steatosis (i.e., >66% of fat-containing hepatocytes). The severity of steatosis seems to correlate with the level of HCV replication (i.e., HCV RNA levels in serum) [3], and it significantly reduces or disappears when patients are successfully treated with antivirals [40]. Interestingly, and according to our results, as the liver disease progresses to cirrhosis (i.e., F4 METAVIR

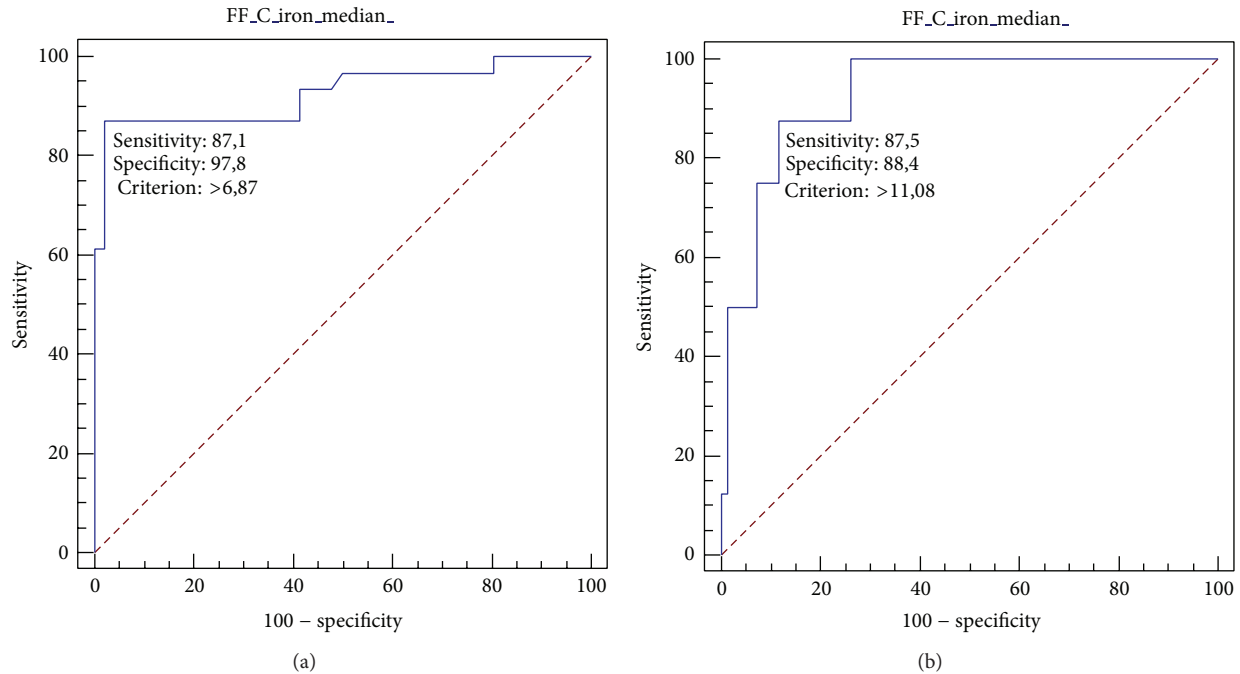


FIGURE 5: ROC curve analysis of MRI PDFF for patients with steatosis $S \geq 1$ (S_0 versus S_1 - S_2). The area under the ROC curve is 0.926 (95% CI 0.74–0.94) (a). ROC curve analysis of MRI PDFF for patients with steatosis $S = 2$ (S_0 - S_1 versus S_2). The area under the ROC curve is 0.929 (95% CI 0.806 to 0.968) (b).

stage of fibrosis), there is a trend of reduction of parenchymal steatosis [41], a phenomenon already observed in NAFLD [42]. Some longitudinal studies underscored the role of steatosis in fibrosis progression. In a recent study on paired liver biopsies performed in 135 untreated patients with chronic C hepatitis [43], steatosis was the only independent factor predictive of fibrosis progression. The progression of fibrosis was significantly related to the percentage of hepatocytes with steatosis [43]. Given the clinical importance of steatosis detection and grading in chronic viral C hepatitis, we aimed to assess the clinical value of MRI PDFF as a noninvasive biomarker of fatty liver, finding a significant, strong correlation of the MRI PDFF with the histological FF. According to the results of Tang et al. [10], we noticed that MRI PDFF values are lower than histological figures, and MRI PDFF cutoff values to distinguish between different steatosis grades are not comparable with the histological ones. This is not surprising, since histologic examination assesses the percentage of fat-containing cells in the biopsy specimens and does not measure the volumetric fat content in a wide portion of liver parenchyma. With MRI PDFF, the proportion of mobile protons contained within fat molecules of three-dimensional liver voxels is quantified [8, 10, 12]. Therefore, MRI PDFF and histological FF assess different aspects of steatosis.

Our study has some limitations. As mentioned above, the lack of patients with a grade 3 steatosis may be considered an intrinsic limitation when examining a cohort of patients affected by chronic viral C hepatitis. Therefore, we were not able to assess the diagnostic performance of PDFF for discriminating between S_0 - S_2 and S_3 patients. In addition, we

did not find cases of clinically significant MRI-detectable iron overload (i.e., MRI T_2^* values < 6.3 ms [29]), and the presence of hemosiderin deposits was appreciable in only few cases. This may be due to the low number of cirrhotic patients in our cohort; in fact, it is known that histologically detectable iron is more frequently associated with advanced parenchymal fibrosis and cirrhosis [44]. Therefore, we were not able to reliably assess the influence of hepatic iron accumulation on the MRI PDFF measurements. Nevertheless, we decided to introduce T_2^* decay as a confounding covariate in the partial correlation model, finding that its influence on the correlation between MRI PDFF and histological FF was not significant. A point of strength of our study is that we kept a reasonably low time-interval between MRI, liver biopsy, and TE (< 10 days), thus avoiding any meaningful change in the hepatic fat content during the biopsy-MRI imaging interim. In addition, we performed a double check of the influence of parenchymal fibrosis on MRI PDFF measurements, introducing TE values of liver stiffness in the partial correlation model and both TE values and METAVIR stage of fibrosis in the multiple linear regression analysis.

5. Conclusions

MRI PDFF is a promising technique for the noninvasive assessment of liver steatosis in patients with chronic viral C hepatitis. In particular, MRI PDFF has shown a strong correlation with the histological FF, and this correlation seems to be influenced by neither the stage of parenchymal fibrosis nor the necroinflammatory activity. In addition, MRI PDFF allows discrimination between different histological

grades of steatosis with good diagnostic accuracy. Further studies on larger cohort of patients involving adequate control groups are needed to get a complete clinical validation of this technique in patients with chronic viral C hepatitis.

Conflict of Interests

The authors declare that there is no conflict of interests regarding the publication of this paper.

Acknowledgments

This study was supported by a grant from Fondazione Carige.

References

- [1] F. Negro, "Mechanisms and significance of liver steatosis in hepatitis C virus infection," *World Journal of Gastroenterology*, vol. 12, no. 42, pp. 6756–6765, 2006.
- [2] T. Asselah, L. Rubbia-Brandt, P. Marcellin, and F. Negro, "Steatosis in chronic hepatitis C: why does it really matter?" *Gut*, vol. 55, no. 1, pp. 123–130, 2006.
- [3] L. E. Adinolfi, M. Gambardella, A. Andreana, M.-F. Tripodi, R. Utili, and G. Ruggiero, "Steatosis accelerates the progression of liver damage of chronic hepatitis C patients and correlates with specific HCV genotype and visceral obesity," *Hepatology*, vol. 33, no. 6, pp. 1358–1364, 2001.
- [4] L. Fernández-Salazar, B. Velayos, R. Aller, F. Lozano, J. A. Garrote, and J. M. González, "Percutaneous liver biopsy: patients' point of view," *Scandinavian Journal of Gastroenterology*, vol. 46, no. 6, pp. 727–731, 2011.
- [5] A. Qayyum, D. M. Chen, R. S. Breiman et al., "Evaluation of diffuse liver steatosis by ultrasound, computed tomography, and magnetic resonance imaging: which modality is best?" *Clinical Imaging*, vol. 33, no. 2, pp. 110–115, 2009.
- [6] S. B. Reeder, I. Cruite, G. Hamilton, and C. B. Sirlin, "Quantitative assessment of liver fat with magnetic resonance imaging and spectroscopy," *Journal of Magnetic Resonance Imaging*, vol. 34, no. 4, p. spcone, 2011.
- [7] C. H. Wu, M. C. Ho, Y. M. Jeng et al., "Quantification of hepatic steatosis: a comparison of the accuracy among multiple magnetic resonance techniques," *Journal of Gastroenterology and Hepatology*, vol. 29, no. 4, pp. 807–813, 2014.
- [8] B. K. Kang, E. S. Yu, S. S. Lee et al., "Hepatic fat quantification: a prospective comparison of magnetic resonance spectroscopy and analysis methods for chemical-shift gradient echo magnetic resonance imaging with histologic assessment as the reference standard," *Investigative Radiology*, vol. 47, no. 6, pp. 368–375, 2012.
- [9] A. E. Bohte, J. R. van Werven, S. Bipat, and J. Stoker, "The diagnostic accuracy of US, CT, MRI and 1H-MRS for the evaluation of hepatic steatosis compared with liver biopsy: a meta-analysis," *European Radiology*, vol. 21, no. 1, pp. 87–97, 2011.
- [10] A. Tang, J. Tan, M. Sun et al., "Nonalcoholic fatty liver disease: MR imaging of liver proton density fat fraction to assess hepatic steatosis," *Radiology*, vol. 267, no. 2, pp. 422–431, 2013.
- [11] T. Yokoo, M. Bydder, G. Hamilton et al., "Nonalcoholic fatty liver disease: diagnostic and fat-grading accuracy of low-flip-angle multiecho gradient-recalled-echo MR imaging at 1.5 T," *Radiology*, vol. 251, no. 1, pp. 67–76, 2009.
- [12] S. Meisamy, C. D. Hines, G. Hamilton et al., "Quantification of hepatic steatosis with T1-independent, T2-corrected MR imaging with spectral modeling of fat: blinded comparison with MR spectroscopy," *Radiology*, vol. 258, no. 3, pp. 767–775, 2011.
- [13] B. Guiu, J.-M. Petit, R. Loffroy et al., "Quantification of liver fat content: comparison of triple-echo chemical shift gradient-echo imaging and in vivo proton MR spectroscopy," *Radiology*, vol. 250, no. 1, pp. 95–102, 2009.
- [14] S. R. Mehta, E. L. Thomas, J. D. Bell, D. G. Johnston, and S. D. Taylor-Robinson, "Non-invasive means of measuring hepatic fat content," *World Journal of Gastroenterology*, vol. 14, no. 22, pp. 3476–3483, 2008.
- [15] H. I. Awai, K. P. Newton, C. B. Sirlin, C. Behling, and J. B. Schwimmer, "Evidence and recommendations for imaging liver fat in children, based on systematic review," *Clinical Gastroenterology and Hepatology*, vol. 12, no. 5, pp. 765–773, 2014.
- [16] M. A. Fischer, D. Nanz, C. S. Reiner et al., "Diagnostic performance and accuracy of 3-D spoiled gradient-dual-echo mri with water-and fat-signal separation in liver-fat quantification: comparison to liver biopsy," *Investigative Radiology*, vol. 45, no. 8, pp. 465–470, 2010.
- [17] J.-P. Kühn, M. Evert, N. Friedrich et al., "Noninvasive quantification of hepatic fat content using three-echo Dixon magnetic resonance imaging with correction for t_2^* relaxation effects," *Investigative Radiology*, vol. 46, no. 12, pp. 783–789, 2011.
- [18] B. Henninger, C. Kremser, S. Rauch et al., "Evaluation of liver fat in the presence of iron with MRI using T2* correction: a clinical approach," *European Radiology*, vol. 23, no. 6, pp. 1643–1649, 2013.
- [19] M. Bydder, T. Yokoo, G. Hamilton et al., "Relaxation effects in the quantification of fat using gradient echo imaging," *Magnetic Resonance Imaging*, vol. 26, no. 3, pp. 347–359, 2008.
- [20] H. Yu, C. A. McKenzie, A. Shimakawa et al., "Multiecho reconstruction for simultaneous water-fat decomposition and T2* estimation," *Journal of Magnetic Resonance Imaging*, vol. 26, no. 4, pp. 1153–1161, 2007.
- [21] I. S. Idilman, H. Aniktar, R. Idilman et al., "Hepatic steatosis: quantification by proton density fat fraction with MR imaging versus liver biopsy," *Radiology*, vol. 267, no. 3, pp. 767–775, 2013.
- [22] H. Yu, A. Shimakawa, C. A. McKenzie, E. Brodsky, J. H. Brittain, and S. B. Reeder, "Multiecho water-fat separation and simultaneous R_2^* estimation with multifrequency fat spectrum modeling," *Magnetic Resonance in Medicine*, vol. 60, no. 5, pp. 1122–1134, 2008.
- [23] I. S. Idilman, O. Keskin, A. H. Elhan, R. Idilman, and M. Karcaaltincaba, "Impact of sequential proton density fat fraction for quantification of hepatic steatosis in nonalcoholic fatty liver disease," *Scandinavian Journal of Gastroenterology*, vol. 49, no. 5, pp. 617–624, 2014.
- [24] A. Ghotb, S. M. Noworolski, E. Madden et al., "Adipose tissue and metabolic factors associated with steatosis in HIV/HCV coinfection: histology versus magnetic resonance spectroscopy," *Journal of Acquired Immune Deficiency Syndromes*, vol. 55, no. 2, pp. 228–231, 2010.
- [25] D. G. Mitchell, V. J. Navarro, S. K. Herrine et al., "Compensated hepatitis C: unenhanced MR imaging correlated with pathologic grading and staging," *Abdominal Imaging*, vol. 33, no. 1, pp. 58–64, 2008.
- [26] A. Orlacchio, F. Bolacchi, M. Cadioli et al., "Evaluation of the severity of chronic hepatitis C with 3-TIH-MR spectroscopy," *The American Journal of Roentgenology*, vol. 190, no. 5, pp. 1331–1339, 2008.

- [27] M. Dewey, T. Schink, and C. F. Dewey, "Frequency of referral of patients with safety-related contraindications to magnetic resonance imaging," *European Journal of Radiology*, vol. 63, no. 1, pp. 124–127, 2007.
- [28] P. Thampanitchawong and T. Piratvisuth, "Liver biopsy: complications and risk factors," *World Journal of Gastroenterology*, vol. 5, no. 4, pp. 301–304, 1999.
- [29] E. Angelucci, A. Giovagnoni, G. Valeri et al., "Limitations of magnetic resonance imaging in measurement of hepatic iron," *Blood*, vol. 90, no. 12, pp. 4736–4742, 1997.
- [30] F. Paparo, L. Cevasco, D. Zefiro et al., "Diagnostic value of real-time elastography in the assessment of hepatic fibrosis in patients with liver iron overload," *European Journal of Radiology*, vol. 82, no. 12, pp. e755–e761, 2013.
- [31] L. Sandrin, B. Fourquet, J. M. Hasquenoph et al., "Transient elastography: a new noninvasive method for assessment of hepatic fibrosis," *Ultrasound in Medicine and Biology*, vol. 29, no. 12, pp. 1705–1713, 2003.
- [32] M. Ziol, A. Handra-Luca, A. Kettaneh et al., "Noninvasive assessment of liver fibrosis by measurement of stiffness in patients with chronic hepatitis C," *Hepatology*, vol. 41, no. 1, pp. 48–54, 2005.
- [33] P. Bedossa and T. Poynard, "An algorithm for the grading of activity in chronic hepatitis C," *Hepatology*, vol. 24, no. 2, pp. 289–293, 1996.
- [34] N. D. Theise, "Liver biopsy assessment in chronic viral hepatitis: a personal, practical approach," *Modern Pathology*, vol. 20, supplement 1, pp. S3–S14, 2007.
- [35] D. E. Kleiner, E. M. Brunt, M. Van Natta et al., "Design and validation of a histological scoring system for nonalcoholic fatty liver disease," *Hepatology*, vol. 41, no. 6, pp. 1313–1321, 2005.
- [36] R. Bülow, B. Mensel, P. Meffert, D. Hernando, M. Evert, and J. P. Kühn, "Diffusion-weighted magnetic resonance imaging for staging liver fibrosis is less reliable in the presence of fat and iron," *European Radiology*, vol. 23, no. 5, pp. 1281–1287, 2013.
- [37] P. Bedossa, D. Dargère, and V. Paradis, "Sampling variability of liver fibrosis in chronic hepatitis C," *Hepatology*, vol. 38, no. 6, pp. 1449–1457, 2003.
- [38] R. H. Marshall, M. Eissa, E. I. Bluth, P. M. Gulotta, and N. K. Davis, "Hepatorenal index as an accurate, simple, and effective tool in screening for steatosis," *American Journal of Roentgenology*, vol. 199, no. 5, pp. 997–1002, 2012.
- [39] L. Rubbia-Brandt, R. Quadri, K. Abid et al., "Hepatocyte steatosis is a cytopathic effect of hepatitis C virus genotype 3," *Journal of Hepatology*, vol. 33, no. 1, pp. 106–115, 2000.
- [40] D. Kumar, G. C. Farrell, C. Fung, and J. George, "Hepatitis C virus genotype 3 is cytopathic to hepatocytes: reversal of hepatic steatosis after sustained therapeutic response," *Hepatology*, vol. 36, no. 5, pp. 1266–1272, 2002.
- [41] L. Rubbia-Brandt, P. Fabris, S. Paganin et al., "Steatosis affects chronic hepatitis C progression in a genotype specific way," *Gut*, vol. 53, no. 3, pp. 406–412, 2004.
- [42] M. Abdelmalek, J. Ludwig, and K. D. Lindor, "Two cases from the spectrum of nonalcoholic steatohepatitis," *Journal of Clinical Gastroenterology*, vol. 20, no. 2, pp. 127–130, 1995.
- [43] L. Fartoux, O. Chazouillères, D. Wendum, R. Poupon, and L. Serfaty, "Impact of steatosis on progression of fibrosis in patients with mild hepatitis C," *Hepatology*, vol. 41, no. 1, pp. 82–87, 2005.
- [44] M. Pirisi, C. A. Scott, C. Avellini et al., "Iron deposition and progression of disease in chronic hepatitis C: role of interface hepatitis, portal inflammation, and HFE missense mutations," *American Journal of Clinical Pathology*, vol. 113, no. 4, pp. 546–554, 2000.

Clinical Study

Partial Splenic Embolization with Transarterial Chemoembolization in Patients with Hepatocellular Carcinoma Accompanied by Thrombocytopenia

Yoshihiko Ooka, Tetsuhiro Chiba, Sadahisa Ogasawara, Tenyu Motoyama, Eiichiro Suzuki, Akinobu Tawada, Fumihiko Kanai, and Osamu Yokosuka

Department of Gastroenterology and Nephrology, Graduate School of Medicine, Chiba University, 1-8-1 Inohana, Chuo-ku, Chiba 260-8670, Japan

Correspondence should be addressed to Tetsuhiro Chiba; techiba@faculty.chiba-u.jp

Received 2 July 2014; Revised 31 August 2014; Accepted 2 September 2014; Published 15 September 2014

Academic Editor: Satoru Murata

Copyright © 2014 Yoshihiko Ooka et al. This is an open access article distributed under the Creative Commons Attribution License, which permits unrestricted use, distribution, and reproduction in any medium, provided the original work is properly cited.

Background. Thrombocytopenia often makes the introduction of systemic treatment difficult in patients with cirrhosis and hepatocellular carcinoma (HCC). We retrospectively evaluated the long-term effects of partial splenic embolization (PSE) with transarterial chemoembolization (TACE) in patients with HCC patients accompanied by thrombocytopenia. **Patients and Methods.** Twenty-one patients with HCC complicated by severe thrombocytopenia (platelet count, $<5.0 \times 10^4/\text{mm}^3$) were treated with PSE and TACE. Both the safety and platelet-increasing effect was evaluated in these patients. **Results.** Seventeen of 21 patients (81.0%) showed increased platelet counts to $\geq 5.0 \times 10^4/\text{mm}^3$. Subsequently, 13 patients (61.9%) successfully received systemic chemotherapy. Platelet counts and serum levels of total bilirubin, as well as neutrophil counts, improved significantly one month after treatment. However, serum levels of albumin and hemoglobin decreased significantly one month after treatment. Severe adverse events, including acute liver failure and portal vein thrombus, were observed in two patients. **Conclusion.** PSE with selective TACE made it possible for patients with HCC and severe thrombocytopenia to receive systemic chemotherapy. Although PSE with TACE was safe and tolerable for most patients, the extent of PSE with TACE in a wide area of the liver may increase the risk for fatal liver failure.

1. Introduction

Hepatocellular carcinoma (HCC) frequently develops in patients with cirrhosis. A considerable number of patients with HCC have thrombocytopenia secondary to hypersplenism. Since cirrhotic patients with severe thrombocytopenia are at greater risk for bleeding, treatments against HCC such as liver transplantation, resection, local ablation therapy, and transarterial chemoembolization (TACE) can be performed following a platelet transfusion in those patients. Therefore, there have been minimal differences in treatment strategy between patients with or without severe thrombocytopenia.

Sorafenib has shown survival benefit in patients with advanced HCC patients [1, 2]. However, sorafenib has several

side effects such as decreased platelet counts and bleeding. Therefore, patients with severe thrombocytopenia are difficult to treat with sorafenib, and their treatment options are limited; they can only receive repetitive TACE or the best supportive treatment. These findings indicate that a new strategy to treat patients with advanced HCC and severe thrombocytopenia is needed.

Over the past 20 years, partial splenic embolization (PSE) has been an interventional radiological treatment for thrombocytopenia due to hypersplenism [3, 4]. This procedure usually results in an increase of platelet count. Recent reports show that PSE has a platelet-increasing effect and allows for the introduction of interferon therapy or systemic chemotherapy [5–8]. Therefore, we considered that PSE and TACE should be performed simultaneously to allow

the introduction of systemic chemotherapy. The aim of this study was to assess the safety and effectiveness of PSE with TACE for patients with HCC and severe thrombocytopenia.

2. Patients and Methods

2.1. Patients. Medical records were retrieved for patients with HCC who were treated by PSE with TACE from November 2010 to October 2012 at Chiba University Hospital. Patients were included if they met the following criteria: (i) no indication for surgical resection or locoregional therapy, (ii) severe thrombocytopenia (platelet count, $<5.0 \times 10^4/\text{mm}^3$), (iii) Child-Pugh A or B, (iv) Eastern Cooperative Oncology Group (ECOG) performance status 0 or 1, and (v) follow-up dynamic computed tomography (CT) 1 week after PSE with TACE. This study was approved by the Research Ethics Committee of Graduate School of Medicine, Chiba University.

2.2. PSE and TACE Procedure. All patients received sedative premedication with intravenous pentazocine and hydroxyzine. The procedure was performed under the local anesthesia using 1% xylocaine. A femoral artery approach was used for catheterization. Patients underwent baseline angiography of the celiac trunk, superior mesenteric artery, hepatic artery, and splenic artery using a peripheral arterial approach. First, we performed PSE according to Takatsuka method [9]. We placed a 4-Fr catheter into the splenic artery as near the splenic hilum as possible. A 2.2-, 2.4-, or 2.7-Fr microcatheter was coaxially advanced as distally as possible into a branch of the intrasplenic artery. We left the microcoils straight in the branch of the splenic artery. About 5-mm sized gelatin sponges were implanted proximal to the microcoils. Lower branches of the splenic artery were embolized using 0.035 inch coils (Tornado or Nester; Cook Inc., Bloomington, IN, USA). The length of coils was determined by that of the targeted arteries. It has been recommended that the final embolization rate of spleen is about 70% [9]. However, giving priority to the safety of patients, this procedure was repeated until a splenic infarction of about 40% to 60% was achieved, as shown on digital subtraction angiography. After PSE procedure was completed, we performed the TACE. Highly selective catheterization was performed with a microcatheter to obtain complete obstruction of the nourishing arteries and avoid damage to nontumor tissue. Cisplatin or epirubicin was emulsified with lipiodol and miriplatin was suspended with lipiodol. These were administered before embolization. Additional Gelpart (Nippon Kayaku Co., Ltd., Tokyo, Japan) was used to complete the embolization procedure. Lipiodol CT was performed at the end of the procedure to confirm the embolized area in the liver. Methylprednisolone (125 mg intravenously for 1–3 days) and naproxen (400 mg per oral for 1 week) were given to relieve postembolic syndrome. Antibiotic prophylaxis was given for 1 week to avoid infectious complications.

2.3. Follow-Up. Dynamic CT was performed in all patients 1 week after the procedure to confirm the area of splenic infarction. When a patient with extrahepatic progression

successfully showed an increase in platelet counts ($\geq 5.0 \times 10^4/\text{mm}^3$) 1 month after PSE with TACE, systemic chemotherapy was started. Follow-up dynamic CT was performed every 2–3 months. In patients without extrahepatic progression, dynamic CT was performed every 3–4 months after PSE with TACE to evaluate the therapeutic effect of TACE. When patients showed status that met the criteria proposed by the 2010 Japan Society of Hepatology Consensus Guidelines for TACE-refractoriness [10] and an increase in platelet counts ($\geq 5.0 \times 10^4/\text{mm}^3$), systemic chemotherapy was started. In patients with HCC controlled by TACE, re-TACE with PSE was performed when HCC progressed. In patients with platelet counts sustained $<5.0 \times 10^4/\text{mm}^3$, re-TACE with PSE was performed until it could not be continued.

2.4. Calculation of Splenic Volume and Noninfarcted Splenic Volume. Splenic and noninfarcted splenic volumes in each patient were calculated using a three-dimensional workstation (Zio Station, Zio Software Inc., Tokyo, Japan). We used volume data from a portal phase multidetector row CT scan taken before and 1 week after the procedure. We performed the masking manually so that only the enhanced spleen remained on the workstation. Masking volume was calculated automatically by the workstation and we made it noninfarcted splenic volume.

2.5. Assessment of Adverse Events. We calculate the rate of adverse events in total of 32 PSE with TACE procedures in 21 patients to evaluate safety. Adverse events were evaluated according to the National Cancer institute Common Terminology Criteria for Adverse Events (CTCAE) ver. 4.0 (URL: http://ctep.cancer.gov/protocolDevelopment/electronic_applications/ctc.htm#ctc_40).

2.6. Statistical Analysis. The change of neutrocyte counts, platelet counts, hemoglobin, albumin, prothrombin time-international normalized ratio (PT-INR), total bilirubin, and Child-Pugh score after PSE with TACE was evaluated before and after PSE with TACE. The paired *t*-test with a two-tailed test was used to compare between the data before and after PSE with TACE. All statistical analyses were performed using SPSS software (IBM SPSS Statistics 18; SPSS Japan).

3. Results

3.1. Patient Characteristics and Outcomes. Twenty-one patients (20 males and one female; mean age, 63.0 ± 9.1) with HCC and severe thrombocytopenia received PSE with TACE. Table 1 shows the characteristics of the 21 patients. The causes of chronic liver damage were hepatitis C virus (HCV) ($n = 14$), hepatitis B virus (HBV) ($n = 3$), and non-HBV and non-HCV ($n = 4$). Seventeen patients were in Barcelona Clinic Liver Cancer- (BCLC-) B stage and four patients were in BCLC-C stage. Mean splenic volume before PSE was 630.5 ± 239.0 mL. The mean platelet count before treatment was $4.2 \pm 0.7 \times 10^4/\text{mL}$. Seventeen patients showed an increase in platelet counts $\geq 5.0 \times 10^4/\text{mm}^3$ after PSE with TACE for 1 month, although the platelet counts in

TABLE 1: Patient data.

Number	Age	Gender	Etiology	BCLC	C-P score	Splenic volume (mL)	Extent of necrosis (%)	Platelet count ($\times 10^4/\text{mm}^3$)		Hospital time (days)	Introduction of SC
								Before	After 1 month		
1	48	M	HCV	B	5	578.4	45.3	4.8	11.7	11	Success
2	60	M	HCV	B	5	990.5	38.9	3.9	6.0	10	Success
3 ^a	64	M	NBNC	B	7	1116.6	39.1	3.9	5.6	11	Failure
4	57	M	HCV	B	5	528.3	40.6	2.7	4.3	13	Failure
5 ^b	65	M	HCV	B	7	426.3	36.3	2.4	ND	12	Failure
6	48	M	HBV	C	6	948.1	68.5	4.8	17.5	20	Success
7	63	M	HCV	B	6	656.7	72.5	4.6	15.1	15	Success
8	78	F	HCV	C	5	727.0	42.7	3.7	6.0	9	Success
9	55	M	HCV	B	5	401.3	19.5	4.9	7.2	12	Success
10	82	M	NBNC	B	8	472.4	40.2	4.8	8.7	9	NA
11	55	M	HBV	B	7	896.8	21.0	4.1	6.1	8	NA
12 ^c	66	M	HCV	B	7	815.9	30.2	4.5	4.6	12	NA
13	54	M	NBNC	B	5	469.5	23.5	4.6	13.1	11	Success
14	64	M	HBV	B	5	469.5	20.1	4.8	13.7	9	Success
15	64	M	HCV	B	5	997.7	31.1	3.9	9.4	10	Success
16	61	M	HCV	B	6	411.9	47.7	4.6	7.3	9	NA
17	76	M	HCV	B	6	287.7	51.2	4.4	7.9	12	Success
18	53	M	HCV	C	6	270.3	81.6	4.9	15.4	8	Success
19 ^d	65	M	HCV	B	8	785.5	77.0	3.4	ND	17	Failure
20	68	M	NBNC	C	6	491.1	30.1	3.4	8.7	20	Success
21	77	M	HCV	B	6	499.6	36.0	4.8	7.7	10	Success
Mean	63.0 \pm 9.1					630.5 \pm 239.0	42.5 \pm 17.6	4.2 \pm 0.7	9.3 \pm 3.8	11.4 \pm 3.5	

^aComplicated by portal vein thrombosis, ^blost to follow-up, ^cno effect despite two additional PSE, ^dcomplicated by lethal liver failure; BCLC, Barcelona Clinical Liver Center; C-P, Child-Pugh; SC, systemic chemotherapy; HBV, hepatitis B virus; HCV, hepatitis C virus; NBNC, non-HBV and non-HCV; PSE, partial splenic embolization; ND, not determined; NA, not applicable.

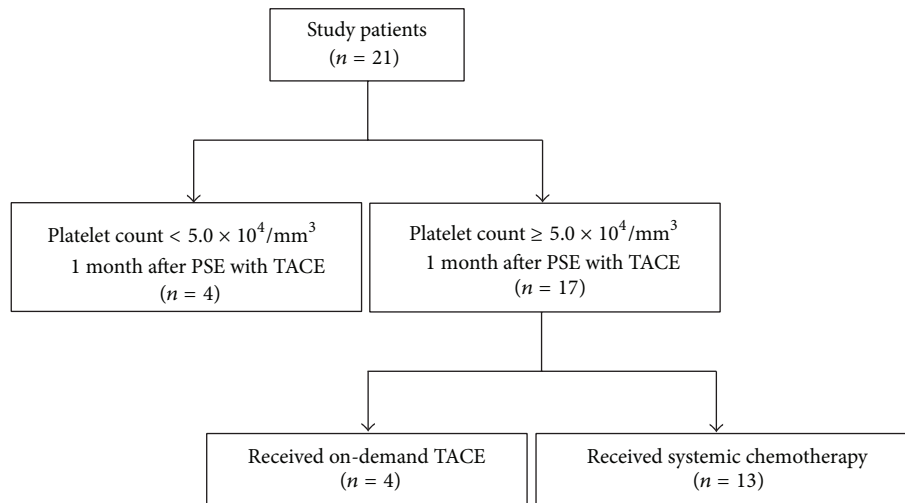


FIGURE 1: Patient outcomes.

four patients remained $<5.0 \times 10^4/\text{mm}^3$ (Figure 1). Among them, one died within 1 month because of liver failure, one showed portal vein thrombosis, one was lost to follow-up, and one exhibited totally no effect despite two additional PSE procedures. Four of 17 patients showed a successful increase in platelet counts and a simultaneous anti-HCC effect by TACE. Thereafter, they received on-demand TACE but not systemic chemotherapy. Eventually, 13 of 21 patients (61.9%) received systemic chemotherapy after first PSE with TACE. Notably, no patients withdrew or decreased the dose of their systemic chemotherapy because of thrombocytopenia. Four patients, who failed first-time systemic chemotherapy, received additional TACE with PSE before second-line systemic chemotherapy. One patient had variceal bleeding and received endoscopic variceal ligation and injection sclerotherapy before PSE and TACE. The 3 patients who experienced variceal bleeding after the procedure had severe liver dysfunction caused by HCC progression or were receiving sorafenib. Therefore, a causal connection between PSE and variceal bleeding was unclear.

3.2. Changes in Laboratory Data. Table 2 shows the changes in the neutrocyte count, platelet count, hemoglobin level, albumin level, PT-INR, total bilirubin level, and Child-Pugh score before treatment, one week later and one month later. The neutrocyte count increased significantly 1 week after treatment ($P = 0.001$). The albumin and hemoglobin levels decreased significantly 1 week after treatment ($P < 0.001$ and $P = 0.012$, resp.). Child-Pugh score deteriorated significantly 1 week after treatment ($P = 0.021$). The platelet count, total bilirubin level, and neutrocyte count improved significantly 1 month after treatment ($P < 0.001$, $P = 0.039$, and $P < 0.001$, resp.). Although the albumin and hemoglobin levels decreased significantly 1 month after treatment ($P = 0.036$ and $P = 0.046$, resp.), they improved compared with those of 1 week after treatment. However, neither PT-INR nor the Child-Pugh score changed significantly between before and after treatment.

3.3. Adverse Events. Major adverse events observed in 32 PSE with TACE procedures (in 21 patients) were shown in Table 3. Thirteen patients underwent the procedure once, 5 underwent the procedure twice, and 3 underwent the procedure thrice. In $>30\%$ procedures, increased levels of aspartate aminotransferase (AST)/alanine aminotransferase (ALT), pain, ascites, and increased level of blood bilirubin were observed. Most of these adverse events improved without treatment or with only conservative treatment. PSE often causes severe complications such as splenic abscess, splenic rupture, pneumonia, refractory ascites, and pleural effusion [11, 12]. Neither splenic rupture nor pneumonia was observed in this study. Although splenic abscess was observed in one patient, he was improved by systemic administration of antibiotics. Although fourteen and 5 patients exhibited ascites and pleural effusion, respectively, these complications were temporary but not refractory.

One patient died because of liver failure. He had multiple HCCs that occupied $>50\%$ of the liver and underwent PSE with TACE in a wide area of the liver. One patient developed portal vein thrombosis. A reevaluation of the dynamic CT images revealed a mural thrombus in the portal vein before treatment. The thrombus resolved following warfarin administration.

4. Discussion

PSE is a useful procedure to improve hypersplenism and portal hypertension and their complications [13–18]. However, there are only a few reports that are available about PSE in patients with HCC [19–21]. In those reports, PSE with TACE was mainly performed to decrease complications of portal hypertension such as variceal bleeding. However, endoscopic therapy is the method most commonly used to prevent variceal bleeding. Considering that PSE has several severe complications [13, 22], the advantage of PSE was relatively small with regard to the treatment of gastroesophageal varices. Systemic chemotherapy using anticancer agents such

TABLE 2: Changes of the laboratory data between before treatment and 1 month after partial splenic embolization with transarterial chemoembolization.

	Pretreatment		After 1 week		After 1 month		
	Data	Data	Mean of difference	P value	Data	Mean of difference	P value
Platelet counts ($\times 10^4/\text{mm}^3$)	4.3 \pm 0.6	5.6 \pm 2.1	0.9 (-0.1 to 2.0)	0.083	9.3 \pm 4.0	4.9 (3.2 to 6.7)	<0.001
Hemoglobin (g/dL)	12.3 \pm 1.8	11.5 \pm 2.0	-0.7 (-1.2 to 0.2)	0.012	11.8 \pm 1.4	-0.5 (-1.0 to -0.0)	0.046
Neutrocyte counts (/mm ³)	1,878 \pm 851	4,269 \pm 2,797	2,241 (1,016 to 3,047)	0.001	2,565 \pm 1,055	687 (408 to 965)	<0.001
Total bilirubin (mg/dL)	1.5 \pm 0.8	1.7 \pm 0.8	0.2 (0.0 to 0.5)	0.063	1.3 \pm 0.6	-0.2 (-0.4 to 0.0)	0.039
Albumin (g/dL)	3.6 \pm 0.2	3.2 \pm 0.4	-0.4 (-0.6 to -0.3)	<0.001	3.5 \pm 0.3	-0.1 (-0.3 to 0.0)	0.036
PT-INR	1.16 \pm 0.14	1.21 \pm 0.21	0.03 (-0.01 to 0.07)	0.123	1.12 \pm 0.14	-0.04 (-0.08 to 0.01)	0.092
Child-Pugh score	5.8 \pm 0.9	6.3 \pm 0.7	0.5 (0.1 to 0.9)	0.021	5.9 \pm 0.7	0.1 (-0.3 to 0.4)	0.748

PT-INR, prothrombin time-international normalized ratio.

TABLE 3: Adverse events.

	n = 32	
	Any grade number (%)	\geq grade 3 number (%)
Increased AST/ALT levels	24 (75)	9 (28)
Pain	19 (59)	0
Increased ALP level	15 (46)	0
Ascites	14 (44)	0
Increased bilirubin level	11 (34)	2 (6)
Anorexia	6 (19)	0
Pleural effusion	5 (16)	0
Fever	4 (13)	0
Decreased leukocyte counts	3 (9)	2 (6)
Increased PT-INR	3 (9)	2 (6)
Hyperkalemia	3 (9)	1 (3)
Hypocalcemia	3 (9)	0
Constipation	3 (9)	0
Increased CPK level	3 (9)	0
Decreased neutrocyte counts	2 (6)	2 (6)
Hyperuricemia	2 (6)	1 (3)
Nausea	2 (6)	0
Diarrhea	2 (6)	0
Hematoma	2 (6)	0
Increased creatinine level	2 (6)	0
Hepatic failure	1 (3)	1 (3)
Portal vein thrombosis	1 (3)	1 (3)
Splenic abscess	1 (3)	0
Splenic rupture	0	0
Pneumonia	0	0

AST, aspartate aminotransferase; ALT, alanine aminotransferase; ALP, alkaline phosphatase; PT-INR, prothrombin time-international normalized ratio; CPK, creatine phosphokinase.

as sorafenib is now available for patients with advanced HCC. However, patients with severe thrombocytopenia, one of the complications of hypersplenism, cannot be treated with systemic chemotherapy because of chemotherapy-induced platelet-decreasing effect. Improving the severe thrombocytopenia enables those patients to receive systemic chemotherapy. No reports have considered the use of PSE to introduce systemic chemotherapy to patients with advanced HCC and severe thrombocytopenia. Thus, we evaluated the efficacy

and safety of PSE for the purpose of introducing systemic chemotherapy to patients with HCC.

Our treatment strategy for patients with HCC and severe thrombocytopenia was simultaneous PSE and TACE. If the first procedure did not achieve the goal, we repeated the procedure when HCC progressed. This strategy has several advantages. First, if PSE does not achieve the purpose in the first session, patients undergo TACE. Second, thrombocytopenia may improve as well as portal hypertension, which prevents other complications. Our results showed that >80% of patients demonstrated an increase in platelet counts after PSE with TACE. In addition, approximately 60% of patients successfully received systemic chemotherapy for HCC. It has been reported that recurrence of thrombocytopenia was observed in some cases treated with PSE [3, 4]. Because more than half of the patients received sorafenib administration within one year after PSE in this study, continuous effect of PSE against thrombocytopenia remains undetermined. However, no patients withdrew or decreased the dose of their systemic chemotherapy because of thrombocytopenia. Taken together, these results indicate that TACE with PSE is an effective method for patients with HCC and severe thrombocytopenia.

Most of adverse events which occurred after PSE with TACE were temporary and controllable. However, severe adverse events including portal vein thrombosis and liver failure occurred in two patients. One patient was complicated with portal vein thrombosis, which was successfully treated with warfarin, and the thrombus resolved gradually. The other patient, who had been treated with PSE and TACE in a wide area in the liver, died because of liver failure. Considering that the extent of splenic infarcted area after PSE was relatively high (77.0%), not only TACE but also PSE may have been involved in liver failure. Previous reports demonstrated that severe complications of PSE often develop when the extent of infarcted area is >70.0% [13, 21, 22]. Therefore, liver failure might develop after PSE even without simultaneous TACE in this case. Taken together, the PSE treatment area should be <70.0% at one session in order to prevent severe complications. This study had several limitations. First, patient population was small. Second, our study had only one arm and we did not compare patients who were treated with only TACE. Further studies are needed to clarify the efficacy of PSE with TACE.

5. Conclusion

In conclusion, PSE for patients with HCC severe thrombocytopenia was useful to increase platelet counts and made it possible to introduce systemic chemotherapy. PSE with selective TACE is tolerable in most cases, but the extent of PSE with TACE in a wide area of the liver may increase the risk for fatal liver failure.

Conflict of Interests

None of the authors has conflict of interests.

References

- [1] J. M. Llovet, S. Ricci, V. Mazzaferro et al., "Sorafenib in advanced hepatocellular carcinoma," *New England Journal of Medicine*, vol. 359, no. 4, pp. 378–390, 2008.
- [2] A.-L. Cheng, Y.-K. Kang, Z. Chen et al., "Efficacy and safety of sorafenib in patients in the Asia-Pacific region with advanced hepatocellular carcinoma: a phase III randomised, double-blind, placebo-controlled trial," *The Lancet Oncology*, vol. 10, no. 1, pp. 25–34, 2009.
- [3] B. Sangro, I. Bilbao, I. Herrero et al., "Partial splenic embolization for the treatment of hypersplenism in cirrhosis," *Hepatology*, vol. 18, no. 2, pp. 309–314, 1993.
- [4] P. Stanley and T. C. Shen, "Partial embolization of the spleen in patients with thalassemia," *Journal of Vascular and Interventional Radiology*, vol. 6, no. 1, pp. 137–142, 1995.
- [5] Y. Miyake, M. Ando, E. Kaji, T. Toyokawa, M. Nakatsu, and M. Hirohata, "Partial splenic embolization prior to combination therapy of interferon and ribavirin in chronic hepatitis C patients with thrombocytopenia," *Hepatology Research*, vol. 38, no. 10, pp. 980–986, 2008.
- [6] C. R. Kauffman, A. Mahvash, S. Kopetz, R. A. Wolff, J. Ensor, and M. J. Wallace, "Partial splenic embolization for cancer patients with thrombocytopenia requiring systemic chemotherapy," *Cancer*, vol. 112, no. 10, pp. 2283–2288, 2008.
- [7] M. Kato, N. Shimohashi, J. Ouchi et al., "Partial splenic embolization facilitates completion of interferon therapy in patients with chronic HCV infection and hypersplenism," *Journal of Gastroenterology*, vol. 40, no. 11, pp. 1076–1077, 2005.
- [8] M. Takahara, Y. Miyake, H. Miyatake et al., "Partial splenic embolization facilitates the adherence to peginterferon in chronic hepatitis C with thrombocytopenia," *Internal Medicine*, vol. 50, no. 22, pp. 2731–2736, 2011.
- [9] H. Shimizu, K. Takatsuka, A. Yoshida, E. Yoshimatsu, K. Matsui, and S. Iwabuchi, "Partial splenic embolization reverses insulin resistance in patients with liver cirrhosis," *Internal Medicine*, vol. 48, no. 10, pp. 747–751, 2009.
- [10] M. Kudo, N. Izumi, N. Kokudo et al., "Management of hepatocellular carcinoma in Japan: consensus-based clinical practice guidelines proposed by the Japan society of hepatology (JSH) 2010 updated version," *Digestive Diseases*, vol. 29, no. 3, pp. 339–364, 2011.
- [11] R. Shah, G. H. Mahour, E. G. Ford, and P. Stanley, "Partial splenic embolization: an effective alternative to splenectomy for hypersplenism," *The American Surgeon*, vol. 56, no. 12, pp. 774–777, 1990.
- [12] K. Zhu, X. Meng, J. Qian et al., "Partial splenic embolization for hypersplenism in cirrhosis: a long-term outcome in 62 patients," *Digestive and Liver Disease*, vol. 41, no. 6, pp. 411–416, 2009.
- [13] G. N'Kontchou, O. Seror, V. Bourcier et al., "Partial splenic embolization in patients with cirrhosis: efficacy, tolerance and long-term outcome in 32 patients," *European Journal of Gastroenterology and Hepatology*, vol. 17, no. 2, pp. 179–184, 2005.
- [14] K. G. Koconis, H. Singh, and G. Soares, "Partial splenic embolization in the treatment of patients with portal hypertension: a review of the english language literature," *Journal of Vascular and Interventional Radiology*, vol. 18, no. 4, pp. 463–481, 2007.
- [15] M. Miyazaki, H. Itoh, T. Kaiho et al., "Partial splenic embolization for the treatment of chronic idiopathic thrombocytopenic purpura," *The American Journal of Roentgenology*, vol. 163, no. 1, pp. 123–126, 1994.
- [16] A. Moreno, R. Bárcena, J. Blázquez et al., "Partial splenic embolization for the treatment of hypersplenism in cirrhotic HIV/HCV patients prior to pegylated interferon and ribavirin," *Antiviral Therapy*, vol. 9, no. 6, pp. 1027–1030, 2004.
- [17] R. Pandey, R. Garg, V. Darlong, J. Punj, and A. Kumar, "Role of splenic artery partial embolization in a patient with portal hypertension and pancytopenia undergoing hysterectomy under anesthesia," *AANA Journal*, vol. 80, no. 2, pp. 96–98, 2012.
- [18] J. J. Gu, X. H. He, W. T. Li et al., "Safety and efficacy of splenic artery coil embolization for hypersplenism in liver cirrhosis," *Acta Radiologica*, vol. 53, no. 8, pp. 862–867, 2012.
- [19] R. Roversi, S. Ricci, P. I. Gambari et al., "Splenic embolization and hepatic chemoembolization: combined transcatheter treatment of hepatocellular carcinoma in cirrhosis with hypersplenism," *La Radiologia Medica*, vol. 85, no. 4, pp. 444–449, 1993.
- [20] M.-J. Han, H.-G. Zhao, K. Ren, D.-C. Zhao, K. Xu, and X.-T. Zhang, "Partial splenic embolization for hypersplenism concomitant with or after arterial embolization of hepatocellular carcinoma in 30 patients," *CardioVascular and Interventional Radiology*, vol. 20, no. 2, pp. 125–127, 1997.
- [21] J.-H. Huang, F. Gao, Y.-K. Gu, W.-Q. Li, and L.-W. Lu, "Combined treatment of hepatocellular carcinoma with partial splenic embolization and transcatheter hepatic arterial chemoembolization," *World Journal of Gastroenterology*, vol. 13, no. 48, pp. 6593–6597, 2007.
- [22] T. Sakai, K. Shiraki, H. Inoue et al., "Complications of partial splenic embolization in cirrhotic patients," *Digestive Diseases and Sciences*, vol. 47, no. 2, pp. 388–391, 2002.

Research Article

Volume Change and Liver Parenchymal Signal Intensity in Gd-EOB-DTPA-Enhanced Magnetic Resonance Imaging after Portal Vein Embolization prior to Hepatectomy

Ayako Akiba,¹ Satoru Murata,¹ Takahiko Mine,¹ Shiro Onozawa,¹ Tetsuro Sekine,¹ Yasuo Amano,¹ Youichi Kawano,² Eiji Uchida,² and Shin-ichiro Kumita¹

¹ Department of Radiology, Center for Advanced Medical Technology, Nippon Medical School, 1-1-5 Sendagi, Bunkyo-ku, Tokyo 113-8602, Japan

² Department of Surgery for Organ Function and Biological Regulation, Nippon Medical School, 1-1-5 Sendagi, Bunkyo-ku, Tokyo 113-8602, Japan

Correspondence should be addressed to Ayako Akiba; anyako@nms.ac.jp

Received 3 July 2014; Accepted 30 August 2014; Published 11 September 2014

Academic Editor: Per Kristian Hol

Copyright © 2014 Ayako Akiba et al. This is an open access article distributed under the Creative Commons Attribution License, which permits unrestricted use, distribution, and reproduction in any medium, provided the original work is properly cited.

Purpose. To investigate the liver volume change and the potential of early evaluation by contrast-enhanced magnetic resonance imaging (MRI) using gadolinium-ethoxybenzyl-diethylenetriamine pentaacetic acid (Gd-EOB-DTPA) after portal vein embolization (PVE). **Materials and Methods.** Retrospective evaluations of computed tomography (CT) volumetry of total liver and nonembolized areas were performed before and 3 weeks after PVE in 37 cases. The percentage of future liver remnant (%FLR) and the change ratio of %FLR (%FLR ratio) were calculated. Prospective evaluation of signal intensities (SIs) was performed to estimate the role of Gd-EOB-DTPA-enhanced MRI as a predictor of hypertrophy in 16 cases. The SI contrast between embolized and nonembolized areas was calculated 1 week after PVE. The change in SI contrast before and after PVE (SI ratio) was also calculated in 11 cases. **Results.** %FLR ratio significantly increased, and SI ratio significantly decreased (both $P < 0.01$). There were significant negative correlations between %FLR and SI contrast and between %FLR and SI ratio (both $P < 0.01$). **Conclusion.** Hypertrophy in the nonembolized area after PVE was indicated by CT volumetry, and measurement of SI contrast and SI ratio in Gd-EOB-DTPA-enhanced MRI early after PVE may be useful to predict the potential for hepatic hypertrophy.

1. Introduction

Portal vein embolization (PVE) of unilateral hepatic lobe prior to extended hepatectomy can result in liver parenchymal ischemia and induce contralateral liver hypertrophy [1–3]. This change is induced by growth factors such as hepatocyte growth factor (HGF), transforming growth factor- α (TGF- α), and epidermal growth factor (EGF) produced by the intestine and carried into the portal vein [4, 5]. They are stimulated after PVE, and hepatocyte growth is promoted as they flow into the nonembolized area preferentially [4–6]. In such cases, it is important to predict the future liver remnant (FLR) volume to perform the surgery safely. However, there is no consensus on early predictive factors based on imaging.

Gadolinium-ethoxybenzyl-diethylenetriamine pentaacetic acid (Gd-EOB-DTPA) has been used in clinical practice as a magnetic resonance (MR) contrast agent. After intravenous injection, Gd-EOB-DTPA is metabolized by 2 routes: receptor-specific uptake in hepatocytes with subsequent biliary excretion and glomerular filtration in the kidney with subsequent urinary excretion. It is eliminated in urine and feces in almost equal amounts (43.1–53.2% and 41.6–51.2%, resp.) [7, 8]. In biliary excretion, Gd-EOB-DTPA is gradually taken up by hepatocytes and eventually excreted via the biliary pathway without any change in its chemical structure [7, 8], and it has also been used for the evaluation of liver function in recent years [7, 9–14]. Based on these considerations, we assumed that change in signal intensity (SI) in Gd-EOB-DTPA-enhanced magnetic

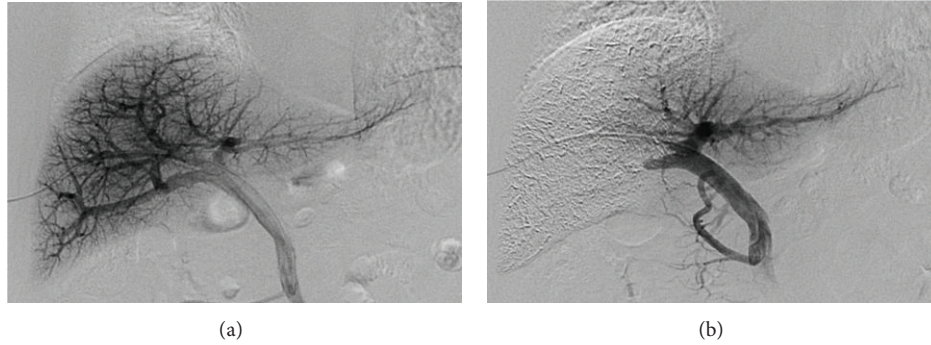


FIGURE 1: PVE procedure. (a) Direct portogram after portal vein branches were punctured via a transhepatic approach under ultrasound guidance. (b) Final portogram showing occlusion of the target portal vein branches and the patency of the veins supplying the nonembolized lobe.

resonance imaging (MRI) could be applied in the assessment of liver parenchymal damage after PVE, and Gd-EOB-DTPA-enhanced MRI could facilitate early predictions based on imaging. The purposes of this study were to investigate the volume change in PVE prior to extended hepatectomy by computed tomography (CT) volumetry and the efficacy of Gd-EOB-DTPA-enhanced MRI early after PVE to predict potential compensated hepatic hypertrophy.

2. Materials and Methods

2.1. Patients. This study was approved by the ethics committee of our hospital. All patients provided written informed consent to receive the iodine contrast agent, Gd-EOB-DTPA, and PVE and to participate in this study. Thirty-seven patients (27 men and 10 women) with a median age of 71 years (range, 57–83) underwent PVE prior to extended hepatectomy between January 2006 and December 2013 (Table 1). Of these, 33 underwent right portal vein embolization, and 4 whose left portal veins were occluded by tumor underwent anterior segmental PVE. The underlying diseases were 18 hilar cholangiocarcinomas, 7 hepatocellular carcinomas, 5 intrahepatic bile duct cancers, 4 gallbladder cancers, 2 metastatic liver cancers, and 1 cystic duct cancer. Twenty-seven patients underwent extended right hepatectomy, and 2 patients underwent extended left hepatectomy. The other 8 patients could not undergo their predetermined operations because of a rapid increase in the size of the tumor or the emergence of lymph node metastases. Although 6 of the 7 patients with hepatocellular carcinoma had liver cirrhosis, all exhibited almost normal liver function (the Child-Pugh score was Grade A). The other 31 patients had normal livers.

All 37 patients underwent CT volumetry prior to PVE and at 21 ± 4.4 days after PVE. Additionally, prospective evaluation of Gd-EOB-DTPA-enhanced MRI was performed in 16 patients (12 men, 4 women; median age, 70.5 years; range, 57–83 years) who underwent PVE between January 2011 and December 2013.

2.2. PVE Technique. All patients underwent PVE under local anesthesia approximately 3 weeks before the scheduled date

TABLE 1: Patient characteristics ($n = 37$).

Parameters	Patients, $n = 37$
Sex (men/women)	27/10
Age (median [range])	71 (57–83)
Underlying disease	
Hilar cholangiocarcinoma	18
Hepatocellular carcinoma	7
Intrahepatic bile duct cancer	5
Gallbladder cancer	4
Metastatic liver cancer	2
Cystic duct cancer	1
Operative procedure	
Extended right hepatectomy	27
Extended left hepatectomy	2
None*	8
Embolized vessel	
Right portal vein	33
Anterior segmental branch	4

*Operation could not be performed owing to rapid increase in tumor size and so forth.

of their surgery. Under ultrasound guidance, portal vein branches were punctured via a transhepatic approach with an 18 G needle (PTC needle, Hakko, Japan), and a size 5- or 6-French sheath (Super Sheath, MEDIKIT, Miyazaki, Japan) was inserted. Direct portography (Figure 1(a)) was achieved via a 4-French cobra catheter (C-MRT, MEDIKIT, Japan). Depending on the anatomy of the portal vein and the therapeutic purpose involved, the origin of the right portal vein or the anterior and/or the posterior branches were occluded with a balloon catheter (Selecon MP catheter II, TERUMO, Japan). A mixture of absolute ethanol and iodized oil (10–20 mL of absolute ethanol (maximum 0.4 mL/kg) mixed with iodized oil at a ratio of 2:1 ethanol:oil) was infused via a sheath or the tip of the balloon catheter. Twenty minutes after injection, embolization of the ipsilateral lobe and patency of the remnant lobe were confirmed (Figure 1(b)).

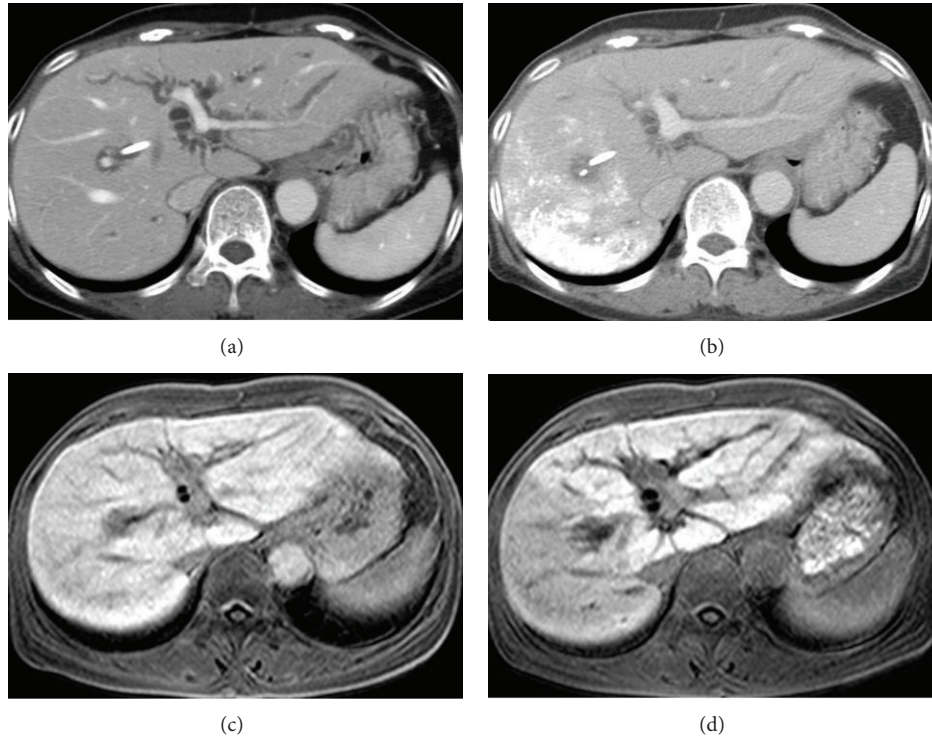


FIGURE 2: CT and MRI findings before and after PVE. (a) Contrast-enhanced CT before PVE showing a homogenous enhancement effect in the whole liver parenchyma. (b) CT 3 weeks after PVE of the right portal vein, showing accumulation of iodized oil mixed with ethanol in the right hepatic lobe and hypertrophy of the left lobe. (c) Gd-EOB-DTPA-enhanced MRI before PVE, also showing a homogenous enhancement effect. (d) Gd-EOB-DTPA-MRI 1 week after PVE of the right portal vein, showing a reduction in SI in the right hepatic lobe.

2.3. Retrospective Evaluation of CT Volumetry. Dynamic enhanced CT was performed in all patients ($n = 37$) before and approximately 3 weeks (21 ± 4.4 days) after PVE by using mainly 64-line multidetector CT (Light Speed VCT, GE Healthcare, USA). The images in the portal phase were utilized for volumetry (Figures 2(a) and 2(b)). The areas of the total liver and the nonembolized portion were measured in each slice of 5 mm in thickness, and then total liver volume (TLV) and FLR were calculated from these data. The ratio of TLV and FLR ($FLR \times 100/TLV$) was defined as the %FLR, and the ratio of %FLR before and after PVE (post-%FLR/pre-%FLR) was defined as the %FLR ratio.

2.4. Prospective Evaluation of Signal Intensity Change in Gd-EOB-DTPA-Enhanced MRI. To estimate the relationship between the degree of SI contrast after PVE and the volume change, Gd-EOB-DTPA-enhanced MRI was performed approximately 1 week after PVE (7.31 ± 1.2 days) in 16 patients. Of these, 11 patients also underwent MRI before PVE. In all cases, a 1.5 T MRI system (Intera, Philips, The Netherlands) was used. The parameters used were 3D GRE, TR 3.36 ms, TE 1.08 ms, and a flip angle of 15° . The images were obtained 15 minutes after the injection of Gd-EOB-DTPA (Figures 2(c) and 2(d)).

Average SIs in liver parenchyma without vessel and bile duct in the embolized and nonembolized areas were measured in 3 slices from each area. The ratio of the average

SIs in the embolized area and the nonembolized area (SI in embolized area/SI in nonembolized area) was defined as SI contrast. Furthermore, the ratio of the SI contrast before and after PVE (post-SI contrast/pre-SI contrast) was defined as the SI ratio.

2.5. Statistical Analysis. All data were analyzed with the Statistical Package for the Social Sciences software (version 20, SPSS, Chicago, IL). The changes in %FLR and SI contrast were analyzed with Student's *t*-test. The correlations between %FLR ratio and both post-SI contrast and SI ratio were analyzed via Spearman's correlation. Differences with a significance value of $P < 0.05$ were considered statistically significant.

3. Results

The PVE procedure was successfully performed in all patients. There were 28 patients with fever of more than 37.5°C , and all fevers subsided within 5 days. Eleven patients required nonsteroidal anti-inflammatory drugs for abdominal pain. None of the patients showed pulmonary complications such as pulmonary hypertension and embolism on clinical examination (less than Grade 1 in Common Terminology Criteria for Adverse Events version 4.0). Other

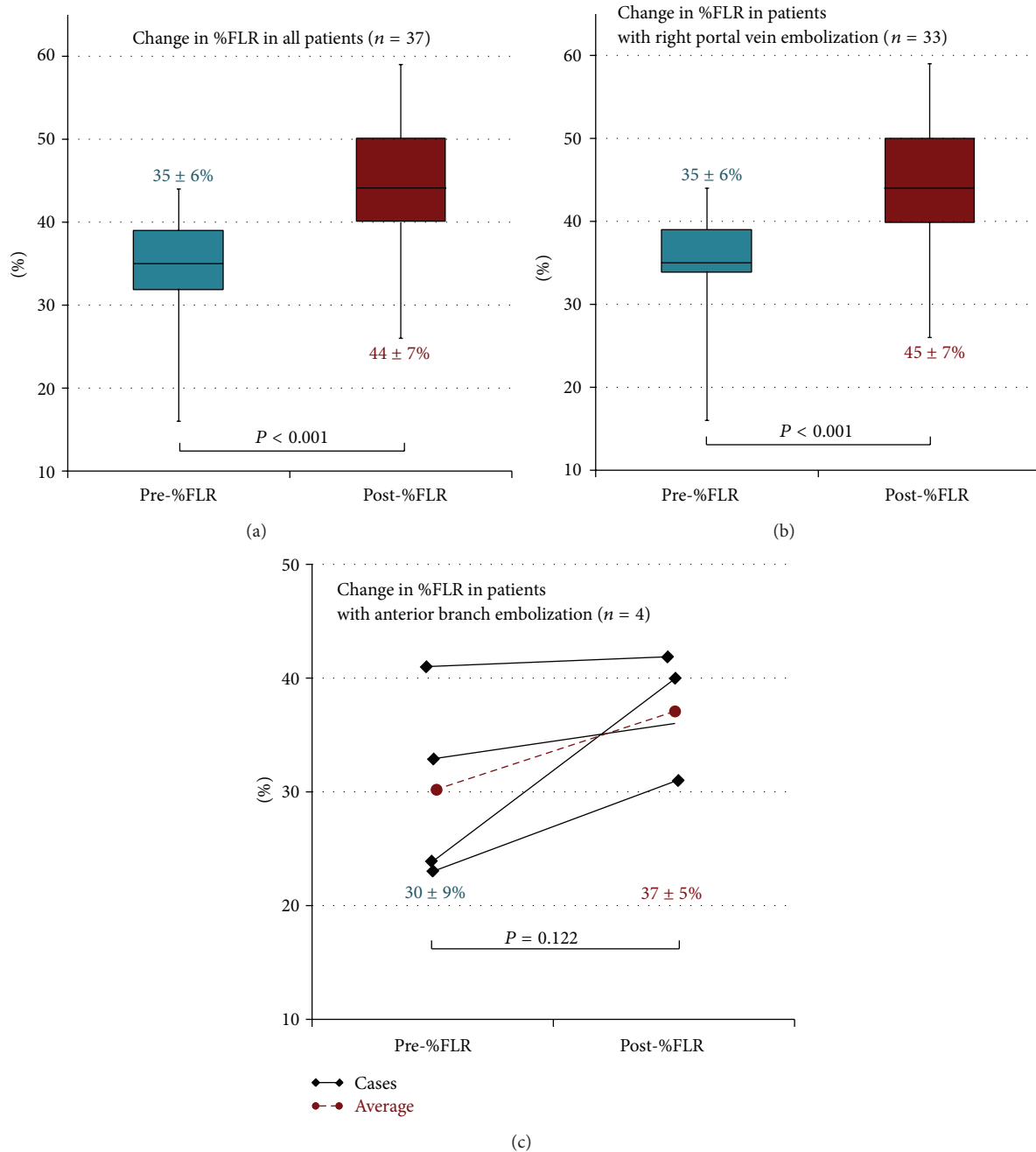


FIGURE 3: Changes in %FLR. (a) %FLR increased significantly after PVE in all 37 cases ($P < 0.001$). (b) In 33 cases in which the right portal vein branch was embolized, %FLR increased significantly after PVE ($P < 0.001$). (c) In 4 cases in which the anterior segmental portal vein was embolized, there was not a statistically significant difference in %FLR before and after PVE ($P = 0.122$).

major complications that could potentially impede the operation did not occur. Twenty-nine patients could undergo the scheduled operation. Although the other 8 patients could not undergo their predetermined operations, this was not due to any adverse effect of PVE but due to acute progression of cancer.

3.1. Changes in %FLR. The mean pre-%FLR and post-%FLR values were $35\% \pm 6\%$ and $44\% \pm 7\%$, respectively. %FLR

increased significantly after PVE ($P < 0.001$, Figure 3(a)). In the patients whose right portal vein branches were embolized, the mean pre-%FLR was $35\% \pm 6\%$ and the mean post-%FLR was $45\% \pm 7\%$. %FLR increased significantly after PVE ($P < 0.001$, Figure 3(b)). In patients whose anterior segmental portal veins were embolized, the mean pre-%FLR was $30\% \pm 9\%$ and the mean post-%FLR was $37\% \pm 5\%$. There was no significant difference in %FLR before and after PVE ($P = 0.122$, Figure 3(c)).

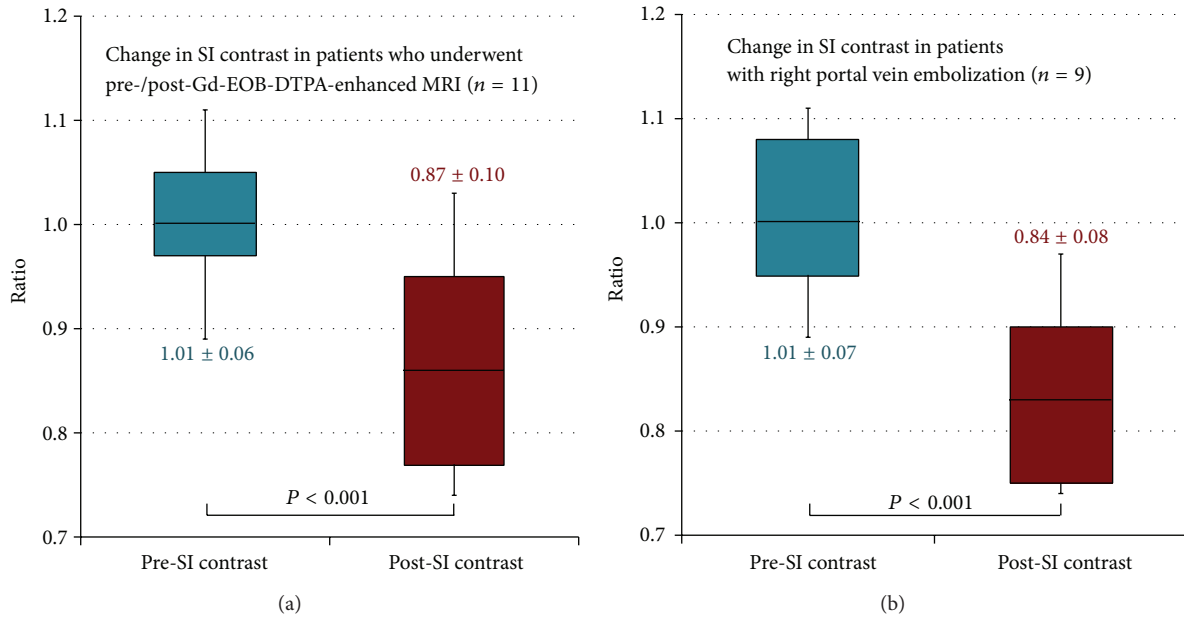


FIGURE 4: Changes in SI contrast. (a) SI contrast decreased significantly after PVE ($P < 0.001$) in 11 patients who underwent Gd-EOB-DTPA-enhanced MRI before and after PVE. (b) In 9 patients whose right portal vein branches were embolized, SI contrast decreased significantly ($P < 0.001$).

3.2. *Pre-SI Contrast and Post-SI Contrast.* The mean pre-SI contrast was 1.01 ± 0.06 , and the mean post-SI contrast was 0.87 ± 0.10 . SI contrast decreased significantly after PVE ($P < 0.001$, Figure 4(a)). In the patients whose right portal vein branches were embolized, the mean pre-SI contrast was 1.01 ± 0.07 and the mean post-SI contrast was 0.84 ± 0.08 . SI contrast decreased significantly ($P < 0.001$, Figure 4(b)). In the cases of anterior segmental portal vein embolization, the mean pre-SI contrast was 1.02 ± 0.00 and the mean post-SI contrast was 1.01 ± 0.04 . There was not a significant difference in SI contrast before and after PVE ($P = 0.66$).

3.3. *%FLR, Post-SI Contrast, and SI Ratio.* There were significant negative correlations between %FLR ratio and post-SI contrast ($P = 0.005$, Figure 5) and between %FLR ratio and SI ratio ($P = 0.001$). In the patients whose right portal vein branches were embolized, the difference in the negative correlation between %FLR ratio and post-SI contrast was not statistically significant ($P = 0.065$). There was a significant negative correlation between %FLR ratio and SI ratio ($P = 0.007$). In the cases of anterior segmental portal vein embolization, the correlations could not be informatively analyzed because the number of cases was not large enough.

4. Discussion

Generally, the degree of hepatocyte proliferation is directly proportional to the degree of stimulation [15]. Surgical resection or trauma can encourage the rapid growth of viable hepatocytes in the remnant liver, and liver function can normalize within 2 weeks, even where the damage extends to

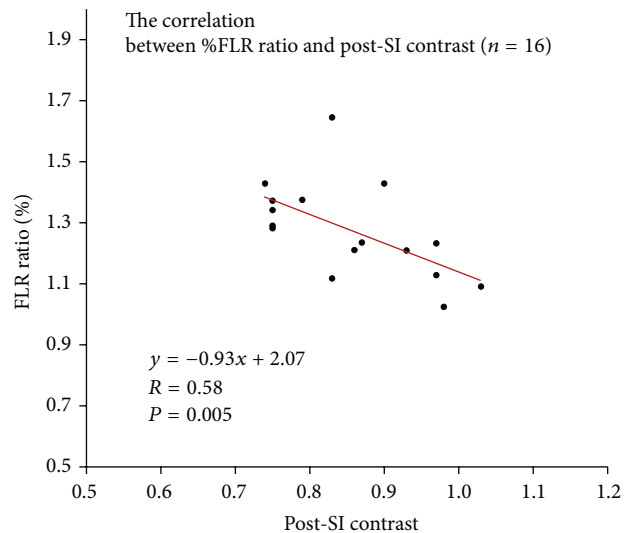


FIGURE 5: The correlations between %FLR ratio and post-SI contrast. There was a significant negative correlation between %FLR ratio and post-SI contrast ($P = 0.005$) in 16 patients who underwent Gd-EOB-DTPA-enhanced MRI after PVE.

up to two-thirds of the liver [16–18]. On the other hand, the peak in the generation of hepatocytes after PVE is delayed 3-4 days in comparison with that after liver resection [6]; apoptosis after PVE is thought to be weaker than that after liver resection. Thus, it takes approximately 2–6 weeks to achieve sufficient hypertrophy of the residual parenchyma [1]. It is important to accurately predict potential compensated hepatic hypertrophy early after PVE to facilitate safe surgery.

To evaluate the damage to hepatocytes after PVE, we prospectively measured the SI change in Gd-EOB-DTPA-enhanced MRI based on the following rationale. The SI of liver parenchyma after injection of Gd-EOB-DTPA depends on its uptake by hepatocytes and biliary excretion [7, 9–14]. Uptake of Gd-EOB-DTPA shortens the T1 relaxation time of the liver [9–14]. It is also known that liver damage compromises the transporter that incorporates Gd-EOB-DTPA [10, 14]. Therefore, insufficiency of hepatocytes impedes the uptake of Gd-EOB-DTPA and decreases SI [10]. In this study, post-SI contrast was significantly reduced in comparison with pre-SI contrast. This suggests that PVE results in inhibition of the incorporation of Gd-EOB-DTPA in embolized areas. Thus, the reduction in SI contrast may reflect the degree of liver damage.

A significant negative correlation between %FLR and SI ratio was observed in this study; lower SI contrast was associated with higher %FLR. Thus, it could be considered that the FLR volume will increase more if the damage to the embolized area and the reduction in uptake of Gd-EOB-DTPA are more severe. On the basis of the principle of hepatocyte regeneration, the uptake of Gd-EOB-DTPA in the nonembolized area might increase. Hence, if the difference in the degree of contrast enhancement by Gd-EOB-DTPA between the embolized and nonembolized areas is greater, the FLR volume may be predicted to increase more. The same result was apparent in the patients whose right portal vein branches were embolized.

On the other hand, in the patients whose anterior segmental portal veins were embolized, %FLR did not increase as in the patients whose right portal vein branches were embolized. Furthermore, the mean SI contrast hardly changed (from 1.02 to 1.01), in contrast to the significant decrease in the mean from 1.01 to 0.84 evident in the cases of right portal vein embolization. We surmise that the reason is as follows. Occlusion of left portal venous branches by tumor invasion or oppression had occurred gradually in the course of tumor progression at the time of PVE. In this process, a gradual influx of the growth factors into the total right lobe had already commenced; hence, the degree of stimulation of hepatocyte generation in the posterior lobe after PVE of the anterior segmental branch only was not sufficient, being less than that of the patients who underwent PVE of the whole right portal vein.

In this study, although the patients whose SI contrast decreased significantly in Gd-EOB-DTPA-enhanced MRI achieved acceptable hypertrophy, the patients whose SI contrast changed only slightly did not achieve sufficient hypertrophy. This suggests that hypertrophy of nonembolized area is less likely to be achieved in cases with negative SI change 1 week after PVE. At that time, switching to another treatment instead of surgery or additional procedures such as arterial embolization can be considered. This decision can be made earlier than in cases followed only by CT performed 3 weeks after PVE. Thus, Gd-EOB-DTPA-enhanced MRI soon after PVE may provide useful information with regard to selecting an adequate therapeutic alternative, even in the patients with rapidly growing tumors.

Our study has 2 main limitations. We utilized the ratio of embolized and nonembolized areas as an indicator of the uptake of Gd-EOB-DTPA, and these data were considered adequate for prediction of the degree of liver volume change after PVE. However, some studies have used absolute values corresponding to T1 relaxation times via the look-locker sequence for the evaluation of liver function [19–21], and we are considering further evaluation using these parameters for the early evaluation of PVE. Second, our sample size was not large, which limited the capacity for analysis of all factors affecting %FLR and SI contrast. Particularly, differences in the parameters of hepatocytes between the right and left hepatic lobes would be more informatively identified with a larger number of patients; we are planning a subsequent study focusing on this aspect.

In conclusion, the tendency for hypertrophy to develop in the nonembolized area after PVE of the right portal branch was indicated by CT volumetry. Moreover, the SI contrast measurement between the embolized and nonembolized areas in Gd-EOB-DTPA-enhanced MRI 1 week after PVE may be a feasible predictor of the potential for hepatic hypertrophy.

Conflict of Interests

The authors declare that there is no conflict of interests regarding the publication of this paper.

References

- [1] N. Akamatsu, Y. Sugawara, and D. Hashimoto, "Surgical strategy for bile duct cancer: advances and current limitations," *World Journal of Clinical Oncology*, vol. 2, pp. 94–107, 2011.
- [2] R. Avritscher, E. Duke, and D. C. Madoff, "Portal vein embolization: rationale, outcomes, controversies and future directions," *Expert Review of Gastroenterology and Hepatology*, vol. 4, no. 4, pp. 489–501, 2010.
- [3] J. H. Shin, H.-K. Yoon, J. Kwon et al., "Volumetric analysis of the liver after right portal vein embolization: mid-term follow-up based on embolization score," *Clinical Radiology*, vol. 65, no. 4, pp. 288–296, 2010.
- [4] E. K. Abdalla, M. E. Hicks, and J. N. Vauthey, "Portal vein embolization: rationale, technique and future prospects," *British Journal of Surgery*, vol. 88, no. 2, pp. 165–175, 2001.
- [5] G. K. Michalopoulos and R. Zarnegar, "Hepatocyte growth factor," *Hepatology*, vol. 15, no. 1, pp. 149–155, 1992.
- [6] K. C. Lee, H. Kinoshita, K. Hirohashi, S. Kubo, and R. Iwasa, "Extension of surgical indications for hepatocellular carcinoma by portal vein embolization," *World Journal of Surgery*, vol. 17, no. 1, pp. 109–115, 1993.
- [7] T. Katsube, M. Okada, S. Kumano et al., "Estimation of liver function using T1 mapping on Gd-EOB-DTPA-enhanced magnetic resonance imaging," *Investigative Radiology*, vol. 46, pp. 277–283, 2011.
- [8] B. Hamm, T. Staks, A. Mühler et al., "Phase I clinical evaluation of Gd-EOB-DTPA as a hepatobiliary MR contrast agent: safety, pharmacokinetics, and MR imaging," *Radiology*, vol. 195, no. 3, pp. 785–792, 1995.
- [9] T. Heye, S.-R. Yang, M. Bock et al., "MR relaxometry of the liver: significant elevation of T1 relaxation time in patients with liver

- cirrhosis," *European Radiology*, vol. 22, no. 6, pp. 1224–1232, 2012.
- [10] N. Tsuda, M. Okada, and T. Murakami, "Potential of gadolinium-ethoxybenzyl-diethylenetriamine pentaacetic acid (Gd-EOB-DTPA) for differential diagnosis of nonalcoholic steatohepatitis and fatty liver in rats using magnetic resonance imaging," *Investigative Radiology*, vol. 42, no. 4, pp. 242–247, 2007.
- [11] S. A. Schmitz, A. Mühler, S. Wagner, and K.-J. Wolf, "Functional hepatobiliary imaging with gadolinium-EOB-DTPA. A comparison of magnetic resonance imaging and ¹⁵³gadolinium-EOB-DTPA scintigraphy in rats," *Investigative Radiology*, vol. 31, no. 3, pp. 154–160, 1996.
- [12] H.-K. Ryeom, S.-H. Kim, J.-Y. Kim et al., "Quantitative evaluation of liver function with MRI using Gd-EOB-DTPA," *Korean Journal of Radiology*, vol. 5, no. 4, pp. 231–239, 2004.
- [13] T. Kim, T. Murakami, Y. Hasuike et al., "Experimental hepatic dysfunction: evaluation by MRI with Gd-EOB-DTPA," *Journal of Magnetic Resonance Imaging*, vol. 7, no. 4, pp. 683–688, 1997.
- [14] U. Motosugi, T. Ichikawa, H. Sou et al., "Liver parenchymal enhancement of hepatocyte-phase images in Gd-EOB-DTPA-enhanced MR imaging: which biological markers of the liver function affect the enhancement?" *Journal of Magnetic Resonance Imaging*, vol. 30, no. 5, pp. 1042–1046, 2009.
- [15] D. M. Black and K. E. Behrns, "A scientist revisits the atrophy-hypertrophy complex: hepatic apoptosis and regeneration," *Surgical Oncology Clinics of North America*, vol. 11, no. 4, pp. 849–864, 2002.
- [16] L. G. Koniaris, I. H. McKillop, S. I. Schwartz, and T. A. Zimmers, "Liver regeneration," *Journal of the American College of Surgeons*, vol. 197, no. 4, pp. 634–659, 2003.
- [17] G. K. Michalopoulos and M. C. DeFrances, "Liver regeneration," *Science*, vol. 276, no. 5309, pp. 60–65, 1997.
- [18] N. L. Bucher and M. N. Swaffield, "The rate of incorporation of labeled thymidine into the deoxyribonucleic acid of regenerating rat liver in relation to the amount of liver excised," *Cancer research*, vol. 24, pp. 1611–1625, 1964.
- [19] C. Thomsen, P. Christoffersen, O. Henriksen, and E. Juhl, "Prolonged T_1 in patients with liver cirrhosis: an in vivo MRI study," *Magnetic Resonance Imaging*, vol. 8, no. 5, pp. 599–604, 1990.
- [20] I. Kay and R. M. Henkelman, "Practical implementation and optimization of one-shot T_1 imaging," *Magnetic Resonance in Medicine*, vol. 22, no. 2, pp. 414–424, 1991.
- [21] K. Horsthuis, A. J. Nederveen, M.-W. de Feiter, C. Lavini, P. C. F. Stokkers, and J. Stoker, "Mapping of T_1 -values and gadolinium-concentrations in MRI as indicator of disease activity in luminal crohn's disease: a feasibility study," *Journal of Magnetic Resonance Imaging*, vol. 29, no. 2, pp. 488–493, 2009.

Research Article

Improved Efficacy of Transcatheter Arterial Chemoembolization Using Warmed Miriplatin for Hepatocellular Carcinoma

Daisuke Yasui,¹ Satoru Murata,¹ Shiro Onozawa,¹ Takahiko Mine,¹ Tatsuo Ueda,¹ Fumie Sugihara,¹ Chiaki Kawamoto,² Eiji Uchida,³ and Shin-ichiro Kumita¹

¹ Department of Radiology/Center for Advanced Medical Technology, Nippon Medical School, 1-1-5 Sendagi, Bunkyo-ku, Tokyo 113-8603, Japan

² Division of Gastroenterology and Hepatology, Department of Internal Medicine, Nippon Medical School, 1-1-5 Sendagi, Bunkyo-ku, Tokyo 113-8603, Japan

³ Department of Surgery, Nippon Medical School, 1-1-5 Sendagi, Bunkyo-ku, Tokyo 113-8603, Japan

Correspondence should be addressed to Daisuke Yasui; ledhotcp@nms.ac.jp

Received 25 June 2014; Accepted 17 August 2014; Published 8 September 2014

Academic Editor: Pascal Niggemann

Copyright © 2014 Daisuke Yasui et al. This is an open access article distributed under the Creative Commons Attribution License, which permits unrestricted use, distribution, and reproduction in any medium, provided the original work is properly cited.

The aim of this study was to evaluate the efficacy and safety of transcatheter arterial chemoembolization (TACE) using warmed and nonwarmed miriplatin for hepatocellular carcinoma. Eighty patients (117 nodules), treated between January 2010 and June 2013, were evaluated. Thirty-two and 85 nodules were treated with nonwarmed and warmed miriplatin, respectively. The efficacy of TACE was evaluated on a per nodule basis according to treatment effect (TE). Adverse events were evaluated according to the Common Terminology Criteria for Adverse Events (CTCAE) v4.0. TE grades were significantly improved in the warmed group compared to the nonwarmed group (nonwarmed: TE 4, 12.5%; TE 3, 0%; TE 2, 15.6%; TE 1, 71.9%; warmed: TE 4, 34.1%; TE 3, 5.9%; TE 2, 9.4%; TE 1, 50.6%; $P = 0.017$). Multivariate analysis revealed significant impact of warming miriplatin on objective response rate (odds ratio, 12.35; 95% confidence interval, 2.90–90.0; $P = 0.0028$). CTCAE grades of elevated aspartate and alanine transaminase after TACE were significantly higher in the warmed group ($P = 0.0083$ and 0.0068 , resp.); however, all adverse events were only transient. The use of warmed miriplatin in TACE significantly improved TE without causing serious complications.

1. Introduction

Transcatheter arterial chemoembolization (TACE) is a standard therapy for intermediate stage unresectable hepatocellular carcinoma (HCC) [1]. Previous randomized controlled studies have shown that TACE prolongs survival and controls symptoms of HCC [2, 3].

Doxorubicin, epirubicin, cisplatin, and mitomycin C have been widely used as chemotherapeutic agents, either alone or in combination [4]. It is known that epirubicin, cisplatin, and mitomycin C can cause arteritis after injection, leading to hepatic artery occlusion and development of extrahepatic collateral pathways [5]. This change in vascular anatomy can make repetitive TACE difficult and limits the long-term efficacy of TACE.

A new platinum agent, miriplatin ((*SP-4-2*)-[(1*R,2R*)-cyclohexane-1,2-diamine-*N,N'*] bis (tetradecanoato-*O*))

platinum monohydrate; Dainippon Sumitomo Pharma, Osaka, Japan), was recently developed [6, 7]. It is a lipophilic platinum complex that can be easily suspended in Lipiodol (Guerbet, Aulnay-sous-Bois, France) and gradually releases active platinum compounds in tumor tissue [7]. According to the experience in our facility (296 sessions of TACE using miriplatin in the past 4 years), miriplatin is likely to cause minimal damage to the hepatic artery (unpublished data). Thus, TACE using miriplatin can be performed repeatedly as needed [8].

Another advantage of miriplatin is its less severe toxicity profile compared to other agents, resulting from gradual release of platinum into serum [9, 10].

Less damage to feeding arteries and less severe adverse effects make miriplatin suitable for TACE; however, when compared to other agents, the clinical outcomes of TACE using miriplatin have not been satisfactory [11–13]. It has

been reported that the high viscosity and the large oil droplet of miriplatin can cause early occlusion of feeding vessels, leading to inadequate accumulation in tumors [11]. The viscosity of miriplatin suspension has been shown to decrease as temperature increases, dropping from 50 mPa·s at 25°C to 12 mPa·s at 60°C [14, 15]. Therefore, local tumor control could be improved by using warmed miriplatin in TACE, as warming miriplatin will reduce its viscosity and increase miriplatin accumulation in the tumor.

Thus, the purpose of this study was to evaluate and compare the efficacy of nonwarmed miriplatin versus warmed miriplatin in TACE and to review the adverse events in both treatment groups.

2. Materials and Methods

This study was approved by the local institutional review board. The review board waived the need for informed consent given the retrospective design of the study.

2.1. Patients. Patients were eligible for this retrospective study if they were diagnosed with HCC by either contrast-enhanced dynamic computed tomography or dynamic magnetic resonance imaging using gadolinium ethoxybenzyl diethylenetriamine pentaacetic acid. A total of 100 patients (140 nodules) were initially selected and met all the following requirements: 1 nodule per hepatic segment and a well-demarcated and hypervascular lesion (Figure 1). Among those, 20 patients (23 nodules) were excluded for the following reasons: 6 patients (7 nodules) for difficulty in selective catheterization of the feeding artery (beyond the second branch of the proper hepatic artery); 9 patients (11 nodules) for massive arteriportal shunts (A-P shunt) in which a segmental portal vein was visualized on hepatic arteriography; and 5 patients (5 nodules) for inadequate miriplatin accumulation in the target lesion because of large tumor size or anastomosis with vital vessels (pericardial and pulmonary veins) (Figure 1).

A total of 80 patients (117 nodules) were finally selected (Figure 1). TACE with nonwarmed miriplatin was performed on 22 patients (32 nodules) between January 2010 and December 2010. This included 17 men and 5 women, with a median age of 68 years (range, 51–83 years) (Table 1). TACE using warmed miriplatin was initiated in January 2011 in order to improve local tumor control by reducing viscosity. Fifty-eight patients (85 nodules) were treated with warmed miriplatin between January 2011 and June 2013. This included 34 male and 24 female patients, with a median age of 73 years (range, 50–91 years) (Table 1).

2.2. Treatment Procedure. The entire treatment procedure was performed under local anesthesia by administering lidocaine subcutaneously. A 4-French sheath (Super Sheath; Medikit, Miyazaki, Japan) was inserted via the femoral artery. Feeding arteries were routinely selected beyond the second branch of the proper hepatic artery and were cannulated with 2.0-French microcatheters (Gold Crest-MRT; Koshin medical, Tokyo, Japan). The miriplatin suspension was prepared by directly mixing miriplatin powder with

lipiodol. The miriplatin/lipiodol suspension was prepared at 25°C for the nonwarmed miriplatin group. For preparing warmed miriplatin, lipiodol was mixed with miriplatin powder first and then the miriplatin/lipiodol suspension was immersed in a hot water bath for more than 5 minutes, which was kept at 55°C as measured using a thermometer inside a clean container placed in an electric range. The stability of miriplatin/lipiodol suspension at this temperature was confirmed by the manufacturer. The standard full dosage of the TACE protocol was miriplatin 120 mg. The miriplatin/lipiodol suspension was administered slowly under fluoroscopic guidance immediately after preparation without causing reflux, until the vascular bed of the target nodule was fully filled with the suspension, as confirmed under fluoroscopy. Thus, the amount of the miriplatin/lipiodol suspension was not predetermined, but rather decided by angiographic findings. Finally, the feeding arteries were embolized with ready-made 2 mm pieces of gelatin sponge (Gelpart; Nippon Kayaku, Tokyo, Japan), until complete stasis of the feeding arteries was obtained.

2.3. Evaluation of Treatment Effect. The response to TACE was evaluated on a per nodule basis, according to the 4-grade system: treatment effect (TE) grades 1–4 [16]. Pretreatment nodule size was measured using the most recent image (within 3 months) prior to the first treatment. The product of long and short axes length in the maximum cross section was calculated for each nodule before and after TACE, and nodules were classified according to the change in size: grade 4 (TE 4), 100% reduction in size or complete tumor necrosis; grade 3 (TE 3), 50% to 100% reduction in size; grade 2 (TE 2), <50% reduction to <25% increase in size; and grade 1 (TE 1), more than 25% increase in size. Objective response rate (ORR), defined as the proportion of TE 3 and 4 cases to the total, and disease control rate (DCR), defined as the proportion of TE 2, 3, and 4 cases to the total, were compared between the nonwarmed and warmed miriplatin groups. The dose of miriplatin used in each session was also compared between the 2 groups. Multivariate analysis was performed to identify factors that had significant influence on ORR.

2.4. Evaluation of the Effect of Anticancer Agents on the Hepatic Artery. Arterial damage to the hepatic artery was defined as vessel irregularity, stenosis, or occlusion. It was evaluated on a per regimen basis, independent of other analyses. All patients were assigned to three groups according to anticancer agent used in TACE: epirubicin/cisplatin, nonwarmed miriplatin, and warmed miriplatin, considering both past treatment and the treatment included in this study. Therefore, patients with multiple treatment history using different agents were assigned to more than one group. Preoperative arterial damage was evaluated with celiac arteriography prior to the treatment using each agent. Postoperative celiac arteriography before the usage of other agents was compared with the preoperative one. Damage to the hepatic artery was evaluated according to the 5-grade system: grade 0, no obvious damage; grade 1, irregular vessel wall; grade 2, vessel narrowing; grade 3, stenosis; and grade 4, occlusion. Severe damage was defined

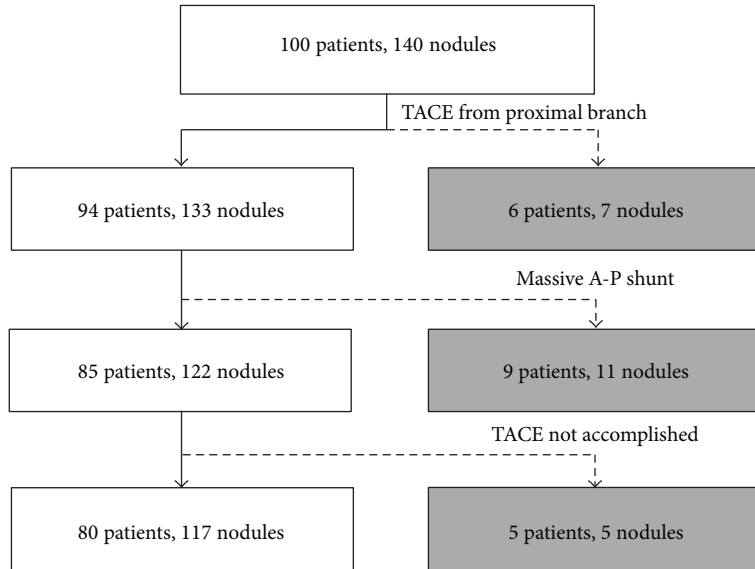


FIGURE 1: Patient enrollment. Gray boxes indicate patients excluded from the study. TACE: transcatheter arterial chemoembolization; A-P: arteriportal.

as grade 3 and grade 4. The level of arterial damage was classified into 4 levels: level 1, the proper hepatic artery; level 2, lobar branches; level 3, segmental branches; and level 4, subsegmental branches. Development of A-P shunt was also evaluated. The evaluation was performed by two observers (D.Y and T.M), independently and blinded to each other. After individual evaluation, the findings were disclosed and discrepancy in the findings was discussed by 2 observers.

2.5. Follow-Up. Either contrast-enhanced computed tomography or magnetic resonance imaging was performed every 3 to 6 months after TACE. The end of the follow-up period was defined as either the last patient visit or the addition of other treatments: TACE with other agents, radiofrequency ablation, or surgery. The entire follow-up period was completed in September 2013.

2.6. Adverse Events. Common Terminology Criteria for Adverse Events (CTCAE) version 4.0 was used to evaluate the safety of TACE using warmed miriplatin. Adverse events were evaluated on a per treatment session basis. Levels of aspartate transaminase (AST), alanine transaminase (ALT), total bilirubin, and complete blood counts were measured, and pre- and postoperative values were compared between the 2 groups. Eosinophilia, which is among the characteristic adverse events of miriplatin (defined as more than 450 cells/ μ L), was also evaluated. Data obtained closest to the first treatment (within 1 month) were used as preoperative values. Either peak or trough data after the procedure were evaluated. Abnormal values were monitored to check for their return to the baseline. Incidence of constitutional symptoms, such as pyrexia and vomiting, was reviewed. Severe complications, such as liver failure, liver infarction, liver abscess, and bile duct necrosis, were also reviewed.

2.7. Statistical Analysis. Statistical analysis was performed using R 2.15.1 (CRAN: the Comprehensive R Archive Network at <http://cran.r-project.org/>). The parameters related to the patient and nodule characteristics, details of treatment, and adverse events were assessed with the Student's *t*-test, the Mann-Whitney *U*-test, and the Fisher's exact test. TE grades were assessed with the Mann-Whitney *U*-test. Logistic regression analysis was performed to identify factors that had significant impact on ORR, among potential prognostic factors: sex, hepatitis B virus infection, tumor size, values of α -fetoprotein (AFP) and des-gamma-carboxyprothrombin (DCP), Barcelona Clinic Liver Cancer (BCLC) stage, history of TACE, warming miriplatin, dose of miriplatin, and preoperative severe hepatic arterial damage [17–19]. Two-way ANOVA test was performed to reveal interaction between previous treatment history or preoperative severe arterial damage and warming miriplatin. Kappa value was calculated to assess the degree of interobserver agreement in evaluation of the hepatic arterial damage.

3. Results

3.1. Demographic Data and Tumor Profiles. Demographic data and parameters related to the patients and nodules are summarized in Table 1. No significant differences in age, sex, etiology of underlying chronic liver disease, Child-Pugh score, BCLC stage, or performance status (Eastern Cooperative Oncology Group classification) were observed between the nonwarmed and warmed miriplatin groups ($P = 0.086, 0.10, 0.093, 0.73, 0.72,$ and $0.15,$ resp.). Preoperative AFP and DCP values were not available in 9 cases. No significant difference was observed in AFP and DCP values and nodule size (the product of long and short axes length) ($P = 0.80, 0.15,$ and $0.72,$ resp.).

TABLE 1: Profile of patients and nodules.

	Nonwarmed group (<i>n</i> = 22)	Warmed group (<i>n</i> = 58)	<i>P</i> value
Age, years	68 (51–83)	73 (50–91)	0.086
Sex, <i>n</i> (%)			
Male/female	17/5 (77.3/22.7%)	34/24 (58.6/41.4%)	0.10
Etiology, <i>n</i> (%)			0.093
HCV	14 (63.6%)	44 (75.9%)	
HBV	1 (4.5%)	7 (12.1%)	
Alcohol	5 (22.7%)	3 (5.2%)	
Others	2 (9.2%)	4 (6.8%)	
Child-Pugh, <i>n</i> (%)			0.73
5–6 (Class A)	13 (59.1%)	33 (56.9%)	
7–9 (Class B)	8 (36.4%)	23 (39.7%)	
10 (Class C)	1 (4.5%)	2 (3.4%)	
Median score	6.4	6.5	
BCLC stage, <i>n</i> (%)			0.72
0 (very early)	0 (0%)	0 (0%)	
A (early)	0 (0%)	0 (0%)	
B (intermediate)	8 (36.4%)	21 (36.2%)	
C (advanced)	12 (54.5%)	36 (62.1%)	
D (terminal)	2 (9.1%)	1 (1.7%)	
PS, <i>n</i> (%)			0.15
0	6 (27.3%)	23 (39.7%)	
1	13 (59.1%)	33 (56.9%)	
2	2 (9.1%)	2 (3.4%)	
3	1 (4.5%)	0 (0%)	
AFP (ng/mL)	282.8 ± 723.1	415.5 ± 1454.3	0.80
DCP (mAU/mL)	1562.6 ± 5241.2	581.3 ± 2913.8	0.15
Nodule size (mm ²)	388.6 ± 398.0	383.1 ± 468.0	0.72
History of TACE	18 (81.8%)	32 (55.2%)	0.038*
Agent			
EPI alone	8/18 (44.4%)	4/32 (12.5%)	
CDDP alone	6/18 (33.3%)	12/32 (37.5%)	
MPT alone	0/18 (0%)	5/32 (15.6%)	
Multiple agents	4/18 (22.3%)	11/32 (34.4%)	
Number of sessions			0.087
1	11/18 (61.1%)	17/32 (53.1%)	
2	4/18 (22.2%)	9/32 (28.1%)	
3	1/18 (5.6%)	4/32 (12.5%)	
4–6	2/18 (11.1%)	2/32 (6.3%)	
Preoperative severe arterial damage	7 (31.8%)	6 (10.3%)	0.037*
Follow-up period (months)	8.5 ± 7.6 (2–36)	7.7 ± 6.0 (2–29)	0.68
≥3 months	19 (86.4%)	49 (84.5%)	1.00
≥6 months	11 (50%)	31 (53.4%)	0.81
Interval between image and TACE (months) [†]			0.084
<1 month	26/29 (89.7%)	62/87 (71.3%)	
1–2 months	1/29 (3.4%)	18/87 (20.7%)	
2–3 months	2/29 (6.9%)	7/87 (8.0%)	

Age is presented as median (range).

AFP, DCP, nodule size, and follow-up period are presented as mean ± standard deviation.

Range of follow-up period is shown in the parentheses.

* *P* < 0.05.

[†] Interval between preoperative image and treatment was evaluated on a per treatment session basis.

HCV: hepatitis C virus; HBV: hepatitis B virus; AFP: alpha-fetoprotein; DCP: des-gamma-carboxyprothrombin; BCLC: Barcelona Clinic Liver Cancer; PS: performance status (Eastern Cooperative Oncology Group classification); TACE: transcatheter arterial chemoembolization; EPI: epirubicin; CDDP: cisplatin; MPT: miriplatin.

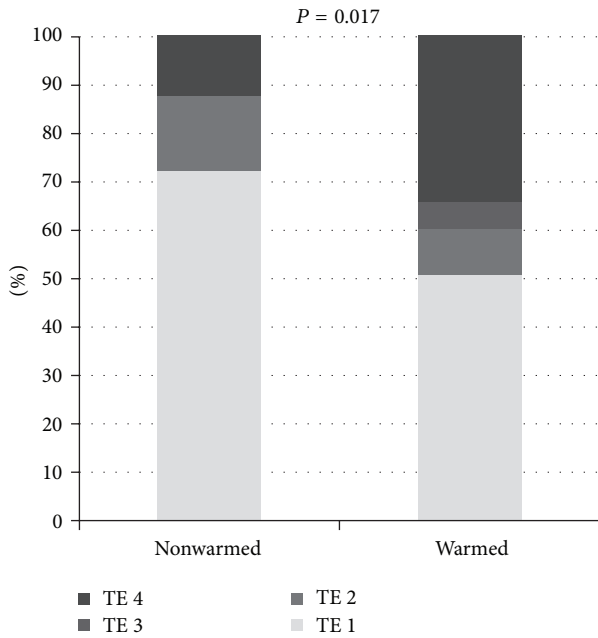


FIGURE 2: Treatment effect. The bar graph shows the distribution of treatment effect (TE) grades.

Eighteen cases (81.8%) and 32 cases (55.2%) had a previous history of TACE in the nonwarmed and warmed miriplatin groups, respectively (Table 1). Conventional lipiodol-TACE was performed using epirubicin, cisplatin, or miriplatin in previous sessions. Gelatin sponge was used as embolization material. The ratio of nodules with previous TACE history was significantly higher in the nonwarmed miriplatin group ($P = 0.038$). No significant difference was observed in the number of previous treatment sessions between the 2 groups ($P = 0.087$).

No significant difference was observed in follow-up period ($P = 0.68$). More than 80% of the nodules were followed up for more than 3 months and about half of the nodules were followed up for more than 6 months: longer follow-up period than previous studies [20, 21]. Frequency of preoperative severe arterial damage was significantly higher in the nonwarmed group ($P = 0.037$). There was no significant difference in the interval between preoperative image evaluation and treatment between the 2 groups ($P = 0.084$).

3.2. Treatment Effect. Warming miriplatin had an impact on TE grades. TE grades were significantly higher in the warmed miriplatin group than in the nonwarmed miriplatin group ($P = 0.017$; Figure 2). In the nonwarmed miriplatin group, 4 lesions were classified as TE 4 (12.5%), 0 as TE 3 (0%), 5 as TE 2 (15.6%), and 23 as TE 1 (71.9%); thus, ORR and DCR were 12.5% and 28.1%, respectively. In contrast, in the warmed miriplatin group, 29 lesions were classified as TE 4 (34.1%), 5 as TE 3 (5.9%), 8 as TE 2 (9.4%), and 43 as TE 1 (50.6%); thus, ORR and DCR were 40.0% and 49.4%, respectively. ORR was significantly higher in the warmed group ($P = 0.0042$), while there was no significant difference in DCR ($P = 0.059$).

TABLE 2: Results of logistic regression analysis.

Factors	Odds ratio (95% CI)	P value
Sex (female)	0.39 (0.12–1.17)	0.10
HBV infection	0.30 (0.046–1.49)	0.16
Tumor size (mm ²)	1.00 (1.00–1.00)	0.13
AFP (ng/mL)	1.00 (1.00–1.00)	0.16
DCP (mAU/mL)	1.00 (1.00–1.00)	0.14
BCLC stage C	0.77 (0.24–2.43)	0.66
BCLC stage D	36.55 (0.70–3635.77)	0.078
History of TACE	0.78 (0.27–2.24)	0.64
Warming miriplatin	12.35 (2.90–90.0)	0.0028**
Miriplatin dose (mg)	0.99 (0.96–1.01)	0.43
Severe hepatic arterial damage	0.59 (0.10–2.73)	0.52

** $P < 0.01$.

CI: confidence interval; HBV: hepatitis B virus; AFP: alpha-fetoprotein; DCP: des-gamma-carboxyprothrombin; BCLC: Barcelona Clinic Liver Cancer; TACE: transcatheter arterial chemoembolization.

TACE using both nonwarmed miriplatin and warmed miriplatin was performed on 3 nodules. TE 1 was obtained in all cases after TACE using nonwarmed miriplatin. Treatment effect improved to TE 4 in 1 case (Figure 3); however, no improvement was observed in the other 2 nodules after TACE using warmed miriplatin. No significant difference was observed in the amount of administered miriplatin (33.5 ± 16.7 mg in the nonwarmed miriplatin group versus 42.9 ± 29.8 mg in the warmed miriplatin group; $P = 0.18$).

Logistic regression analysis revealed that warming miriplatin had a significant impact on ORR (odds ratio, 12.35; 95% confidence interval, 2.90–90.0; $P = 0.0028$; Table 2). Other factors did not have a significant impact on ORR.

Since significant difference was observed in previous treatment history and preoperative severe arterial damage, two-way ANOVA test was performed to reveal interaction between these factors and warming miriplatin. No significant interaction was observed between previous treatment history and warming miriplatin ($P = 0.24$) and between preoperative severe hepatic arterial damage and warming miriplatin ($P = 0.38$).

3.3. Angiographic Evaluation after TACE. Forty-three cases were included in the epirubicin/cisplatin treatment group. Thirty cases were included in the nonwarmed miriplatin group, considering 8 cases in the warmed miriplatin group with past treatment history using nonwarmed miriplatin. Postoperative angiography was not available in 12 cases in the warmed miriplatin group; therefore, 46 cases were included.

Discrepancy in arterial damage grade evaluation was observed in 7 cases, while that in arterial damage level evaluation was observed in 2 cases with the epirubicin/cisplatin group (κ value: 0.71 and 0.77, resp.). Discrepancy in arterial damage grade evaluation was observed in 2 cases with both nonwarmed and warmed miriplatin groups (κ value: 0.85 and 0.70, resp.). Agreement on arterial damage level was obtained in all cases with the nonwarmed and warmed miriplatin



FIGURE 3: A case of hepatocellular carcinoma treated with warmed miriplatin. (a) Arterial phase of contrast-enhanced computed tomography (CT) before treatment. The white circle shows an enhanced lesion compatible with hepatocellular carcinoma. (b) Common hepatic arteriography showing a tumor stain (black circle). Occlusion and aneurysm formation are noted in the hepatic arterial branch, presumably caused by previous transcatheter arterial chemoembolization (TACE) using cisplatin (black arrow). (c) Early phase of CT during arteriography with the catheter tip placed in the common hepatic artery, 6 months after the first session of TACE using nonwarmed miriplatin. Obvious enhancement was observed, which indicated recurrence (white circle). (d) Celiac arteriography showing tumor stain (black circle). (e) Selective angiography with a microcatheter placed in a feeding artery. TACE was performed using warmed miriplatin in this session. (f) Arterial phase of contrast-enhanced CT, 4 months after the second session of TACE. Lipiodol accumulated densely in the target lesion, and the tumor size was decreased with no evidence of recurrence.

TABLE 3: Evaluation of the effect of anticancer agents on the hepatic artery.

	Epirubicin/cisplatin (<i>n</i> = 43)	Nonwarmed miriplatin (<i>n</i> = 30)	Warmed miriplatin (<i>n</i> = 46)
Damage grade			
0 (no damage)	25 (58.1%)	22 (73.3%)	44 (95.7%)
1 (irregularity)	5 (11.6%)	6 (20.0%)	2 (4.3%)
2 (narrowing)	1 (2.4%)	0 (0%)	0 (0%)
3 (stenosis)	3 (7.0%)	0 (0%)	0 (0%)
4 (occlusion)	9 (20.9%)	2 (6.7%)	0 (0%)
Damage level			
1 (PHA)	1/18 (5.6%)	0/8 (0%)	0/2 (0%)
2 (lobar branch)	3/18 (16.7%)	0/8 (0%)	0/2 (0%)
3 (segmental branch)	6/18 (33.3%)	3/8 (37.5%)	1/2 (50%)
4 (subsegmental branch)	8/18 (44.4%)	5/8 (62.5%)	1/2 (50%)
A-P shunt formation			
Yes	2 (4.7%)	3 (10.0%)	0 (0%)
No	41 (95.3%)	27 (90.0%)	46 (100%)
Number of sessions			
1	28 (65.1%)	24 (80.0%)	27 (58.7%)
2	10 (23.3%)	5 (16.7%)	14 (30.4%)
3	1 (2.3%)	1 (3.3%)	4 (8.7%)
4–6	4 (9.3%)	0 (0%)	1 (2.2%)

Data in this table were obtained from consensus of two radiologists.

PHA: proper hepatic artery; A-P shunt: arteriportal shunt.

groups. Agreement on A-P shunt formation was obtained in all cases with all groups. Discrepancy in the findings was discussed by two observers and consensus was formed in all cases.

According to the consensus, severe arterial damage was observed in 12 of 43 cases (27.9%) with the epirubicin/cisplatin group, in 2 of 30 cases (6.7%) with the nonwarmed miriplatin group, and in 0 of 46 cases (0%) with the warmed miriplatin group (Table 3). There was no significant difference in the number of treatment sessions ($P = 0.164$).

3.4. Adverse Events. Severe complications, such as liver abscess, bile duct necrosis, and liver infarction, and complications above CTCAE grade 4 were not observed in either group. There was no 30-day mortality.

Grades of AST and ALT elevation after treatment were significantly higher in the warmed miriplatin group ($P = 0.0083$ and 0.0068 , resp.; Table 4), although no significant difference was observed in preoperative values ($P = 0.14$ and 0.32 , resp.). Return to the preoperative level within 1 month was observed in all cases, with the exception of 1 and 2 cases in the nonwarmed and warmed miriplatin groups, respectively, in which sustained mild elevation of AST and ALT (80–150 IU/L) was observed. These cases were managed conservatively.

No significant difference was observed in grades of anemia ($P = 0.060$; Table 4); however, transfusion was necessary in 2 cases. No obvious relationship between anemia and TACE was identified, and recovery to the preoperative

level was observed in all cases within 1 month. Data on eosinophilia was missing in 2 sessions with the nonwarmed miriplatin group and in 25 sessions with the warmed miriplatin group. No significant difference was observed in occurrence of eosinophilia ($P = 0.26$). No significant difference was observed in other parameters.

4. Discussion

In this study, the improved efficacy of warmed miriplatin compared to nonwarmed miriplatin when used in TACE for HCC was demonstrated; both TE and ORR were improved in the warmed miriplatin group. DCR was also better in the warmed miriplatin group, although this difference was not significant. No significant difference was observed in patient profiles or parameters related to each nodule, except history of TACE and preoperative severe hepatic arterial damage, which was more frequent in the nonwarmed miriplatin group. However, logistic regression analysis revealed that these parameters had no significant impact on objective response. Two-way ANOVA tests also revealed that there was no significant interaction between these parameters and warming miriplatin. On the contrary, Seko et al. reported that history of TACE had significant impact on tumor response [20]. This discrepancy in conclusion can be attributed to the difference in evaluation method (modified RECIST versus TE), since tumor response can be evaluated differently with different criteria. Furthermore, they did not consider hepatic arterial damage, which can have direct impact on tumor response. Therefore this study gives more comprehensive

TABLE 4: Adverse events.

	Nonwarmed group (29 sessions)	Warmed group (87 sessions)	P value
AST (IU/L), <i>n</i> (%)	46.8 ± 22.4	59.1 ± 50.0	0.14
Grade 1	10 (34.5%)	24 (27.6%)	
Grade 2	5 (17.2%)	20 (23.0%)	
Grade 3	3 (10.3%)	26 (29.9%)	
Grades 4-5	0 (0)	0 (0)	0.0083**
ALT (IU/L), <i>n</i> (%)	35.9 ± 15.6	50.6 ± 56.2	0.32
Grade 1	8 (27.6%)	27 (31.0%)	
Grade 2	1 (3.4%)	14 (16.1%)	
Grade 3	4 (13.8%)	22 (25.3%)	
Grades 4-5	0 (0)	0 (0)	0.0068**
T-Bil (mg/dL), <i>n</i> (%)	1.03 ± 0.75	0.81 ± 0.39	0.25
Grade 1	5 (17.2%)	29 (33.3%)	
Grade 2	3 (10.3%)	8 (9.2%)	
Grade 3	0 (0)	0 (0)	
Grades 4-5	0 (0)	0 (0)	0.22
WBC (/μL), <i>n</i> (%)	3666 ± 1477	3840 ± 1604	0.59
Grade 1	1 (3.4%)	7 (8.0%)	
Grade 2	1 (3.4%)	7 (8.0%)	
Grade 3	3 (10.3%)	9 (10.3%)	
Grades 4-5	0 (0)	0 (0)	0.38
Hb (g/dL), <i>n</i> (%)	12.0 ± 2.0	11.6 ± 1.9	0.32
Grade 1	3 (10.3%)	19 (21.8%)	
Grade 2	1 (3.4%)	10 (11.5%)	
Grade 3	1 (3.4%)	3 (3.4%)	
Grades 4-5	0 (0)	0 (0)	0.060
Plt (×10 ⁴ /μL), <i>n</i> (%)	9.2 ± 4.5	10.8 ± 5.0	0.20
Grade 1	5 (17.2%)	26 (29.9%)	
Grade 2	7 (24.1%)	19 (21.8%)	
Grade 3	2 (6.9%)	14 (16.1%)	
Grades 4-5	0 (0)	0 (0)	0.11
Eosinophilia [†]	13/27 (48.1%)	22/62 (35.5%)	0.26
Pyrexia, <i>n</i> (%)			
Grade 1	11 (37.9%)	35 (40.2%)	
Grade 2	0 (0)	7 (8.0%)	
Grades 3-5	0 (0)	0 (0)	0.22
Vomiting, <i>n</i> (%)			
Grade 1	1 (3.4%)	3 (3.4%)	
Grade 2	1 (3.4%)	0 (0)	
Grades 3-5	0 (0)	0 (0)	0.42
Liver infarction	0	0	—
Liver abscess	0	0	—
Bile duct necrosis	0	0	—

Preoperative values of AST, ALT, T-Bil, WBC, Hb, and Plt are presented as mean ± standard deviation in the first row.

P values in the first row are for comparison of preoperative values, while values in the bottom row are for comparison of CTCAE grades.

**P < 0.01

[†]Data on eosinophilia were missing in 2 sessions with the nonwarmed group and in 25 sessions with the warmed group.

AST: aspartate transaminase; ALT: alanine transaminase; T-Bil: total bilirubin; WBC: white blood cell; Hb: hemoglobin; Plt: platelets.

analysis; however, prospective trial with matched background is desirable to obtain appropriate conclusion.

TACE-induced hepatic arterial damage is a factor that limits the efficacy of this treatment. Good interobserver agreement was obtained in evaluation of the hepatic arterial damage grade and level. Severe arterial damage, which can interfere with injection of anticancer agents and lipiodol, was less frequent with nonwarmed and warmed miriplatin,

compared to epirubicin/cisplatin (6.7% and 0% versus 27.9%). More proximal arterial damage was observed with epirubicin/cisplatin. These facts suggest that miriplatin is more suitable for TACE due to its less severe arterial insult.

However, previous studies have shown inferior local tumor control of TACE using miriplatin compared to other agents, including cisplatin and epirubicin [11–13]. Iwazawa et al. reported that the high viscosity of miriplatin suspension

may result in early occlusion of tumor feeders before sufficient accumulation of miriplatin in the tumor is obtained, and this may be a major factor related to inferior local tumor control [11]. The viscosity of miriplatin has been shown to decrease with increasing temperature [14, 15]; a few studies have revealed improved local tumor control when investigating the efficacy of TACE using warmed miriplatin [20, 21]. However, these studies showed only the short-term TE (less than 3 months); in contrast, our study investigated the longer-term TE (8.5 and 7.7 months in average with the nonwarmed and warmed miriplatin groups, resp.). Another advantage of our study is its practical study design; nodules were followed up until treatments other than miriplatin-TACE were performed. Thus, the efficacy of miriplatin-TACE was genuinely evaluated.

The reason why local tumor control can be improved when using warmed miriplatin remains unclear. According to the hypothesis that agents with high viscosity cause proximal occlusion of feeding arteries, warmed miriplatin, which is therefore less viscous, can be injected to more distal parts of feeding arteries. Distal vessels usually have more vascular beds than proximal vessels, and thus the amount of injected miriplatin suspension may be assumed to increase; however, there was no significant difference in the miriplatin dose between the nonwarmed and warmed miriplatin groups in our study. Additional studies should be performed to reveal the mechanism underlying the improved efficacy of TACE using warmed miriplatin.

Despite the promising results, local tumor control in this study was not comparable to that found in previous studies on TACE using miriplatin [7, 9–12]. This may be attributed to the profile of cases included in this study. The levels of tumor markers investigated in our study (AFP and DCP) were quite high, and these markers are known to be negative prognostic factors given their association with aggressive pathological features [22–24]. Previous clinical studies have also shown that cases with high AFP levels have poor prognoses [25, 26].

With regard to adverse events, CTCAE grades of AST and ALT elevation were significantly higher in the warmed group. There is no consensus on whether elevation of transaminase levels after treatment is caused by damage to normal liver parenchyma or tumor necrosis, so it is difficult to interpret these data. Elevation of transaminase levels was only transient and was managed conservatively. No significant difference was observed in other parameters. Moreover, no serious complications, such as liver infarction, liver abscess, and bile duct necrosis, were observed in either group. These findings indicate that adverse events of TACE using warmed miriplatin are only transient.

Our findings provide evidence that warmed miriplatin can improve the efficacy of TACE; however, this study has some limitations. First, it is a retrospective study, and a randomized controlled study should be considered to further support these findings. There was asymmetry in the numbers of nodules treated in the nonwarmed and warmed groups, which was inevitable given the nature of a retrospective study. This study presented preliminary results on the efficacy of TACE using warmed miriplatin, and a prospective clinical trial is going to be conducted. Second, in order to

establish the advantage of using miriplatin, the relationship between survival benefit and repeatability of TACE should be demonstrated. Moreover, the efficacy of TACE using warmed miriplatin should be compared with TACE using other agents or microspheres.

5. Conclusions

This study demonstrated the safety and improved efficacy of TACE using warmed miriplatin compared to nonwarmed miriplatin for the treatment of HCC.

Conflict of Interests

The authors declare that there is no conflict of interests regarding the publication of this paper.

References

- [1] J. M. Llovet, C. Brú, and J. Bruix, “Prognosis of hepatocellular carcinoma: the BCLC staging classification,” *Seminars in Liver Disease*, vol. 19, no. 3, pp. 329–338, 1999.
- [2] C. M. Lo, H. Ngan, W. K. Tso et al., “Randomized controlled trial of transarterial Lipiodol chemoembolization for unresectable hepatocellular carcinoma,” *Hepatology*, vol. 35, no. 5, pp. 1164–1171, 2002.
- [3] J. M. Llovet, M. I. Real, X. Montaña et al., “Arterial embolisation or chemoembolisation versus symptomatic treatment in patients with unresectable hepatocellular carcinoma: a randomised controlled trial,” *The Lancet*, vol. 359, no. 9319, pp. 1734–1739, 2002.
- [4] A. L. Lewis, M. V. Gonzalez, A. W. Lloyd et al., “DC bead: in vitro characterization of a drug-delivery device for transarterial chemoembolization,” *Journal of Vascular and Interventional Radiology*, vol. 17, part 1, no. 2, pp. 335–342, 2006.
- [5] S. Sahara, N. Kawai, M. Sato et al., “Prospective evaluation of transcatheter arterial chemoembolization (TACE) with multiple anti-cancer drugs (epirubicin, cisplatin, mitomycin c, 5-fluorouracil) compared with TACE with epirubicin for treatment of hepatocellular carcinoma,” *Cardiovascular and Interventional Radiology*, vol. 35, no. 6, pp. 1363–1371, 2012.
- [6] M. Hanada, A. Baba, Y. Tsutsumishita et al., “Intra-hepatic arterial administration with miriplatin suspended in an oily lymphographic agent inhibits the growth of tumors implanted in rat livers by inducing platinum-DNA adducts to form and massive apoptosis,” *Cancer Chemotherapy and Pharmacology*, vol. 64, no. 3, pp. 473–483, 2009.
- [7] T. Okusaka, S. Okada, T. Nakanishi, S. Fujiyama, and Y. Kubo, “Phase II trial of intra-arterial chemotherapy using a novel lipophilic platinum derivative (SM-11355) in patients with hepatocellular carcinoma,” *Investigational New Drugs*, vol. 22, no. 2, pp. 169–176, 2004.
- [8] J. Iwazawa, N. Hashimoto, S. Ohue, O. Muramoto, and T. Mitani, “Chemoembolization-induced arterial damage: evaluation of three different chemotherapeutic protocols using epirubicin and miriplatin,” *Hepatology Research*, vol. 44, pp. 201–208, 2014.
- [9] S. Oguro, S. Hashimoto, T. Tanaka et al., “Short-term therapeutic effects of transcatheter arterial chemoembolization using miriplatin-lipiodol suspension for hepatocellular carcinoma,” *Japanese Journal of Radiology*, vol. 30, no. 9, pp. 735–742, 2012.

- [10] K. Okabe, T. Beppu, K. Haraoka et al., "Safety and short-term therapeutic effects of miriplatin-lipiodol suspension in transarterial chemoembolization (TACE) for hepatocellular carcinoma," *Anticancer Research*, vol. 31, no. 9, pp. 2983–2988, 2011.
- [11] J. Iwazawa, S. Ohue, N. Hashimoto, and T. Mitani, "Local tumor progression following lipiodol-based targeted chemoembolization of hepatocellular carcinoma: a retrospective comparison of miriplatin and epirubicin," *Cancer Management and Research*, vol. 4, no. 1, pp. 113–119, 2012.
- [12] S. Miyayama, M. Yamashiro, Y. Shibata et al., "Comparison of local control effects of superselective transcatheter arterial chemoembolization using epirubicin plus mitomycin C and miriplatin for hepatocellular carcinoma," *Japanese Journal of Radiology*, vol. 30, no. 3, pp. 263–270, 2012.
- [13] T. Handa, Y. Imai, K. Sugawara et al., "Transcatheter arterial chemoembolization for hepatocellular carcinoma: comparison of the therapeutic efficacies between miriplatin and epirubicin," *Hepatology Research*, 2013.
- [14] S. Murata, T. Mine, T. Ueda et al., "Transcatheter arterial chemoembolization based on hepatic hemodynamics for hepatocellular carcinoma," *The Scientific World Journal*, vol. 2013, Article ID 479805, 8 pages, 2013.
- [15] T. Hasegawa, H. Takaki, T. Yamanaka et al., "Experimental assessment of temperature influence on miriplatin and cisplatin iodized-oil suspension viscosity," *Japanese Journal of Radiology*, vol. 31, no. 6, pp. 424–427, 2013.
- [16] M. Kudo, S. Kubo, K. Takayasu et al., "Response Evaluation Criteria in Cancer of the Liver (RECICL) proposed by the Liver Cancer Study Group of Japan (2009 Revised Version)," *Hepatology Research*, vol. 40, no. 7, pp. 686–692, 2010.
- [17] J. Xiao, G. Li, S. Lin et al., "Prognostic factors of hepatocellular carcinoma patients treated by transarterial chemoembolization," *International Journal of Clinical and Experimental Pathology*, vol. 7, no. 3, pp. 1114–1123, 2014.
- [18] K. Yamakado, S. Miyayama, S. Hirota et al., "Subgrouping of intermediate-stage (BCLC stage B) hepatocellular carcinoma based on tumor number and size and Child-Pugh grade correlated with prognosis after transarterial chemoembolization," *Japanese Journal of Radiology*, vol. 32, no. 5, pp. 260–265, 2014.
- [19] M. T. Sellers, S. Huggins, K. Kegley et al., "Multivariate analysis of prognostic factors for survival following doxorubicin-eluting bead transarterial chemoembolization for hepatocellular carcinoma," *Journal of Vascular and Interventional Radiology*, vol. 24, no. 5, pp. 647–654, 2013.
- [20] Y. Seko, K. Ikeda, Y. Kawamura et al., "Antitumor efficacy of transcatheter arterial chemoembolization with warmed miriplatin in hepatocellular carcinoma," *Hepatology Research*, vol. 43, no. 9, pp. 942–949, 2013.
- [21] S.-I. Kora, H. Urakawa, T. Mitsufuji, A. Osame, H. Higashihara, and K. Yoshimitsu, "Warming effect on miriplatin-lipiodol suspension as a chemotherapeutic agent for transarterial chemoembolization for hepatocellular carcinoma: preliminary clinical experience," *Cardiovascular and Interventional Radiology*, vol. 36, no. 4, pp. 1023–1029, 2013.
- [22] S.-Y. Peng, W. J. Chen, P.-L. Lai, Y.-M. Jeng, J.-C. Sheu, and H.-C. Hsu, "High α -fetoprotein level correlates with high stage, early recurrence and poor prognosis of hepatocellular carcinoma: significance of hepatitis virus infection, age, p53 and β -catenin mutations," *International Journal of Cancer*, vol. 112, no. 1, pp. 44–50, 2004.
- [23] K. Yamamoto, H. Imamura, Y. Matsuyama et al., "AFP, AFP-L3, DCP, and GP73 as markers for monitoring treatment response and recurrence and as surrogate markers of clinicopathological variables of HCC," *Journal of Gastroenterology*, vol. 45, no. 12, pp. 1272–1282, 2010.
- [24] T. Suehiro, K. Sugimachi, T. Matsumata, H. Itasaka, A. Take-tomi, and T. Maeda, "Protein induced by vitamin K absence or antagonist II as a prognostic marker in hepatocellular carcinoma. Comparison with alpha-fetoprotein," *Cancer*, vol. 73, no. 10, pp. 2464–2471, 1994.
- [25] S. Savastano, D. Miotto, G. Casarrubea, S. Teso, M. Chiesura-Corona, and G. P. Feltrin, "Transcatheter arterial chemoembolization for hepatocellular carcinoma in patients with child's grade A or B cirrhosis: a multivariate analysis of prognostic factors," *Journal of Clinical Gastroenterology*, vol. 28, no. 4, pp. 334–340, 1999.
- [26] L. Lladó, J. Virgili, J. Figueras et al., "A prognostic index of the survival of patients with unresectable hepatocellular carcinoma after transcatheter arterial chemoembolization," *Cancer*, vol. 88, no. 1, pp. 50–57, 2000.

Clinical Study

Radiofrequency Thermoablation of HCC Larger Than 3 cm and Less Than 5 cm Proximal to the Gallbladder without Gallbladder Isolation: A Single Center Experience

Antonio Orlacchio, Fabrizio Chegai, Costantino Del Giudice, Mariangela Massaccesi, Elisa Costanzo, Elena Di Caprera, and Giovanni Simonetti

Department of Diagnostic and Molecular Imaging, Radiation Therapy and Interventional Radiology, University Hospital "Policlinico Tor Vergata," Viale Oxford 81, 00133 Rome, Italy

Correspondence should be addressed to Antonio Orlacchio; aorlacchio@uniroma2.it

Received 24 February 2014; Accepted 7 August 2014; Published 28 August 2014

Academic Editor: Per Kristian Hol

Copyright © 2014 Antonio Orlacchio et al. This is an open access article distributed under the Creative Commons Attribution License, which permits unrestricted use, distribution, and reproduction in any medium, provided the original work is properly cited.

Radiofrequency ablation (RFA) is an effective minimally invasive treatment for nonsurgical hepatocellular carcinoma (HCC), but ablation of tumors close to the gallbladder could be associated with several complications. We report our experience on the treatment of HCC close to the gallbladder with RFA. Eight RFA procedures were performed in eight patients with HCC larger than 3 cm and less than 5 cm close to the gallbladder. In all cases, a percutaneous approach was used. There were no major complications. Only in two patients a minimal wall thickening of the gallbladder was observed. Contrast enhanced computed tomography carried out after 30 days from the first procedure showed complete necrosis in seven patients (87%). Only one patient had local recurrence at 11 months of followup. Although limited, our experience suggests that, after careful preprocedural planning, in experienced hands and with appropriate technology, percutaneous RFA could be safely performed even for lesions larger than 3 cm located in close adjacency to the gallbladder.

1. Introduction

Hepatocellular carcinoma (HCC) is a leading cause of cancer-related death worldwide, and the burden of this devastating cancer is expected to increase further in coming years [1]. Although surgical resection and liver transplant are considered the gold-standard treatment modalities for HCC, their use is limited by the liver function of patients and lack of donors [2]. Nowadays nonsurgical treatments such as radiofrequency thermoablation (RFA) have been widely accepted as effective means of minimally invasive treatment for nonsurgical HCC [3]. Nevertheless peripheral tumors adjacent to extrahepatic organs were also suggested to be unsuitable because of the risk of heat injury, such as intestinal perforation and pleural effusion. Moreover when these techniques are used to treat tumors that are located in proximity of anatomic structures that might be injured by the thermal process, such as gallbladder, complete tumor

removal is difficult to achieve without incurring the serious risk of causing necrosis or perforation of the wall of the organ [4]. For the above reason, patients with lesions in the so-called high risk location could be commonly excluded from interventional procedures.

Only a few authors suggested that percutaneous treatment can be safely used to ablate tumors close to the gallbladder with some expedients. For example, a more cautious approach can be that of using multiple ethanol injections to eliminate the residual tumor adjacent to the gallbladder after RFA [5]. Others suggest treating these lesions after the injection of sterilized solution into the gallbladder fossa to space out the tumor from the gallbladder [4]. Recently Jiang et al. reported their experience with RFA without gallbladder isolation assisted by a laparoscopic approach [6]. In this study we reported our experience in 8 patients with HCC smaller than 5 cm located in the so-called high risk site that were treated with percutaneous RFA.

2. Materials and Methods

From December 2010 to October 2013 we performed percutaneous RFA in eight patients (5 men and 3 women) with liver cirrhosis and with HCC close to the gallbladder (<1 cm in distance). The mean tumor size was 3.2 cm (range: 2.4–4 cm) and tumor edges were near gallbladder wall from 10 to 0 mm. All patients in our study were selected during the followup for liver cirrhosis and the choice of the percutaneous ablative treatment was carried out by the evaluation of a multidisciplinary team of hepatologists, surgeons, and interventional radiologists [7]. The diagnosis of HCC was carried out in accordance with the guidelines of the European Association for the Study of the Liver (EASL) [8] for the diagnosis of HCC in cirrhotic patients. Tumor diameters ranged between 3.0 and 5 cm (Figure 1). The age of patients ranged from 52 to 78 years (mean \pm SD: 72.43 ± 5.66). Five patients were in Child-Pugh class A and 3 in class B. The α -fetoprotein levels, registered before the procedure, were on average 561.67 \pm 684 ng/mL (range: 25–1870).

Six tumors were located in segment V and two in segment IV. We used RFA and the ablations were performed and monitored according to the recommendations of the equipment manufacturers. Radiofrequency devices used were a 200 W RF generator and an impedance-based multiple-electrode RFA system (Boston Scientific Corporation, Natick, MA, USA). RFA was conducted using an expandable 15 G LeVeen needle, 15 cm long insulated cannula that contained 10 individual hook-shaped electrode arms (Boston Scientific Corporation, Natick, MA, USA). The needles had a maximum diameter of 50 mm when fully deployed.

We performed all liver thermal ablations using an expandable multielectrode system because we think that it is easier to evaluate the position of hooks after their deployment and to predict the volume of thermal effect more accurately with multielectrode system rather than with cool-tip needle. Furthermore the needle position is not influenced by respiratory movements.

The aim of performing radiofrequency ablation in all patients was complete destruction of the lesion with a 5 to 10 mm wide tumor-free margin around all possible aspects of each tumor. The RFA were performed in a single session for all patients. Conscious sedation and local anesthesia were used every time. All ablations were carried out percutaneously under ultrasound and computed tomography guidance. The procedure was performed with conscious sedation and local anesthesia. The routes of electrode insertion were carefully selected according to the feasibility of the needle path and the size and the shape of the lesion.

Needle introduction was performed, depending on the location of the nodule to be treated, in 4 patients through subcostal approach and in 4 patients through intercostal approach. To better conform the shape of the ablated volume to the tumor while reducing the risk of gallbladder perforation by the hook-shaped electrode arms of the device, we decided to insert the needle through the liver surface towards the gallbladder, perpendicularly to the gallbladder right wall.

Before the deploying of the hooks, the distance between the tip of the needle and the gallbladder wall was accurately

checked and kept away from gallbladder wall to avoid direct or thermal injuries.

The efficacy of treatment was assessed by dynamic triphasic CT, 30 days after the procedure. The treatment response was evaluated according to mRECIST criteria [9]. Complete response (CR) was considered the disappearance of any intratumoral arterial enhancement at CT evaluation; partial response (PR) was at least a 30% decrease of the longest diameter of the viable lesion evaluate as contrast enhancement in the arterial phase respect to the preprocedural CT result. Three-phase dynamic CT scans in the 3rd, 6th, and 12th months followup were performed for all patients.

Intraprocedural and postprocedural complications were evaluated according to the classification of the International Society of Radiology (SIR, Society of Interventional Radiology) [10] distinguishing between major (events that lead to substantial morbidity and disability, an increase of care, hospitalization, or a longer hospital stay) and minor complications. The presence of the “postablation syndrome,” defined as fever, nausea, vomiting, and localized pain in the abdomen and referred to the shoulder, was investigated during the first 48 h after treatment.

Moreover the CT scans obtained before and immediately after ablation and subsequently were reviewed by one experienced radiologist for the presence of gallbladder wall thickening of more than 2 mm, abnormal gallbladder wall enhancement, and pericholecystic fluid.

3. Results

In our experience there were no cases of treatment-related deaths. In addition, there were no major complications such as cholecystitis or gallbladder perforation. A minimal wall thickening of the gallbladder (2.0-3.0 mm, $n = 9$) was seen as focal wall enhancement adjacent to the RF ablation zone in 2 patients. All two cases of gallbladder wall thickening after ablation were associated with symptoms.

Postablative syndrome was observed in 6 patients, manifested by fever (four patients), chills (two patients), and localized pain in the abdomen (three patients). All patients reported various degrees of malaise in the days following the procedure such as asthenia, weakness that appeared three to five days after the procedure and lasted on average four days.

No procedure has been interrupted and technical success was obtained in 100% of patients. In all patients, during RFA, a slowly enlarging and coalescing hyperechoic zone appeared around the distal tip of the needle, resulting from vaporization of fluid and formation of microbubbles of gas (Figure 2). At the end of the treatment, an irregular and poorly defined echogenic zone occupied the whole treated area. At the end of the procedures, after the automatic cool-down of the RF system, the generator was reactivated during the needle retraction to prevent the tumor dissemination and to permit the coagulation of the needle channel.

CT control after 30 days from the first procedure showed complete necrosis (no detectable remaining tumor on CT) in seven patients (87%). In the remaining patient, the lesion was treated with chemoembolization.

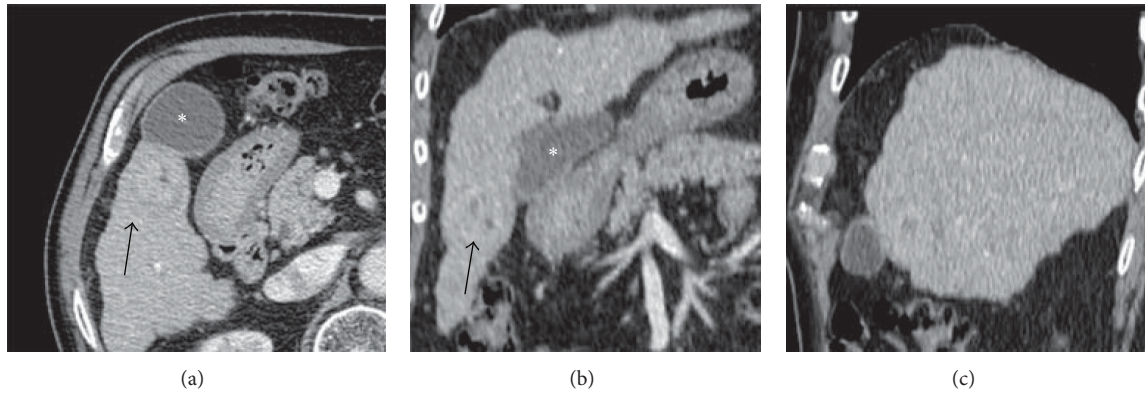


FIGURE 1: CT Preprocedural axial image (a) and multiplanar reconstructions (b, c) show the relationship between hepatocellular carcinoma (black arrow) and the gallbladder (*).

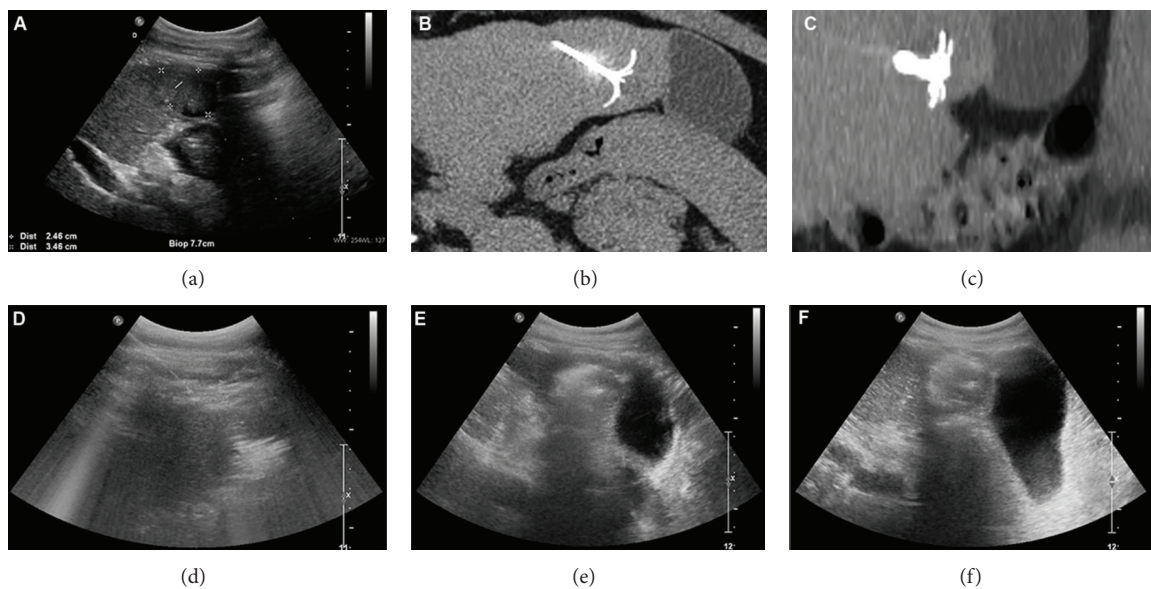


FIGURE 2: Radiofrequency ablation of the hepatocellular carcinoma performed under US and CT control with an expandable needle. (a) US view shows the hepatocellular carcinoma and the planning of the needle insertion in the liver lesion. CT axial (b) and reformatted (c) images depict the position of the needle inside the lesion. (d) US control during radiofrequency shows the hyperechoic zone that covers the entire liver lesion. US controls at the end of the first roll-off (e) and at the end of the procedure (f) do not depict any gallbladder anomalies.

The follow-up times ranged from 12 to 18 months (mean: 15 months) in the patients with completed ablations.

One patient had local recurrence at 11 months. The remaining six patients showed no local recurrence at the end of the follow-up period (Figure 3). None of the patients showed evidence of gallbladder disease.

4. Discussion

RFA is a minimally invasive method used to destroy tumors within solid organs and it has been used for primary liver tumors and for hepatic metastases [11, 12]. Nevertheless, RFA of tumors adjacent to the gallbladder is often accompanied by high risk of gallbladder perforation, acute cholecystitis, or postoperative bleeding [13, 14]. Furthermore, combination therapy or a secondary round of RFA treatment is often

needed to achieve complete tumor eradication [15]. To separate the liver tissue from the gallbladder and to prevent gallbladder injuries during thermal ablation, Cirocchi and colleagues suggested the injection of 40–80 mL of aseptic solution into the gallbladder fossa and cystic plate just before the RFA or the use of a “lift-expand” technique to confirm that the needle tip does not stick into the gallbladder wall [11]. Recently Jiang and coworkers suggested that tumor next to the gallbladder can be safely treated with RFA with laparoscopic guidance without the need of removing or isolating the gallbladder [6].

Although these methods of gallbladder isolation and laparoscopic RFA appear to be safe, they may increase the duration time of the procedure, may have an influence on health care costs of the examination, and may involve additional risks for patients [11].

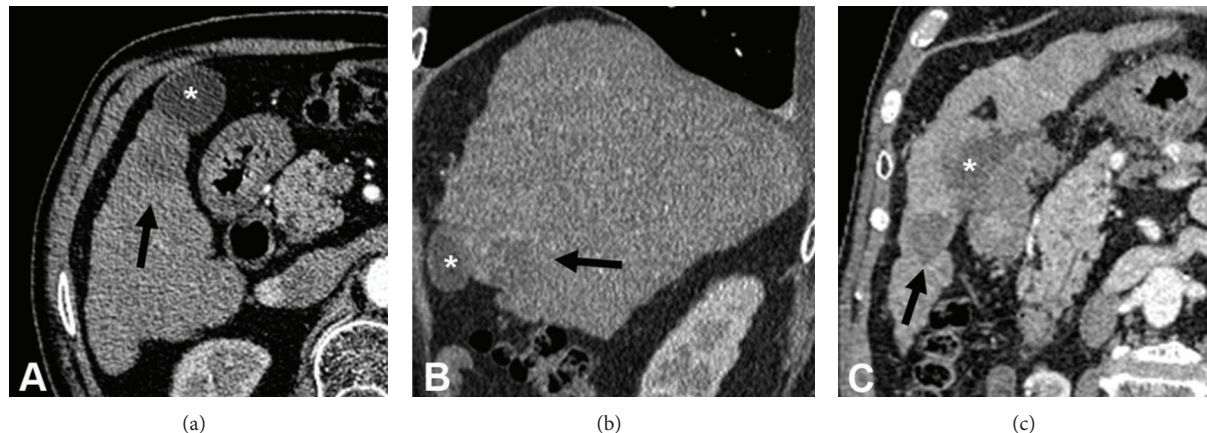


FIGURE 3: Axial CT image (a) and CT multiplanar reconstructions (b, c), performed after six months, show the absence of contrast medium enhancement of the ablated liver lesion (black arrow) without gallbladder (*) damage.

In this report we described eight cases of HCC adjacent to the gallbladder that were successfully treated with percutaneous RFA without gallbladder isolation. Previously Chopra and colleagues [15] conducted a study to assess the feasibility and safety of RFA of hepatic tumors (primitive or metastatic) with a maximum diameter of less than 3 cm, adjacent to the gallbladder. The authors used RFA with an expandable electrode to treat 8 patients (2 patients with HCC and 6 patients with liver metastases). As assessed by CE-CT scan after one month from the procedure, a complete ablation was achieved in all patients except one (87%). Except for gallbladder wall thickening, no complications were reported. The authors concluded that radiofrequency ablation of hepatic tumors adjacent to the gallbladder is feasible and potentially safe for lesions with a maximum diameter less than 3 cm. Our results not only confirm those by Chopra and coworkers but also suggest the feasibility of RFA even in HCC adjacent to the gallbladder larger than 3 cm and less than 5 cm.

To this purpose, a proper knowledge of the available resources and careful preprocedural planning were mandatory.

We decided to use RFA instead of other percutaneous procedures (e.g., percutaneous laser ablation and microwave ablation) because of the opportunity to monitor in real time the necrosis of the tissue, which makes this technique particularly suitable for the treatment of lesions located in the close proximity of critical structures. Indeed, while during percutaneous laser ablation or microwave ablation there are no reliable methods to monitor the evolving necrosis of the hepatic tissue, thus resulting in a wide variability of the amount of liver tissue ablated with different protocols [16], during RFA it is possible to exactly detect the occurrence of the necrosis by monitoring the electrical impedance (Ohm) of the hepatic tissue during the delivery of RF energy. Tissue desiccation causes an increase of the impedance within the ablated volume that prohibits the passage of electrical current and leads the power output from the generator to fall to zero (i.e., roll-off) [17]. In this way it is possible to reproduce a constant volume of necrosis.

The correct selection of the appropriate device to perform the tumor ablation was also a critical issue.

Teratani and colleagues [18] treated 207 patients with hepatocellular carcinoma (HCC) in presumably high risk locations, using a single probe cool-tip electrode, declaring that the use of multiprobe system with extension of the hooks could not be precisely controllable when applied to nodules adjacent to large vessels or extrahepatic organs. Nevertheless we choose an expandable multiple-electrode system and we decided to insert the needle at a direction perpendicular to the gallbladder wall in order to prevent, during the opening of the hooks, the organ perforation. In this way we were sure that the hooks would be positioned in the safety position, according to three spatial dimensions.

5. Conclusions

Although limited, our experience suggests that percutaneous RFA is feasible even for lesions larger than 3 cm located in close adjacency to the gallbladder. Careful preprocedural planning with a proper knowledge of the available technology is mandatory. Obviously, the promising result in these three cases needs to be confirmed in larger series of patients with lesions next to critical structures.

Conflict of Interests

The authors declare that there is no conflict of interests regarding the publication of this paper.

References

- [1] A. P. Venook, C. Papandreou, J. Furuse, and L. L. de Guevara, "The incidence and epidemiology of hepatocellular carcinoma: a global and regional perspective," *The Oncologist*, vol. 15, supplement 4, pp. 5–13, 2010.
- [2] Y. K. Cho, J. K. Kim, W. T. Kim, and J. W. Chung, "Hepatic resection versus radiofrequency ablation for very early stage hepatocellular carcinoma: a markov model analysis," *Hepatology*, vol. 51, no. 4, pp. 1284–1290, 2010.

- [3] Z. W. Peng, Y. J. Zhang, M. S. Chen, X. J. Lin, H. H. Liang, and M. Shi, "Radiofrequency ablation as first-line treatment for small solitary hepatocellular carcinoma: long-term results," *European Journal of Surgical Oncology*, vol. 36, no. 11, pp. 1054–1060, 2010.
- [4] E. Levit, P. Bruners, R. W. Gunther, and A. H. Mahnken, "Bile aspiration and hydrodissection to prevent complications in hepatic RFA close to the gallbladder," *Acta Radiologica*, vol. 53, no. 9, pp. 1045–1048, 2012.
- [5] B. M. Luo, Y. L. Wen, H. Y. Yang et al., "Percutaneous ethanol injection radiofrequency and their combination in treatment of hepatocellular carcinoma," *World Journal of Gastroenterology*, vol. 11, no. 40, pp. 6277–6280, 2005.
- [6] K. Jiang, M. Su, X. Zhao et al., "“One-off” Complete Radiofrequency Ablation of Hepatocellular Carcinoma Adjacent to the Gallbladder by a Novel Laparoscopic Technique Without Gallbladder Isolation," *Cell Biochemistry and Biophysics*, pp. 1–8, 2013.
- [7] R. G. Gish, R. Lencioni, A. M. di Bisceglie, J. Raoul, and V. Mazzaferro, "Role of the multidisciplinary team in the diagnosis and treatment of hepatocellular carcinoma," *Expert Review of Gastroenterology and Hepatology*, vol. 6, no. 2, pp. 173–185, 2012.
- [8] J. Bruix, M. Sherman, J. M. Llovet et al., "Clinical management of hepatocellular carcinoma. Conclusions of the Barcelona-2000 EASL conference. European association for the study of the liver," *Journal of Hepatology*, vol. 35, no. 3, pp. 421–430, 2001.
- [9] R. Lencioni and J. M. Llovet, "Modified recist (mRECIST) assessment for hepatocellular carcinoma," *Seminars in Liver Disease*, vol. 30, no. 1, pp. 52–60, 2010.
- [10] S. N. Goldberg, C. J. Grassi, J. F. Cardella et al., "Image-guided tumor ablation: standardization of terminology and reporting criteria," *Journal of Vascular and Interventional Radiology*, vol. 16, no. 6, pp. 765–778, 2005.
- [11] R. Ciocchi, S. Trastulli, C. Boselli et al., "Radiofrequency ablation in the treatment of liver metastases from colorectal cancer," *The Cochrane Database of Systematic Reviews*, vol. 6, Article ID CD006317, 2012.
- [12] M. H. Chen, W. Yang, K. Yan et al., "Radiofrequency ablation of problematically located hepatocellular carcinoma: tailored approach," *Abdominal Imaging*, vol. 33, no. 4, pp. 428–436, 2008.
- [13] T. Yamamoto, S. Kubo, K. Hirohashi et al., "Secondary hemocholecyst after radiofrequency ablation therapy for hepatocellular carcinoma," *Journal of Gastroenterology*, vol. 38, no. 4, pp. 399–403, 2003.
- [14] K. Kurokohchi, S. Watanabe, T. Masaki et al., "Combination therapy of percutaneous ethanol injection and radiofrequency ablation against hepatocellular carcinomas difficult to treat," *International Journal of Oncology*, vol. 21, no. 3, pp. 611–615, 2002.
- [15] S. Chopra, G. D. Dodd III, M. P. Chanin, and K. N. Chintapalli, "Radiofrequency ablation of hepatic tumors adjacent to the gallbladder: feasibility and safety," *American Journal of Roentgenology*, vol. 180, no. 3, pp. 697–701, 2003.
- [16] C. M. Pacella, G. Bizzarri, G. Francica et al., "Percutaneous laser ablation in the treatment of hepatocellular carcinoma with small tumors: analysis of factors affecting the achievement of tumor necrosis," *Journal of Vascular and Interventional Radiology*, vol. 16, no. 11, pp. 1447–1457, 2005.
- [17] M. A. Arata, H. L. Nisenbaum, T. W. I. Clark, and M. C. Soulen, "Percutaneous radiofrequency ablation of liver tumors with the LeVein probe: is roll-off predictive of response?" *Journal of Vascular and Interventional Radiology*, vol. 12, no. 4, pp. 455–458, 2001.
- [18] T. Teratani, H. Yoshida, S. Shiina et al., "Radiofrequency ablation for hepatocellular carcinoma in so-called high-risk locations," *Hepatology*, vol. 43, no. 5, pp. 1101–1108, 2006.

Review Article

New Imaging Strategies Using a Motion-Resistant Liver Sequence in Uncooperative Patients

Bong Soo Kim, Kyung Ryeol Lee, and Myeng Ju Goh

Department of Radiology, Jeju National University Hospital, Jeju National University School of Medicine, 1753-3 Ara-1-dong, Jeju-si, Jeju-do 690-716, Republic of Korea

Correspondence should be addressed to Bong Soo Kim; 67kbs@medimail.co.kr

Received 30 June 2014; Accepted 17 August 2014; Published 27 August 2014

Academic Editor: Pascal Niggemann

Copyright © 2014 Bong Soo Kim et al. This is an open access article distributed under the Creative Commons Attribution License, which permits unrestricted use, distribution, and reproduction in any medium, provided the original work is properly cited.

MR imaging has unique benefits for evaluating the liver because of its high-resolution capability and ability to permit detailed assessment of anatomic lesions. In uncooperative patients, motion artifacts can impair the image quality and lead to the loss of diagnostic information. In this setting, the recent advances in motion-resistant liver MR techniques, including faster imaging protocols (e.g., dual-echo magnetization-prepared rapid-acquisition gradient echo (MP-RAGE), view-sharing technique), the data under-sampling (e.g., gradient recalled echo (GRE) with controlled aliasing in parallel imaging results in higher acceleration (CAIPIRINHA), single-shot echo-train spin-echo (SS-ETSE)), and motion-artifact minimization method (e.g., radial GRE with/without k-space-weighted image contrast (KWIC)), can provide consistent, artifact-free images with adequate image quality and can lead to promising diagnostic performance. Understanding of the different motion-resistant options allows radiologists to adopt the most appropriate technique for their clinical practice and thereby significantly improve patient care.

1. Introduction

Magnetic resonance (MR) imaging is an excellent imaging modality to evaluate the liver which is vulnerable to a spectrum of neoplastic and nonneoplastic conditions, and MR imaging can provide various types of information that it is able to generate in order to demonstrate reliable display of disease process. Artifacts produced by physiological motion caused by patient respiration and bowel peristalsis are a challenge when using MR imaging for hepatic imaging. Motion artifacts may also distinctly degrade the quality of MR images. Therefore, suppression of motion artifacts is the prime determinant of the diagnostic efficacy of liver MR imaging. With the recent advances in the development of high-performance gradient coils and phased-array torso coils as well as the continuing evolution of software, new pulse sequences have become available for motion-resistant liver MR imaging. In this paper, we discuss motion-resistant MR imaging in terms of its technical basis, advantages and limitations, and primary clinical applications.

2. MR Imaging Sequences

Motion-resistant protocols achieve improved image quality in the setting of noncooperative patients. A strategy for achieving optimal images includes temporally matching the data acquisition and short scanning time by acquiring the critical data for image creation during a short breath-hold time and thus rendering this technique relatively insensitive to patient motion [1]. Another approach used to minimize the impact of respiratory motion in the liver is to modify the data acquisition so as to minimize effects of motion using a radial k-space sampling scheme (Table 1) [2].

2.1. T1-Weighted Sequences

2.1.1. Magnetization-Prepared Rapid-Acquisition Gradient Echo (MP-RAGE) Sequence. The dual GE in-phase (IP) and opposed-phase (OP) sequence has become a routine component of liver MR imaging. This sequence is useful for detecting the presence of fat within the liver and lipid

TABLE 1: Parameters for the motion-resistant protocol used for 3.0T MR imaging scanners.

Parameter	Precontrast sequences			Postcontrast sequences		
	T1-weighted 2D MP-RAGE in-phase/out-of-phase	T2-weighted SS-ETSE	BLADE	T1-weighted 3D-GRE with CAIPIRINHA	T1-weighted 3D-GRE with CAIPIRINHA (echo-sharing technique)	T1-weighted radial 3D-GRE (KWIC technique)
Plane of acquisition	Axial	Axial, coronal	Axial	Axial	Axial	Axial
TR (milliseconds)	1500	1200	3910	4.6	4.7	3.4
TE (milliseconds)	2.3/3.4	150	105	2.2	1.5	1.7
TI (milliseconds)	1200					
Flip angle (°)	20	120	160	12	12	12
Echo train length		102	23	1	2	
Parallel imaging	GRAPPA 2	GRAPPA 2	GRAPPA 2	2D CAIPIRINHA 2 × 2	GRAPPA 2	GRAPPA 2
BW/pixel (Hz)	210/180	710	300	395	870	1040
Matrix (frequency × phase)	256 × 173	320 × 213	320 × 320	384 × 227	384 × 211	320 × 320
FOV (mm)	302 × 304	302 × 394	380 × 380	302 × 227	296 × 299	340 × 340
Number of sections	36	36	36	80	80	80
Section thickness (mm)	5	5	5	2.5	2.5	3.0
Intersectional gap (mm)	1.5	1.5	1.5	0	0	0
Number of signal acquisitions	1	1	1	1	1	1
Fat suppression	None	Fat sat for axial, none for coronal	Fat sat	Fat sat	Fat sat	Fat sat
Respiratory control	BI	BI	FB	BH	FB	BH

BH, breath-hold; BI, breathing-independent; BLADE, proprietary name for periodically rotated overlapping parallel lines with enhanced reconstruction (PROPELLER) in MR systems from Siemens Medical Solutions; BW, bandwidth; Hz, Hertz; CAIPIRINHA, controlled aliasing in parallel imaging results in higher acceleration; FB, free breathing; FOV, field of view; GRE, gradient recalled echo; KWIC, k-space weighted image contrast; MP-RAGE, magnetization-prepared rapid-acquisition gradient echo; sat, saturation; SS-ETSE, single-shot echo-train spin-echo; TE, echo time; TI, inversion time; TR, repetition time.

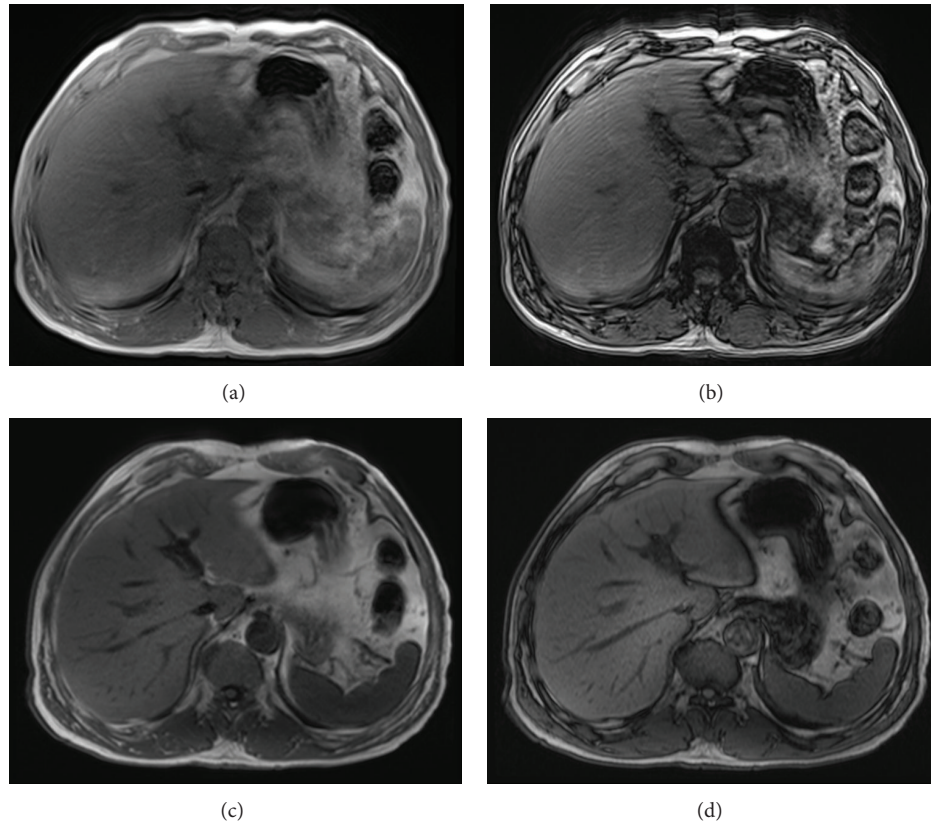


FIGURE 1: MR images obtained in a 67-year-old man. Standard T1-weighted 2D SGE in-phase (a) and out-of-phase (b) images show severe motion artifacts caused by his breathing. The motion-resistant protocol using axial T1-weighted 2D MP-RAGE in-phase (c) and T1-weighted 2D MP-RAGE out-of-phase (d) images demonstrate substantially reduced artifacts and motion-free, high-quality images in this patient.

within adrenal masses in order to characterize them as adenomas [1, 3, 4]. Dual GE IP/OP imaging is performed as multiline GE acquisitions that require patients to suspend their respiration as the sequences are generally 10–20 seconds in duration. A new application of MP-RAGE IP/OP images is able to substitute standard dual GR IP/OP imaging with moderate image quality in the elderly, severely debilitated, and in young children (Figure 1) [5–7]. MP-RAGE operates as a slice-by-slice, single-shot technique used during free breathing. This sequence can be used to obtain motion-free images with acquisition times as short as one second. Magnetization preparation is currently performed with a 180° inversion pulse in order to impart greater T1-weighted information. The sequence acquires data using a very short repetition time (TR) and low flip-angle excitation pulses in order to reduce the acquisition time and maintain the prepared magnetization. SGE IP/OP technique acquires dual echo images simultaneously which has no spatial misregistration between slices, and MP-RAGE IP/OP imaging is a single echo technique, acquired in two separate acquisitions. Therefore, respiratory triggering technique could be needed for preventing misregistration, which results in long acquisition time. Another disadvantage of MR-RAGE IP/OP imaging is presence of bounce-point artifacts seen on inversion recovery sequence. They are

seen at the interface between hepatic vessels and hepatic parenchyma. Notwithstanding these disadvantages, only MP-RAGE IP/OP sequence would be applicable for acquisition of chemical shift imaging in an usual clinical setting, when 2D-GRE is not feasible or might generate nondiagnostic images, such as in the case of uncooperative patients and pediatrics [5].

2.2. T2-Weighted Sequences

2.2.1. Single-Shot, Echo-Train, and Spin-Echo (SS-ETSE) Sequence.

The SS-ETSE sequence is the most widely available, fastest imaging method. This technique is used to fill the entire k-space after a single excitation. It measures only half of the k-space lines and uses the k-space symmetry to regenerate the other half [2]. Images are obtained in less time with one second and with virtually no motion artifact even during free breathing [8]. The SS-ETSE sequence is the mainstay tool for water-sensitive imaging of the upper abdomen in noncooperative patients (Figure 2). In cases of extreme motion, multiple repeated imaging loops of SS-ETSE can offer the benefit of an increased signal-to-noise ratio (SNR) and resolution in conjunction with a motion-correction algorithm, snapshot-to-volume reconstruction [9]. This technique provides low contrast as there is a relatively small T2 difference between

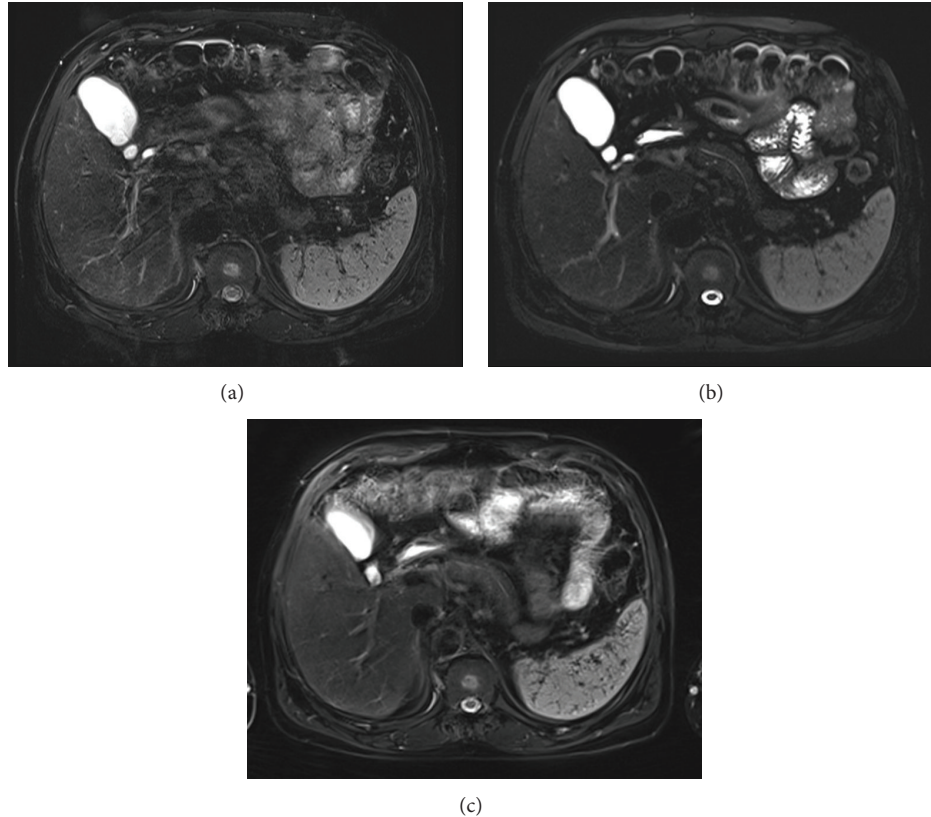


FIGURE 2: MR images obtained in a 53-year-old man with chronic liver disease. The conventional T2-weighted turbo spin-echo image (a) shows motion artifacts in the right posterior section of the liver. The artifact is improved on T2-weighted SS-ETSE (b) and BLADE (c) (proprietary name for periodically rotated overlapping parallel lines with enhanced reconstruction (PROPELLER) in MR systems from Siemens Medical Solutions) MR images. Much better sharpness of the liver edge and pancreas and clearer depiction of the main pancreatic duct are seen on T2-weighted SS-ETSE (b) and BLADE (c).

diseased and normal tissue and it is routinely coupled with fat suppression in order to increase its sensitivity to detect hepatic lesions.

2.2.2. Periodically Rotated Overlapping Parallel Lines with Enhancement Reconstruction (PROPELLER). This T2-weighted radial imaging technique, introduced by Pipe [10], is intrinsically self-navigated as oversampling of the central k-space can be used to reduce motion characteristics and to correct motion artifacts. The motion artifacts in this technique are not propagated in the phase-encoding direction as that changes with each radial section (Figure 2). Instead, the movement artifacts are dispersed throughout the radial sections (streak artifact) and become less prominent. The disadvantages of radial k-space filling include its longer imaging time and residual artifacts for through-plane motion as this technique is section-selective and useful for decreasing in-plane motion artifacts [2].

2.3. Contrast-Enhanced Fat-Suppressed T1-Weighted Three-Dimensional (3D) Gradient Recalled Echo (GRE) Sequence. Contrast-enhanced dynamic MR imaging has a key role in the detection and characterization of focal liver lesions when

using a nonspecific extracellular GBCA [8, 11]. The hepatic arterial-dominant phase is most useful for detecting hypervascular liver tumors such as hepatocellular carcinomas and hypervascular metastases. Hepatic arterial phase images can be more frequently degraded than images from other phases, for example, early hepatic venous phase or interstitial phase. On dynamic MR imaging, poor image quality is generally caused by respiratory motion artifacts. Therefore, strategies to compensate for patient motion must be developed for uncooperative patients. Two motion-resistant methods achieve improved hepatic arterial-dominant phase in uncooperative patients. First, the radial GRE Sequence can be used to modifying the data acquisition in order to minimize the motion effects. Second, the images are acquired during a short breath-hold time before deterioration resulting from respiration using the newly developed, parallel acceleration technique (CAIPIRINHA technique).

2.3.1. Motion-Resistant, Free-Breathing, Three-Dimensional (3D) Radial Fat-Suppressed GRE Sequence. The 3D T1-weighted volumetric-interpolated GRE sequence with rectilinear Cartesian k-space sampling during single breath-hold, as usually performed, is sensitive to motion artifacts and

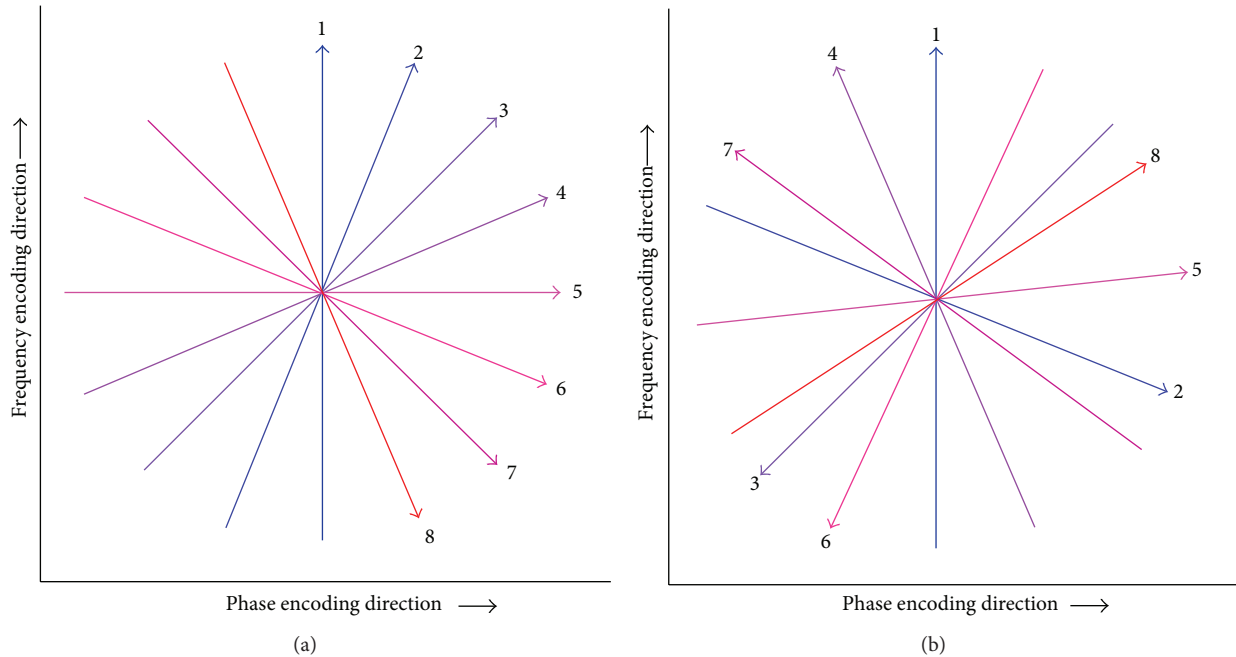


FIGURE 3: Radial k-space sampling system on the interleaved angle-bisection and golden-angle acquisitions. Radial spokes on the interleaved angle-bisection are acquired at a short angular distance. In golden-angle acquisition, the angle is continuously increased by a large angular distance (111.25°), which leads to uniform coverage for an arbitrary number of spokes.

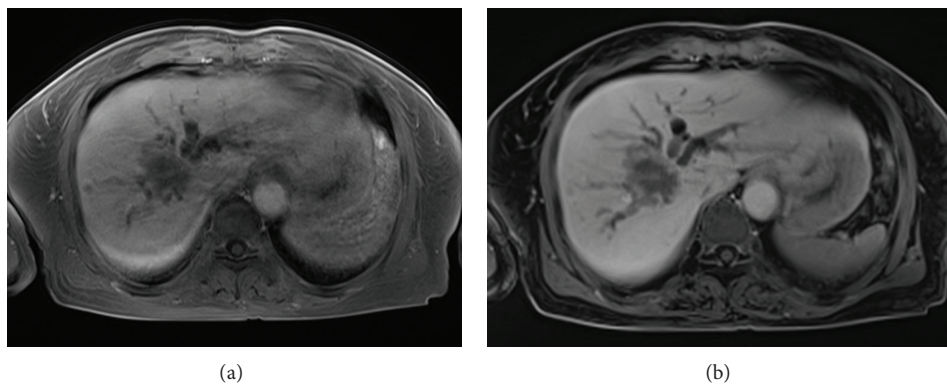


FIGURE 4: MR images obtained in a 70-year-old woman with an intrahepatic mass-forming cholangiocarcinoma. The T1-weighted 3D conventional breath-hold GRE image (a) shows blurred tumor resolution and dilated intrahepatic bile ducts caused by moderate motion artifacts. The free-breathing T1-weighted 3D radial GRE image (b) shows clear definition of the liver tumor and renders increasing conspicuity of bile-duct invasion. No motion artifacts are present in this image.

can result in suboptimal images in patients who cannot adequately hold their breath. Recently, a more motion-robust, 3D GRE sequence has been developed (3D Radial GRE) that uses the “stack-of-stars” scheme to acquire data in a radial, spoke-wheel fashion [12–19]. 3D radial GRE has a higher sampling density at central k-space and under-samples at the k-space margins, with the net effect that images are less sensitive to motion artifacts caused by phase errors [14, 16–18]. There are two radial acquisition methods of the interleaved, angle-bisection scheme and the golden-angle scheme, which differ primarily in the temporal order of radial samplings [19].

In the interleaved angle-bisection scheme, radial spokes are acquired at a small, angular distance, whereas golden-angle acquisition acquires each spoke at a large angular distance from the preceding spoke (Figure 3). The value of golden-angle sampling is that it provides more uniform angular coverage of the k-space than interleaved, angle-bisection sampling. The 3D radial GRE sequence can provide excellent motion-controlled images with high spatial resolution in noncooperative patients, especially sedated children, at the expense of a longer acquisition time (approximately 2-3 minutes) (Figure 4) [12]. Residual artifacts caused by motion and

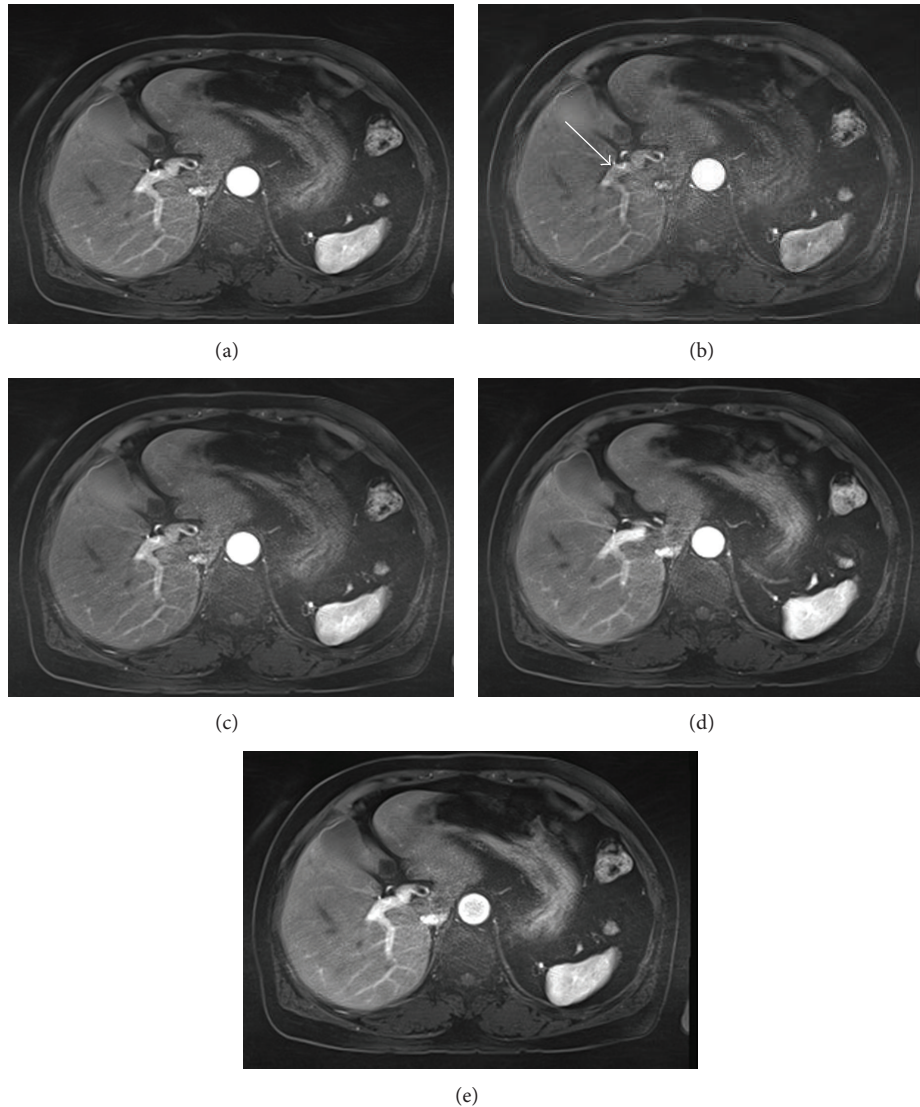


FIGURE 5: MR images obtained in a 68-year-old woman for workup of metastasis. Contrast-enhanced dynamic 3D radial GRE using KWIC during hepatic arterial dominant phase imaging comprised four subframe images. The full-frame 3D radial GRE (a) image shows homogenous enhancement in the portal vein, but not in the hepatic vein. The first subframe image (b) obtained at 5-second temporal resolution demonstrates minimal portal venous enhancement with laminar flow (arrow). On the next serial three subframe images ((c)–(e)), the portal vein and hepatic parenchyma have gradually increasing enhancement.

flow are spread in two dimensions and appear as streaking artifacts on radial imaging, rather than the ghost-like artifacts seen in Cartesian phase-encoding acquisition MR imaging.

2.3.2. Contrast-Enhanced, Motion-Resistant, Dynamic 3D Radial GRE Using *k*-Space Weighted Image Contrast (KWIC). KWIC which is a recently proposed image reconstruction method provides time-resolved sub-frame images as well as full-frame images. The 3D radial KWIC sequence may be able to provide useful motion-insensitive data for dynamic MR imaging, that is, time-resolved subframe images, with reasonably high temporal (approximately 3–5 seconds) and spatial resolution (Figure 5) [15, 19–21]. This reconstruction technique can produce four to 16 subframe KWIC images

per full-frame gridded image. Recently, Chandarana et al. reported that free-breathing, dynamic, 3D radial GRE using golden-angle sampling and compressed sensing allowed high image quality in the hepatic arterial and portal venous phases which were obtained during continuous scanning of 90 seconds, comparable to the 3D, breath-hold GRE sequence [19].

2.3.3. 3D GRE with Controlled Aliasing in Parallel Imaging Results in Higher Acceleration (CAIPIRINHA) Technique. Parallel imaging reduces the imaging time by under-sampling in the phase-encoding direction according to an acceleration factor (R). The limitation of parallel imaging reconstructions are a decrease in the signal-to-noise ratio (SNR) that heavily

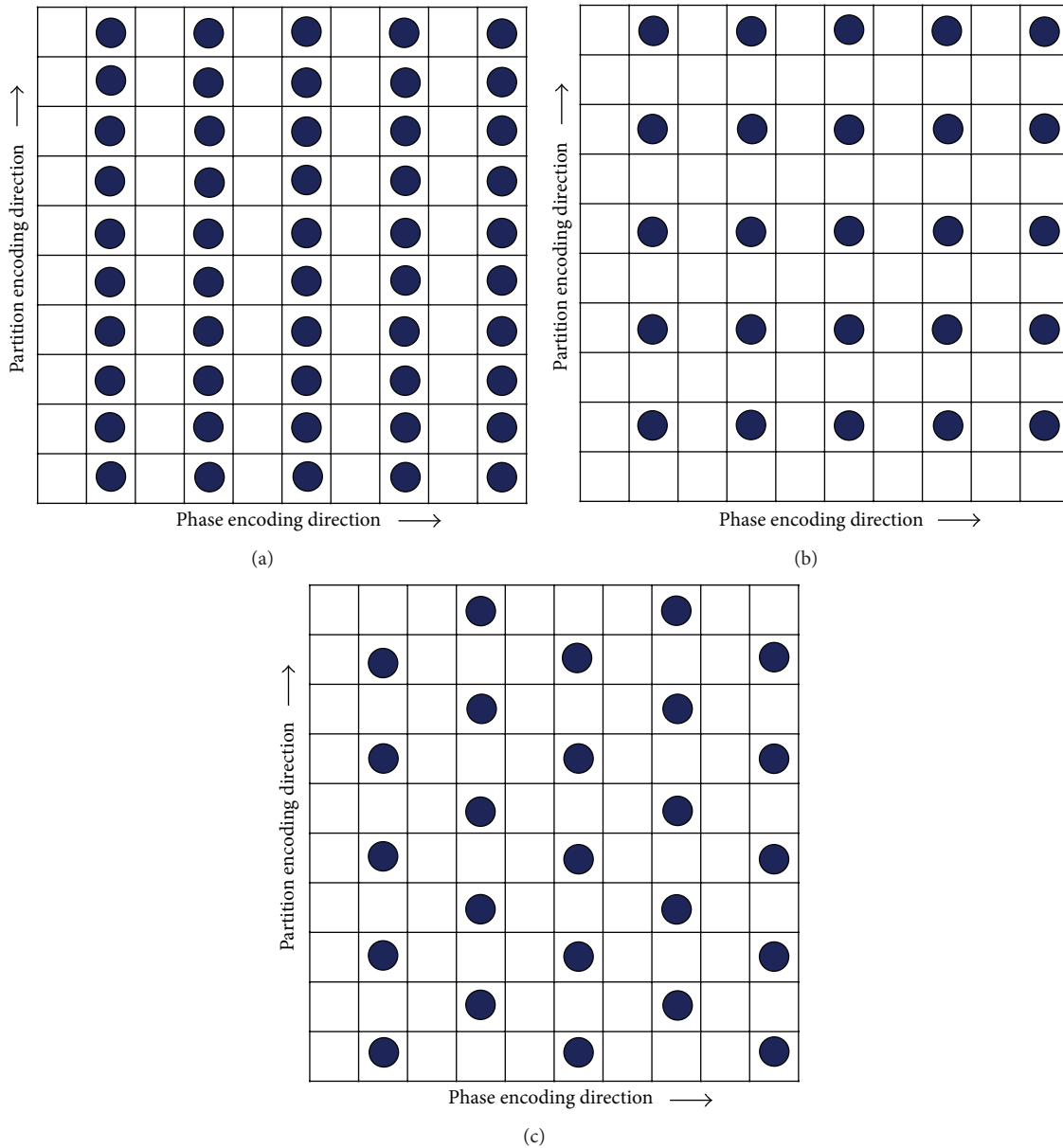


FIGURE 6: Concept of the under-sampling pattern of the CAIPIRINHA technique. The lattice work represents k-space. The black dots indicate the sampling positions, and the empty cells imply omitted sampling. (a) In the 1D parallel acquisition technique for a given total acceleration factor of 2, the under-sampling pattern can occur only in the phase-encoding direction. (b) In the 2D standard parallel acquisition technique without delta shift for a given total acceleration factor 4 (2×2), the under-sampling pattern can be generated concurrently in the phase- and partition-encoding directions. (c) In the 2D CAIPIRINHA technique with a delta shift of 1 for a given total acceleration factor 4 (2×2), data sampling is acquired by shifting every other filled partition-encoding line by as much as 1 in the partition-encoding direction. By shifting the sampling positions in a well-directed manner, aliasing can be shifted and reduced.

depends on the geometry of the coil array used and residual aliasing artifacts at high acceleration factors, which lead to a loss in image quality [22]. With the CAIPIRINHA technique, the acquisition pattern is modified in a controlled way by shifting the sampling positions from their normal positions with respect to each other in the partition-encoding direction, which is often referred to as the delta shift [23, 24]. This reduces the quantity or severity of aliased pixels, which leads to a more innovative parallel imaging reconstruction with

fewer residual aliasing artifacts (Figure 6). This technique could provide higher quality images even at high acceleration factors, which is especially attractive for use in patients with breath-hold difficulties or those with poor compliance (Figure 7).

The CAIPIRINHA technique can reduce the overall acquisition time from 20 to 10 seconds and can shorten the breath-holding time needed to obtain hepatic arterial-dominant phase images (Figure 8) [25]. 3D GRE with

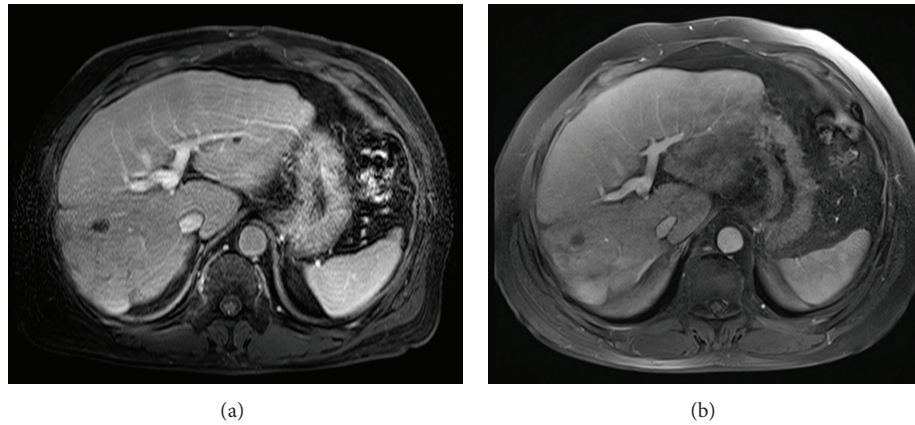


FIGURE 7: MR images in a 65-year-old man with liver cirrhosis. The conventional breath-hold T1-weighted 3D GRE sequence (acquisition time: 23 seconds) and the CAIPIRINHA 3D GRE sequence (acquisition time: 12 seconds) were obtained during the early hepatic venous phase. T1-weighted 3D GRE (a) shows blurred resolution of the intrahepatic vessel and the hepatic margin caused by motion artifacts. Much greater sharpness of the hepatic edge and a clearer depiction of the intrahepatic vessel are shown on the T1-weighted 3D CAIPIRINHA GRE sequence.

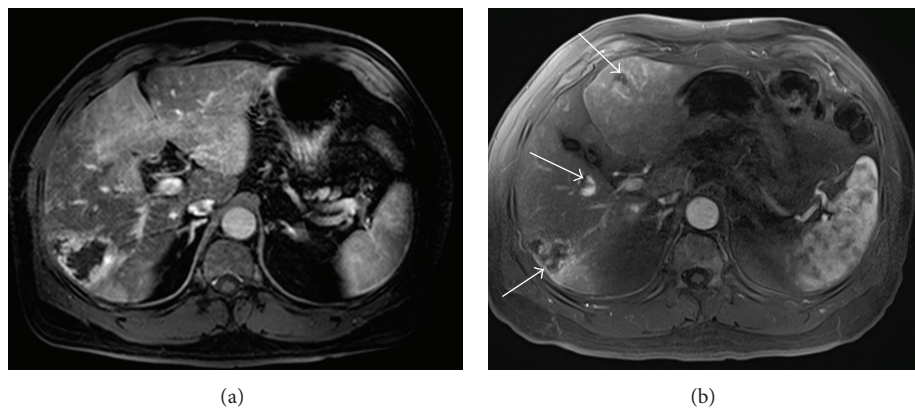


FIGURE 8: MR images obtained in a 61-year-old man with multiple hemangiomas. (a) A hepatic arterial dominant phase image using conventional 3D GRE during a 20-second breath-hold shows respiratory motion artifacts. (b) A hepatic arterial dominant phase image using the CAIPIRINHA 3D GRE sequence during a 12-second breath-hold demonstrates good image quality without artifacts, high spatial resolution, and a well-timed late arterial image and, thus, resulting in detecting an increasing number of hemangiomas (arrows).

CAIPIRINHA technique have better resolution than radial GRE. Therefore, dynamic liver MR imaging using CAIPIRINHA technique is preferentially attempted in patients who can suspend breath-hold of approximately 10 seconds. The primary intention of using dynamic liver MR imaging using CAIPIRINHA technique is judged by the scanning technologist who made determination based on tolerability by patients after performing precontrast scanning. Recently, the rate of transient severe motion (TSM) during the arterial phase has been more frequently reported on dynamic MR imaging using gadoxetate disodium (17% (17 of 99 patients)) [26] which has been increasingly used for the detection and characterization of focal lesions [27, 28]. Pietryga et al. reported that rapid, triple, arterial-phase imaging using the CAIPIRINHA technique during a single breath-hold is an effective method for obtaining well-timed, late arterial-phase image sets with reduced motion artifact in most patients

who experience TSM in the arterial phase [29]. A recently proposed method that includes time-resolved imaging using the echo-sharing technique, such as time-resolved imaging with interleaved stochastic trajectories (TWIST; Siemens) or time-resolved imaging of contrast kinetics (TRICKS; GE), may also provide motion-resistant imaging and have higher signal-to-noise ratios [30, 31]. The CAIPIRINHA technique combined with echo-sharing has a higher sampling density for the central k-space and under-samples for the k-space periphery. This technique can allow whole-liver coverage with multiple, arterial-phase acquisitions (4–15 sets) of higher temporal resolution (approximately 2–5 seconds) during one breath-hold (Figure 9) [31]. The multiple, arterial acquisitions provide the benefit of robustness to some artifacts, in which artifacts that compromise one data set, if transient, may not disturb others and provide more detailed enhancement characteristics of hepatic lesions [29, 32, 33].

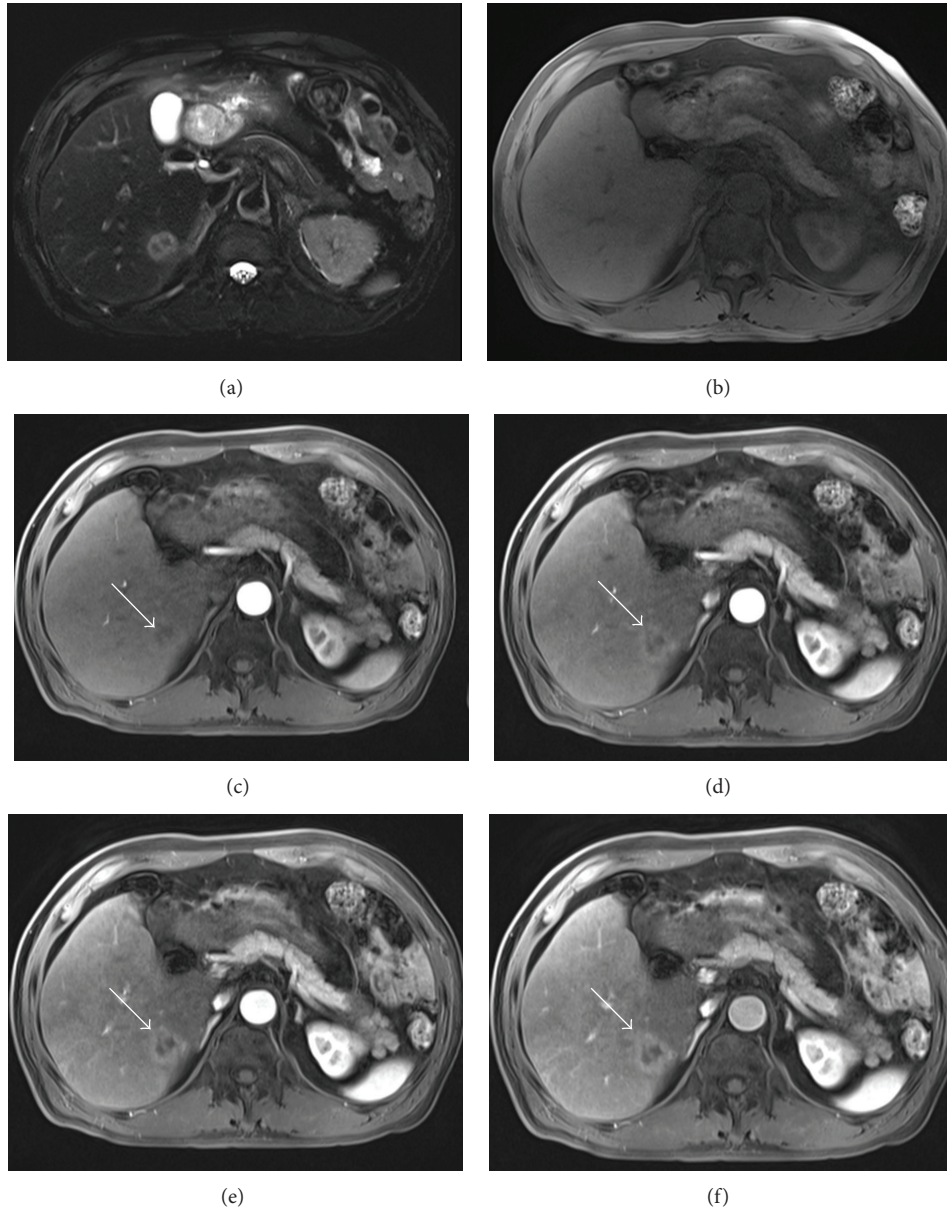


FIGURE 9: MR images obtained in 63-year-old man with a hepatocellular carcinoma. A hepatocellular carcinoma in segment 6 is clearly shown on T2-weighted fat-suppressed SS-ETSE (a). Precontrast (b) and gadolinic acid- (Gd-EOB-DTPA-) enhanced 3D CAIPIRINHA GRE obtained using view-sharing technique ((c)–(f)) images during multiple hepatic arterial dominant phases at 4-second temporal resolution, show gradually increasing hypervascularity of the hepatocellular carcinoma (arrows) compared with that of the liver parenchyma.

3. Conclusion

Liver MR imaging using a variety of motion-resistant sequences is able to enhance the quality of liver imaging in patients who cannot remain motionless. In uncooperative patients, the combination of faster imaging, data under-sampling and the motion-artifact minimization method may eventually provide spatial resolution and image quality that equals that available using conventional MR sequences in cooperative patients. With the continuing improvements in sequence technology and with more clinical experience, the utility of motion-resistant MR imaging for evaluating the

liver in uncooperative patients will be validated and will improve.

Conflict of Interests

The authors declare that there is no conflict of interests regarding the publication of this paper.

Acknowledgments

The authors thank Bonnie Hami, MA (USA), for her editorial assistance in preparing the paper. The authors also thank

Siemens Healthcare for their research support in the form of hardware and software.

References

- [1] B. S. Kim, W. Anghong, Y. H. Jeon, and R. C. Semelka, "Body MR imaging: fast, efficient, and comprehensive," *Radiologic Clinics of North America*, vol. 52, no. 4, pp. 623–636, 2014.
- [2] C. Malamateniou, S. J. Malik, S. J. Counsell et al., "Motion-compensation techniques in neonatal and fetal MR imaging," *American Journal of Neuroradiology*, vol. 34, no. 6, pp. 1124–1136, 2013.
- [3] O. W. Hamer, D. A. Aguirre, G. Casola, J. E. Lavine, M. Woenckhaus, and C. B. Sirlin, "Fatty liver: imaging patterns and pitfalls," *Radiographics*, vol. 26, no. 6, pp. 1637–1653, 2006.
- [4] E. M. Merkle and R. C. Nelson, "Dual gradient-echo in-phase and opposed-phase hepatic MR imaging: a useful tool for evaluating more than fatty infiltration or fatty sparing," *Radiographics*, vol. 26, no. 5, pp. 1409–1418, 2006.
- [5] A. Ferreira, M. Ramalho, R. O. P. de Campos et al., "Comparison of T1-weighted in- and out-of-phase single shot magnetization-prepared gradient-recalled-echo with three-dimensional gradient-recalled-echo at 3.0 tesla: preliminary observations in abdominal studies," *Journal of Magnetic Resonance Imaging*, vol. 35, no. 5, pp. 1187–1195, 2012.
- [6] V. Herédia, M. Ramalho, R. O. P. de Campos et al., "Comparison of a single shot T1-weighted in- and out-of-phase magnetization prepared gradient recalled echo with a standard two-dimensional gradient recalled echo: preliminary findings," *Journal of Magnetic Resonance Imaging*, vol. 33, no. 6, pp. 1482–1490, 2011.
- [7] M. Ramalho, V. Herédia, R. O. P. De Campos, B. M. Dale, R. M. Azevedo, and R. C. Semelka, "In-phase and out-of-phase gradient-echo imaging in abdominal studies: intra-individual comparison of three different techniques," *Acta Radiologica*, vol. 53, no. 4, pp. 441–449, 2012.
- [8] R. C. Semelka, D. R. Martin, and N. C. Balci, "Magnetic resonance imaging of the liver: how I do it," *Journal of Gastroenterology and Hepatology*, vol. 21, no. 4, pp. 632–637, 2006.
- [9] S. Jiang, H. Xue, A. Glover, M. Rutherford, D. Rueckert, and J. V. Hajnal, "MRI of moving subjects using multislice Snapshot images with volume reconstruction (SVR): application to fetal, neonatal, and adult brain studies," *IEEE Transactions on Medical Imaging*, vol. 26, no. 7, pp. 967–980, 2007.
- [10] J. G. Pipe, "Motion correction with PROPELLER MRI: application to head motion and free-breathing cardiac imaging," *Magnetic Resonance in Medicine*, vol. 42, no. 5, pp. 963–969, 1999.
- [11] R. C. Semelka and T. K. G. Helmberger, "Contrast agents for mr imaging of the liver," *Radiology*, vol. 218, no. 1, pp. 27–38, 2001.
- [12] R. M. Azevedo, R. O. P. de Campos, M. Ramalho, V. Herédia, B. M. Dale, and R. C. Semelka, "Free-breathing 3D T1-weighted gradient-echo sequence with radial data sampling in abdominal MRI: preliminary observations," *American Journal of Roentgenology*, vol. 197, no. 3, pp. 650–657, 2011.
- [13] S. Bamrungchart, E. M. Tantaway, E. C. Midia et al., "Free breathing three-dimensional gradient echo-sequence with radial data sampling (radial 3D-GRE) examination of the pancreas: comparison with standard 3D-GRE volumetric interpolated breathhold examination (VIBE)," *Journal of Magnetic Resonance Imaging*, vol. 38, no. 6, pp. 1572–1577, 2013.
- [14] H. Chandarana, T. K. Block, A. B. Rosenkrantz et al., "Free-breathing radial 3D fat-suppressed T1-weighted gradient echo sequence: a viable alternative for contrast-enhanced liver imaging in patients unable to suspend respiration," *Investigative Radiology*, vol. 46, no. 10, pp. 648–653, 2011.
- [15] K. W. Kim, J. M. Lee, Y. S. Jeon et al., "Free-breathing dynamic contrast-enhanced MRI of the abdomen and chest using a radial gradient echo sequence with K-space weighted image contrast (KWIC)," *European Radiology*, vol. 23, no. 5, pp. 1352–1360, 2013.
- [16] V. Rasche, R. W. de Boer, D. Holz, and R. Proksa, "Continuous radial data acquisition for dynamic MRI," *Magnetic Resonance in Medicine*, vol. 34, no. 5, pp. 754–761, 1995.
- [17] K. S. Hee and L. Dougherty, "Dynamic MRI with projection reconstruction and KWIC processing for simultaneous high spatial and temporal resolution," *Magnetic Resonance in Medicine*, vol. 52, no. 4, pp. 815–824, 2004.
- [18] E. Spuentrup, M. Katoh, A. Buecker et al., "Free-breathing 3D steady-state free precession coronary MR angiography with radial k-space sampling: comparison with cartesian k-space sampling and cartesian gradient-echo coronary MR angiography—pilot study," *Radiology*, vol. 231, no. 2, pp. 581–586, 2004.
- [19] H. Chandarana, L. Feng, T. K. Block et al., "Free-breathing contrast-enhanced multiphase MRI of the liver using a combination of compressed sensing, parallel imaging, and golden-angle radial sampling," *Investigative Radiology*, vol. 48, no. 1, pp. 10–16, 2013.
- [20] J. H. Kim, J. M. Lee, J. H. Park et al., "Solid pancreatic lesions: characterization by using timing bolus dynamic contrast-enhanced MR imaging assessment—a preliminary study," *Radiology*, vol. 266, no. 1, pp. 185–196, 2013.
- [21] Y. Fujinaga, A. Ohya, H. Tokoro et al., "Radial volumetric imaging breath-hold examination (VIBE) with k-space weighted image contrast (KWIC) for dynamic gadoteric acid (Gd-EOB-DTPA)-enhanced MRI of the liver: advantages over Cartesian VIBE in the arterial phase," *European Radiology*, vol. 24, no. 6, pp. 1290–1299, 2014.
- [22] K. P. Pruessmann, M. Weiger, M. B. Scheidegger, and P. Boesiger, "SENSE: sensitivity encoding for fast MRI," *Magnetic Resonance in Medicine*, vol. 42, no. 5, pp. 952–962, 1999.
- [23] M. H. Yu, J. M. Lee, J. H. Yoon, B. Kiefer, J. K. Han, and B. I. Choi, "Clinical application of controlled aliasing in parallel imaging results in a higher acceleration (CAIPIRINHA)-volumetric interpolated breathhold (VIBE) sequence for gadoteric acid-enhanced liver MR imaging," *Journal of Magnetic Resonance Imaging*, vol. 38, no. 5, pp. 1020–1026, 2013.
- [24] K. L. Wright, M. W. Harrell, J. A. Jesberger et al., "Clinical evaluation of CAIPIRINHA: comparison against a GRAPPA standard," *Journal of Magnetic Resonance Imaging*, vol. 39, no. 1, pp. 189–194, 2014.
- [25] Y. S. Park, C. H. Lee, I. S. Kim et al., "Usefulness of controlled aliasing in parallel imaging results in higher acceleration in gadoteric acid-enhanced liver magnetic resonance imaging to clarify the hepatic arterial phase," *Investigative Radiology*, vol. 49, no. 3, pp. 183–188, 2014.
- [26] M. S. Davenport, B. L. Vigiante, M. M. Al-Hawary et al., "Comparison of acute transient dyspnea after intravenous administration of gadoteric acid disodium and gadobenat dimeglumine: effect on arterial phase image quality," *Radiology*, vol. 266, no. 2, pp. 452–461, 2013.

- [27] K. Mohajer, A. Frydrychowicz, J. B. Robbins, A. G. Loeffler, T. D. Reed, and S. B. Reeder, "Characterization of hepatic adenoma and focal nodular hyperplasia with gadoxetic acid," *Journal of Magnetic Resonance Imaging*, vol. 36, no. 3, pp. 686–696, 2012.
- [28] U. Motosugi, T. Ichikawa, H. Morisaka et al., "Detection of pancreatic carcinoma and liver metastases with gadoxetic acid-enhanced MR imaging: comparison with contrast-enhanced multi-detector row CT," *Radiology*, vol. 260, no. 2, pp. 446–453, 2011.
- [29] J. A. Pietryga, L. M. Burke, D. Marin, T. A. Jaffe, and M. R. Bashir, "Respiratory motion artifact affecting hepatic arterial phase imaging with gadoxetate disodium: examination recovery with a multiple arterial phase acquisition," *Radiology*, vol. 271, no. 2, pp. 426–434, 2014.
- [30] M. D. Agrawal, P. Spincemaille, K. W. Mennitt et al., "Improved hepatic arterial phase MRI with 3-second temporal resolution," *Journal of Magnetic Resonance Imaging*, vol. 37, no. 5, pp. 1129–1136, 2013.
- [31] H. J. Michaely, J. N. Morelli, J. Budjan et al., "CAIPIRINHA-Dixon-TWIST (CDT)-Volume-interpolated breath-hold examination (VIBE): a new technique for fast time-resolved dynamic 3-dimensional imaging of the abdomen with high spatial resolution," *Investigative Radiology*, vol. 48, no. 8, pp. 590–597, 2013.
- [32] K. Mori, H. Yoshioka, N. Takahashi et al., "Triple arterial phase dynamic MRI with sensitivity encoding for hypervascular hepatocellular carcinoma: comparison of the diagnostic accuracy among the early, middle, late, and whole triple arterial phase imaging," *The American Journal of Roentgenology*, vol. 184, no. 1, pp. 63–69, 2005.
- [33] H.-S. Hong, H. S. Kim, M.-J. Kim, J. de Becker, D. G. Mitchell, and M. Kanematsu, "Single breath-hold multiarterial dynamic MRI of the liver at 3T using a 3D fat-suppressed keyhole technique," *Journal of Magnetic Resonance Imaging*, vol. 28, no. 2, pp. 396–402, 2008.